EXCITED-STATE DYNAMICS IN DONOR-ACCEPTOR SYSTEMS FOR ENERGY CONVERSION

JULIAN ROBERT OCHSMANN

Dissertation

zur Erlangung des Grades
"Doktor der Naturwissenschaften"
im Promotionsfach Chemie
am Fachbereich Chemie, Pharmazie und Geowissenschaften
der Johannes Gutenberg-Universität
in Mainz

Oktober 2015

DECLARATION

I hereby declare that I wrote this dissertation submitted without any unauthorized external assistance and used only sources acknowledged in the work. All textual passages which are appropriated verbatim or paraphrased from published and unpublished texts as well as all information obtained from oral sources are duly indicated and listed in accordance with bibliographical rules. In carrying out this research, I complied with the rules of standard scientific practice as formulated in the statutes of Johannes Gutenberg University Mainz to insure standard scientific practice.

Mainz, November 2015

Julian Robert Ochsmann

SUMMARY

This thesis covers the investigation of excited-state dynamics in donor-acceptor systems for energy conversion by means of ultrafast time-resolved optical spectroscopy. The main part of this work focuses on the photophysics of organic solar cells consisting of diketopyrrolopyrrole-based (DPP) low-bandgap copolymers as electron donors blended with fullerenes as electron acceptors in a bulk heterojunction morphology.

A second part is dedicated to the study of artificial primary photosynthetic reaction centers based on porphyrins, quinones and ferrocenes as light harvesting, electron accepting, and electron donating moiety, respectively, with the aim to create long-lived charge-separated states.

Time-resolved photoluminescence spectroscopy and transient absorption spectroscopy revealed that singlet-exciton lifetimes in the low-bandgap polymers PTDPP-TT and PFDPP-TT are short (< 20 ps) and that in blends of the polymers with $PC_{71}BM$ geminate recombination of bound charge-transfer states is a major loss channel. In addition, fast non-geminate recombination of free charges into the polymers triplet states was observed in both blend systems. For the PDPP5T:$PC_{71}BM$ donor-acceptor system it was found that processing the polymer:fullerene blend with a high-boiling point co-solvent, i.e. *ortho*-dichlorobenzene (o-DCB), drastically changes active layer morphology and increases solar cell performance, due to more intimately mixed donor and acceptor materials and pronounced percolation pathways to the electrodes, facilitating charge carrier generation and extraction. Fast triplet-state formation was observed in both of the PDPP5T:$PC_{71}BM$ blend systems, as the polymer triplet state can be populated from triplet charge-transfer states. Multivariate curve resolution (MCR) analysis showed a strong fluence dependence pointing to non-geminate recombination of charges into the polymer triplet-state.

On the artificial primary photosynthetic reaction centers transient absorption spectroscopy verified that photoinduced charge transfer is efficient in quinone-porphyrin (Q-P) and porphyrin-ferrocene (P-Fc) diads as well as in quinone-porphyrin-ferrocene (Q-P-Fc) triads. However, it was also shown that in the P-Fc and Q-P-Fc systems the charge-separated states recombine into the respective porphyrin triplet state. The charge-separated state in the Q-P diad could significantly be stabilized upon the addition of a Lewis acid.

ZUSAMMENFASSUNG

In dieser Arbeit werden die Dynamiken angeregter Zustände in Donor-Akzeptor Systemen für Energieumwandlungsprozesse mit ultraschneller zeitaufgelöster optischer Spektroskopie behandelt. Der Hauptteil dieser Arbeit legt den Fokus auf die Erforschung der Photophysik organischer Solarzellen, deren aktive Schichten aus diketopyrrolopyrrole (DPP) basierten Polymeren mit kleiner Bandlücke als Elektronendonatoren und Fullerenen als Elektronenakzeptoren bestehen.

Ein zweiter Teil widmet sich der Erforschung von künstlichen primären Photosynthesereaktionszentren, basierend auf Porphyrinen, Quinonen und Ferrocenen, die jeweils als Lichtsammeleinheit, Elektronenakzeptor beziehungsweise als Elektronendonatoren eingesetzt werden, um langlebige ladungsgetrennte Zustände zu erzeugen.

Zeitaufgelöste Photolumineszenzspektroskopie und transiente Absorptionsspektroskopie haben gezeigt, dass Singulettexzitonenlebenszeiten in den Polymeren PTDPP-TT und PFDPP-TT Polymeren kurz sind ($< 20\,\mathrm{ps}$) und dass in Mischungen der Polymere mit $PC_{71}BM$ geminale Rekombination von gebundenen Ladungstransferzuständen ein Hauptverlustkanal ist. Zudem wurde in beiden Systemen schnelle nichtgeminale Rekombination freier Ladungen zu Triplettzuständen auf dem Polymer beobachtet. Für das Donor-Akzeptor System PDPP5T:$PC_{71}BM$ wurde nachgewiesen, dass die Zugabe eines Lösungsmittels mit hohem Siedepunkt, und zwar *ortho*-Dichlorbenzol, die Morphologie der aktiven Schicht stark beeinflusst und die Solarzelleneffizienz verbessert. Der Grund hierfür ist, dass die Donator- und Akzeptormaterialien besser durchmischt sind und sich Perkolationswege zu den Elektroden ausgebildet haben, was zu einer verbesserten Ladungsträgergeneration und Extraktion führt. Schnelle Bildung des Triplettzustands wurde in beiden PDPP5T:$PC_{71}BM$ Systemen beobachtet, da der Triplettzustand des Polymers über Laungstransferzustände mit Triplettcharakter populiert werden kann. "Multivariate curve resolution" (MCR) Analyse hat eine starke Intensitätsabhängigkeit gezeigt, was auf nichtgeminale Ladungsträgerrekombination in den Triplettzustand hinweist.

In den künstlichen primären Photosynthesereaktionszentren hat transiente Absorptionsspektroskopie bestätigt, dass photoinduzierter Ladungstransfer in Quinon-Porphyrin (Q-P) und Porphyrin-Ferrocen (P-Fc) Diaden sowie in Quinon-Porphyrin-Ferrocen (Q-P-Fc) Triaden effizient ist. Es wurde jedoch auch gezeigt, dass in den P-Fc und Q-P-Fc Systemen die ladungsgetrennten Zustände in den Triplettzustand der jeweiligen Porphyrine rekombinieren. Der ladungsgetrennte Zustand konnte in der Q-P Diade durch Zugabe einer Lewissäure signifikant stabilisiert werden.

현 논문은 ultrafast time-resolved optical spectroscopy를 이용하여 에너지 변환 도너-억셉터 시스템 내의 excited-state dynamics를 다루었다. 현 연구는 bulk heterojunction morphology를 구성하는 도너 역할의 diketopyrrolopyrrole-based (DPP) low-bandgap copolymer와 억셉터 역할의 fullerene이 혼합된 유기태양전지의 photophysics를 보고하고자 한다.

두 번째 파트는 long-lived charge-separated states을 형성하기 위해 집광성 물질의 porphyrins, 전자받개 quinones과 전자주개 ferrocenes을 사용한 인공 광합성 반응을 주로 다루었다.

Time-resolved photoluminescence spectroscopy 와 transient absorption spectroscopy를 이용하여, low-bandgap polymers PTDPP-TT와 PFDPP-TT 내에서 singlet-exciton의 lifetimes이 ($< 20\,\mathrm{ps}$) 미만임을 밝히고, 폴리머와 $PC_{71}BM$의 blend 상에서 bound charge-transfer states의 geminate recombination이 주요한 loss channel 임을 보고하였다. 또한, polymers triplet states내로 자유전하의 빠른 non-geminate recombination이 두 blend system에서 모두 관찰되었다. PDPP5T:$PC_{71}BM$ 도너-억셉터 시스템 내에서, 높은 끓는 점을 가지는 두 용액 (i.e. *ortho*-dichlorobenzene (o-DCB))을 사용한 polymer:fullerene blend는 active layer의 모폴로지를 급격하게 변화시키고 태양전지의 효율을 증가시킨다. 이는 친밀히 섞인 도너/억셉터 물질과 전극으로의 뛰어난 percolation으로 인하여 용이한 전하 생성과 extraction을 야기하기 때문이다. Polymer triplet state이 triplet charge-transfer states로부터 형성된 것과 같이 PDPP5T:$PC_{71}BM$ blend system에서 빠른 triplet-state 형성이 관찰되었다. Multivariate curve resolution (MCR) 분석은 전하의 non-geminate recombination이 폴리머 triplet-state과 밀접하게 의존하고 있음을 보여주었다.

인공적인 광합성 반응시, transient absorption spectroscopy은 photoinduced charge transfer이 quinone-porphyrin-ferrocene (Q-P-Fc) triads에서와 같이 quinone-porphyrin (Q-P)와 porphyrin-ferrocene (P-Fc) diads내에서 매우 효과적임을 증명하였다. 그러나 P-Fc 와 Q-P-Fc system내에서 전하분리상태는 각각의 porphyrin triplet state와 재결합함을 보여주었다.

PUBLICATIONS

SCIENTIFIC PUBLICATIONS PRESENTED IN THIS WORK

J. R. Ochsmann, D. Chandran, D. W. Gehrig, H. Anwar, P.K. Madathil, K.-S. Lee, and F. Laquai, "Triplet state formation in photovoltaic blends of DPP-type copolymers and $PC_{71}BM$", *Macromol. Rapid Commun.* 2015, 36, 1122-1128. DOI: 10.1002/marc.201400714

J. R. Ochsmann, M. Turbiez, and F. Laquai, "Excited-state dynamics in PDPP5T:$PC_{71}BM$ photovoltaic blends", *in preparation*

J. Melomedov, J. R. Ochsmann, M. Meister, F. Laquai and K. Heinze "Tuning reductive and oxidative photoinduced electron transfer in amide linked anthraquinone-porphyrin-ferrocene architectures", *Eur. J. Inorg. Chem.* 2014, 11, 1984-2001. DOI: 10.1002/ejic.201400118

J. Melomedov, J. R. Ochsmann, M. Meister, F. Laquai and K. Heinze "Aminoferrocene and Ferrocene Amino Acid as Electron Donors in Modular Porphyrin-Ferrocene and Porphyrin-Ferrocene-Porphyrin Conjugates", *Eur. J. Inorg. Chem.* 2014, 18, 2902-2915. DOI: 10.1002/ejic.201402138

FURTHER PUBLICATIONS

A. K. C. Mengel, C. Förster, A. Breivogel, K. Mack, J. R. Ochsmann, F. Laquai, V. Ksenofontov, and K. Heinze "A Heteroleptic Push-Pull Substituted Iron(II) Bis(tridentate) Complex with Low-Energy Charge-Transfer States", *Chem. Eur. J.* 2014, 2, 704-714. DOI: 10.1002/chem.201404955

D. Chandran, T. Marszalek, W. Zajaczkowski, P. K. Madathil, R. K. Vijayaraghavan, Y.-H. Koh, S.-Y. Park, J. R. Ochsmann, W. Pisula, K.-S. Lee, "Thin film morphology and charge carrier mobility of diketo-pyrrolopyrrole based conjugated polymers", *Polymer* 2015, 73, 205-213. DOI: 10.1016/j.polymer.2015.07.043

CONFERENCE CONTRIBUTIONS

02/2013	Poster presentation at IRTG Meeting, Seoul, Korea.
03/2013	Poster presentation at the annual meeting of the German Physical Society (DPG), Regensburg, Germany.
05/2013	Poster presentation at Hybrid and Organic Photovoltaics (HOPV) Conference 2013, Seville, Spain.
08/2013	Poster presentation at IRTG Meeting, Hamburg, Germany.
12/2013	Poster presentation at MRS Fall Meeting, Boston, MA, USA.
02/2014	Oral presentation at IRTG Meeting, Daejon, Korea.
04/2014	Oral presentation at MRS Spring Meeting, San Francisco, CA, USA.
07/2014	Poster presentation at IRTG Meeting, Mainz, Germany.
02/2015	Poster presentation at IRTG Meeting, Gonjiam, Korea.
03/2015	Oral presentation at the annual meeting of the German Physical Society (DPG), Berlin, Germany.
05/2015	Poster presentation at Hybrid and Organic Photovoltaics (HOPV) Conference 2015, Rome, Italy.
07/2015	Poster presentation at IRTG Meeting, Berlin, Germany.
11/2015	Poster presentation at Solar Future 2015 Symposium, KAUST, Saudi Arabia.

ACKNOWLEDGMENTS

The acknowledgments are only contained in the print version of this thesis.

CONTENTS

LIST OF FIGURES

LIST OF TABLES

ACRONYMS

A acceptor

a-Si amorphous silicon

AFM atomic force microscopy

AM 1G air mass 1 global

AM 1.5G air mass 1.5 global

BDT benzodithiophene

BDTT thienylbenzodithiophene

BHJ bulk heterojunction

BT benzothiadiazole

CCD charge coupled device

CT charge-transfer

CuPC copper phthalocyanine

CV cyclic voltammetry

cw continuous wave

D donor

DIO 1,8-diiodooctane

DOS density of states

DPP diketopyrrolopyrrole

DSSC dye sensitized solar cells

EA electro-absorption

EFA evolving factor analysis

EQE external quantum efficiency

FF fill factor

FRET Förster Resonance Energy Transfer

GDM Gaussian Disorder Model

GPC Gel permeation chromatography

GSB ground state bleach

HOMO highest occupied molecular orbital

IC internal conversion

ICBA indene-C60-bis-adduct

IPCC Intergovernmental Panel on Climate Change

IPCE incident photon to current efficiency

ISC intersystem crossing

ITO indium tin oxide

IQE internal quantum efficiency

J_{SC} short circuit current density

$J-V$ current-voltage

LUMO lowest unoccupied molecular orbital

MCR multivariate curve resolution

MCP multichannel plate

MEH-PPV poly(2-methoxy-5-(2'-ethyl-hexyloxy)-1,4-phenylene vinylene)

MDMO-PPV poly(2-methoxy-5-(3,7-dimethyloctyloxy)-1,4-phenylene vinylene)

MIM metal-insulator-metal

MPP maximum power point

Nd:YAG neodymium-doped yttrium aluminum garnet

Nd:YVO_4 neodymium-doped yttrium orthovanadate

NREL National Renewable Energy Laboratory

NIR near-infrared

NDI naphthalene diimides

o-DCB *ortho*-dichlorobenzene

OLED organic light emitting diode

OFET organic field effect transistor

OPA optical parametric amplifiers

OPV organic photovoltaic

OSC organic solar cell

O_3 ozone

$PC_{61}BM$ [6,6]-phenyl-C61-butyric acid methyl ester

$PC_{71}BM$ [6,6]-phenyl-C71-butyric acid methyl ester

PCE power conversion efficiency

PDI perylene diimide

PDPP5T poly(diketopyrrolopyrrole-*alt*-quinquethiophene)

PTDPP-TT poly[3,6-dithiene-2-yl-2,5-di(2-decyltetradecyl)-pyrrolo[3,4-c]pyrrole-1,4-dione-5′,5"-diyl-*alt*-thieno[3,2-b]thienyl]

PFDPP-TT poly[3,6-difuran-2-yl-2,5-di(2-decyltetradecyl)-pyrrolo[3,4-c]pyrrole-1,4-dione-5′,5"-diyl-*alt*-thieno[3,2-b]thienyl]

PDPPTPT poly[2,5-bis(2-hexyldecyl)-2,3,5,6-tetrahydro-3,6-dioxopyrrolo[3,4-c]pyrrole-1,4-diyl-*alt*-[2,2′-(1,4-phenylene)bisthiophene]-5,5′-diyl]

PCDTBT poly[N-9′-heptadecanyl-2,7-carbazole-alt-5,5-(4′,7′-di-2-thienyl-2′,1′,3′-benzothiadiazole)]

PCPDTBT poly[2,6-(4,4-bis-(2-ethylhexyl)-4H-cyclopenta[2,1-b;3,4-b′]-dithiophene)-alt-4,7-(2,1,3-benzothiadiazole)

PSBTBT Poly[(4,4-dioctyldithieno(3,2-b:2′,3′-d)silole)-2,6-diyl-alt-(2,1,3-benzothiadiazole)-4,7-diyl]

PTB7 polythieno[3,4-*b*]-thiophene-*co*-benzodithiophene

$PffBT_4T$-2OD
Poly[(5,6-difluoro-2,1,3-benzothiadiazol-4,7-diyl)-alt-(3,3‴-di(2-octyldodecyl)-2,2′;5′,2″;5″,2‴-quaterthiophen-5,5‴-diyl)]

PdTAP palladium-tetraanthraporphyrin

PPV *p*-phenylene vinylene

PEDOT:PSS poly(3,4-ethylenedioxythiophene) poly(styrenesulfonate)

PIA photoinduced absorption spectroscopy

PIDT-PhanQ
poly(indacenodithiophene-co-phenanthro[9,10-b]quinoxaline)

PA photoinduced absorption

P3HT poly(3-hexylthiophene)

R2R roll-to-roll

SE stimulated emission

SKPM scanning Kelvin probe microscopy

Si-PCPDTBT Poly[(4,4-dioctyldithieno(3,2-b:2′,3′-d)silole)-2,6-diyl-alt-(2,1,3-benzothiadiazole)-4,7-diyl]

SMU source measure unit

SSC spatially separated charges

SVD singular value decomposition

TA transient absorption

TEM transmission electron microscopy

TT thieno[3,4-*b*]thiophene

TOF time-of-flight

TR-PL time-resolved photoluminescence

UV ultra-violet

UV-vis ultra-violet-visible

vis visible

vis-NIR visible-near infrared

V_{OC} open circuit voltage

YVO_4 yttrium orthovanadate

IAF 5-Iodoacetamidofluorescein

1 INTRODUCTION

Meeting the world's ever growing energy demand is one of today's most challenging problems. As the world population and its wealth rises, the consumption of resources rises as well. In the 20th century the world population quadrupled as the world's energy consumption increased by a factor of 16.[1] Assuming that every person on the planet will have the same standard of living as the inhabitants of the most developed countries, the energy needs will triple or quadruple by 2050.[2] This exponentially growing demand of energy cannot be met by the limited availability of fossil energy sources.[3] In addition, anthropogenic global warming primarily caused by the emission of greenhouse gases from industry, transport, and agriculture is a serious threat. In 2014, the Intergovernmental Panel on Climate Change (IPCC) reported that the human influence on the climate system is clear and that since the 1950s, the atmosphere and ocean have warmed, the amounts of ice and snow have decreased and sea level has risen.[4] Extreme weather events such as warm temperature extremes and heavy precipitation events in a number of regions have increased, which can lead to decreased crop yields or the flooding of populated areas.[5]

These examples show that it is of utmost importance to find alternative and sustainable energy sources, in order to meet the increasing global energy challenge. In this respect, solar power holds huge potential, as solar irradiation, striking the surface of the earth, covers approximately 10^4 times the world's energy demand.[1] Additionally, the sun is a stable energy source, which is expected to last for another 5 billion years.[6] Among the technologies harvesting solar power, photovoltaics is the most established with an increasing number of solar cell module installations worldwide. These commercially available modules are built of mainly silicon-based solar cells, which exhibit favorable power conversion efficiencies exceeding 20 % and good stability with lifespans of 20 to 30 years.[7] However, their production and installation is energy-intensive and expensive.[1]

A promising alternative technology is organic photovoltaics (OPV), which have the potential of producing solar cells using less energy and at lower costs. Organic solar cells are based on organic semiconducting small molecules or polymers, which can be evaporated or solution processed onto a variety of differently shaped substrates, including flexible and light-weight substrates.[2] This opens up new applications such as integration of OPV into portable electronic devices or into clothes and other textiles. In the field of building-integrated

photovoltaics, semi-transparent organic solar cells could be used to tint windows and to produce electrical energy at the same time.

A record efficiency of 11.5 % for an organic single-junction solar cell was achieved in June 2015 as certified by the National Renewable Energy Laboratory (NREL).[8] Although organic solar cells on the lab scale have surpassed the 10-%-benchmark, which was seen by many as the hurdle for commercialization, long-term stability and large-scale production is still an issue.[9] Therefore, in order to be competitive with their inorganic counterparts, the efficiencies of organic solar cells have to be further improved. The primary photoexcitations in organic solar cells are tightly bound electron-hole pairs, so-called excitons, which require a donor-acceptor structure with an energy offset in order to be separated into free charges. Improvements in device performance are mainly driven by the synthesis of novel donor and acceptor materials with improved absorption properties and optimized energy level alignments.

A promising strategy to improve the light harvesting properties and thereby the efficiency of organic solar cells is to design so-called low-bandgap polymers as electron-donor materials with an absorption maximum shifted towards the near-infrared wavelength region. When such a low-bandgap polymer is mixed with a suitable electron acceptor having a complementary absorption in the UV-vis region, such as $PC_{71}BM$, broader overlap of the absorption with the spectrum of the sun is achieved, compared to other photoactive blends based on mid-bandgap polymers such as poly(3-hexylthiophene) (P3HT). When low-bandgap polymer/fullerene blends are used as the active layer in organic solar cells one would expect an increase in photocurrent, due to the larger number of photons absorbed. However, often the efficiency and the photocurrent of OPV devices based on low-bandgap polymers are much lower than expected. Thus, it is essential to gain a deeper understanding of the underlying mechanisms that lead to a reduced device efficiency, in order to guide the design and synthesis of novel donor-acceptor systems for use in organic photovoltaics.

Another attractive approach of using solar energy is artificial photosynthesis. Nature shows us very impressively how to harvest, convert and store the abundant energy provided by the sun. In photosynthetic reaction centers of plants algae, and bacteria absorbed photons are converted very efficiently into chemical energy via a cascade of charge-transfer reactions. Considerable research effort has been devoted to mimic the primary charge-transfer reaction centers of natural photosystems based on molecular donor-acceptor systems.[10, 11, 12, 13] Artificial primary reaction centers consist of non-covalently or covalently bound donor-acceptor units, where porphyrins, ferrocenes or carotenoid polyenes are used as donor components and quinones, porphyrins or fullerenes are used as acceptor components.[14] In this

thesis, covalently-linked quinone-porphyrin and porphyrin-ferrocene dyads as well as quinone-porphyrine-ferrocene triads are investigated.

In this work, the excited-state dynamics in donor-acceptor systems for organic solar cells and for artificial photosynthesis reaction centers are investigated with sophisticated optical spectroscopy techniques, such as time-resolved photoluminescence spectroscopy (TR-PL) and ultrafast transient absorption (TA) pump-probe spectroscopy in combination with advanced data analysis methods such as multivariate curve resolution (MCR) analysis. The main focus of this work is to unravel the different photophysical processes occurring in organic solar cells based on low-bandgap polymers and to identify loss channels leading to reduced efficiency of the devices.

This thesis consists of 8 chapters. This chapter presents a motivation for this work and briefly introduces the topics treated. *Chapter 2* provides the theoretical background needed for understanding the physics of molecular systems. Furthermore organic solar cells and the photophysics occurring therein are presented. Finally, an overview of materials for organic solar cells is given together with a short summary of the current state of research on organic photovoltaics. *Chapter 3* introduces the experimental methods used in this work. *Chapter 4* examines the excited-state dynamics of polymers PTDPP-TT and PFDPP-TT. Triplet-state formation in blends of the respective polymers with $PC_{71}BM$ is discussed. *Chapter 5* deals with the comprehensive study of the photophysics occurring in the polymer PDPP5T and compares PDPP5T:$PC_{71}BM$ blends prepared under different processing conditions. *Chapter 6* analyzes photoinduced electron transfer pathways in amide-linked anthraquinone-porphyrin-ferrocene structures, mimicing photosynthesic reaction centers. *Chapter 7* presents the synthesis of new Porphyrin-Ferrocene and Porphyrin-Ferrocene-Porphyrin conjugates and their excited-state dynamics. The results presented in Chapters 4, 6 and 7 were published in peer-reviewed journals and are therefore a collection of published articles. The articles presented in Chapters 6 and 7 are the result of a collaboration with the group of Professor Katja Heinze from the Johannes Gutenberg-Universität Mainz. My contribution to this work are pages 125-127 (pp 1997-1999) in Chapter 6 and pages 141-143 (pp 2911-2912) in Chapter 7 presenting the results of time-resolved transient absorption spectroscopy of selected compounds. *Chapter 8* summarizes the results obtained on organic solar cells and compares it to other recent publications. Moreover, a critical acclaim of this work is given together with suggestions for future research.

2 THEORETICAL BACKGROUND

2.1 ORGANIC SEMICONDUCTORS

Organic electronic devices rely on organic semi-conducting small molecules, oligomers or polymers. They are characterized by a backbone of carbon atoms linked by an alternation of single and double-bonds, giving rise to the so called conjugated π-electron system which is the origin for their semi-conducting properties. In 1977, Chiang et al. discovered that iodine-doped polyacetylene is highly conductive,[15] laying the foundation for extensive research on organic conducting and semi-conducting materials. This discovery was rewarded in 2000 with a Nobel Prize for Chemistry to Alan Heeger, Alan A. MacDiarmid and Hideki Shirakawa.[16]

The electronic structure of organic semiconductors derives from the chemical properties of carbon. The carbon atom has a total of six electrons in the configuration $1s^2 2s^2 2p^2$. The four electrons in the outer shell are valence electrons that are involved in the binding processes. The 2s and 2p orbitals form hybrid orbitals which are linear combinations of the wave functions of the atomic orbitals. In organic semiconductors planar trigonal sp^2-hybrid orbitals are formed from the 2s, $2p_x$ and $2p_y$ orbitals leading to coplanar 120° binding angles between the atoms participating in the binding process. The bonds formed by sp^2-hybrid orbitals are called σ-bonds. The fourth electron in the $2p_z$ orbital, that is perpendicular to the plane formed by the sp^2-orbitals, also forms a π-bond with another carbon atom. Thus, a double bond between two carbon atoms is created. The simplest example for such a molecule that is forming σ- and π-bonds by sp^2-hybridization is the ethylene-molecule C_2H_4. Figure 1 shows the structure of ethylene (a) and the electron density of the carbon atoms in the ethylene molecule (b and c).

By adding a finite number of carbon atoms in a linear chain one obtains polyacetylene, where the carbon atoms are linked by an alternation of single and double bonds. The electrons, forming the σ-bonds, are localized between the carbon atoms and do not contribute to electrical conductivity, while the electrons in the π-orbitals are delocalized over the polymer chain and give rise to the semiconducting properties of conjugated molecules. The π-electron system is also responsible for the optical properties of conjugated small molecules and polymers, where the bonding π-orbital is usually the highest occupied molecular orbital (HOMO) and the anti bonding π^*-orbital is the lowest unoccupied molecular orbital (LUMO). The energetic differ-

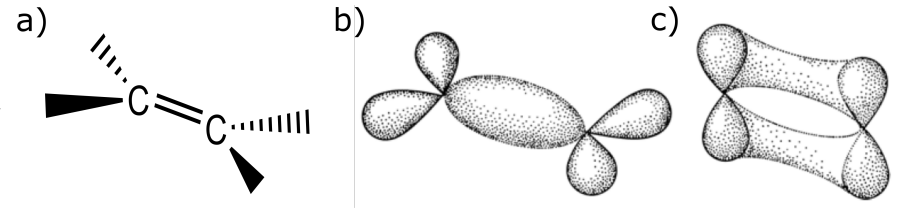

Figure 1: (a) Chemical Structure of ethylene. (b) Electron density of the hybridized carbon electrons in ethylene (trigonal sp^2-hybridization). (c) Electron density of the $2p_z$ electrons in the π-bond of ethylene. Figure b and c reprinted from Haken and Wolf,[17] figure 4.17. chapter 4, page 73, with permission of Springer Science+Business Media.

ence between HOMO and LUMO is often defined as the band-gap of organic semiconductors. Optical transitions occur via an excitation of an electron from the π-orbital into the π^*-orbital.

The width of the optical band-gap in organic semiconductors is determined by the size of the conjugated system, similar to a quantum well. The longer the conjugation length of the molecular system, the longer the wavelength with which the π to π^*-transition can be triggered/induced. Figure 2 shows different small conjugated molecules together with their main absorption wavelengths. The absorption wavelengths are in the UV-vis region with absorption coefficients around $10^5\,cm^{-1}$. This example shows that conjugated molecules are ideal materials for optoelectronic applications, because of their semiconductive nature as well as their favorable and tunable optical properties. In conjugated polymers the effective absorption characteristics also depend on the distribution of conjugation lengths, that is caused by structural distortions and system defects.

2.2 ABSORPTION AND EMISSION OF ELECTROMAGNETIC RADIATION BY MOLECULAR SYSTEMS

In this section we will shortly introduce the basic concepts of light-matter interaction. In particular, we will discuss absorption and emission processes in the framework of *Einstein's rate equations*, the *selection rules for optical transitions*, the *Franck-Condon Principle*, and the attenuation of light by matter, described by the *Lambert-Beer-Bouger-law*.

2.2.1 *Absorption, induced and spontaneous emission - Einstein coefficients*

When a molecule in the state k with energy E_k is placed into a radiation field with spectral energy density $w_\nu(\nu)$ it can absorb a photon with a certain energy $h\nu$ which will excite the molecule into a higher state i with the energy $E_i = E_k + h\nu$. This transition is called induced

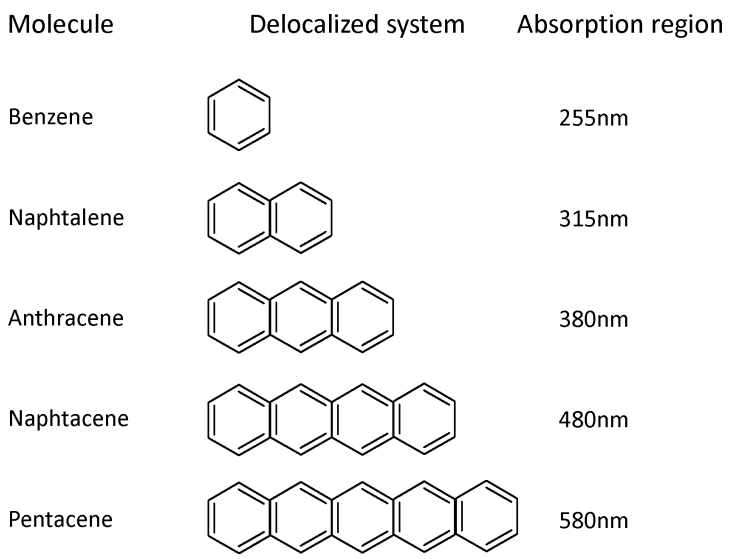

Figure 2: Acenes as an example for conjugated small molecules together with their corresponding absorption regions. With increasing size of the π-electron system the main absorption wavelength also increases. Figure adapted from Dickerson and Geis.[18]

absorption and occurs with a certain probability that depends on the frequency of the electromagnetic radiation. The rate at which energy is taken up from the radiation field or the probability per second of this transition

$$\frac{dP_{ki}^{abs}}{dt} = B_{ki} w_\nu(\nu) \tag{1}$$

is proportional to the product of the *Einstein coefficient for absorption* B_{ki}, and the spectral energy density of the radiation field $w_\nu(\nu) = n(\nu)h\nu$ where $n(\nu)$ is the number of photons $h\nu$ per unit volume within the frequency interval $\Delta\nu = 1\,s^{-1}$.

An incident photon with the energy $h\nu = E_i - E_k$ can also interact with a molecule in the higher energy state i and trigger the emission of a second photon with the same energy and propagation direction, setting the molecule into the lower state k with the energy $E_k = E_i - h\nu$. This process is called induced (or stimulated) emission. The probability per second for this transition is, analogous to equation 1, given by

$$\frac{dP_{ik}^{ind.em.}}{dt} = B_{ik} w_\nu(\nu) \tag{2}$$

with the *Einstein coefficient for induced emission* B_{ik}.

A molecule in an excited state i can also spontaneously emit a photon of defined energy into an arbitrary direction. If we assume that it

emits a photon of the energy $h\nu = E_i - E_k$, then the probability for this transition is given by

$$\frac{dP_{ik}^{spont.em.}}{dt} = A_{ik} \tag{3}$$

where A_{ik} is the *Einstein coefficient for spontaneous emission*. This transition is only dependent on the wave functions of the initial i and final state k of the molecule, not on the radiation field.[19] Figure 3 visualizes the processes occurring in this simplified two level system.

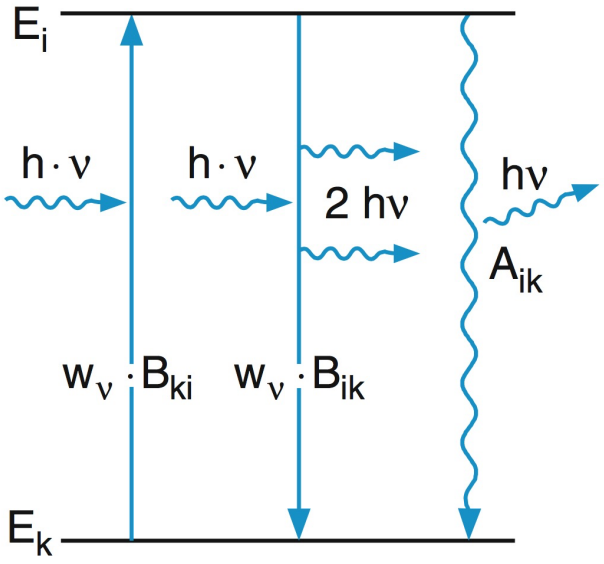

Figure 3: Simplified two-level energy diagram illustrating the processes of induced absorption, induced and spontaneous emission. Figure reprinted from Demtröder,[19] figure 7.1, chapter 7, page 248, with permission of Springer Science+Business Media.

Einstein showed that the transition rates for absorption and induced emission are equal[20]

$$B_{ki} = B_{ik} \tag{4}$$

and that

$$\frac{A_{ik}}{B_{ik}} = \frac{8\pi h\nu^3 n_0^3}{c^3}, \tag{5}$$

where n_0 is the index of refraction, and c is the speed of light. A relation between the *Einstein coefficient* B_{ki} and experimental absorption parameters is given by

$$B_{ki} = \frac{2303c}{hn_0N_A}\int \frac{\epsilon(\nu)d\nu}{\nu}, \tag{6}$$

where N_A is *Avogadro's number*, and $\epsilon(\nu)$ is the decadic molar extinction coefficient, which is a measure for the ability of a molecule in a given solvent to absorb light at a specific wavelength or frequency. The dimensionless quantity of the oscillator strength f is related to the spectrum of the molar extinction coefficient $\epsilon(\nu)$ and can be expressed by the Einstein coefficient B_{ki}

$$f = \frac{m_e h\nu}{\pi e^2} B_{ki} \tag{7}$$

with m_e and e being the mass and the elementary charge of the electron, respectively. Values for f are normalized so that its maximum value is 1. For $\pi \rightarrow \pi*$ - transitions f can take values close to 1 for certain compounds, when ϵ - values are in the order of $10^5\,cm^{-1}$. For further details see reference [21].

2.2.2 *Selection rules and Franck-Condon Principle*

When looking at a molecular system in solution or in the solid state one has to take into account the vibrational states of the molecule and the spin state of the electrons that are involved in electronic transitions as well. In quantum mechanics in principle all physical properties of a molecular system can be obtained if the wave function Ψ of the system is known. Ψ can be determined by solving the Schrödinger equation

$$\hat{H}\Psi = E\Psi, \tag{8}$$

where $\hat{H}$ is the Hamilton operator, and E is the total energy of the system. The optical transition probability between states k and i in the quantum mechanical formulation is given by

$$B_{ki} \propto | < \Psi_k | \mathbf{M} | \Psi_i > |^2 \tag{9}$$

where $\mathbf{M}$ is the dipole moment operator. Strictly speaking, in this case, it is the transition dipole moment, because it characterizes the transition between electronic states and does not describe a classical dipole moment. In the *Born-Oppenheimer approximation* it is assumed that the electronic and the vibrational part of the wave function Ψ are independent of each other, because electronic transitions are much faster than the vibrational motions of the nuclei. The transition of an electron from a lower to a higher state occurs on the time scale of $10^{-15}\,s$, while typical timescales of nuclear motions are on the order of 10^{-10} to $10^{-12}\,s$. Hence Ψ can be factorized into an electronic part, a vibrational part, and a spin part

$$\Psi = \psi_e \chi_\nu \psi_s. \tag{10}$$

With expression 10 the optical transition probability (equation 9) between two states i and k can be written as

$$B_{ki} \propto | < \psi_{ek}|\mathbf{M}|\psi_{ei} > |^2 | < \chi_{vk}|\chi_{vi} > |^2 | < \psi_{sk}|\psi_{si} > |^2. \quad (11)$$

The dipole moment operator $\mathbf{M}$ only appears in the first term since in line with the *Born-Oppenheimer approximation* the nuclei are too slow to react to the electronic movement and the spin is insensitive to the electric field. Equation 11 provides information about the transition probabilities. If any of the terms is zero, the transition probability will vanish and the corresponding transition will not be allowed. The transition probabilities are described by the *selection rules*:

- The first term in equation 11 describes dipole transitions: A transition is dipole allowed, when the transition moment $T_{ki} = | < \psi_{ek}|\mathbf{M}|\psi_{ei} > |$ is different from zero. Because the dipole moment operator $\mathbf{M}$ is a sum of odd operators, the wave functions ψ_{ek} and ψ_{ei} have to be of opposite symmetry for T_{ki} not to vanish.

- The second term is the square of the *Franck-Condon factor* that describes the amplitude of the vibrational transitions. It can be written as $| < \chi_{kv''}|\chi_{iv'} > |$, with the indices v'' and v' describing the vibrational states in the electronic levels i and k, respectively. According to the *Franck-Condon principle* which is based on the *Born-Oppenheimer approximation* electronic transitions occur vertically in a coordinate diagram from the lowest vibrational state $(v'' = 0)$ of the lower electronic level into the vibrational state of the upper electronic level whose wave function has the most overlap with the $(v'' = 0)$ wave function. Figure 4 shows an energy diagram visualizing the *Franck-Condon principle*.

- The third term is related to spin transitions. Only optical transitions, in which the spin of the electron does not change are allowed, i.e. the spin quantum number S has to be conserved. Only when there is strong spin-orbit coupling, as could be induced by an atom with a high atomic number Z, spin forbidden transitions become probable. This so called *heavy-atom effect*, leads to intersystem crossing between singlet and triplet states.

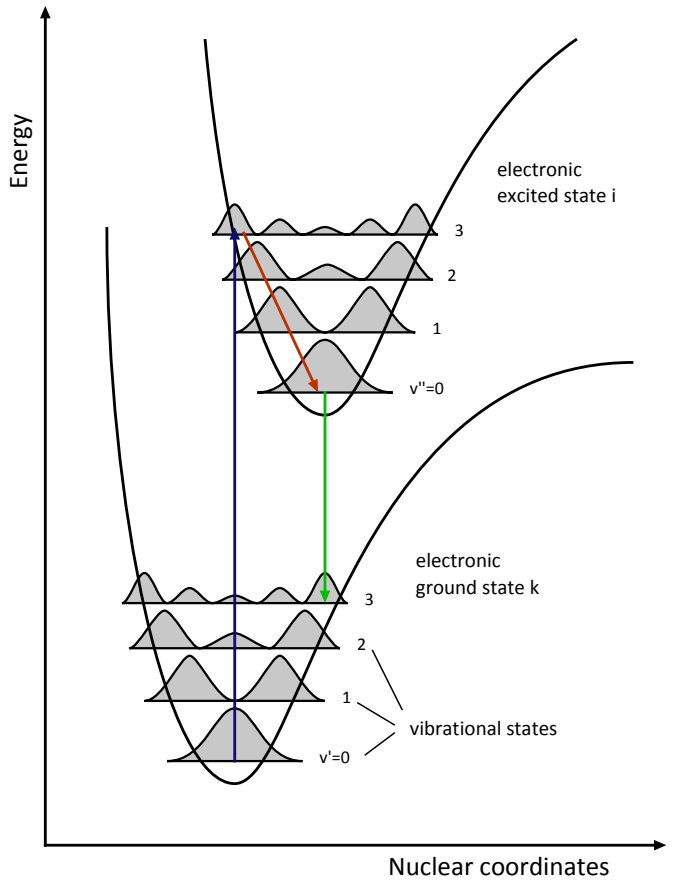

Figure 4: Schematic illustration of the *Franck-Condon principle*. Because electronic transitions occur much faster than nuclear vibrations, vibronic transitions always occur vertically in the diagram. The absorption probability is high, when the spatial overlap of the vibrational wave functions in the initial and final electronic states is significant. Here, this is the $E_k(v' = 0) \rightarrow E_i(v'' = 3)$ - transition. The same principle holds true for emission, which usually occurs after internal conversion to the lowest vibrational state $v'' = 0$ of the excited electronic state i (for more details about radiative and non-radiative transitions see section 2.3).

2.2.3 *Experimental aspects of absorption*

In the previous two subsections an introduction to light absorption and emission on a microscopic quantum mechanical level was given. However, in most experiments where the optical properties of a material are investigated the macroscopic optical properties of a crystal or an ensemble of chromophores are measured. In absorption spectroscopy, for instance, the attenuation of light passing through a thin film of material or a dilute solution of molecules is measured. In this subsection we will present the basic concept of absorption spectroscopy on the basis of the *Lambert-Beer-Bouger law*.

In steady-state absorption and time-resolved absorption experiments the light transmitted through a sample of a certain thickness d is measured. Electromagnetic radiation of a given wavelength with intensity I that is traveling through a material with a very small thickness dx is always attenuated by the same fraction of intensity

$$dI = -\alpha I dx \tag{12}$$

The absorption coefficient α is a specific material constant and has the dimension of an inverse length. By integrating equation 12 an expression for the attenuation of monochromatic radiation over an arbitrary layer thickness d is obtained:

$$\int_{I(0)}^{I(d)} \frac{dI}{I} = -\int_{0}^{d} \alpha dx \tag{13}$$

$$\Longleftrightarrow \ln \frac{I(d)}{I(0)} = -\alpha d \tag{14}$$

$$\Longleftrightarrow I(d) = I(0) e^{-\alpha d}. \tag{15}$$

This is the *Lambert-Beer-Bouger-law*. Figure 5 illustrates the absorption of light with the initial intensity $I(0)$ in a material layer of thickness d. The transmitted light has the reduced intensity $I(d)$.

The absorption of molecules in a virtually transparent solvent is proportional to the concentration c in g/L or mol/L:

$$\alpha = \epsilon' c \tag{16}$$

Accordingly, ϵ' is the molar extinction coefficient. The transmittance T of a layer is given by

$$T = \frac{I(d)}{I(0)} = e^{-\alpha d}, \tag{17}$$

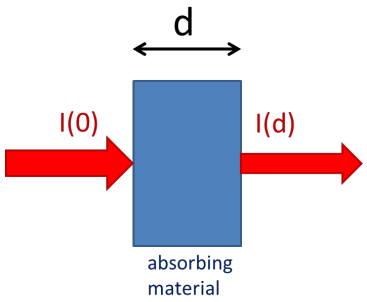

Figure 5: Graphic illustration of the absorption of monochromatic light with the initial intensity $I(0)$ by a material of thickness d. The transmitted light has the reduced intensity $I(d) = I(0)e^{-\alpha d}$.

which is the transmitted fraction of the light with the initial intensity $I(0)$. Equation 15 and 16 can be combined to give a useful expression for experimental work

$$A' = -\ln\left(\frac{I(d)}{I(0)}\right) = \epsilon' c d. \tag{18}$$

A' is the absorbance. However, in spectroscopy the absorbance is usually defined via the decadic logarithm

$$A = -\log\left(\frac{I(d)}{I(0)}\right) = \epsilon c d. \tag{19}$$

The decadic molar extinction coefficient ϵ is related to ϵ' by $\epsilon = \epsilon'/\ln 10 = \epsilon'/2.303$. The absorbance (equation 19) is linearly dependent on the concentration of the molecules in solution and the layer thickness. Generally, using spectrophotometers the linear dependence remains valid until $A = 2\,\mathrm{OD}$, which corresponds to a transmittance of 1 %.

2.3 RADIATIVE AND NON-RADIATIVE TRANSITIONS

After the discussion of the basic concepts of absorption and emission of electromagnetic radiation by molecules in the previous section, now the different radiative and non-radiative transition processes occurring in molecular systems after the absorption of light will be treated.

Figure 6 shows a Jablonski-diagram with different radiative (straight lines) and non-radiative (wavy lines) transition processes between electronic and vibrational states such as absorption, fluorescence, phosphorescence, internal conversion (IC) and intersystem crossing (ISC). In addition, at the bottom of figure 6, exemplary absorption, fluorescence and phosphorescence spectra are depicted that illustrate typical

spectral positions and shapes of optical spectra that can be obtained experimentally. The electronic ground state of a molecule is usually named S_0, the first electronically excited singlet state S_1, the second S_2 and so forth. The first and second triplet excited states T_1 and T_2 are shown in the Jablonski-diagram, too. The vertical lines corresponding to absorption processes, all start at the lowest vibrational level of the electronic ground state S_0, since according to Boltzmann statistics at room temperature nearly all molecules are in this state, and end at higher vibrational states of higher electronic states S_1 and S_2. The probabilities with which these transitions occur are given by the *selection rules* described earlier. In the following subsections the transition processes occuring after absorption are discussed in more detail.

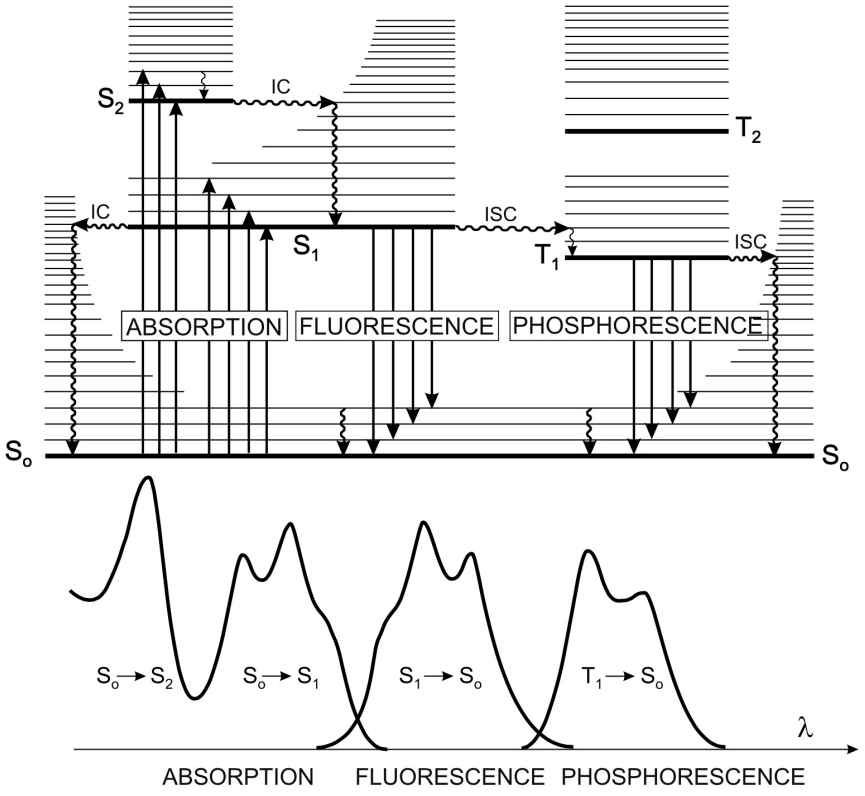

Figure 6: Jablonski-Diagram illustrating transition processes that can occur in a molecule. The graphic underneath shows the corresponding position and exemplary shapes of optical absorption, fluorescence and phosphorescence spectra. Reprinted from Valeur,[21] figure 3.1, page 35. Copyright Wiley-VCH Verlag GmbH & Co. KGaA. Reproduced with permission.

2.3.1 *Internal conversion*

Internal conversion (IC) is a radiationless transition between two electronic states of the same spin multiplicity, which is relevant for mo-

lecules in solution or in the solid state, where the energy is dissipated to the environment in the form of rotational, vibrational and translational energy. When a molecule relaxes non-radiatively within one electronic state (usually S_1) from a higher vibrational level to the lowest vibrational level ($v'' = 0$) this process is also called IC. This process, which is a direct consequence of the *Boltzmann distribution*, occurs within 10^{-13} to 10^{-11} s and is the reason why fluorescence emission normally occurs from the 0th vibrational level of S_1. Internal conversion from S_2 to S_1 is more probable than IC from S_1 to S_0, because the energy difference of the former transition is much smaller than that of the latter. Therefore IC from S_1 to S_0 competes with fluorescence and intersystem crossing to the triplet state from which subsequent phosphorescence emission might occur.

2.3.2 *Fluorescence*

An electronic transition from S_1 to S_0 in which a photon is emitted is called *fluorescence*. According to the *Franck-Condon principle* radiative fluorescence transitions occur vertical in the energy diagram (compare section 2.2.2) with the probability of the transition determined by the spatial overlap of the vibrational wave function of each electronic state. Since emission always occurs from the lowest vibrational level of S_1 into higher vibrational states of S_0 its spectral shape is independent of the excitation wavelength and appears at longer wavelengths than the absorption spectrum. The vibrational levels of the S_0 and S_1 states are similar, giving rise to the 'mirror image rule' for $S_0 \rightarrow S_1$ absorption and $S_1 \rightarrow S_0$ emission spectra illustrated in figure 6. In theory the 0-0 transitions of absorption and emission should be at the same spectral position. However, often the 0-0 transition of fluorescence is redshifted relative to the 0-0 transition of absorption, which is *e.g.* due to solvation effects. Many organic molecules have an electric dipole character in their ground state which becomes even more pronounced after optical excitation leading to an increased rearrangement of solvent molecules and in turn to a lowering of the energy difference between S_1 and S_0. Hence the emitted photon has a lower energy than the absorbed photon. This difference in spectral position of the 0-0 transitions is called *Stokes shift*. Figure 7 shows an absorption and a fluorescence spectrum of the organic dye 5-Iodoacetamidofluorescein (IAF), exemplifying the 'mirror image rule' and the *Stokes shift*.

The process of fluorescence emission itself occurrs on a similar time scale as absorption, but the time span (fluorescence lifetime) between induced absorption and fluorescence emission, which is a spontaneous emission process, ranges from several picoseconds to nanoseconds depending on the system. The temporal evolution of the radiative $S_1 \rightarrow S_0$ fluorescence transitions of an ensemble of mo-

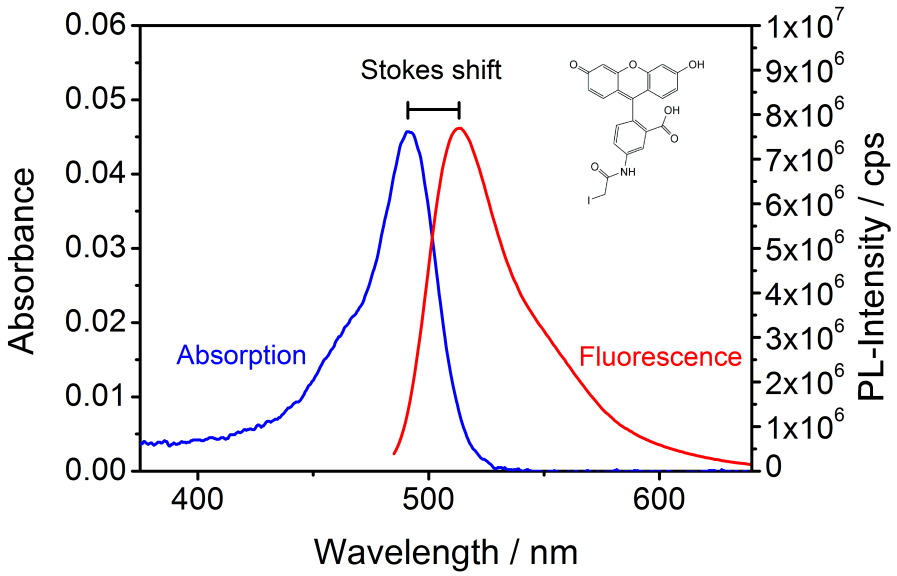

Figure 7: Emission and absorption spectrum of 5-Iodoacetamidofluorescein (IAF) illustrating the 'mirror image rule' and the *Stokes shift*. The inset shows the molecular structure of the dye molecule IAF. [22]

lecules follows an exponential curve and is hence similar to the dynamics of the radioactive decay. From the experimentally measured exponential decay of the fluorescence intensity the average lifetime of the molecules in the S_1 excited state can be determined. In the example of the dye IAF, the average fluorescence lifetime was determined to be ~ 4 ns.[22]

2.3.3 *Intersystem crossing*

The transition of a photoexcitation between electronic states with different spin multiplicity is called *intersystem crossing* (ISC). Usually this transition occurs between vibrational states with the same or similar energy. An example for such an ISC would be the transition from the 0 vibrational level of S_1 to a higher vibrational level of T_1 as depicted in figure 6. In principle ISC is a forbidden transition due to the spin selection rules, but spin-orbit coupling allows transition probabilities larger than zero. ISC occurs on the time scale of 10^{-7} to 10^{-9} s and can thus compete with other de-excitation pathways from S_1 such as fluorescence or internal conversion.

2.3.4 *Phosphorescence*

The spin forbidden radiative $T_1 \rightarrow S_0$ transition is called *phosphorescence*. In solution at room temperature the slow process of phosphorescence (10^{-6} to 1 s) competes with intersystem crossing and vibrational relaxation to S_0 due to numerous collisions with solvent mo-

Table 1: Characteristic times of transition processes in molecules.[21]

absorption	10^{-15} s
vibrational relaxation	10^{-12} to 10^{-10} s
lifetime of the excited state S_1	10^{-10} to 10^{-7} s $\rightarrow$ Fluorescence
intersystem crossing (ISC)	10^{-10} to 10^{-8} s
internal conversion (IC)	10^{-11} to 10^{-9} s
lifetime of the excited state T_1	10^{-6} to 1 s $\rightarrow$ Phosphorescence

lecules and hence phosphorescence emission intensities are usually rather low. At low temperatures or in the solid state, however, phosphorescent emission can be more intense and its lifetime can reach seconds to minutes. Phosphorescence is observed at larger wavelengths than fluorescence, because the 0 vibrational level of the triplet state T_1 is lower in energy than the 0 vibrational level of the S_1 state.

2.4 EXCITONS AND ENERGY TRANSFER

Organic solar cells (OSC) belong to the class of excitonic solar cells,[23, 24] since the primary excitations in these cells are bound electron-hole pairs or excitons. The concept of this quasi-particle, first proposed by Yakov Frenkel in 1931,[25] is important in understanding the photophysics of excitonic solar cells. In the following subsection different exciton models, and energy transfer mechanisms, which are often used to describe exciton migration in organic semiconductors will be presented.

2.4.1 *Exciton models*

Absorption of a photon in a material with periodic structure promotes an electron into an excited state with an energy similar to the band gap of the material system. The electron leaves behind a positively charged quasi-particle that is called hole. The entity of the spatially separated but coulombically bound electron-hole pair is called *exciton*. This quasi-particle is electrically neutral and can transport energy within the material system without transporting net electric charge. In inorganic semiconductors the dielectric constant ϵ_r is large ($\geqslant$12) leading to an efficient separation of electron and hole at room temperature. The Coulomb attraction of electron and hole in these materials is effectively screened by the cores of the atoms and the free electrons. Such excitons are called *Mott-Wannier excitons*.[26] The distance between electron and hole is one order of magnitude bigger than the lattice constant and their binding energy is around k_bT at room temperature. In a first approximation the Coulomb attraction of electron and hole in the bulk material can be described by a Coulomb

potential divided by the dielectric constant ϵ_r, which describes the screening effect of the bulk, consisting of all atomic cores and electrons

$$E_C(r) = \frac{-e^2}{4\pi\epsilon_r\epsilon_0 r} \tag{20}$$

with the elementary charge e, the vacuum permittivity ϵ_0, and the distance r between electron and hole. It is apparent, that the higher ϵ_r is, the smaller the Coulomb attraction gets. For the hydrogen atom in free space ϵ_r equals one, since there are no screening effects.[27]

In organic semiconductors ϵ_r is around 3, leading to tightly bound electron-hole pairs, which are called *Frenkel excitons*. Here, the electron-hole pair is localized on one molecule within the lattice structure with a binding energy of 0.5 eV at room temperature. In order to overcome this binding energy to separate electron and hole an electron-accepting material with sufficient driving force has to be introduced. Figure 8 shows schematic drawings of Frenkel and Mott-Wannier excitons as well as a third type of exciton, the *charge-transfer* (CT) *exciton*.

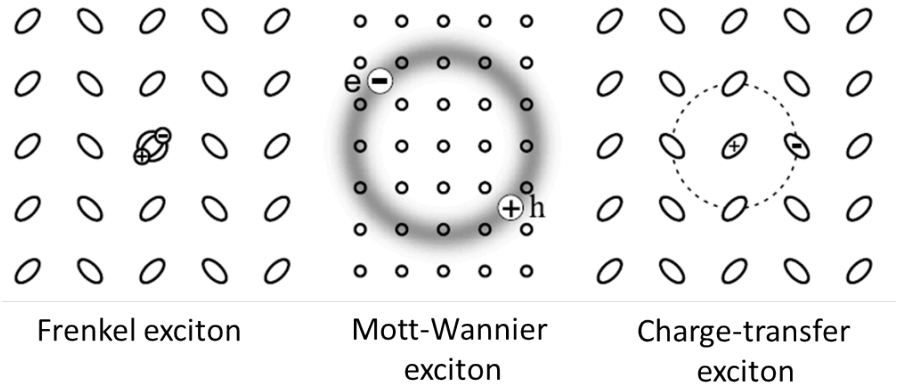

Figure 8: Schematic drawing of different kinds of excitons in organic and inorganic semiconductors: (a) Frenkel excitons in organic semiconductors are located on one single molecule within the lattice structure. (b) The electron-hole distance of Mott-Wannier excitons in inorganic semiconductors is much larger than the lattice constant. (c) Electron and hole of charge transfer excitons in organic semiconductors are located on neighboring molecules. They are still bound by the Coulomb potential. Reprinted from Schwoerer and Wolf,[28] figure 6.13, page 150. Copyright Wiley-VCH Verlag GmbH & Co. KGaA. Reproduced with permission.

The electron and hole of the CT exciton sit on different neighboring molecules and thus their distance is higher than in the case of Frenkel excitons, but they still feel their mutual Coulomb attraction. The CT exciton has an electronically neutral character, but displays a static electric dipole moment, which can give rise to the Stark effect.[29] Such CT excitons are also created in organic blend systems at the

interface of electron donor and acceptor - a prominent example is the P3HT/PCBM interface. The energy of a CT exciton is given by

$$E_{CT} = I_D - E_A - P_{eh}(r) - E_C(r) \tag{21}$$

where I_D is the ionization potential of the donor, E_A is the electron affinity of the acceptor, P_{eh} the polarization energy of an electron-hole pair at a separation r, and $E_C(r)$ the coulombic binding energy of the ion-pair.[30]

These three types of excitons introduced above can be further distinguished by their spin characteristics. Excitons can have either singlet or triplet character, depending on their total spin quantum number. If the spins of electron and hole are anti-parallel, the total spin quantum number is 0 and they are termed singlet excitons. If the spins are parallel, the total spin is 1 and they are termed triplet excitons.

2.4.2 *Förster energy transfer*

The migration of excitons in an organic solid at room temperature is usually described by successive energy transfer from their current location (the donor site) to an acceptor location. In the case of a conjugated polymer the donor and acceptor sites can be on the same polymer chain or on another nearby polymer section. Because of kinks, twists and defects in the polymer backbone, there is a distribution of different conjugation lengths and hence a distribution of energies, which determine the overall optical and energetic properties of the system under study. The distribution of different molecular sites with distinct energies is called the density of states (DOS). Exciton migration in such a system is considered to be a hopping process between neighboring sites with a tendency of the exciton to relax to sites with lower energy. One single intermolecular or site to site hopping process of a singlet exciton can be described by *Förster energy transfer* also known as *Förster Resonance Energy Transfer* FRET. This energy transfer from a donor (D) to an acceptor (A) site can be written as

$$D* + A \rightarrow D + A*. \tag{22}$$

The prerequisite for this process is, that the emission spectrum of D overlaps at least partially with the absorption spectrum of A. The wave functions of D and A molecule do not need to overlap. FRET is radiationless energy transfer mediated by dipole-dipole interactions with a rate described by

$$k_{FRET} = k_D \left(\frac{R_0}{R}\right)^6, \tag{23}$$

where k_D is the rate of decay of the excited donor in the absence of an acceptor, R is the distance between donor and acceptor, and R_0 is the *Förster radius* - the distance at which the energy transfer efficiency is 50 % (around 4 nm to 10 nm for molecules in solution). The Förster radius is given by

$$R_0 = \frac{9\ln(10)}{128\pi^5 N_A}\frac{\kappa^2\Phi_D}{n^4}J, \tag{24}$$

with N_A being Avogadro's constant, κ an orientation factor taking into account the relative direction of the two dipoles, n the refractive index of the medium, Φ_D the fluorescence quantum yield of the donor in the absence of an acceptor, and J being the spectral overlap of the donor emission and acceptor absorption.[31]

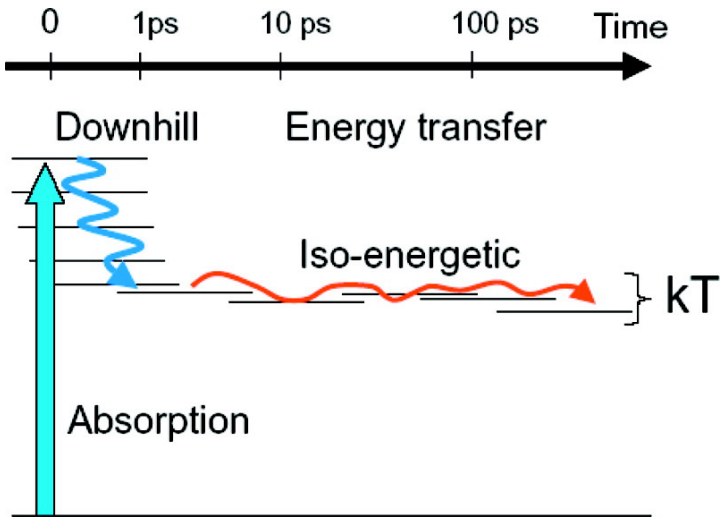

Figure 9: Schematic illustration of the change in singlet exciton energy and hopping rate over time. Figure reprinted with permission from Scheblykin et al.[32] Copyright 2007 American Chemical Society.

In contrast to the incoherent hopping process of exciton migration it has also been found recently, that coherent intrachain exciton migration can occur in conjugated polymers.[33] Furthermore, it is interesting to note, that the dynamics of incoherent exciton migration strongly depend on the energy of the initial exciton and that energy transfer slows down over time after photogeneration of the excited state due to dispersive relaxation within the DOS into the lower energy tail of the DOS. From there exciton migration depends to a great extent on thermal energy to promote hopping. Figure 9 illustrates the dependence of the exciton dynamics on the initial excited state energy and the time after photogeneration as well as on the energetic landscape. This general picture is also applicable to other excited states such as triplet excitons or charges.[34]

2.4.3 *Dexter energy transfer*

While hopping of singlet excitons can be described by a Förster type energy transfer, the migration of triplet excitons is described by *Dexter energy transfer*. Dexter energy transfer relies on the exchange of electrons between the donor and acceptor molecules. Hence, besides the spectral overlap of donor emission and acceptor absorption, the spatial overlap of wavefunctions has to be sufficiently large. This means, that the distance between the interaction partners has to be small (less than 1 nm) in order for the energy transfer to be efficient. The transfer rate decreases exponentially as the spatial separation R of donor and acceptor molecules increases

$$k_{Dexter} \propto \exp\left(\frac{-2R}{L}\right), \tag{25}$$

with L being the van-der-Waals distance.[35] Dexter energy transfer is also called *short-range energy transfer*. In contrast to Förster Resonance Energy Transfer (FRET), Dexter energy transfer is applicable to both singlet and triplet excitons. Figure 10 shows illustrations of the singlet Förster type energy transfer and singlet and triplet Dexter type energy transfer mechanisms.

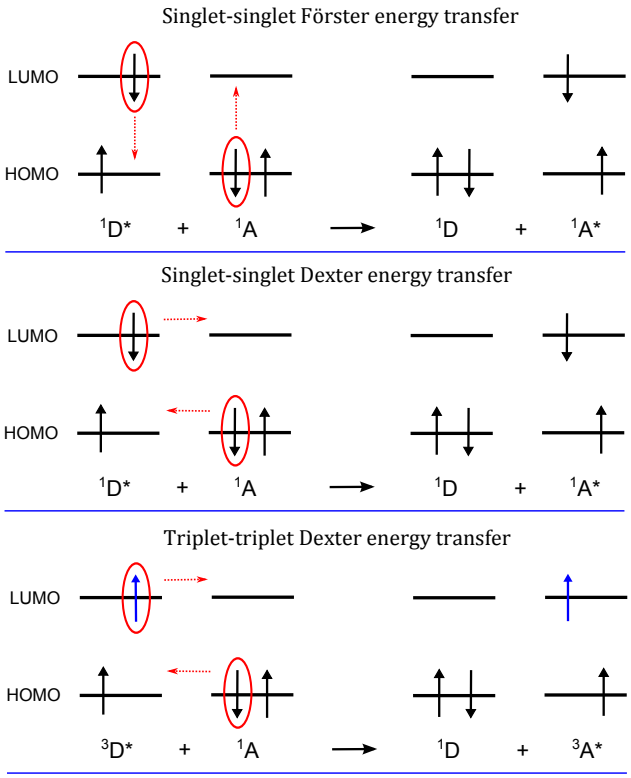

Figure 10: Schematic illustration of Förster and Dexter type energy transfer mechanisms. Figure adapted from [36].

2.5 ORGANIC SOLAR CELLS

In this section an introduction to the working principle of organic solar cells (OSC) and the photophysics occurring in the devices will be given. The photophysics of OSCs will also be discussed in more detail in section 2.6. Furthermore, basic design layouts and device physics of OSCs will be presented. In the last part of this section characterization methods for OSCs will be shown.

2.5.1 *Working principle*

An organic solar cell (OSC) generally consists of a thin film of organic semiconducting material sandwiched between two electrodes, one of them being transparent, so that the solar illumination reaches the organic semiconductor. Different design concepts will be discussed in the next subsection.

Upon the absorption of a photon by the organic semiconducting material an electron is promoted from the HOMO to the LUMO level. The hereby created primary photoexcitation is, due to the low dielectric constant of the organic materials ($\epsilon_r \sim 3$), a strongly bound exciton-hole pair or Frenkel exciton with binding energies ranging between 0.35 and 1 eV, which exceed the thermal energy $k_B T$ at room temperature by an order of magnitude.[37] Hence, in order to create free charges in an OSC a second material with electron accepting character, i.e. a lower lying LUMO level, has to be introduced. The exciton, created on the electron donating material (donor) migrates through the bulk until it reaches the interface to the electron accepting material (acceptor) where the exciton can be transferred into the LUMO of the acceptor (A), while the hole remains on the HOMO of the donor (D). The driving force for this electron transfer reaction is the difference of the electron affinities or LUMO levels of D and A, respectively.[38] Figure 11 illustrates the electron transfer in an OSC. When the electron is transferred to the acceptor either a bound charge-transfer (CT) exciton (or CT state) is generated or electron and hole are immediately spatially separated into free charges which have overcome their mutual Coulomb attraction and can subsequently be extracted at the electrodes. While free charges can eventually contribute to the photocurrent of a solar cell, bound CT states would require a strong electric field to be spilt into free charges that can be extracted from the device. The overall device efficiency is determined by a cascade of processes that all have to be optimized in order to yield a good device performance. These processes are:[39]

i) absorption of light by the active layer of the solar cell

ii) exciton quenching at the donor/acceptor interface

iii) charge carrier separation and dissociation

iv) charge carrier diffusion to and extraction at the respective electrodes

The simultaneous optimization of all these processes is an intricate challenge and the exact interplay of all the different factors leading to an improved device performance is still not fully understood.

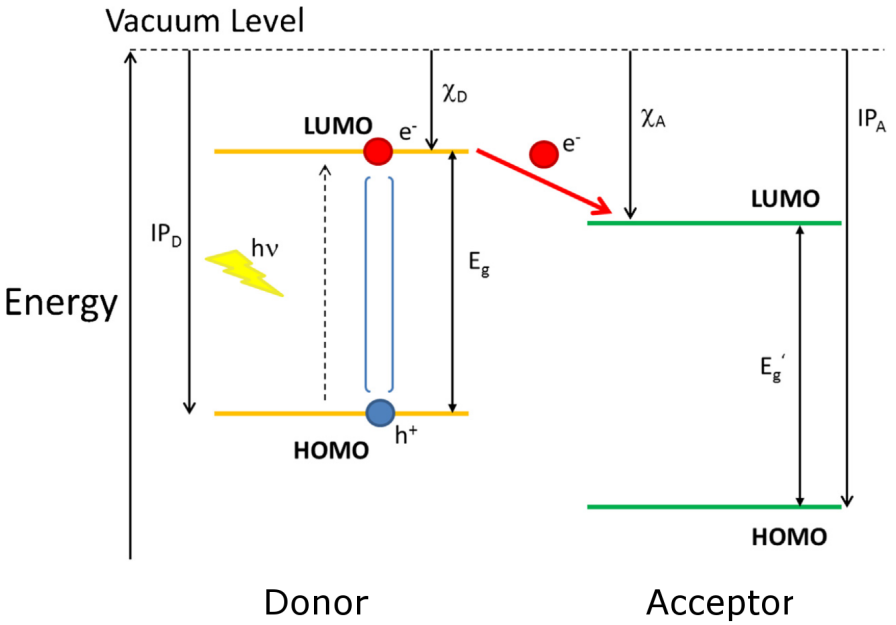

Figure 11: Energy level alignment in an organic solar cell (OSC) consisting of an electron donor and acceptor material. Upon light absorption and exciton formation an electron transfer from the donor to the acceptor takes place (red arrow) resulting in either a CT state or spatially separated charges (SSC). Here IP_D, IP_A, χ_D and χ_A are the donor's and acceptor's ionization potentials and electron affinities, respectively. Figure reprinted from Scharber and Sariciftci under the CC BY license.[37].

2.5.2 *Architecture of organic solar cells*

The design of the active layer of OSCs has a strong influence on charge carrier generation, separation, and extraction. Typical diffusion lengths L_D of excitons in organic materials of 10 nm have to be considered.[41] Over the years different active layer designs have been developed. Figure 12 shows drawings of three OSC devices, that differ in the design concept for their active layer. In a *single layer* (and single material) OSC, depicted in figure 12a, only excitons created close to the small depletion region of a Schottky contact can be separated by the prevalent electric field, limiting the size of the 'active region'.

In a *bilayer solar cell device* (12b) thin layers of donor and acceptor materials are evaporated or spincoated on top of each other. The acceptor facilitates charge separation as discussed in the previous sub-

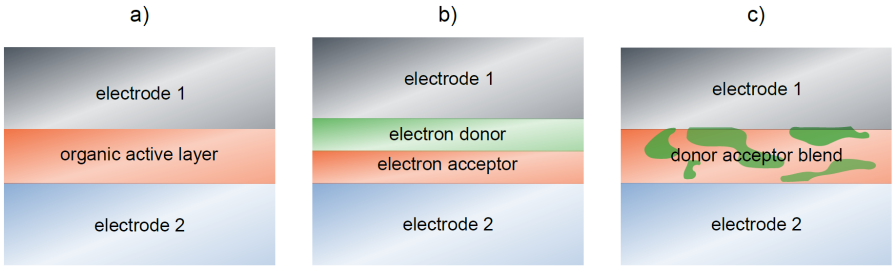

Figure 12: Three different OPV device architectures: (a) single layer solar cell, (b) bilayer solar cell, and (c) bulk heterojunction (BHJ) solar cell. Figure reprinted from Etzold.[40]

section. After charge transfer the electron on the acceptor and the hole on the donor can be separately transported to the respective electrodes. Bimolecular recombination is efficiently suppressed in these devices. However, the active region is still small, since only excitons created within a distance L_D to the donor/acceptor interface can be split into charges. Such a bilayer device was first presented in 1986 by Tang et al.[42] They used a CuPC/perylene tetracarboxylic derivative bilayer and obtained a power conversion efficiency (PCE) of 1 %.

The drawback of the long distances excitons have to travel to finally reach the rather small donor/acceptor-interface area in the bilayer device was overcome by the introduction of the bulk heterojunction (BHJ) by Yu et al. in 1995.[43] They mixed the donor polymer poly(2-methoxy-5-(2'-ethyl-hexyloxy)-1,4-phenylene vinylene) (MEH-PPV) with the fullerene C_{60} as acceptor and spin-cast ~ 100 nm thin films creating an active layer with an interpenetrating network of separated donor and acceptor phases giving rise to a solar cell with a PCE of 2.9 %. Figure 12c shows a schematic of the morphology of an organic BHJ. In comparison to the bilayer architecture the area of the donor/acceptor heterojunction is much larger and extends over the whole layer thickness. Hence, also the active region extends over the whole layer thickness and excitons created on either the donor or acceptor have relatively short distances to diffuse to the interface.

Once charges are separated at the BHJ interface, holes are transported within the donor phase to the anode and electrons are transported in the acceptor phase to the cathode. In the ideal case, percolation pathways of pure donor and acceptor phases exist, which allow charges to reach the electrodes without recombining or getting trapped in dead ends.[44, 45] Charge carrier extraction in an OSC is driven by the internal electric field generated by the difference between the work functions of the two electrodes. Often, in a standard device architecture indium tin oxide (ITO) is used as the transparent anode and aluminum is used as the reflecting back electrode (cathode). The electrode materials have to be matched to the energy levels of the donor and acceptor materials to guarantee ohmic contacts

and hence an efficient sweep out of charges. In the next subsection the characteristics and differences between the Schottky barrier and ohmic contacts will be explained in more detail.

2.5.3 *Schottky contact versus Ohmic contact*

A rectifying metal-semiconductor junction is termed *Schottky contact*. The energy level alignment in a Schottky contact of a high work function metal and an n-type semiconductor is shown in figure 13. Here, E_F denotes the energy of the Fermi level, E_C and E_V are the energies of the conduction and valence bands, respectively. Φ_B is the Schottky barrier height, a measure for the potential energy barrier for electrons. The electron densities in the materials at 0 K are qualitatively indicated by the gray color. If a metal with a high work function (lower Fermi level) is brought into intimate contact with an n-type semiconductor (higher Fermi level), electrons will flow from the semiconductor to the metal until the Fermi levels of the two materials are equal. This causes a built up of charges at the interface, creating a potential gradient following Poisson's equation[46]

$$\frac{d^2V(x)}{d^2x} = \frac{\rho(x)}{\epsilon_0 \epsilon_r}, \tag{26}$$

where V is the electric potential as a function of the distance x, $\rho(x)$ the electron density, ϵ_0 the vacuum permittivity, and ϵ_r the dielectric constant of the material. This phenomenon is also called band bending. The region of the bended bands is the depletion region for majority carriers (electrons in n-type semiconductors).

Such a Schottky contact, giving rise to a potential energy barrier for charge carriers, is undesirable in organic BHJ solar cells, where the metal-semiconductor junction should enable efficient sweep out of charge carriers. However, not all metal-semiconductor junctions have rectifying character. If a low work function metal is combined with an n-type semiconductor, having a lower Fermi level than the metal, the obtained metal-semiconductor junction allows for the current to flow in both directions. Such a contact is called ohmic contact.

2.5.4 *Characterization of organic solar cells*

In general, the working principle of organic solar cells (OSC), photodetectors, and organic light emitting diodes (OLEDs) can be simplified with the metal-insulator-metal (MIM) model. This model is valid as long as the semiconductor is not doped and there is no significant build-up of space charge in the device as could be induced by unbalanced transport of holes and electrons.[45] The diode character of such an MIM device is due to the different injection barriers created at the metal-'insulator' contacts by the HOMO and LUMO levels

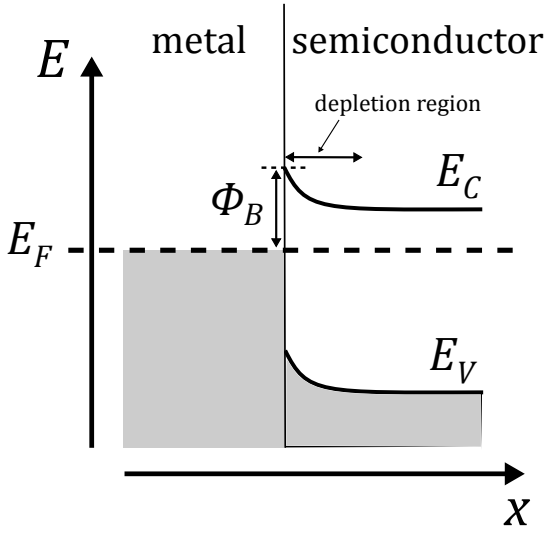

Figure 13: Simplified schematic of the energy level alignment in a Schottky barrier of a metal and an n-type semiconductor. E_F is the energy of the Fermi level, Φ_B is the Schottky barrier height, E_C and E_V are the energies of the conduction and valence bands, respectively. Figure adapted from [47].

of the semiconductor and the respective work functions of the metals. Figure 14 shows four different working regimes of such a MIM device. The electrode materials ITO and aluminum are represented by their respective Fermi levels and the semiconductors conduction and valence bands are represented by its HOMO and LUMO levels, respectively. In this simplified model band bending effects occuring at the metal-semiconductor interface are neglected.

The working regimes displayed in figure 14 can be attributed to points or regions in a current-voltage ($J-V$) curve of a solar cell device. Figure 15 shows an exemplary $J-V$ curve of a solar cell (black curve), where the working regimes are labeled with the corresponding letters a)-d) from figure 14. Under short circuit conditions, when the ITO and aluminum contacts are on the same potential (figure 14a), the energy bands of the semiconductor are tilted. Under illumination, photogenerated charge carriers can drift to the aluminum (electrons) and ITO (holes) electrodes. A photocurrent at short circuit condition (J_{SC}) can be measured (figure 15a). If the internal electric field is further increased by an additional external electric field in reverse direction, the bands are further tilted (figure 14b). Under dark conditions only a small injection current flows. This is the regime where photodetectors operate or where diodes exhibit blocking behavior. Here, upon illumination, charge carriers can be easily extracted (figure 15b). Figure 14c shows the flat band condition, where the applied field is opposite in sign to the built-in potential, but of the same magnitude. This is the open circuit configuration, from which the open-circuit voltage (V_{OC}) can be determined (figure 15c). Here, charge carriers

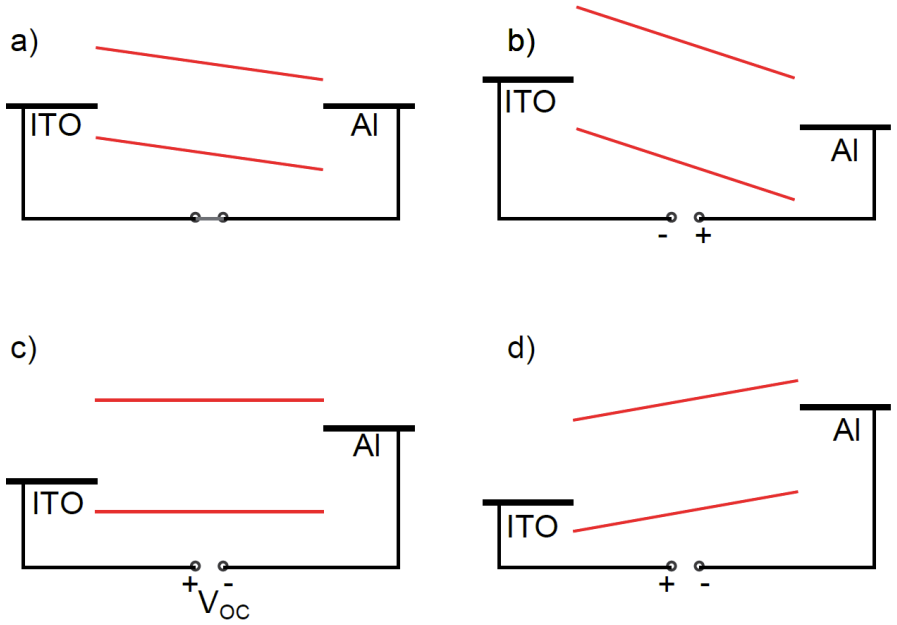

Figure 14: Working regimes of thin film organic semiconductor devices exemplified by a simplified metal-insulator-metal (MIM) model: (a) At short-circuit conditions the Fermi levels of the electrodes are aligned and the bands are tilted. (b) By increasing the field in the reverse direction the bands are even more tilted and charge extraction is enhanced. (c) At open-circuit conditions, when the magnitude of an external forward bias equals the internal field, the bands are flat. (d) If the forward bias is increased, the energy bands are tilted in the opposite direction, allowing for an efficient charge carrier injection. Band-bending effects at the ohmic contacts are neglected. Figure reprinted from Etzold. [40]

are not extracted anymore and hence there is no net current flow. Figure 14d displays the forward bias condition, where charge carriers are efficiently injected into the device and the direction of the current inside of the device is reversed. This is the forward direction of diodes and the operating regime of OLEDs (figure 15d).[45, 48]

2.5.4.1 *Current-voltage characteristics - Figures of merit*

The performance of a solar cell is specified by four figures of merit: (i) The power conversion efficiency η (PCE), (ii) the short circuit current density (J_{SC}), (iii) the open circuit voltage (V_{OC}), and (iv) the fill factor (FF). To determine these figures of merit a current-voltage ($J-V$) characteristic of the solar cell is recorded by sweeping an applied voltage from negative to positive values (usually from -1 to $1\,V$) under artificial standardized illumination (AM 1.5G, for further details see section 2.7.3) imitating natural solar irradiance, and measuring the current. A typical $J-V$ curve under illumination (solid black curve) is presented in figure 15 together with a $J-V$ curve in the dark, i.e. without illumination (dashed black curve), and the power density of

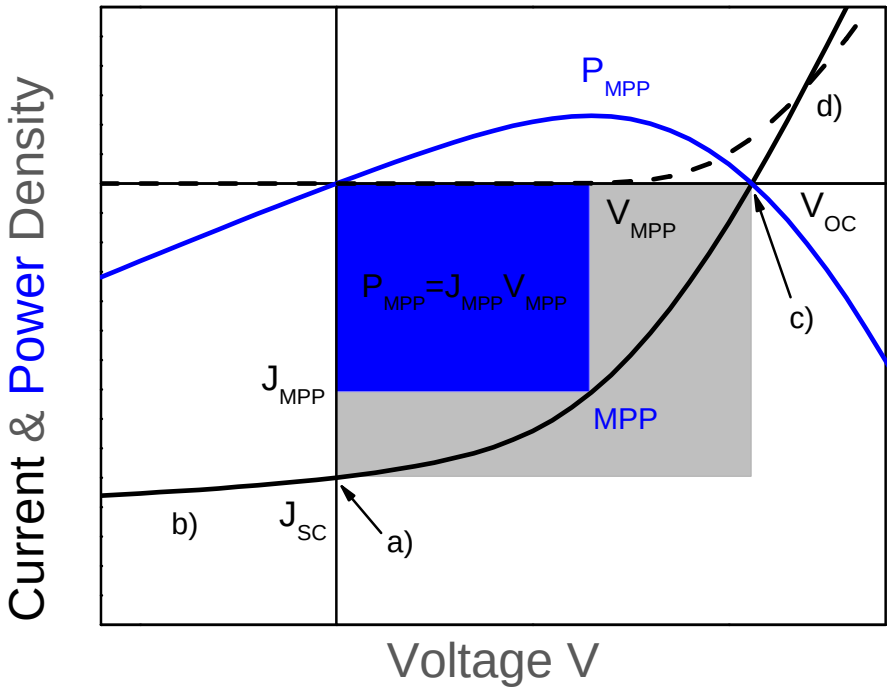

Figure 15: Typical current-voltage ($J-V$) characteristics of an organic solar cell (OSC) measured in the dark (black dashed line) and under illumination (solid black line) together with the power density (blue line). The solar cell delivers its maximum power density $P_{MPP} = J_{MPP}V_{MPP}$ at the maximum power point (MPP), where the area of the blue square is maximized. An ideal solar cell would deliver a maximum power density given by the product of the short circuit current density (J_{SC}) and the open circuit voltage (V_{OC}) (gray area).

the solar cell under illumination (solid blue curve). From such a $J-V$ characteristic the values for the short circuit current and the open circuit voltage can immediately be read from the intersection of the $J-V$ curve with the y- and x-axis, respectively. The short circuit current density (J_{SC}) is the maximum current extractable from the device, when the applied voltage is zero (at short circuit conditions). The open circuit voltage (V_{OC}) is the maximum voltage obtainable from the device, when no net current is flowing in the external circuit. The power conversion efficiency η of a solar cell is defined as the ratio of the electrical power P_{MPP} produced by the solar cell at the maximum power point (MPP) to the illumination power incident on the solar cell P_{in} and can also be expressed by J_{SC}, V_{OC}, and FF

$$\eta = \frac{P_{MPP}}{P_{in}} = \frac{J_{MPP}V_{MPP}}{P_{in}} = \frac{J_{SC}V_{OC}FF}{P_{in}}. \tag{27}$$

A graphical definition of the FF is given in figure 15 as the ratio of the blue rectangle to the gray rectangle, i.e. the ratio of the product of the current density and the voltage at the maximum power point

(MPP) to the product of the short-circuit current and the open-circuit voltage

$$FF = \frac{J_{MPP}V_{MPP}}{J_{SC}V_{OC}} = \frac{P_{MPP}}{J_{SC}V_{OC}}. \tag{28}$$

The FF is an ideality factor, giving the ratio of the maximum obtainable power density output to the theoretical, but not obtainable, power density output. In an ideal solar cell the FF would be one (rectangular shaped $J-V$ curve), meaning that there are no field dependent losses. Such a field dependence can be induced by field dependent charge generation or charge transport and extraction as well as an unbalanced electron and hole mobility of the donor and acceptor materials.[49]

2.5.4.2 *External quantum efficiency*

The *external quantum efficiency* (EQE) gives information about how efficiently a solar cell absorbs photons at a given wavelength and converts them into extracted charges.

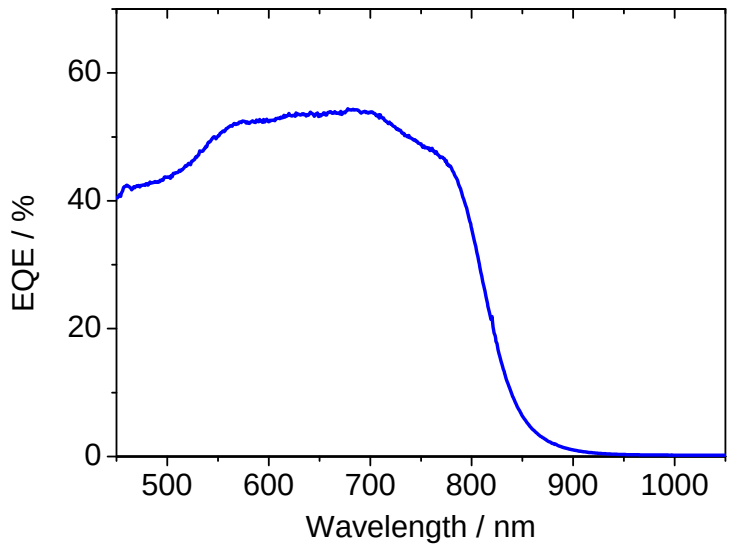

Figure 16: External quantum efficiency (EQE) spectrum of a PDPP5T:$PC_{71}BM$ solar cell.

The EQE, also known as the incident photon to current efficiency (IPCE), is defined as the ratio of the number of electrons extracted at the electrodes to the number of photons incident on the active area of the solar cell at a given wavelength λ:

$$EQE(\lambda) = \frac{\#\text{extracted charges}}{\#\text{incident photons}} = \frac{N_{el}(\lambda)}{N_{ph}(\lambda)}. \tag{29}$$

The EQE can be experimentally determined by illuminating the solar cell sample with monochromatic light and simultaneously measuring the current flow. By successively measuring the current at different wavelengths the entire EQE spectrum can be obtained. When two materials with complementary absorption spectra are used in the active layer of an OSC the EQE spectrum can give insight into the contribution of charge generation of the individual components. Figure 16 shows an EQE spectrum of a PDPP5T:$PC_{71}BM$ solar cell.

From the EQE spectrum an estimate of the short circuit current density (J_{SC}) under AM 1.5G illumination can be calculated

$$J_{SC} = \frac{e}{hc} \int \lambda \times EQE(\lambda) \times P_{AM1.5G}(\lambda) d\lambda, \tag{30}$$

where e is the elementary charge, h is Planck's constant, c the speed of light, and $P_{AM1.5G}(\lambda)$ is the power of the AM 1.5G spectrum at a given wavelength λ.

2.6 PHOTOPHYSICAL PROCESSES IN ORGANIC SOLAR CELLS

In section 2.5.1 we briefly presented the photophysics occurring in an organic solar cell upon absorption of a photon. In this section we will discuss in more detail the mechanisms of charge transfer, charge dissociation, charge carrier transport and the loss processes which limit the power conversion efficiency of organic solar cells.

In section 2.5.1 the photophysics occurring in an organic solar cell upon absorption of a photon were briefly presented. In this section the mechanisms of charge transfer, charge dissociation, charge carrier transport and the loss processes which limit the power conversion efficiency of organic solar cells will be discussed in more detail.

2.6.1 *Charge transfer and charge dissociation*

In the following two subsections the mechanisms governing charge transfer (CT) and charge transfer state dissociation will be discussed on basis of the review "Charge Photogeneration in Organic Solar Cells" published by Clark and Durrant in 2010.[50]

2.6.1.1 *Marcus's theory of nonadiabatic electron transfer*

After photogeneration of an exciton on the donor and its subsequent diffusion to the donor/acceptor interface electron transfer can occur. *Marcus's theory of semiclassical nonadiabatic electron transfer*, developed in 1956,[51] describes the electron transfer processes in molecular systems[52] and has also been extended to conjugated polymer blends.[53] It is a semiclassical theory, because the electronic processes are treated quantum mechanically, while nuclear motions are

treated classically. The electron transfer reaction can be written as a transition from the reactant $^1D*/A$ to the product D^+/A^-, a transition from an excited donor/neutral acceptor complex to an interfacial charge separated state. All nuclear motions are combined into one general, so that the reaction diagram can be presented in a 2-dimensional plot with two intersecting harmonic oscillators (parabolas), one for the reactant $^1D^*/A$ and one for the product D^+/A^- as shown in figure 17. By vibrational motions the reactant can reach the intersection point of the two parabolas from which, obeying energy conservation rules and the Franck-Condon principle, an isoenergetic electron transfer into the charge separated state D^+/A^- is possible. The activation barrier that has to be overcome is $\Delta G^\dagger$, which according to the Marcus theory is a function of the energy difference ΔG° between the relaxed reactant and product states (Gibbs free energy) and the reorganization energy λ:

$$\Delta G^\dagger = \frac{(\lambda + \Delta G^\circ)^2}{4\lambda}. \tag{31}$$

The reorganization energy λ is the energy that is required to bring the reactant from the equilibrium position to the new equilibrium position of the charge separated product state. It consist of an 'inner' contribution from the rearrangement of the molecules itself and of an 'outer' contribution from the surrounding solvent molecules, that have to rearrange themselves to adapt to the new product state.

The electron transfer rate k_{ET} in Marcus theory can be determined from perturbation theory similar to Fermi's golden rule

$$k_{ET} = \frac{2\pi}{\hbar\sqrt{4\pi\lambda k_B T}} V^2 \exp\left(-\frac{(\lambda + \Delta G^\circ)^2}{4\lambda k_B T}\right), \tag{32}$$

where V is the electronic coupling between the reactant and product states. Note that equation 32 is only valid for weak electronic coupling when electron transfer occurs nonadiabatically. From the exponential term, corresponding to the Franck-Condon factor, it can be seen that the electron transfer rate increases with increasing $-\Delta G^\circ$ until $-\Delta G^\circ = \lambda$, where k_{ET} reaches its maximum value and the reaction has no activation barrier. When $-\Delta G^\circ$ however further increases k_{ET} decreases again. The region, where $-\Delta G^\circ > \lambda$, is called the Marcus inverted region. This region was first observed experimentally 30 years after the development of Marcus theory.[54]

2.6.1.2 *Onsager-Braun theory of charge dissociation*

After charge transfer at the donor/acceptor interface the hereby created hole on the donor and electron on the acceptor are still not free, fully separated charges but have to overcome their mutual Coulomb

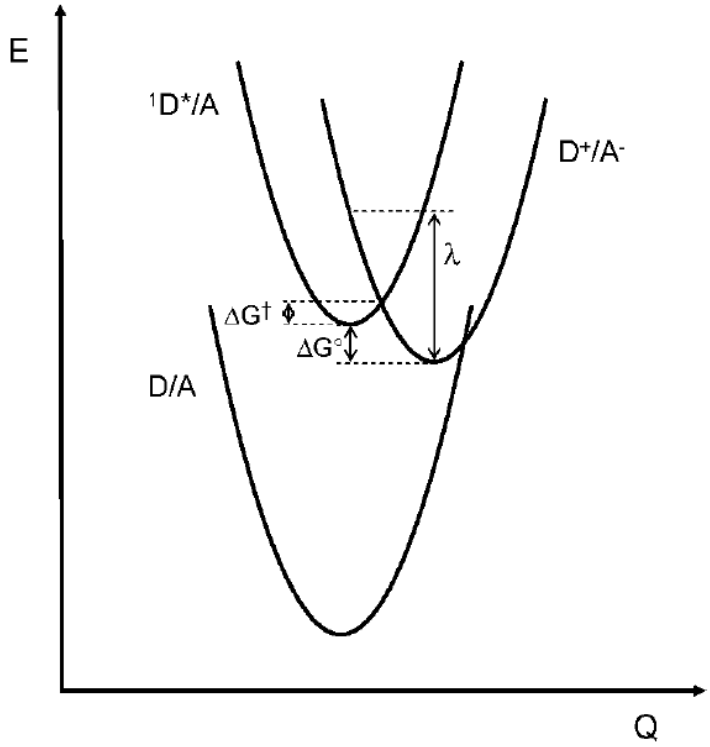

Figure 17: Energy diagram illustrating the concept of *Marcus's nonadiabatic electron transfer theory*. In the Energy E *versus* generalized reaction coordinate Q - diagram the energy parabolas of the reactant $^1D*/A$ and the product D^+/A^- as well as the neutral state D/A are plotted. ΔG° is the Gibb's free energy, $\Delta G^\dagger$ is the activation barrier, and λ is the reorganization energy. For further details see text. Reprinted with permission from Clarke and Durrant.[50] Copyright 2010 American Chemical Society.

attraction, which is in the range of 0.1 to 0.5 eV.[50] There is still an ongoing debate over the exact mechanism of charge dissociation from charge-transfer states. In 1934 Onsager developed a model to describe the dissociation of electron-hole pairs in a weak electrolyte undergoing Brownian random motion and stated that the dissociation of a CT state into free charges occurs with an escape probability $P(E)$ that depends on the strength of the applied electric field E, the distance a at which electron and hole are generated and the temperature.[55] The process of charge dissociation is in kinetic competition with geminate recombination of the CT states. Later, in 1984, Braun extended Onsager's model by introducing a finite CT state lifetime, which is especially important for solids.[56]

Figure 18 illustrates the principles of *Onsager-Braun theory*. The plot shows the Coulomb potential of the hole V acting on the electron after the charge transfer reaction as a function of the electron-hole distance. After photogeneration of an exciton with the photon energy $h\nu$ and subsequent charge transfer reaction at the donor/acceptor interface a

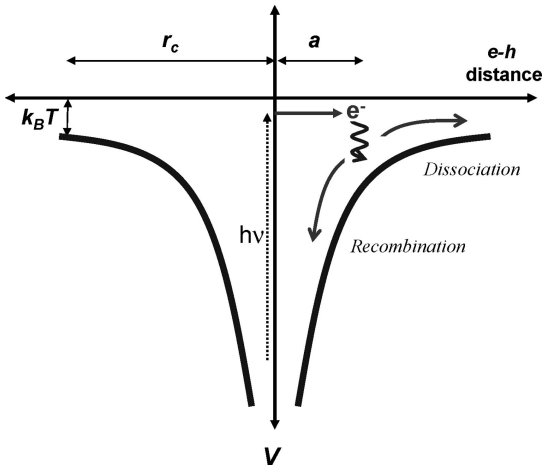

Figure 18: Potential energy diagram illustrating *Onsager-Braun theory*. The Coulomb attraction V is plotted as a function of the electron-hole (e-h) separation. Here, r_C is the Coulomb capture radius and a is the thermalization length. Further details are given in the text. Reprinted with permission from Clarke and Durrant.[50] Copyright 2010 American Chemical Society.

localized hole on the donor and a 'hot' electron on the acceptor are generated at a separation distance a, where the electron thermalizes (thermalization length). Furthermore a Coulomb capture radius r_C is defined. This is the distance at which the Coulomb energy equals the thermal energy $k_B T$:

$$r_C = \frac{e^2}{4\pi\epsilon_r\epsilon_0 k_B T} \tag{33}$$

where e is the charge of an electron, ϵ_r is the dielectric constant of the surrounding medium, ϵ_0 is the permittivity of vacuum, k_B is Boltzmann's constant and T is the temperature. If the thermalization length a is larger than r_C, charges will be fully dissociated. However, if a is smaller than r_C, CT state dissociation into free charges and geminate recombination back to the ground state will be in kinetic competition. With the electric-field-dependent dissociation rate $k_d(E)$ and the rate constant for geminate recombination k_f the escape probability $P(E)$ can be written as

$$P(E) = \frac{k_d(E)}{k_f + k_d(E)} = k_d(E)\tau(E) \tag{34}$$

where $\tau(E)$ is the finite lifetime of the CT state as introduced by Braun. According to Onsager the dissociation rate is defined as

$$k_d(E) = \nu \exp\frac{-\Delta E}{k_B T}\left[1 + b + \frac{b^2}{3} + \frac{b^3}{18} + \cdots\right] \tag{35}$$

where ν is the separation attempt frequency

$$\nu = \frac{3\langle\mu\rangle e}{4\pi\langle\epsilon_r\rangle\epsilon_0 a^3} \tag{36}$$

and b the effective field parameter

$$b = \frac{e^2 E}{8\pi\langle\epsilon_r\rangle\epsilon_0 k_B^2 T^2} \tag{37}$$

with $\langle\mu\rangle$ being the spatially averaged sum of the electron and hole mobilities and $\langle\epsilon_r\rangle$ the spatially averaged dielectric constant taking the blending of different materials into account. ΔE is the Coulomb attraction of the initially generated electron-hole pair after thermalization:

$$\Delta E = \frac{e^2}{4\pi\langle\epsilon_r\rangle\epsilon_0 a}. \tag{38}$$

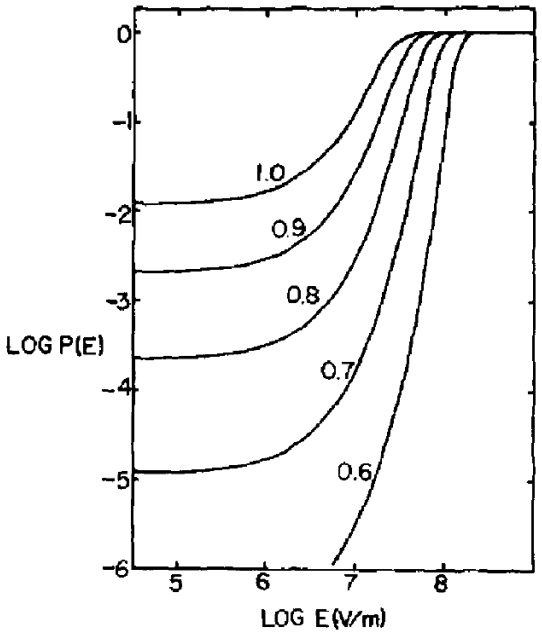

Figure 19: Electric field dependence of the escape probability $P(E)$ at different thermalization lengths a. The fit parameters were $\langle\epsilon_r\rangle = 3.0$, $\langle\mu\rangle = 1 \times 10^{-4}\,m^2V^{-1}s^{-1}$, $T = 300$ K and $\tau = 10^{-8}$ s. Reprinted with permission from Braun.[56] Copyright *J. Chem. Phys.* **1984**, AIP Publishing LLC.

Figure 19 shows a plot of the escape probability $P(E)$ *versus* electric field E at different thermalization lengths a. It is apparent that at low electric fields the escape probability increases with thermalization length a. However, significant charge dissociation is only predicted at higher electric fields around 10^7 V cm^{-1}.

2.6.2 *Charge carrier mobility*

Once free charge carriers are created in a solar cell device they have to move to the respective electrodes in order to contribute to the photocurrent. Charge carrier transport in a perfect crystal can be described by band theory, where the Schrödinger equation is solved for the ensemble of lattice sites with Bloch waves as solution.[57] While band theory is a suitable model for inorganic semiconductors, it is less suitable for amorphous organic semiconductors, due to the high degree of energetic disorder in these systems, caused by kinks, defects or bond angle distortions along the polymer backbone. Typical conjugation lengths consist of 5 to 15 monomer units.[58] In organic semiconductors charge carrier transport is often treated as a hopping process of charges from site to site, similar to the migration process of neutral excited states (excitons) discussed in section 2.4.

2.6.2.1 *Gaussian Disorder Model*

The *Gaussion Disorder Model* GDM is based on two assumptions:

- Individual molecules or chain segments are positioned on a lattice.
- For many degree of freedoms, *e.g.* orientation of dipole moments or conjugation lengths, the density of states (DOS) can be treated as Gaussian:[59]

$$\rho(E) = \frac{1}{\sqrt{2\pi\sigma^2}} \exp\left[-\frac{E^2}{2\sigma^2}\right], \tag{39}$$

where E is the energy relative to the center of the DOS and σ is the width of the distribution, which is a measure for the energetic disorder of the system.[60] In conjugated polymers σ takes values of 50 to 100 meV.[61] Figure 20 shows the equilibration of a charge carrier within the Gaussian DOS until it reaches the mean energy $< E >$ of the DOS given by

$$< E >= -\frac{\sigma^2}{kT} \tag{40}$$

which is defined for an infinite number of sites. This is a static property of the GDM and it represents the average energy of a charge carrier in the system.[59] The Gaussian shape of the GDM has been verified theoretically and experimentally.[62, 63, 64]

The dynamic properties of the GDM, *i.e.* the hopping process of charged excited states (electrons or holes) from one localized energy

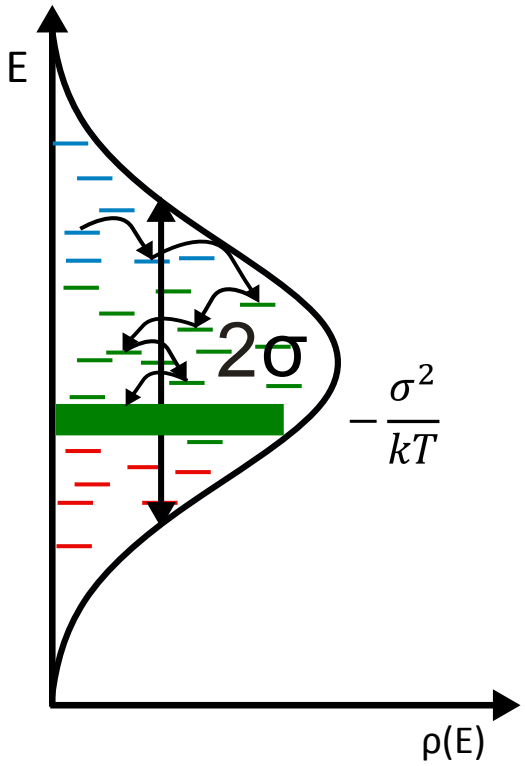

Figure 20: Density of states diagram illustrating the Gaussian disorder model. Equilibration of a charge carrier within a Gaussian density of states DOS is shown by the arrows. The green line indicates the mean energy $< E >$ of a charge carrier in the system given by $-\frac{\sigma^2}{kT}$. Figure reprinted from Kim.[65]

site i to a neighboring energy site j, is assumed to be of the *Miller-Abrahams* type[66]

$$\nu_{ij} = \nu_0 \cdot \exp(-2\alpha R_{ij}) \cdot \begin{cases} \exp\left(-\frac{E_j - E_i}{k_B T}\right), & E_j > E_i \\ 1, & E_j < E_i. \end{cases} \tag{41}$$

This rate, given by equation 41, describes a phonon-assisted tunneling process with the phonon vibration frequency ν_0, the overlap factor α, the distance between sites i and j R_{ij} and the respective site energies E_i and E_j. The first exponential term accounts for a decrease in energetic coupling with an increase in site separation. Hence, charge carrier hopping is more probable for adjacent sites than for more distant sites. The last term is a Boltzmann factor for a jump upward in energy $(E_j > E_i)$ and 1 for a downhill jump $(E_j < E_i)$. For hopping transitions there is no other activation barrier that has to be overcome by charge carriers than the difference in site energy. In the presence of an electric field the factor $-e\vec{r}\vec{F}$ is included in the top right expression of equation 41 for an upward jump. Here, e is the elementary charge, the vector $\vec{r}$ is the distance between sites and $\vec{F}$ is the electric field

vector. Thus, in the *Miller-Abrahams* formalism a downward jump is not accelerated by an electric field and depends only on the energy difference between sites i and j.[67]

The macroscopic mobility μ is field and temperature dependent:

$$\mu(T,F) = \mu_0 \cdot \exp\left[-\left(\frac{2\sigma}{3k_BT}\right)^2\right] \cdot \exp\left[C\sqrt{F}\left(\left(\frac{\sigma}{k_BT}\right)^2 - \Sigma^2\right)\right]. \quad (42)$$

Here, μ_0 is the zero-field mobility at infinite temperature, σ is the energetic disorder, Σ is the positional disorder (distribution of jump distances) and $C = 2.9 \times 10^{-4}\,cm^{1/2}V^{-1/2}$ is an empirically determined constant.[60]

2.6.3 *Loss channels in organic solar cells*

The overall power conversion efficiency η of an organic solar cell is a product of the absorption efficiency (the ratio of incident photons to absorbed photons), the efficiency of exciton diffusion to and quenching at the interface, and the charge carrier extraction efficiency:

$$\eta = \eta_{absorption}\eta_{quenching}\eta_{separation}\eta_{extraction}. \quad (43)$$

In each of the steps needed for photocurrent generation, there are certain loss mechanisms limiting the overall device performance. The different photophysical processes leading to photocurrent generation and the different loss mechanisms are schematically illustrated in figure 21.

The absorption efficiency $\eta_{absorption}$ is mainly determined by the optical density of the material. However, scattering and absorption in parasitic domains can also have a negative influence on $\eta_{absorption}$. The morphology of the active layer and the lifetime of excitons in the donor and acceptor materials influence the quenching efficiency $\eta_{quenching}$. If the donor or acceptor domain sizes are too big and/or the exciton lifetime is too short, excitons might not reach the interface within their lifetime, reducing in this way $\eta_{quenching}$. Geminate recombination of charges is a loss channel, that competes with the separation of charges and thus affects the charge separation efficiency $\eta_{separation}$. The extraction of free charges in a solar cell device is in competition with the non-geminate recombination of charges, hereby reducing the charge extraction efficiency $\eta_{extraction}$. The loss mechanisms of geminate and non-geminate recombination are of great interest to understand and optimize organic solar cells and will be discussed in more detail in the following two subsections.

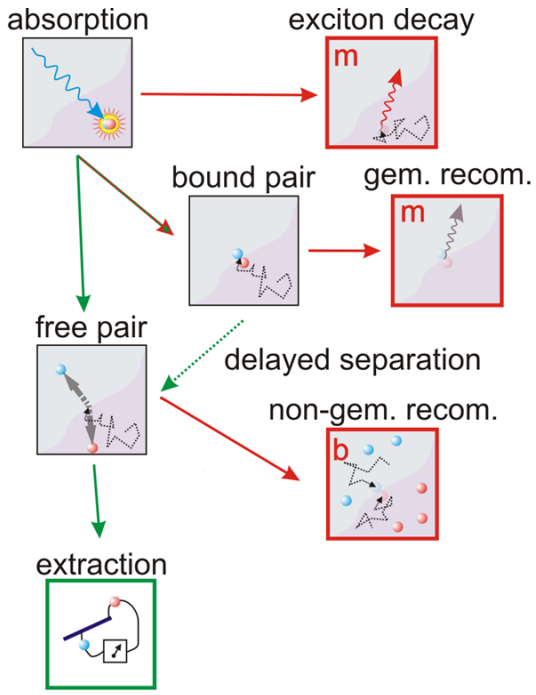

Figure 21: Graphical illustration of photophysical events occuring in an organic bulk heterojunction (BHJ) solar cell, that either lead to photocurrent generation (green boxes and arrows) or represent loss channels in a device (red colored boxes and arrows). The letters 'm' and 'b' are for monomolecular and bimolecular processes, respectively. Figure adapted from Howard and Laquai.[68]

2.6.3.1 *Geminate recombination*

Geminate recombination describes the recombination of bound charge pairs at the interface, that have been generated from exciton quenching by charge transfer at the donor/acceptor interface and have not overcome their mutual Coulomb attraction. As mentioned earlier (see section 2.6.1.2) the dissociation of charge transfer (CT) states is in kinetic competition with geminate recombination. It has been shown that CT states are immobile.[69] Hence, the recombination dynamics of bound interfacial charge-transfer states is independent of their density N_{CT} and depends solely on their lifetime:

$$\frac{d}{dt}N_{CT} = -k_g N_{CT}, \tag{44}$$

The dynamics of geminate recombination can thus be described with a single exponential with the recombination rate constant k_g. This characteristic decay behavior helps to distinguish different kinds of species in the analysis of transient absorption (TA) experiments.

2.6.3.2 *Non-geminate recombination*

After exciton quenching at the donor/acceptor interface and successful charge dissociation into spatially separated charges, these free charges have to diffuse to the electrodes in order to contribute to the photocurrent. However, it might happen that such a free charge carrier meets another free charge carrier of opposite charge at the interface and they undergo *non-geminate recombination*. This kind of recombination is called non-geminate, because these charge carriers are likely to originate from different excitons. A theoretical description for such a recombination process was first given by Langevin for the recombination of ions in gases.[30] A prerequisite for Langevin recombination is that the mean free path of a charge carrier is less than the Coulomb capture radius r_C of two opposite charge carriers as introduced in section 2.6.1.2. This prerequisite can be considered fulfilled in organic BHJ solar cells due to the limited length of conjugated chain segments or by the hopping distance between neighboring sites.[70] The Langevin recombination rate R is proportional to the product of the electron and hole densities n and p:

$$R = \gamma n p. \tag{45}$$

As charges in the solar cell are created from excitons the total number of electrons must equal the total number of holes ($n = p$) and equation 45 can be written as

$$R = \gamma n^2. \tag{46}$$

With increasing mobility of electrons μ_e and holes μ_h, the probability of an encounter of charges at the interface also increases. Thus, the proportionality factor can be written as

$$\gamma = \frac{e(\mu_e \mu_h)}{\epsilon_0 \epsilon_r}, \tag{47}$$

where e is the elementary charge, ϵ_0 the vacuum permittivity and ϵ_r the dielectric constant of the medium. Essentially, non-geminate recombination is accelerated with increasing charge carrier density and/or increasing charge carrier mobility. When applying this formalism to the recombination dynamics of free charge carriers in an organic BHJ, deviations from the Langevin recombination rate are frequently observed.[71, 72, 73, 74] These deviations can easily be understood, since the Langevin formalism was developed for the recombination of ions in the gas phase that differs from the recombination of charges in organic semiconductors. After charge separation in an organic BHJ electrons and holes are confined to the donor and acceptor phases, respectively. Charge carrier recombination can only

occur when two opposite charges meet at the interface. This strongly reduces the recombination rate in organic semiconductors that are not three dimensionally isotropic and homogeneous as are the gas phases for which Langevin theory was originally developed.[70] Furthermore, increased disorder close to the donor/acceptor interface can shift the energy levels and this way hamper the recombination by rejecting charge carriers.[70] In addition, a higher recombination order than 2 (exponent in equation 46) was observed in organic semiconductors, that can be caused by a reduced dimensionality in recombination or a charge carrier dependent mobility.[75] The consideration of all these effects leads to the modified Langevin recombination rate

$$R = \xi \frac{e(\mu_e \mu_h)}{\epsilon_0 \epsilon_r} n^{\lambda+1}, \tag{48}$$

with a prefactor ξ, also called the Langevin reduction factor, and the generalized reaction order $\lambda + 1$. The charge carrier density dependent decay (non-geminate recombination) of free charges helps in the interpretation of transient absorption data. In particular, the two decay mechanisms geminate and non-geminate recombination are discernible because of their different decay behavior.

2.7 MATERIALS FOR ORGANIC SOLAR CELLS

The active layer of organic solar cells consists of conjugated small molecules or polymers. Usually, two different materials with different optical and electrochemical porperties are used. One material serves as the electron donor and the other as the electron acceptor. Often, the donor material absorbs the bigger fraction of the incident light in comparison to the acceptor. This is especially the case for organic solar cells based on a small molecule or polymer as donor and the fullerene C_{60} as acceptor, since C_{60} has a negligible absorption in the vis-NIR spectral region. Over the last decades tremendous research effort has been put into the development of novel organic donor and acceptor materials on the basis of different design strategies.

The first organic solar cell based on two materials (electron donor and electron acceptor) was a bilayer solar cell produced by evaporation of small conjugated molecules, namely copper phtalocyanine and a perylene tetracarboxylic derivative as donor and acceptor materials, respectively. This solar cell, presented by Tang in 1986 had a power conversion efficiency of 1 %, which was remarkable at that time.[42] In 1993, Sariciftci showed the potential of the fullerene C_{60} as acceptor material in organic photovoltaics (OPV).[76] Today, fullerene and its derivatives are still widely-used acceptors, due to their high electronegativity, multiple degeneration of the LUMO level, favorable

crystalization behavior, as well as their isotropic electron transport and high mobility.

Another milestone in the development of OPV was the invention of the bulk heterojunction (BHJ). Efficient solution processed organic BHJ solar cells were independently realized in 1995 by the groups of Heeger and Friend with polymer/fullerene and polymer/polymer blends, respectively.[43, 77] For more details on device architecture and the BHJ concept see section 2.5.2.

2.7.1 *Donor materials*

In 1993, Wudl and Srdanov developed the donor polymer poly(2-methoxy-5-(2'-ethyl-hexyloxy)-1,4-phenylene vinylene) (MEH-PPV).[78] This polymer was used together with the fullerene derivative [6,6]-phenyl-C61-butyric acid methyl ester ($PC_{61}BM$), invented by Hummelen et al. [79] in the first solution processed organic BHJ solar cell presented in 1995 by Yu et al. from Heeger's group.[43] Derivatives of phenylene vinylene backbones such as MEH-PPV or poly(2-methoxy-5-(3,7-dimethyloctyloxy)-1,4-phenylene vinylene) (MDMO-PPV) are important representatives of conjugated semiconducting donor polymers, whose application in organic optoelectronic devices was studied intensively in subsequent years. At the beginning of the 21st century the efficiency of PPV-based OSC devices could be improved to values of more than 3%,[80, 81] However, the drawback of the PPV-type materials is their large bandgap and low mobility.

Research efforts were focused onto new materials with improved optical and electrical properties, like thiophene-based donor polymers which exhibit good thermal and chemical stability. The most prominent polythiophene is poly(3-hexylthiophene) (P3HT), which has an optical bandgap of 1.9 eV. Optimized P3HT/$PC_{61}BM$ devices yield power conversion efficiencies (PCE) of around 5 %.[82] For many years P3HT was the standard hole conducting donor polymer in research, especially due to its ease of processability, acceptable hole mobility, long stability, and its commercial availability on a multi-gram scale.[70, 83] These beneficial factors also made P3HT a suitable candidate for large scale roll-to-roll (R2R) fabrication processes of solar cell modules.[84, 85] Today, P3HT is maybe the most famous, but at least the most studied conjugated polymer for OPV applications.[86] Disadvantages of P3HT are e.g. the low V_{OC} when blended with $PC_{61}BM$ and the absorption restricted to below 600 nm.

Another interesting class of hole conducting donor-type conjugated polymers are the poly(2,7)carbazoles,[87] such as poly[2,6-(4,4-bis-(2-ethylhexyl)-4H-cyclopenta[2,1-b;3,4-b']-dithiophene)-alt-4,7-(2,1,3-benzothiadiazole) (PCDTBT) synthesized in 2007 by Leclerc et al. [88] With this polymer the open circuit voltage could be enhanced to ~ 0.88 V and a new record power conversion efficiency of ~ 6 % with external

quantum efficiency values approaching unity was reported in 2009 by Park et al.[89]

The disadvantage of all the aforementioned donor materials for organic solar cells is that the short circuit current obtained in devices is relatively low compared to other thin film solar technologies, like dye sensitized solar cells (DSSC) or amorphous silicon (a-Si) solar cells. Silicon has a bandgap of 1.1 eV and thus has a much better overlap with the solar spectrum than e.g. P3HT with an optical bandgap of ~ 1.9 eV.[9] Hence, in order to improve the power conversion efficiency of organic solar cells, novel donor materials with lower bandgaps have been developed with the potential to produce higher short circuit currents in OSCs due to better photon-harvesting properties. A prominent example of such a low-bandgap polymer is poly[2,6-(4,4-bis-(2-ethylhexyl)-4H-cyclopenta[2,1-b;3,4-b′]-dithiophene)-alt-4,7-(2,1,3-benzothiadiazole) (PCPDTBT). By bridging the thiophenes in PCPDTBT with a Si-atom instead of the C-atom Si-PCPDTBT (a.k.a. PSBTBT) was obtained, which resulted in an even more favorable solid state morphology, leading to power conversion efficiencies around 5 %.[90, 91]

The class of PTB-polymers developed by Yu et al.[92] is the first class of polymers, where a low lying HOMO level and a small bandgap where obtained simultaneously, leading to relatively large values for V_{OC} and J_{SC} in combination with fullerene acceptors.[9] An optimized solar cell cell composed of polythieno[3,4-*b*]-thiophene-*co*-ben-zodithiophene (PTB7) and the fullerene derivative $PC_{71}BM$ in an inverted structure was reported by He et al. in 2012 exhibiting a PCE of ~ 9 %, a V_{OC} of 0.74 V and a J_{SC} of 17.2 mA cm^{-2}.[93] Although PTB7 shows an impressive device performance, it suffers from strong degradation, which hampers its commercial applicability in large solar cell modules.[40]

The most efficient single-junction organic solar cells up-to-date rely on low-bandgap polymers blended with fullerene derivatives. In 2014 Liu et al. published results on organic solar cells based on the polymer PffBT4T-2OD blended with different fullerene derivatives, namely $PC_{61}BM$, $PC_{71}BM$ and $TC_{71}BM$, yielding PCE values of 10.4 %, 10.5 %, and 10.8 %, respectively.[94] Since June 2015 Yan's group holds a new record with an OSC reaching a PCE of 11.5 % as certified by National Renewable Energy Laboratory (NREL).[8] For more details on low-bandgap polymers and design strategies see section 2.7.3.

2.7.2 *Acceptor materials*

As mentioned in the previous subsection, nowadays in the most efficient organic solar cells fullerene derivatives are used as electron acceptors. While buckminster fullerene C_{60} is suitable for use in organic bilayer devices where the donor and acceptor small molecules are evaporated under high vacuum, it cannot be used for solution

processed bulk-heterojunction devices, becuase its solubility is limited. With the introduction of the soluble fullerene derivative $PC_{61}BM$ in 1995 by Hummelen et al.[79] the research in the field of solution processed organic BHJ solar cells was accelerated. Employed in OSCs fullerene derivatives show favorable packing properties, isotropic and high electron mobility. However, C_{60} shows little to no absorption in the visible range and hence does not contribute to the harvesting of photons in the BHJ. The fullerene C_{70} and its derivatives, e.g. $PC_{71}BM$, exhibit more favorable interpenetration properties compared to $PC_{61}BM$ and enhanced absorption in the visible region, which generally leads to larger photocurrents.[95, 96] The drawback of $PC_{61}BM$ and $PC_{71}BM$ is that they have relatively low-lying LUMO levels which often leads to thermalization losses and in turn to a reduced open circuit voltage V_{OC}. In P3HT/$PC_{61}BM$ solar cells for instance, V_{OC} is limited to $\sim 0.6\,V$. With the introduction of the fullerene derivative ICBA with a LUMO at $-3.74\,eV$ the open circuit voltage in P3HT cells could be improved to $0.85\,V$, leading to an enhanced PCE of 6.5 %.[97, 98]

As the synthesis and purification of fullerene derivatives is challenging, the absorption in the visible spectral region is rather small, and the tunability of the HOMO and LUMO levels is limited, considerable research effort is still put into developing alternative acceptor materials. Perylene derivatives, such as perylene diimides (PDI), are a promising class of acceptor type molecules, due to their tunable electrical and optical properties, their ease of processing, and their superior light- and heat-stability.[39] PDI derivatives absorb in the visible part of the spectrum and complement the absorption of low-bandgap polymers. Hence, when both material types are combined an optimum coverage of the solar spectrum can be reached. Issues originating from aggregation of PDI molecules are addressed by synthesizing non-planar structures. In combination with a low-bandgap polymer donor a PCE of 2.77 % could be achieved using such a non-planar structure.[99] Recently, a new record for polymer/PDI solar cells was set by Zhao et al. with the difluorobenzothiadiazole donor polymer PffBT4T-2DT and the PDI derivative SF-PDI_2.[100] Their solar cell yields a PCE of 6.3 % with an open circuit voltage of $0.98\,V$, demonstrating the potential of PDI derivatives as electron acceptor materials in OPV.

Further non fullerene small molecule acceptors are based on bifluoroylidene,[101] diketopyrrolopyrrole (DPP),[102] benzothiadiazole (BT),[103] pentacene[104] or naphthalene diimides (NDI).[105]

In addition to small molecule acceptors also the potential of polymers as electron acceptor in organic BHJ solar cells is being investigated. The advantage of polymer/polymer or all-polymer solar cells over polymer/fullerene solar cells is that their morphology is more stable and thus they are less sensitive to mechanical stress, which is interesting for the application in flexible devices.[106, 107] In addi-

tion, the electrochemical and optical properties of donor and acceptor can be adapted to each other more easily. For a long time the efficiencies reported for all-polymer solar cells were rather small with values not significantly exceeding 3 %,[108, 109, 110] but recently a PDI and NDI based polymer acceptor showed a PCE of 6.17 % in conjunction with the donor polymer PBDTTT-CT.[111]

2.7.3 *Low bandgap polymers*

Before solar radiation reaches the earth's surface it has to travel through the atmosphere, where the radiation is attenuated in specific regions of the spectrum according to the air mass that the light passes.[6] At the equator the irradiation of the sun reaching the earth's surface is defined as the air mass 1 global (AM 1G) spectrum, whereas the irradiation spectrum of the sun incident at sea level at a zenith angle of 48° is defined as the air mass 1.5 global (AM 1.5G) spectrum. Light at this incidence angle has to travel 1.5 times the length of the atmosphere compared to when incident at the zenith. The AM 1.5G spectrum is the standard spectrum used to characterize solar cells when measuring $J-V$ curves. It is similar to the irradiation of the sun at latitudes corresponding to the USA or Central Europe.

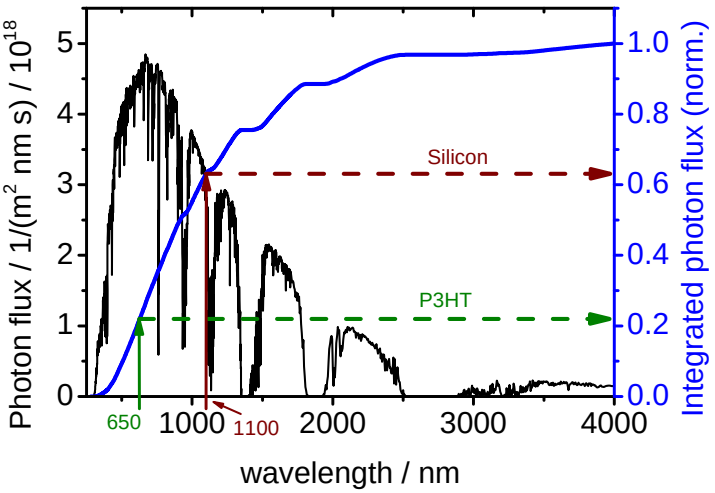

Figure 22: AM 1.5G spectrum presented as the photon flux (black curve). The integrated and normalized photon flux is presented as the blue curve (right y-axis). With a silicon based material, having an absorption onset at 1100 nm around 60 % of the solar irradiation can be absorbed. However, when using P3HT as absorber material only around 20 % of the sun's photons can be collected, reducing the potential photocurrent of the solar cell.

Figure 22 shows the AM 1.5G spectrum (black line) based on data from NREL.[112] The spectrum shows the photon flux dependent on the wavelength. This representation was preferred over the incident power, because for a solar cell rather the amount of photons that

can potentially be absorbed and converted into electrons in a specific wavelength region is of interest, than the energy of the photons. The AM 1.5G spectrum extends from the UV region at a wavelength of roughly 300 nm over the visible region into the NIR wavelength region beyond 4000 nm. The photon flux has a maximum at around 650 nm. At specific wavelength regions there are dips in the spectrum, corresponding to the absorption of gases and vapors, notably, ozone (O_3), oxygen, carbon dioxide, and water.[113] From 650 nm onwards the photon flux decreases with increasing wavelength. However, in the NIR spectral region lies a significant part of the overall spectral intensity. The blue curve in figure 22 represents the integrated and normalized photon flux of the AM 1.5G spectrum. From the integrated photon flux shown on the right y-axis we can estimate, that with an absorber material like silicon, having a band gap of 1.1 eV corresponding to 1100 nm, around 60 % of the sun's photons from the AM 1.5G spectrum can be harvested, while using a mid bandgap polymer such as P3HT with an absorption onset at ~ 650 nm only around 20 % of the photon flux is covered. It is thus apparent that increasing the absorption of donor polymers to longer wavelengths, i.e. lowering the band gap, enhances the amount of photons absorbed in the active layer which can be potentially converted into charges and in turn can contribute to the photocurrent. It should be noted however, that due to the lower energy of longer wavelength photons the voltage difference that the device can produce is limited. Therefore there is an optimum band gap, at which the power conversion efficiency of organic solar cells can be maximized.[6] According to equation 27 the efficiency of a solar cell can be optimized by maximizing the product of the open circuit voltage (V_{OC}), the short circuit current density (J_{SC}), and the fill factor (FF):

$$\xi = V_{OC} \times J_{SC} \times FF. \tag{49}$$

Optimizing all the three parameters in a single material system remains a challenge, but significant progress in understanding the link between polymer design and these factors has been made over the past decade.[114] V_{OC} and J_{SC} can be optimized by engineering the band gap and energy levels. The open circuit voltage in a OSC can be expressed by the empirical relation

$$V_{OC} = \frac{1}{e}\left(\left|E_{HOMO}^{donor}\right| - \left|E_{LUMO}^{acceptor}\right|\right) - 0.3V, \tag{50}$$

where e is the elementary charge, E are the energy levels given in eV, and 0.3 V is a typical loss found in BHJ solar cells. When lowering the band gap of the donor, the donor's HOMO should be kept sufficiently low to guarantee a high open circuit voltage.

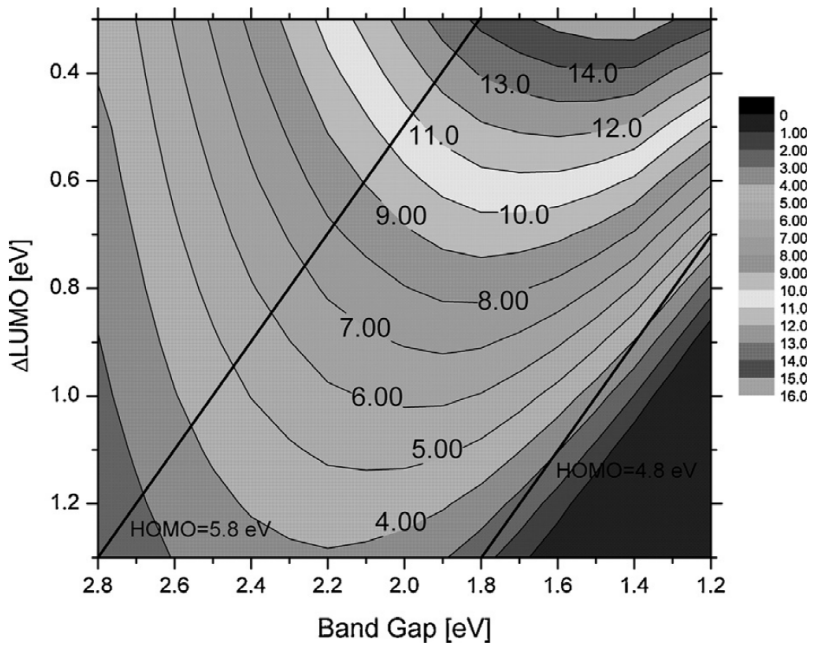

Figure 23: Contour plot of the power conversion efficiency (PCE) of a bulk heterojunction (BHJ) solar cell in dependence of the polymer/PCBM LUMO level offset (ΔLUMO) and the donor polymer band gap. The LUMO level of PCBM is at 4.3 eV. The PCE was calculated using equation 50 assuming an EQE of 80 % and a FF of 0.75. Black lines indicate constant HOMO levels of 5.8 eV and 4.8 eV. Figure reprinted from Scharber and Sariciftci under the CC BY license.[37]

Based on relation 50 Scharber at al. developed a model to estimate the optimum band gap of a conjugated polymer donor and the maximum power conversion efficiency achievable in an organic BHJ solar cell with PCBM as acceptor.[115, 37] Figure 23 shows a contour plot of the efficiency in dependence of the LUMO level offset ΔLUMO and the optical band gap, assuming typical values for the external quantum efficiency (EQE = 80 %) and the fill factor (FF = 0.75). This model delivers a maximum PCE of 15 % and an optimum band gap of 1.45 eV, corresponding to an absorption onset of the low-bandgap polymer at 855 nm. As mentioned in the previous subsection the current record efficiency for a single-junction organic BHJ solar cell based on a low-bandgap polymer blended with PCBM has a value of 11.5 %. Hence, current polymer/PCBM solar cells are already well performing, but there is still space for improvement. The performance of OSCs still needs to be optimized in order to become suitable for mass production.

The FF remains the least understood of the three factors in equation 49 contributing to the device efficiency. The FF is influenced by many factors, including the mobility of electrons and holes and the balance between them, interface recombination, morphology, and miscibility

between donor and acceptor.[116] Yet, it is still a challenge how to directly influence the FF. From a materials design perspective alone it is important to control the molecular planarity, the packing properties, the degree of crystallinity, and the molecular weight. Furthermore, it is meaningful to control the charge carrier mobility by incorporating high-mobility units.[114]

2.7.4 *Design strategies for low-bandgap polymers*

There are several factors influencing the band gap of a conjugated polymer - among these are[6]

i. bond-length alternation,

ii. intra-chain charge transfer,

iii. aromaticity,

iv. substituent effects,

v. intermolecular interactions,

vi. π-conjugation length.

While factors i.-iv. can be directly influenced by the molecular design, factors v. and vi. also depend on the ensemble- or bulk properties of the materials.

There are two main approaches to lower the bandgap in organic semiconducting polymers. The first is based on stabilizing the quinoidal form by influencing the bond-length alternation (i.) and the second approach relies on alternating donor and acceptor units within one repeat unit of the polymer in order to induce an intra-chain charge transfer (ii.).

2.7.4.1 *Quinoid polymers*

Conjugated molecules in the ground state have two resonant forms: an aromatic form and a quinoid form. In the ground state the quinoid form is usually less stable, because of its smaller bandgap - achieving a stable quinoid form therefore reduces the bandgap. It has been shown by Yu et al. that the introduction of a thieno[3,4-*b*]thiophene (TT) unit can stabilize the quinoidal form of a polymer.[117, 92]

An example for a *quinoid polymer*, i.e. a polymer where the quinoid form is stabilized by the introduction of a TT unit, is PTB7.[119] Figure 24 shows the two resonance forms of the PTB7 repeat unit. In the excited state the quinoid form is stabilized additionally. However, this usually also lowers the open circuit voltage V_{OC} by pulling up the HOMO level. A more popular approach of designing low-bandgap polymers is using donor-acceptor copolymer architectures.

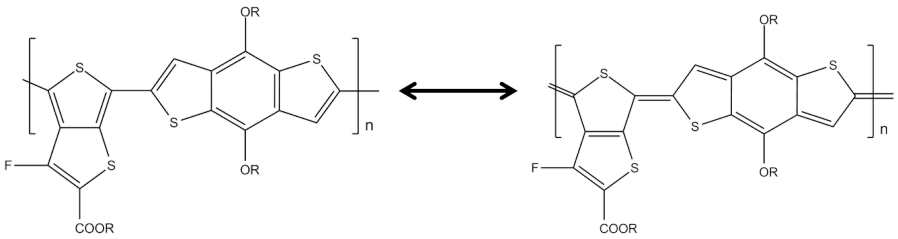

Figure 24: The two resonance forms of PTB7: aromatic and quinoid form. R = 2-ethylhexyl. Figure reprinted from Mangold.[118]

2.7.4.2 *Donor-acceptor copolymer approach*

In donor-acceptor copolymers electron-rich (donor) and electron-deficient (acceptor) moieties are alternated along the polymer backbone, leading to push-pull driving forces within the polymer. As intramolecular charge transfer takes place, the double bond character between the donor and acceptor units is increased, leading to more planarized polymer chains and hence a more delocalized π-electron system. According to molecular orbital perturbation theory the delocalization of the π-electrons leads to hybridization of the molecular orbitals and a redistribution of the electrons within the molecular system.[114, 120] This orbital mixing effect is illustrated in figure 25. The two resulting hybrid orbitals have a higher HOMO and a lower LUMO level, resulting in a smaller effective bandgap of the donor-acceptor copolymer.

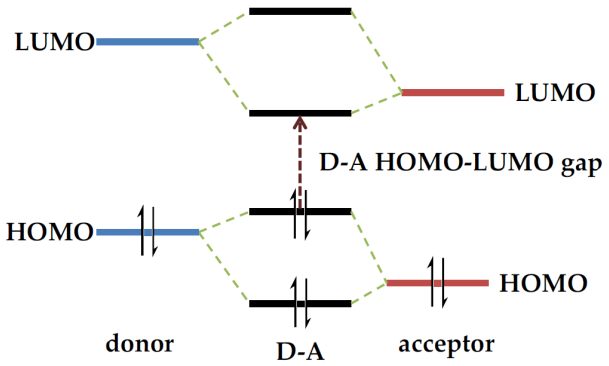

Figure 25: Energy diagram illustrating orbital mixing in donor-acceptor copolymers. Alternating donor and acceptor moieties in the conjugated polymer lead to new hybrid orbitals with a higher HOMO and lower LUMO level, thus reducing the effective bandgap of the donor-acceptor copolymer. Figure reprinted from Gehrig.[39]

The advantage of designing low-bandgap polymers using the donor-acceptor approach is that the optical and electrical properties can be well tuned by selecting and combining different donor and acceptor units. Figure 26 shows typical donor and acceptor moieties used in the design of low-bandgap D-A copolymers. The HOMO is usually

located on the donor moiety, whereas the LUMO is located on the acceptor moiety.[6]

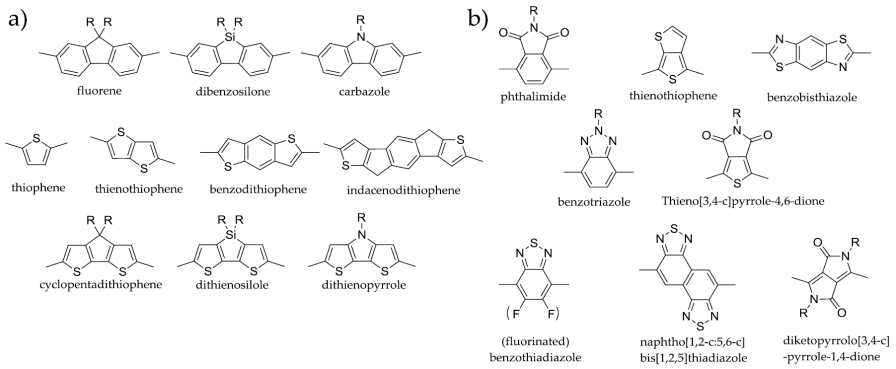

Figure 26: Typical building blocks used in donor-acceptor copolymers: (a) electron-rich donor moieties, and (b) electron-deficient acceptor moieties. Figure reprinted from Gehrig.[39]

High efficiencies of more than 7 % have been achieved in BHJ solar cells using low-bandgap donor-acceptor copolymers blended with $PC_{71}BM$.[121, 122, 123, 124] Recently, record efficiencies even exceeding 10 % in single-junction cells have been reported.[94] In the following subsection we will take a closer look at donor-acceptor copolymers based on the diketopyrrolopyrrole (DPP) building block.

2.7.5 *DPP-based donor-acceptor copolymers*

In this work the research focus lies on the photophysical properties of DPP-based donor-acceptor copolymers applied in organic BHJ solar cells. Donor-acceptor copolymers and small molecules based on the electron-accepting DPP moiety have gained considerable attention, in particular for the application in organic solar cells and organic field effect transistors (OFETs), due to their relatively low HOMO and LUMO levels and their high charge carrier mobility. Power conversion efficiencies as high as 8 % in (BHJ) solar cells with $PC_{71}BM$ as electron acceptor have been reported.[125, 126] Applied in OFETs DPP-based copolymers have reached record mobility values of 10.5 $cm^2\ V^{-1}\ s^{-1}$ for holes and 3 $cm^2\ V^{-1}\ s^{-1}$ for electrons.[127, 128] These values are greater than those for amorphous silicon, which are in the range of 0.1 to 1 $cm^2\ V^{-1}\ s^{-1}$.[129]

The chromophore DPP belongs to the class of the so-called 'high-performance pigments'.[130] A 3,6-diphenyl-substituted DPP was first synthesized by Farnum et al. in 1974.[131] In the 1980s 2,5-diketopyrrolo-[3,4-c]pyrrole derivatives were commercialized.[132] Due to their deep color, and outstanding light and weather fastness they were also used in inks, plastics, paints, and lacquers.[133, 130] The most prominent example is *Pigment Red 254* which was the basis for the red Ferrari finish.[134, 135]

Because of the beneficial electronic properties, the stability, and strong fluorescence emission of specifically substituted DPP derivatives in the solid state, their potential as building blocks in conjugated small molecules and polymers for different optoelectronic applications such as solid-state dye lasers,[136] OLEDs,[137] two-photon absorption,[138], OPVs,[139] and OFETs[140] has been investigated.[133, 141]

For the application of DPP-based copolymers in organic solar cells and field effect transistors in many studies thiophene moieties were used as the electron donating block. Figure 27 shows several structures of polymers based on DPP and thiophene. Bijleveld et al. presented polymer **1** (PDPP3T), which consists of alternating electron deficient DPP units and three electron rich thiophene units.[142] The onset of optical absorption in a thin film was at 1.3 eV and the HOMO and LUMO levels were determined by cyclic voltammetry (CV) to be at −5.17 and −3.61 eV *versus* vacuum. The high molecular weight fraction of the polymer PDPP3T with $M_n = 54\,kg\,mol^{-1}$ was blended with $PC_{71}BM$ and applied as the active layer in an OSC. The obtained open circuit voltage of 0.65 V, short circuit current of $11.8\,mA\,cm^{-2}$, and the fill factor of 0.6 resulted in a power conversion efficiency (η) of 4.7 %. The optimum bulk heterojunction morphology and hence device performance was reached by spincoating the active layer materials from a solution of chloroform and the solvent additive diiodoctane (DIO). Applying the pure polymer in an OFET resulted in a device with ambipolar charge carrier transport characteristics exhibiting hole mobilities of $0.04\,cm^2\,V^{-1}s^{-1}$ and electron mobilities of $0.01\,cm^2\,V^{-1}s^{-1}$.[142]

Wienk et al. reported OSCs with a PCE η of 4 % using polymer **2** blended with $PC_{71}BM$ in a ratio of 1:2 by weight spincasted from a solvent mixture of chloroform and o-DCB in a ratio of 4:1 by volume with a corresponding J_{SC} of $11.3\,mA\,cm^{-2}$, V_{OC} of 0.61 V, and a FF of 0.58.[139] The optical bandgap was determined to be 1.4 eV and the molecular weight M_n was $20\,kg\,mol^{-1}$. The structurally similar copolymer **3**, that differs in the absence of the alkyl chains on two of the four thiophene units and has longer branched alkyl chains attached to the DPP unit, was presented by Liu et al.[143] They blended the polymer with $PC_{71}BM$ (1:1 w/w) and spincoated the active layer from a solvent mixture of chloroform and o-DCB (1:4 v/v). The optimized cells had a J_{SC} of $14.8\,mA\,cm^{-2}$, a V_{OC} of 0.63 V, and a FF of 0.60, yielding a PCE of 5.6 %. The addition of o-DCB as a co-solvent drastically improved the device performance, which is especially due to an optimized morphology leading to a higher short circuit current in the optimized device. When chloroform was used as the only solvent Liu et al. obtained a device with a J_{SC} of only $2.8\,mA\,cm^{-2}$, a similar V_{OC} of 0.63 V, and a similar FF of 0.61. Due to the decrease in J_{SC} the PCE is only around 1 %. In general, finding the right solvent mixture or solvent additive in order to improve the morphology of

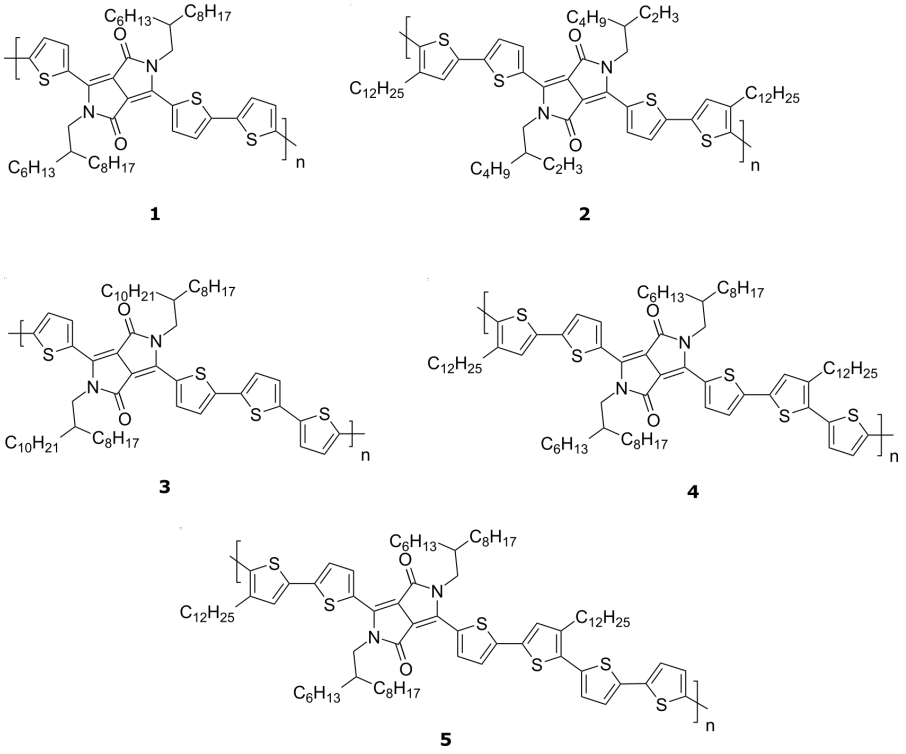

Figure 27: Chemical structures of diketopyrrolopyrrole (DPP) - thiophene alternating copolymers.

the active layer is of utmost importance for optimizing OSCs based on low-bandgap polymers such as DPP-based donor-acceptor copolymers.

Li et al. synthesized polymers **4** and **5**, each with an additional thiophene unit. The idea was to increase the length of the electron-rich π-conjugation segment by adding additional thiophene units, which alternate with the more isolated electron-deficient DPP unit. This leads to an increase of the HOMO and LUMO levels of the polymer and an increase in the driving force for charge generation. However, the open circuit voltage is expected to decrease. The quantum efficiency for charge generation of polymer **4** was indeed beneficial, leading to a relatively high J_{SC} of 16.4 mA cm^{-2}. Compared to polymers **1 - 3** the V_{OC} was lower with a value of 0.56 V and the FF of 0.64 was slightly higher, resulting in a PCE of 5.8 %. The performance of polymer **5** in conjunction with $PC_{71}BM$ was slightly worse than that of polymer **4**, exhibiting a PCE of 5.9 % with J_{SC} = 14.3 mA cm^{-2}, V_{OC} = 0.56 V, and FF = 0.65. The molecular weight M_n of polymer **4** and **5** was 37 kg mol^{-1} and 38 kg mol^{-1}, their optical bandgap was 1.46 eV and 1.48 eV, respectively. Applied in OFET devices these DPP-polymers show ambipolar charge carrier transport. However, the electron mobilities μ_e of both polymers were one order of magnitude smaller than the hole mobilities μ_h. This is probably due to the high LUMO level in the polymers, which hinders efficient injection of electrons from the gold contacts of

the OFET devices and increases the probability for electron trapping at the SiO_2 surface. For polymer **4** μ_h equaled 1.5×10^{-2} cm² $V^{-1}s^{-1}$ and $\mu_e = 1.5 \times 10^{-3}$ cm² $V^{-1}s^{-1}$. In OFETs built with **5** μ_h and μ_e took values of 5.0×10^{-2} and 3.0×10^{-3} cm² $V^{-1}s^{-1}$, respectively. In chapter 5 experimental results on the polymer PDPP5T, which has the same structure as polymer **4** will be discussed.

Yiu et al. presented polymers **6a-d** (PDPP2FT) shown in figure 28, that are related to polymer **1** with the difference that the thiophene units adjacent to the DPP unit were replaced by furane units and the branched alkyl chains were replaced by long linear alkyl chains or smaller branched alkyl chains.[144] It had been shown by Woo et al. earlier that incorporation of the furan co-monomer into the polymer backbone increases solubility.[145] As a result smaller 2-ethylhexyl (2EH) alkyl side chains are necessary to guarantee for the solubility of the PDPP2FT polymer in common solvents (polymer **6d**), while the analogous thiophene-based polymer needs larger 2-hexyldecyl (2HD) alkyl side chains to be solution processable.[142, 145] Yiu et al. argued, that replacing the branched alkyl chains by long linear alkyl side chains leads to an increased polymer planarity that may promote self-assembly into extended crystalline domains with longer range backbone alignment, which might ultimately be beneficial for OPV device performance.[144] With polymer **6b** they obtained a PCE of 6.5 % which is significantly higher than the power conversion efficiencies that were obtained with PDPP3T-2HD (4.7 %) and PDPP2FT-2EH (5 %) with branched alkyl chains. The increase in PCE is due to an increased FF of 0.64 and increased J_{SC} of 14.8 mA cm^{-2}. The V_{OC} remained similar at 0.65 V. Furthermore, they showed that the linear side chains in polymers **6a-c** reduced the π-π-stacking distances between backbones and increased the correlation lengths of both π-π-stacking and lamellar spacing.[144]

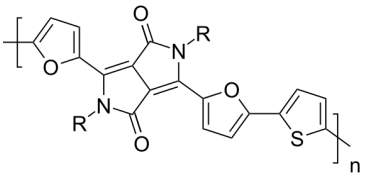

6a: R=$C_{12}H_{25}$
6b: R=$C_{14}H_{29}$
6c: R=$C_{16}H_{33}$

6d: R=2-ethylhexyl

Figure 28: Chemical structure of PDPP2FT polymers with different side chains. Polymers **6a-c** have long linear alkyl chains. Polymer **6d** has branched alkyl chains.

Another promising approach in designing DPP-based donor-acceptor copolymers is using benzodithiophene (BDT) as electron-rich comonomer.

Figure 29 shows molecular structures of copolymers based on an alternation of DPP and BDT units along the polymer backbone.

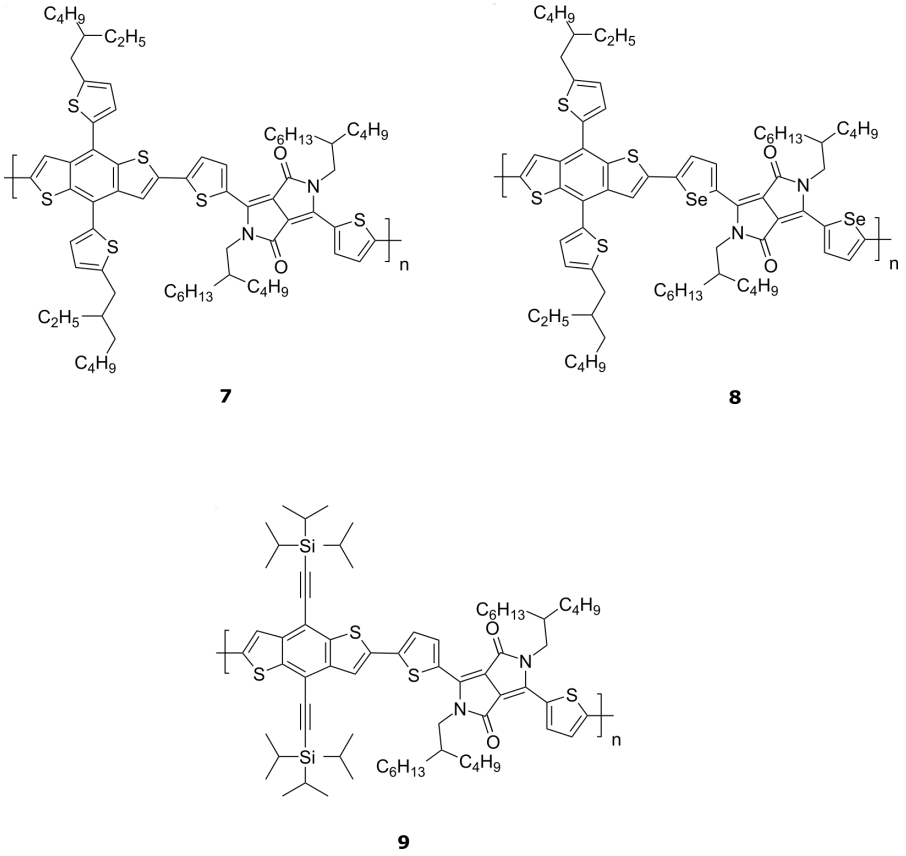

Figure 29: Chemical structures of benzodithiophene (BDT) - thiophene alternating copolymers.

In 2012, Dou et al. presented a single-layer BHJ solar cell based on polymer **7** blended with $PC_{71}BM$, which had a J_{SC} of 13.5 mA cm^{-2}, a V_{OC} of 0.74 V, and FF of 0.65, resulting in a PCE of 6.5 %.[146] The relatively high V_{OC} value is due to the attachment of the thiophene moieties to the BDT unit to create the thienylbenzodithiophene (BDTT) unit, which in turn lowers the HOMO and LUMO levels. The optical bandgap $E_g = 1.44$ eV was determined from the absorption onset. The HOMO and LUMO energies were determined from CV measurements to be −5.30 and −3.63 eV, respectively and the molecular weight M_n was found to be 41 kg mol^{-1}. The same polymer **7** was also applied in a tandem solar cell device together with a P3HT:ICBA front cell. The PCE of this tandem cell was 8.6 % with J_{SC} = 8.26 mA cm^{-2}, V_{OC} = 1.56 V, and FF = 0.67 as certified by NREL.[146]

In a later study Dou et al. replaced the thiophene moieties adjacent to the DPP unit in polymer **7** by selenophene units in order to lower the bandgap and enhance the charge carrier mobility. The optical bandgap of the new polymer **8** was determined to be 1.38 eV and M_n was 38 kg mol^{-1}. The HOMO and LUMO levels were measured by

CV to be at −5.25 eV and −3.70 eV, respectively. In a single junction device the maximum PCE was 7.2 % with a J_{SC} of 16.8 mA cm^{-2}, a V_{OC} of 0.69 V, and a FF of 0.62. In a tandem solar cell architecture with P3HT:ICBA as the additional solar cell the average PCE of a set of 20 devices was 9.5 % with a J_{SC} of 9.44 mA cm^{-2}, a V_{OC} of 1.52 V, and a FF of 0.66.

The best performing organic BHJ solar cell employing a DPP-based donor-acceptor copolymer up-to-date was presented in 2014 by Kim et al.[126] Their high molecular weight polymer **9** ($M_n = 76$ kg mol^{-1}) blended with $PC_{71}BM$ reached a maximum PCE of 8 % with a J_{SC} of 16.21 mA cm^{-2}, a V_{OC} of 0.76 V, and a FF of 0.65. The hole mobility determined in OFET devices was 0.12 cm^2 V^{-1} s^{-1}. The high values for V_{OC} and the HOMO level (−5.50 eV) resulted from the electron withdrawing effect of the carbon-carbon triple bond in the triisopropylsilylethynyl (TIPS) side moieties. They estimated the LUMO level to be at −4.00 eV and E_g to be at 1.44 eV.

The above examples show the high potential of DPP-based donor-acceptor copolymers for the application in organic solar cells with the so far highest reported power conversion efficiency of 8 % being competitive with other low-bandgap polymers designed for organic solar cells.

3

EXPERIMENTAL METHODS

3.1 SOLAR CELL PREPARATION

Figure 30 shows a typical layout of an organic solar cell. A thin layer of poly(3,4-ethylenedioxythiophene) poly(styrenesulfonate) (PEDOT:PSS) is spincoated on an indium tin oxide (ITO) covered glass substrate. PEDOT:PSS is a transparent hole transporter, which reduces the surface roughness of the ITO layer. Futhermore it facilitates the extraction of holes from the active layer. The active layer is either evaporated or spincoated on top of the PEDOT:PSS layer and finally an aluminum cathode is evaporated on the active layer. The ITO layer serves as the transparent anode and the PEDOT:PSS layer is a hole-conducting layer that facilitates the extraction of holes from the device. Depending on the material system used as the active layer a thin interlayer of calcium between the active layer and the aluminum top electrode can enhance the device performance by facilitating the extraction of electrons.

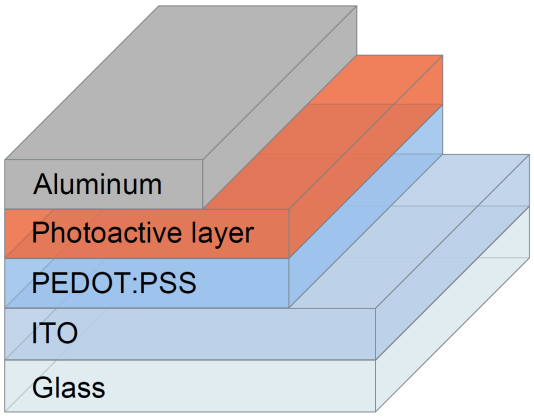

Figure 30: Typical device layout of an organic solar cell. A glass substrate is covered with ITO, which serves as the transparent anode material. Usually PEDOT:PSS is used as a hole conductor to facilitate hole extraction. On top of the active layer a thin aluminum cathode is evaporated. Figure reprinted from [40].

The solar cells in this work were all prepared based on the above layout. In detail the steps of the device preparation were as follows:

- Square shaped indium tin oxide (ITO) covered glass substrates from Präzisions Glas und Optik (PGO) with the dimensions of 24 × 24 mm were treated by wet etching to remove the ITO from the sides of the substrates, so that a 12 mm wide ITO stripe remains in the middle (see figure 31).

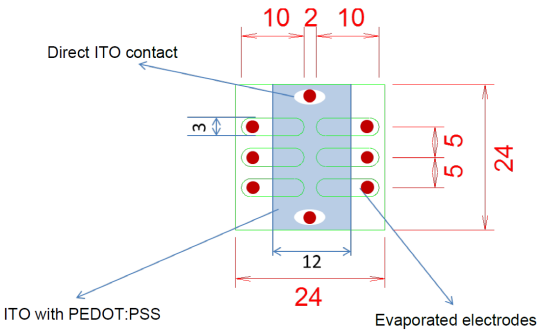

Figure 31: Top view of the solar cell layout used in this work. The blue area represents the transparent anode consisting of a 12 mm wide ITO stripe and a 40 nm thin PEDOT:PSS layer. The overlap of the six green 3 mm wide metal cathodes with the transparent anode defines the pixel size of 14 mm^2. In order to measure the device characteristics the PEDOT:PSS and active material layers were wiped away at the sides to enable direct contact with the ITO layer. Figure reprinted from [40].

- The patterned ITO substrates were successively cleaned in ultrasonic baths of acetone, isopropanol, and water for 10 min, respectively. In between every cleaning step the substrates were dried with nitrogen gas. The cleaned substrates were treated with argon plasma for 15 min.

- A 40 nm thin layer of PEDOT:PSS (Clevios P VP AI 4083, H.C. Starck) was deposited on the ITO layer by spincoating with speeds of 2500 rpm for 5 s and 5000 rpm for 25 s. The samples were then transferred into a nitrogen filled glovebox and were thermally treated at 120 °C for 30 min to remove residual water in the PEDOT:PSS films.

- The photoactive layer was spincoated on the annealed PEDOT:PSS layer from polymer/fullerene solutions, that had been stirred over night to guarantee that the polymers are fully dissolved. The spincoating speed and hence the thickness of the active layer were optimized for each material system. Typical thicknesses of the active layer are around 100 nm.

- The top electrodes (or back electrodes) were vaccum evaporated at a pressure of $\leqslant 10^{-6}$ mbar through an evaporation mask, which created six pixels on each substrate with a size of 14 mm^2. Depending on the material system, only 100 nm of aluminum was evaporated or an additional 5 nm interlayer of calcium was evaporated in addition.

- The active layer and the PEDOT:PSS layer were wiped away above and below the pixels in order to make a direct contact with the ITO layer. For device characterization each pixel was measured

individually. To protect the thin metal electrodes additional silver paste was applied on the pixels (red dots in figure 31).

3.2 SOLAR CELL CHARACTERIZATION

Solar cells were characterized by measuring current-voltage ($J-V$) characteristics and external quantum efficiency. Both characterization methods are described in detail in section 2.5.4. Here, we summarize the technical aspects of our setups.

3.2.1 *Current-voltage characteristics*

The figures of merit, the short circuit current, the open circuit voltage, the fill factor, and the power conversion efficiency were determined by measuring $J-V$ characteristics of the solar cells.

All $J-V$ characteristics were recorded in a nitrogen filled glove box. Solar cells were illuminated with an artificial AM 1.5G spectrum produced by a solar simulator (K.H. Steuernagel Lichttechnik GmbH, Germany) and a voltage was applied with a Keithley 236 source measure unit (SMU). The current flow through the solar cells was measured simultaneously with the same device.

3.2.2 *External quantum efficiency measurements*

The EQE, i.e. the ratio of extracted charge carriers to incident photons on the solar cell in dependence on the photon wavelength, was measured by illuminating an individual pixel of a solar cell with the output of a tungsten halogen lamp passing a TRIAX 180 monochromator. The current flow was measured with a Keithley 236 SMU. The number of incident photons at each wavelength was determined with a calibrated silicon photodiode.

3.3 STEADY STATE UV-VIS ABSORPTION SPECTROSCOPY

Steady state absorption spectra were recorded with a Perkin-Elmer Lambda 25 spectrophotometer.

3.4 QUASI STEADY-STATE PHOTOINDUCED ABSORPTION SPECTROSCOPY

In order to identify the absorption signatures of long-lived excited states ($\sim$ µs), such as triplet excitons or charges, photoinduced absorption spectroscopy (PIA) was carried out in quasi steady-state mode. PIA is an all optical pump-probe technique, where the excitation is provided by a square wave modulated monochromatic pump light source. The transmission of the excited sample is subsequently moni-

tored with monochromatic probe light, which can be tuned to various wavelengths in order to measure a broad spectrum from the visible to the NIR wavelength region (500 to 4000 nm). Figure 32 shows a schematic of our PIA setup.

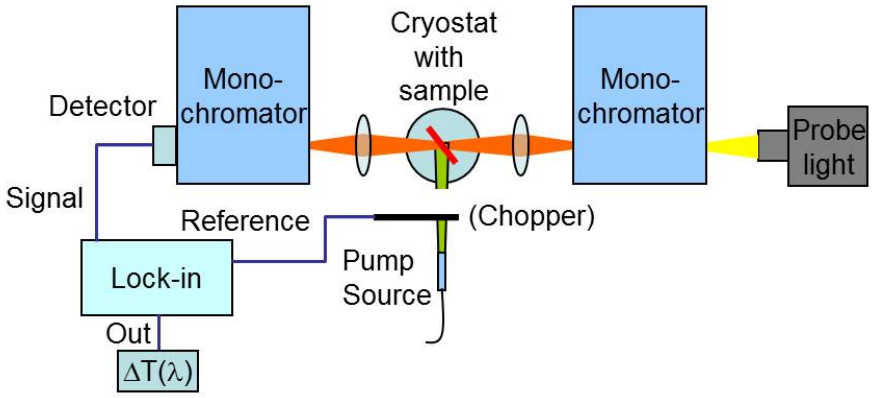

Figure 32: Experimental setup of the quasi steady-state photoinduced absorption measurement. For transmission measurements the chopper is placed behind the monochromator in the pump beam path. The chopper provides the reference for the lock-in amplifier. Figure reprinted from Meister.[147]

The sample was kept in an optical cryostat (Oxford Instruments Optistat CF) and was cooled down to liquid nitrogen temperature (~ 77 K), extending the excited-state lifetime and thus enhancing the signal that can be measured. In the sample chamber Helium gas was used as a heat transfer agent and to ensure an inert atmosphere. The probe light source was a 100 W tungsten lamp (Müller Elektronik Optik DUO150) in combination with a monochromator (LOT Oriel Omni-λ 300), which continuously illuminated the sample. The pump light transmitted by the sample was directed to a second monochromator with the same configuration and set wavelength as the first monochromator to ensure that only light of the set probe wavelength reached the detector and that scattered pump light and photoluminescence emission from the sample were suppressed. Three detectors were used for recording the transmitted probe light: For the spectral range from 500 to 1100 nm an amplified silicon detector (Thorlabs PDA 100A) was used. For the wavelength range from 900 to 1800 nm an amplified germanium detector (Thorlabs PDA 50B) was employed and an amplified and nitrogen-cooled indium antimonide (SbIn) detector covered the region between 1750 to 4000 nm. As pump source a cw-diode laser with an output light of 808 nm was used (Topag LDT-808-150GCB). The pump light was mechanically chopped (Thorlabs MC1000A) with a frequency of 317 Hz to induce a change in transmission ΔT. The detector signal was measured with a dual channel lock-in amplifier (EG&G Princeton Applied Research Model 5210). In order to calculate ΔT/T the transmission of the sample was measured

with and without a previous excitation. In addition, the data was corrected for photoluminescence and scattered light by measuring the signals under excitation illumination, but without the continuous probe light and subtracting these unwanted signals from the PIA signal.

3.5 TRANSIENT ABSORPTION SPECTROSCOPY

Transient absorption spectroscopy (TA) is a time-resolved pump-probe technique, which allows for the investigation of excited-state dynamics by monitoring the temporal change in transmission induced by transient excited states in a thin film or solution sample after excitation with an ultrashort monochromatic laser pulse. In our setup the probe pulse is a broadband supercontinuum white-light pulse, which allows to gather information over an extended spectral range with just one laser pulse. The white-light probe pulse is focused on the sample and the transmitted light is diffracted in a spectrograph onto an array detector in order to resolve the whole spectral information. The temporal resolution is obtained by successively varying the delay between the pump and the probe pulses. Every second probe pulse is recorded without having applied a pump pulse prior to probing in order to calculate the normalized change in transmission:

$$\Delta T/T = \frac{\Delta T_{\text{pump on}} - T_{\text{pump off}}}{T_{\text{pump off}}}. \tag{51}$$

Here, $T_{\text{pump on}}$ is the transmission recorded upon excitation with a pump pulse and $T_{\text{pump off}}$ is the transmission of the probe without a pump.

3.5.1 *Signals in transient absorption spectroscopy*

Typical signals observed in transient absorption spectroscopy are shown in figure 33 and are explained in the following:

- Ground state bleach (GSB): When the sample is excited by the pump pulse there are less molecules in the ground state S_0. As a consequence, the transmission in the region where the molecular system would exhibit an absorption band in the ground state is increased and hence a positive $\Delta T/T$ signal is observed.
- Stimulated emission (SE): If the pump pulse excites fluorescent excited states, the probe pulse can stimulate their radiative decay to the ground state. This causes an additional positive $\Delta T/T$ signal in the region of the sample's fluorescence emission and can be used to track the population evolution of emissive excited states.

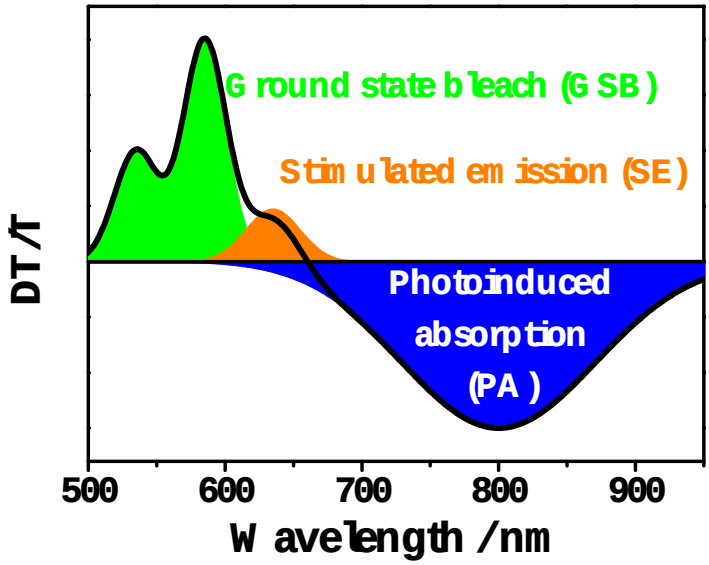

Figure 33: Typical signals observed in transient absorption spectroscopy. The black curve is a resulting spectrum, consisting of the overlay of a ground state bleach (GSB), a stimulated emission (SE), and a photoinduced absorption (PA) signal. Figure adapted from Gehrig.[39]

- Photoinduced absorption (PA): Excited states in the sample can be promoted into even higher lying states by absorption of light from the probe pulse. The absorption of excited states usually leads to a broad negative $\Delta T/T$ signal, due to the overlay of several excited-state transitions. As the spacing between higher lying excited states tends to become smaller, the PA signal usually extends to lower energies into the NIR wavelength region. Several excited-state species such as singlet excitons, charge-transfer states, free charges or triplet excitons can contribute to the PA signal.

In the linear absorption regime, i.e. at low pump fluences where non-linear effects can be neglected, the transient absorption signal is proportional to the number of absorbing species. $\Delta T/T$ for a transition from an initial state i to a final state f can be written as[118]

$$\Delta T/T(\lambda, t) = \sum_{i,f} \sigma_{if}(\lambda) \Delta N_i(t) d, \tag{52}$$

where $\sigma_{if}(\lambda)$ is the cross section for the probed transition, $\Delta N_i(t)$ is the population change of the initial state, and d is the film thickness.

If a wavelength region can be found, where the TA signal $\Delta T/T$ originates from a single transition $i \rightarrow f$ the temporal evolution of the corresponding excited-state species can be directly monitored. However, often the signals from different excited states overlap and further data

analysis is needed in order to evaluate the kinetics of excited states. In section 3.5.3 we present *Multivariate curve resolution analysis* as a tool to disentangle the contributions from different excited-state species to the TA data, in order to obtain pure spectra and kinetics of the different species.

3.5.2 *Experimental setup*

Our transient absorption setup covers a wide dynamic range from ~ 150 fs to 1 ms, covered by two experiments. In a first experiment the time-range up to 4 ns ('short delay') can be measured with a time resolution of ~ 150 fs given by the width of the pump and probe laser pulses. In a second experiment the time-range from 1 ns to 1 ms ('long delay') with 500 ps time resolution can be observed. In both experiments the spectral range from 500 to 1000 nm ('vis') and from 1050 to 1500 nm ('NIR') can be measured with a supercontinuum probe pulse in the respective wavelength regions.

Figure 34 shows a schematic of our home-built TA setup. The 800 nm output of a commercial titanium:sapphire laser system (Coherent LIBRA-HE, 3.5 mJ) with a repetition rate of 1 kHz was split into two beams and directed into two separate commercial optical parametric amplifiers (Coherent OPerA Solo).

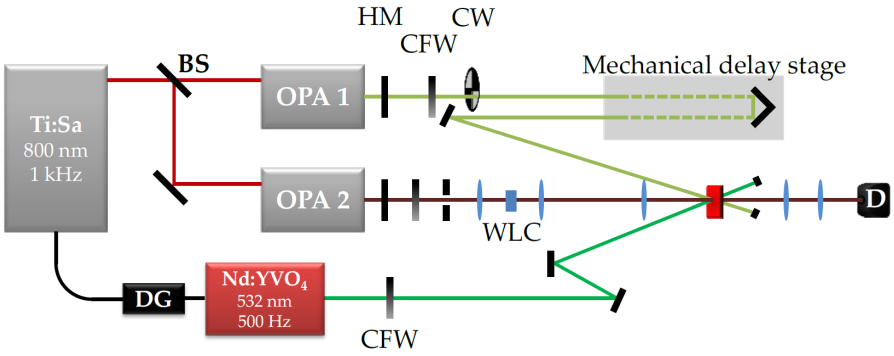

Figure 34: Schematic of the transient absorption setup used in our lab. The abbreviations used in the drawing together with their meaning are as follows: BS - beam splitter; OPA - optical parametric amplifier; HM - hot mirror; CFW - continuous filter wheel; CW - chopper wheel; WLC - white light crystal; D - detector; DG - delay generator. For further explanations see text. Figure reprinted from Gehrig.[39]

One optical parametric amplifier (OPA 1) was used to create the tunable pump pulses in the 'short delay' (ps to ns) experiment. The wavelength is tunable in the range of 285 to 1130 nm and was adjusted according to the material system under study.

OPA 2 was used to generate the seed beam for the probe white-light generation in both the short- and long-delay experiments. For measurements in the 'vis'-range a seed wavelength of 1300 nm was

focused into a c-cut 3 mm thick sapphire window to generate white-light between 500 to 1000 nm. For white-light generation in the 'NIR'-range from 1050 to 1500 nm a seed wavelength of 2100 nm was focused into a c-cut 4 mm thick yttrium orthovanadate (YVO_4) window to generate white light and a 1050 nm long pass filter was added into the path of the white light to block the visible fraction of the supercontinuum.

The variable time delay between pump and probe up to 4 ns was adjusted with a broadband retro-reflector mounted on a mechanical delay stage (Newport IMS600CCHA, 600 mm travel range). Every second pump pulse was blocked by a chopper wheel (with a frequency of 500 Hz), so that $\Delta T/T$ could be calculated from subsequent detector readings. Pump and probe pulses were focused onto the sample in a way, that spatial overlap was guaranteed. The pump beam diameter was always bigger than the probe beam diameter. The transmitted probe beam was diffracted in a spectrograph onto a linear silicon array (256 or 512 pixels) detector (Hamamatsu NMOS linear image sensor S3901-256/512) for the visible and onto a Peltier-cooled linear InGaAs array (512 pixels) detector (Entwicklungsbüro Stresing) for the NIR spectral region.

For measurements in the ns-ms time range ('long delay') with a resolution of 600 ps the frequency doubled output (532 nm) of an actively Q-switched $Nd:YVO_4$ laser (AOT Ltd. MOPA) was used as an excitation source. The pump pulses were electronically triggered at a repetition rate of 500 Hz. The variable time delay between pump and probe pulses was controlled by an electronic delay generator (Stanford Research Systems DG535).

In all experiments the relative angle of the polarization of pump and probe pulse was adjusted to the magic angle of 54.7° in order to avoid any tampering of the observed kinetics due to rotational anisotropy effects.

The TA measurements were performed at room temperature. Molecules in solution were measured in 3 mm thick cuvettes, while thin films of materials for organic solar cells were measured under dynamic vacuum at pressures of $<10^{-4}$ mbar. The thin film samples were prepared on quartz glass substrates from Präzisions Glas und Optik (PGO), which were cleaned and plasma treated in the same way as the ITO-covered glass substrates for solar cell preparation described in section 3.1. The active layer materials were spincoated from solution onto the glass substrates with the same conditions as in the solar cell devices.

3.5.3 *Multivariate curve resolution*

In TA experiments the spectral features of different species often overlap, making the extraction of pure kinetics corresponding to only one

species difficult or even impossible. Hence, it is necessary to further process the data in order to extract meaningful information describing the actual physical processes occurring in the sample. In this thesis the method of choice to analyze the contribution to the TA data from different species was *multivariate curve resolution* (MCR).

The data acquired in a TA pump-probe experiment can be represented as a 2-dimensional data matrix **D**. The measured TA signal $\Delta T/T$ is a function of the time and the wavelength λ. Therefore, **D** is an $m \times n$-matrix with m being the number of time steps measured and n being the number of pixels of the linear array detector and thus the number of wavelength intervals $\Delta\lambda$ detected.

With MCR analysis **D** is factorized into a matrix **C**, containing the concentration profiles (kinetics), and a second matrix **S**, containing the spectra. An additional error matrix **E** is added, describing the difference between the experimental data and its idealized description. This bilinear decomposition of **D** can be written as **D**=**CS**+**E**. A graphical illustration of a bilinear decomposition as used in MCR is depicted in figure 35.

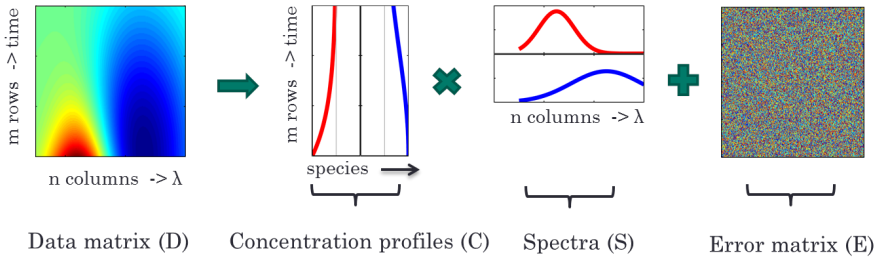

Figure 35: Schematic illustration of multivariate curve resolution (MCR) analysis.

The MCR algorithm used in this work to analyze the TA data was developed by Tauler et al. in order to investigate systems consisting of many components such as absorption spectra in high performance liquid chromatography.[148, 149] MCR is a so called soft-modeling approach, where no initial information about the exact underlying physical mechanisms is necessary. Basic physical and mathematical assumptions, such as non-negativity of spectra or concentrations, are sufficient to obtain a physically meaningful decomposition. The initial guess for the concentration profiles is obtained by an evolving factor analysis (EFA) based on a singular value decomposition (SVD), which also gives information about the number of species present in the sample. In the next step corresponding spectra are calculated with the least square method. Subsequently, these spectra are altered with additional constraints and are used to calculate new concentration profiles. These steps are repeated until a convergence criterion is fulfilled and the best fit is found.

However, it has to be noted that a decomposition obtained by MCR is not a unique solution. The validity of the solution can be verified by additional experiments, such as an independent determination of charge or triplet spectra. In this work the charge spectra of polymers were determined by recording the absorption spectrum of polymer films oxidized with iron(III)-chloride or iodine vapor, while triplet spectra were determined by measuring TA on a polymer film doped with palladium-anthraporphyrin.

A more detailed explanation of the MCR method and its application to the analysis of TA data can be found elsewhere.[150]

3.6 TIME-RESOLVED PHOTOLUMINESCENCE SPECTROSCOPY

Time-resolved photoluminescence spectroscopy (TR-PL) was conducted using a Hamamatsu streak camera system, which enables the spectrally resolved detection of the radiative decay processes in an excited sample on timescales from ps to µs. Its working principle is schematically depicted in figure 36.

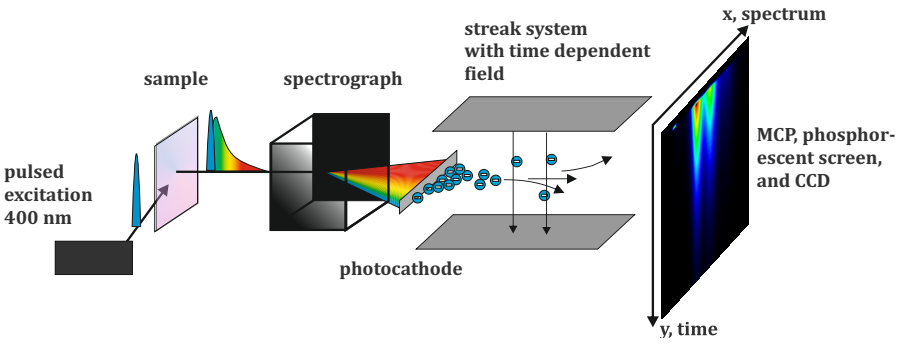

Figure 36: Schematic illustration of a time-resolved photoluminescence experiment.

The sample was excited with the frequency-doubled output (400 nm) of a titanium:sapphire laser system (Coherent LIBRA-HE) with a repetition rate of 1 kHz and a pulse length of ~ 100 fs. The fluorescence emission of the sample was collected with a telescope and focused into the entrance slit of the streak camera system. The incoming light was diffracted horizontally (x-axis) with a spectrograph onto a small photocathode, which converts the photons into electrons. The generated electrons are then accelerated by a time-dependent field in the vertical direction (y-axis), which is synchronized with the pulsed laser excitation. As a result electrons reach the multichannel plate (MCP) at different heights with respect to the y-axis, depending on their respective time of generation at the photocathode. Behind the MCP the amplified electron signal is converted by a phosphorescent screen back into photons and detected by a 2-dimensional CCD camera, delivering a spectrally and temporally resolved image.

3.7 TIME-OF-FLIGHT TECHNIQUE

With the *time-of-flight* (TOF) *technique* charge carrier mobilities can be determined by measuring the transit time of a photogenerated charge carrier package through an organic material layer (~ µm) sandwiched between two electrodes. One of these electrodes has to be (semi-) transparent, so that an excitation laser pulse can be transmitted. Figure 37 illustrates a typical TOF experiment.

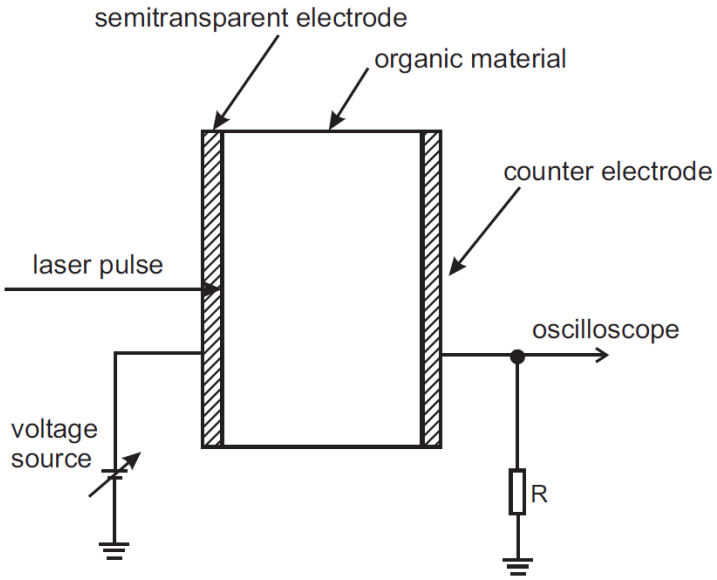

Figure 37: Schematic illustration of a time-of-flight experiment. Figure reprinted from Laquai.[151]

Upon illumination of the sample at the semitransparent electrode with a short laser pulse (~ ns) excitons are created in the organic material. A fraction of the excitons is converted into free charge carriers by the applied electric field. Depending on the polarity of these charge carriers they are either immediately discharged by the semitransparent electrode, causing an initial current spike to be detected by the oscilloscope or they drift as a charge carrier package through the whole material layer until they reach the counter electrode, where they can be detected as a current drop over the external resistance R. Figure 38 shows a typical TOF transient for ideal non-dispersive charge transport. Here, the photocurrent is plotted versus time. At t_0 upon excitation of the sample with a short laser pulse a clear current spike is visible, which shows the generation of charge carriers. After the initial current spike a plateau region is established, indicating the migration of the charge carrier package through the bulk. When the charge carrier package is completely discharging at the counter electrode the measured photocurrent is decreasing. The shape of this extraction tail marks the broadening of the charge carrier package induced over the time of migration through the bulk. Often, the pho-

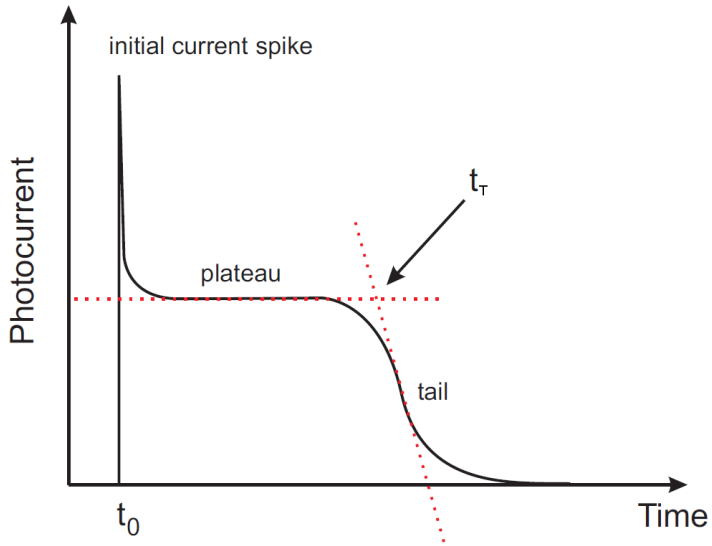

Figure 38: Typical time-of-flight transient for non-dispersive charge transport. Figure adapted from Laquai.[151]

tocurrent transients recorded by TOF are dispersive and do not exhibit this ideal non-dispersive transport behavior as presented in figure 38. Dispersive transport can be due to large disorder in the organic films or the presence of trap states.

The charge carrier mobility μ can be determined with the following equation

$$\mu = \frac{d}{t_T \times F}, \tag{53}$$

where d is the thickness of the organic layer, t_T is the transit time, and F is the electric field applied between the two electrodes. In the case of non-dispersive charge transport t_T can be determined by fitting two straight lines to the plateau and tail region and reading the time from the intersection of the lines as indicated in figure 38 by the two dotted red lines. If charge transport is strongly dispersive, t_T can be obtained by fitting lines to the data plotted in a double-logarithmic fashion.

The samples for the TOF measurements were prepared similar to the organic solar cell devices. The same ITO-covered glass substrates from Präzisions Glas und Optik (PGO) were used and cleaned as described in section 3.1. The thick polymer solution with a concentration of 200 mg mL^{-1} was spincoated directly onto the substrate with a low spincoating speed od 700 rpm resulting in a 3.7 µm thick layer. On top of this polymer layer a 10 nm thin aluminum electrode was evaporated in order to create a semitransparent cathode for determining hole mobilities.

During the TOF measurements the sample was kept under dynamic vacuum at a pressure of less than 10^{-5} mbar. As excitation source the

third harmonic (355 nm) of an Nd:YAG laser was directed onto the semitransparent aluminum electrode. Photocurrent transients were recorded with a digital oscilloscope (Tektronix TDS 524A) triggered by the laser pulse.

For further details on the TOF technique the reader is referred to reference [151].

4

TRIPLET STATE FORMATION IN PHOTOVOLTAIC BLENDS OF DPP-TYPE COPOLYMERS AND $PC_{71}BM$

Macromolecular Rapid Communications

Macromolecular Journals

Communication

Triplet State Formation in Photovoltaic Blends of DPP-Type Copolymers and $PC_{71}BM$

Julian R. Ochsmann, Deepak Chandran, Dominik W. Gehrig, Husna Anwar, Pramod Kandoth Madathil, Kwang-Sup Lee,* Frédéric Laquai*

The exciton dynamics in pristine films of two structurally related low-bandgap diketopyrrolopyrrole (DPP)-based donor–acceptor copolymers and the photophysical processes in bulk heterojunction solar cells using DPP copolymer:$PC_{71}BM$ blends are investigated by broadband transient absorption (TA) pump-probe experiments covering the vis–near-infrared spectral and fs–μs dynamic range. The experiments reveal surprisingly short exciton lifetimes in the pristine polymer films in conjunction with fast triplet state formation. An in-depth analysis of the TA data by multivariate curve resolution analysis shows that in blends with fullerene as acceptor ultrafast exciton dissociation creates charge carriers, which then rapidly recombine on the sub-ns timescale. Furthermore, at the carrier densities created by pulsed laser excitation the charge carrier recombination leads to a substantial population of the polymer triplet state. In fact, virtually quantitative formation of triplet states is observed on the sub-ns timescale. However, the quantitative triplet formation on the sub-ns timescale is not in line with the power conversion efficiencies of devices indicating that triplet state formation is an intensity-dependent process in these blends and is reduced under solar illumination conditions, as free charge carriers can be extracted from the photoactive layer in devices.

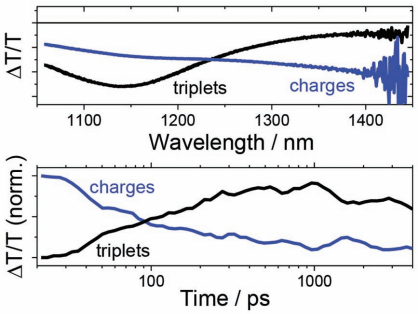

J. R. Ochsmann, D. W. Gehrig, Assoc. Prof. F. Laquai[+]
Max Planck Research Group for Organic Optoelectronics
Max Planck Institute for Polymer Research
Ackermannweg 10, 55128 Mainz, Germany
E-mail: laquai@mpip-mainz.mpg.de
Dr. D. Chandran,[++] Dr. P. K. Madathil, Prof. K.-S. Lee
Department of Advanced Materials
Hannam University
Daejeon 305-811, Korea
E-mail: kslee@hnu.kr
H. Anwar
Department of Physics
Mount Holyoke College, 50 College St, South Hadley, MA 01075, USA
[+]Present address: Physical Sciences and Engineering Division (PSE), Material Science and Engineering (MSE), Solar and Photovoltaics Engineering Research Center (SPERC), King Abdullah University of Science and Technology (KAUST), Thuwal 23955-6900, Kingdom of Saudi Arabia;
E-mail: frederic.laquai@kaust.edu.sa
[++]Present address: School of Chemical Sciences & National Institute for Cellular Biotechnology, Dublin City University, Glasnevin, Dublin-9, Ireland

1. Introduction

Substantial research efforts have been devoted to the development of a better understanding of the physics of organic solar cells and improving their efficiency, as they offer the potential of energy-efficient and low-cost large-area production, are intrinsically lightweight, and allow the production of flexible devices. A promising approach to increase the efficiency of organic solar cells is to use low-bandgap materials as absorbers, since they increase the overlap of the photoactive layer's absorption with the solar spectrum in the low-energy near-infrared (NIR) wavelength region and thereby increase the photon collection of the device. Recently, low-bandgap materials based on electron-deficient diketopyrrolopyrrole (DPP) building blocks as acceptors have been very successfully introduced for application in solution-processed organic bulk heterojunction (BHJ) solar cells and organic thin film transistors (OTFT).[1,2] Their high charge carrier mobility, strong absorption, and stability make them excellent candidates for both, OPV and OTFT devices.[3–13] In single layer bulk

DOI: 10.1002/marc.201400714

heterojunction OPV devices several polymers based on DPP building blocks have already been employed as electron donor.[2,14,15] Furthermore, they have been successfully used in tandem and triple junction solar cells, as they have the advantage of absorbing light mostly in the NIR spectral region, complementary to the absorption of some ubiquitous mid-bandgap polymers such as P3HT or PCDTBT and still yield high photocurrents which allows for current matching in multijunction devices. In fact, tandem devices in which one cell is based on the DPP-type donor polymer PDPP5T in combination with PCDTBT:PCBM or P3HT:PCBM subcells have shown power conversion efficiencies (PCE) of 7.0% and 7.23%, respectively.[16,17] In this study, we report the photovoltaic performance of two DPP-based copolymers and we study their excited state dynamics, namely, the exciton and charge carrier dynamics, in pristine films and in blends with $PC_{71}BM$ as electron acceptor as typically used in the photoactive layer of single junction organic BHJ solar cells. The first polymer under investigation is poly[3,6-dithiene-2-yl-2,5-di(2-decyltetradecyl)-pyrrolo [3,4-*c*]pyrrole-1,4-dione-5′,5″-diyl-*alt*-thieno[3,2-b]thienyl] (PTDPP-TT), which consists of alternating DPP building blocks and 2,5-di-2-thienylthieno[3,2-b]thiophene units along the polymer backbone. The second polymer studied herein is PFDPP-TT, which has a similar chemical structure as PTDPP-TT, except that the thiophenes adjacent to the DPP moiety were replaced by furan (see Scheme 1).

Janssen and co-workers very recently studied a related polymer, namely, DT-PDPP2T-TT, which in fact has the same chemical structure as PTDPP-TT presented in this study, but in their case had a significantly higher molecular weight of M_n = 447 kg mol^{-1} compared to M_n = 47 kg mol^{-1} for our PTDPP-TT polymer as determined by high-temperature GPC.[18] They demonstrated that in a BHJ solar cell architecture the DT-PDPP2T-TT polymer blended with $PC_{71}BM$ as acceptor exhibits high power conversion efficiencies even for relatively large (≈300 nm) active layer thicknesses, which makes this polymer particularly interesting for large-area production processes such as inkjet printing and roll-to-roll processing. However, here we focus on the excited state dynamics occurring after pulsed laser excitation of the pristine polymer films and photovoltaic blends with PCBM studied by vis–NIR broadband pump-probe transient absorption (TA) spectroscopy covering the ps–µs dynamic range, that is, the dynamic range relevant for exciton recombination, exciton dissociation, charge carrier separation leading to free charge generation, as well as geminate and nongeminate recombination processes. TA spectroscopy has previously been applied to gain a better understanding of the fundamental processes determining the efficiency of DPP polymer:fullerene photoactive blends. For instance, Durrant and co-workers have shown in different studies that excess energy is beneficial for charge separation in certain DPP-type polymers[19] and that in some blends photons absorbed by the DPP polymer do not generate charges due to lack of an energy offset between donor and acceptor.[20] Here, we specifically address in more detail triplet state formation in DPP polymer blends observed under pulsed laser excitation. Triplet state formation in photovoltaic blends has recently gained attention in some other low-bandgap polymer:fullerene systems and different mechanisms such as recombination of bound charge-transfer (CT) states and nongeminate recombination of free charges leading to the population of the triplet manifold are currently discussed.[21–23] Triplet exciton generation was previously discussed for DPP-type polymers, but TA experiments in nitrogen and oxygen atmosphere showed identical signal decay dynamics and thus triplet formation was excluded. However, the triplet energy of the polymer has to be 0.98 eV or above for triplet states to be quenched by oxygen, which may not be the case for the DPP polymer triplet state.[24] In fact, here we show that triplet states are also generated in DPP-type polymer:fullerene blends and become the dominant species present on the ns–µs timescale after pulsed laser excitation. We discuss the mechanism of triplet state formation and its impact on device performance under solar illumination conditions.

2. Results and Discussion

2.1. Photovoltaic Performance

Figure 1a shows the absorption spectra of pristine PTDPP-TT (blue) and pristine PFDPP-TT (red) thin films. Both polymers show a broad and weakly structured absorption covering the wavelength region from 600 to 900 nm and a considerably weaker absorption band at around 400 nm. The absorption maximum of PFDPP-TT is at 825 nm, which is slightly redshifted compared to the absorption maximum of PTDPP-TT around 800 nm. The absorption spectra of polymer:$PC_{71}BM$ blend films are presented in Figure 1b. The spectra exhibit

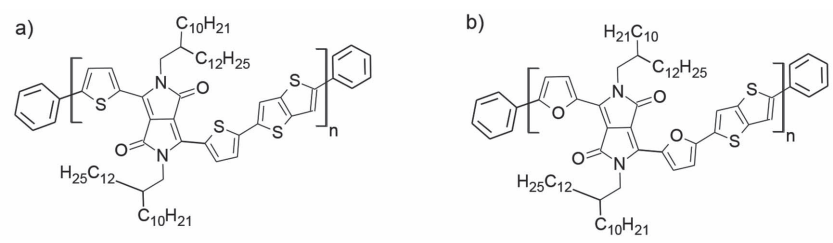

Scheme 1. Chemical structure of a) PTDPP-TT and b) PFDPP-TT.

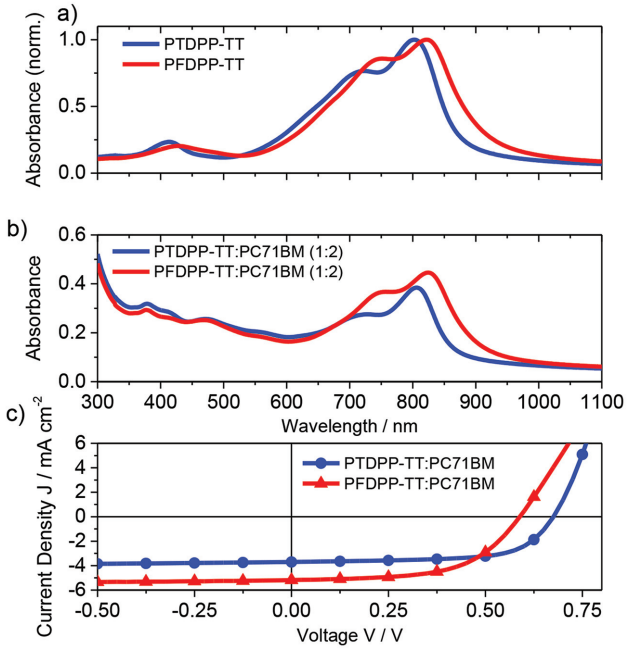

Figure 1. a) Steady-state UV–vis absorption spectra of a pristine PTDPP-TT film (blue line) and PFDPP-TT film (red line). b) Absorption spectrum of a 1:2 (w/w) PTDPP-TT:$PC_{71}BM$ (blue curve; $d \approx 83$ nm) and a 1:2 (w/w) PFDPP-TT:$PC_{71}BM$ blend film (red curve; $d \approx 87$ nm). c) *J–V* characteristics of solar cells using a 1:2 (w/w) PTDPP-TT:$PC_{71}BM$ (blue curve) blend and a 1:2 (w/w) PFDPP-TT:$PC_{71}BM$ (red curve) blend measured at an illumination of 73 mW cm^{-2}.

similar features as the pristine polymer films, with the additional absorption of $PC_{71}BM$ superimposed on the polymer absorption in turn causing a higher absorbance at shorter wavelengths, which extends into the UV spectral region. Hence, both polymer:fullerene blends cover a considerable part of the solar spectrum from the UV to the NIR wavelength region, which is beneficial for solar energy conversion.

The current–voltage (*J–V*) characteristics of as-cast BHJ solar cells built with PTDPP-TT:$PC_{71}BM$ (1:2 by weight, blue curve) and PFDPP-TT:$PC_{71}BM$ (1:2 by weight, red curve) using a solar illumination of 73 mW cm^{-2} are depicted in Figure 1c. The optimal photovoltaic performance for both material systems was achieved by spin-coating the blends from chloroform after an addition of 2% dioodooctane (DIO) per volume as solvent additive. In case of the PTDPP-TT:$PC_{71}BM$ system, an average PCE η of 1.9 ± 0.3% was achieved with a 75 nm thick photoactive layer. The corresponding open circuit voltage (V_{OC}) was 0.67 ± 0.01 V, the short circuit current (J_{SC}) was 3.4 ± 0.5 mA cm^{-2}, and the fill factor (FF) was 0.62 ± 0.04. The best photovoltaic performance for the PFDPP-TT:$PC_{71}BM$ system was obtained for an active layer thickness of 82 nm, yielding an average PCE of 2.2 ± 0.2%, however, a lower V_{OC} of 0.59 ± 0.00 V, but a higher J_{SC} of 4.7 ± 0.4 mA cm^{-2} and a slightly lower FF of 0.58 ± 0.02 in comparison to the PTDPP-TT:$PC_{71}BM$ material system. The difference in average J_{SC} is well in line with a reduced EQE of PTDPP-TT:$PC_{71}BM$ devices across the entire absorption of the photoactive layer. The theoretical J_{SC} calculated from the absorption profiles of PTDPP-TT:$PC_{71}BM$ and PFDPP-TT:$PC_{71}BM$ assuming 100% IQE is 14 and 15.8 mA cm^{-2}, respectively, indicating substantial loss processes occur in these devices. We also note, that the photovoltaic performance of both systems could neither be further improved by annealing of the photoactive layer nor by using a Ca/Al electrode instead of an aluminum electrode only, indicating that electron extraction from the photoactive layer is not a significant efficiency-limiting issue in these blends.

2.2. Exciton Dynamics in Pristine PTDPP-TT and PFDPP-TT Films

Figure 2a shows the short delay (ps–ns) transient absorption pump-probe spectra of a PTDPP-TT film in both the visible (600–1000 nm) and NIR (1150–1400 nm) probe region. The spectra consist of a positive feature roughly in the spectral region from 650 to 900 nm, which we assign to the polymer's ground state bleach (GSB), since it displays the same spectral position and features as the steady-state absorption of the polymer film also shown in Figure 2b for comparison (dark green curve).

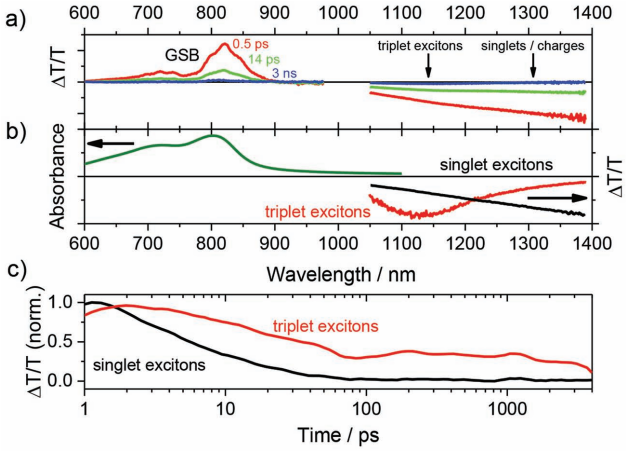

Figure 2. a) ps–ns vis–NIR transient absorption spectra of a pristine PTDPP-TT film at delay times of 0.5 ps (red), 14 ps (green), and 3 ns (blue). Excitation was performed at 800 nm with 5.7 μJ cm^{-2} for the visible and 6 μJ cm^{-2} for the NIR. b) Absorbance of the polymer film (dark green), singlet-induced absorption spectrum obtained from MCR analysis (black), and triplet-induced absorption spectrum (red) obtained on a palladium-anthraporphyrin–doped polymer film (95:5 w/w). c) Dynamics of singlet (black) and triplet (red) excitons obtained by MCR analysis using the separately determined triplet-induced absorption spectrum as input parameter (see Figure 2b).

The TA spectrum in the NIR wavelength range exhibits a broad photoinduced absorption (PA) signal, which extends from 1050 nm further into the NIR. These spectral features are most pronounced shortly after excitation (red curve). However, after only 14 ps most of the signals have already substantially decayed (green curve) and after 3 ns, that is the longest delay time used in our ps–ns experiment, the TA signals have almost vanished. All signals in the ps–ns time regime, namely, the GSB and PA, are predominantly caused by the presence of singlet excitons in the pristine polymer films, which exhibit a surprisingly short lifetime in this polymer compared to other common conjugated polymers.[25,26] However, we note that after 3 ns roughly 5% of the PA signal intensity remain. This residual signal, which peaks at 1150 nm in the pristine polymer film, is assigned to triplet excitons, as its spectral signature is very similar to the photoinduced absorption of a palladium-anthraporphyrin-doped polymer film (see Figure 2b). Here, the palladium-anthraporphyrin effectively sensitizes the polymer's triplet level by successive singlet energy transfer to, and intersystem crossing on the sensitizer followed by triplet energy transfer to the polymer. Surprisingly, in the pristine polymer films triplets are created on a very short timescale, which could indicate ultrafast singlet fission. To further analyze the photophysical processes in the pristine polymer film and to obtain the individual dynamics of singlet and triplet states, we performed multivariate curve resolution (MCR) analysis on the TA data, a soft modeling technique, whose application to the analysis of TA data has recently been presented and discussed by us in greater detail.[27] At first we performed MCR analysis without any further constraints (such as spectra and nonnegativity of concentrations) and in a second run confined the triplet-induced absorption spectrum to the independently measured triplet-induced absorption spectrum (see Figure 2b). While the spectra obtained by MCR analysis show some differences depending on the constraints, the dynamics of the singlet decay and triplet formation are virtually the same (see the Supporting Information), which supports our data analysis and interpretation. The singlet decay can be fit by two exponentials having inverse decay rates of 3 and 17 ps, the former actually very well in line with the rise of the triplet-induced absorption. This ultrafast triplet formation likely indicates singlet fission in these materials as it appears to be too fast for intersystem crossing. The reason for the rather short singlet exciton lifetime of ≈17 ps in the pristine polymer films requires further studies, here we can only speculate that it is due to fast and radiationless internal conversion of excited states to the ground state, possibly via a conical intersection between the two states. We note that the decay of singlet states is virtually similar at higher fluences indicating that the dynamics are not influenced by any higher order processes such as exciton–exciton annihilation. We have also analyzed the dynamics of the triplet-induced absorption in a metallated porphyrin-sensitized sample and obtained a surprisingly short triplet state lifetime of only about 15 ns by fitting the dynamics to a single exponential decay (see Figure S3, Supporting Information). This indicates fast quenching of the triplet states in the polymer, as the triplet lifetime is unusually short compared to other polymers that we have previously investigated. Virtually similar observations regarding the singlet state lifetime and triplet state formation were made for the structurally related PFDPP-TT polymer. The corresponding spectra for this polymer are also shown in Figure S2 (Supporting Information). The inverse decay rates obtained for the singlet exciton decay in pristine PFDPP-TT are 3 and 19 ps, respectively. Here, the triplet state lifetime obtained from the sensitizer-doped polymer film was determined to be ≈11 ns (see Figure S4, Supporting Information). In conclusion, first both polymers exhibit a very similar, but rather short singlet exciton lifetime, which is likely caused by fast nonradiative deactivation (or internal conversion) of excited singlet states and second a small fraction of triplets is created on a very short timescale pointing to fission of singlet states in these materials. In addition to the very short singlet exciton lifetimes of less than 20 ps, we also found surprisingly short triplet state lifetimes in palladium-anthraporphyrin–doped polymer films of 15 and 11 ns for PTDPP-TT and PFDPP-TT, respectively.

2.3. Photophysics of PTDPP-TT:$PC_{71}BM$ and PFDPP-TT:$PC_{71}BM$ Blends

Figure 3a,b displays the vis–NIR pump-probe spectra of the PTDPP-TT:$PC_{71}BM$ blend at short (ps–ns) and long (ns–μs) delay times, respectively. The spectra on both timescales exhibit very similar features: (i) a broad and structured positive signal from 650 to 900 nm and (ii) a negative signal after the zero crossing at 900 nm, which extends further into the NIR wavelength range beyond the spectral detection limit, which finally evolves into a PA peaking at 1150 nm. In line with the aforementioned early time pump-probe spectra obtained on pristine polymer films, we assigned the positive signal to the polymer's GSB. The PA signal that extends into the NIR and is observed at early delay times, for instance, at 0.5 ps (red curve, Figure 3a), resembles the shape of the singlet exciton–induced absorption spectrum, as measured on a pristine PTDPP-TT polymer film. However, we note that the charge-induced absorption spectra, which we independently obtained on a pristine polymer film after oxidation with iodine and also after oxidation with $FeCl_3$ (see Figure S5, Supporting Information),

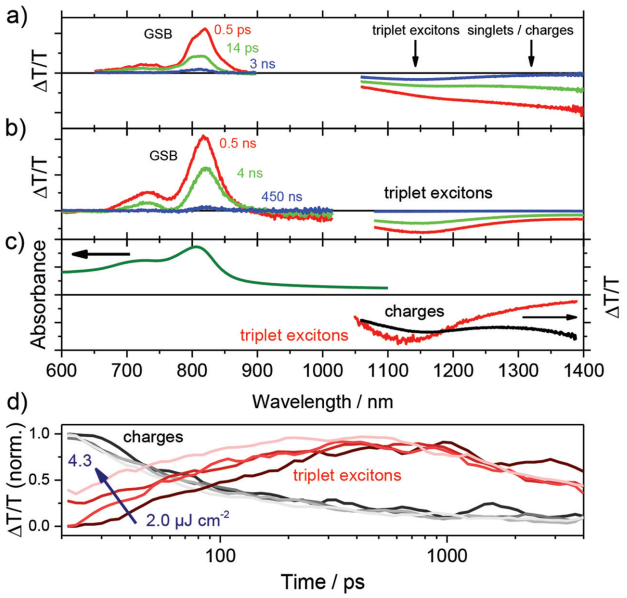

Figure 3. a) ps–ns vis–NIR transient absorption spectra of a 1:2 (w/w) PTDPP-TT:$PC_{71}BM$ blend at delay times of 0.5 ps (red), 14 ps (green), and 3 ns (blue). The pump fluence at 800 nm was 2.7 μJ cm^{-2} for the visible and 2 μJ cm^{-2} for the NIR measurements. b) ns–μs vis–NIR transient absorption spectra of a 1:2 (w/w) PTDPP-TT:$PC_{71}BM$ blend at delay times of 0.5 ns (red), 4 ns (green), and 450 ns (blue). The pump fluence at 532 nm was 74.8 μJ cm^{-2} for the visible and 36.7 μJ cm^{-2} for the NIR measurements. c) Absorption spectrum of a PTDPP-TT:$PC_{71}BM$ blend film (dark green), charge-induced absorption spectrum as obtained from MCR analysis (black), and triplet-induced absorption spectrum (red) obtained on a palladium-anthraporphyrin–doped polymer film. d) Fluence dependence of the dynamics of charges (black) and triplet excitons (red) obtained by MCR analysis using the separately determined triplet-induced absorption spectrum as input parameter (compare panel (c), red curve). The corresponding charge spectrum is shown in panel (c) (black curve). Only data after 20 ps were used to exclude contributions from singlet excitons.

are similar in shape and spectral position to the singlet exciton–induced absorption spectrum, which complicates a clear assignment. Interestingly, the broad PA signal, more specifically the PA at wavelengths longer than 1250 nm, decays very rapidly and the shape of the spectrum changes, resulting in a new peak emerging at 1150 nm. A further analysis of the TA data matrix by evolving factor analysis (EFA, see Figure S6, Supporting Information) and MCR analysis excluding the first 20 ps, in which singlet excitons are expected to be still present in the polymer:fullerene blend, indicates that two species are sufficient to describe the TA data on the 20 ps to ns timescale. The two component spectra determined by MCR analysis are shown in Figure S5 (Supporting Information), which also compares the component spectra with the separately measured triplet-induced absorption and charge-induced absorption spectrum obtained by control experiments. Component 1 is a broad and rather unstructured PA signal, which resembles very much the PA of charges seen in the control experiments. Component 2 can be clearly assigned to the triplet-induced absorption, as its spectral shape and position is almost the same as the triplet-induced absorption spectrum measured on the palladium-anthraporphyrin-doped polymer film. Figure 3d shows the intensity dependence of the dynamics of the two components also obtained by MCR analysis. Interestingly, we observed a fluence-independent decay of component 1 (charges) which extends to 1 ns, while component 2 (triplets) shows a moderate fluence dependent rise, that is, the onset of formation of component 2 shifts to earlier times with increasing fluence as shown in Figure 3d and also supported by EFA (see Figure S6, Supporting Information). We note that, as described above, after 20 ps, that is the starting point for our MCR analysis, all singlet excitons should have either recombined to the ground state due to their short lifetime or should have been quenched by the fullerene, so that component 1 can be assigned to charges. Furthermore, the intensity independent decay of component 1 may point to fast geminate recombination of bound charge pairs, while the intensity dependence of the rise of component 2 implies that triplet states are formed by nongeminate recombination as very recently also reported for other low-bandgap polymer:fullerene blends.[21,22] We note however, that the precise mechanism of the fast recombination process observed in these blends could not be entirely clarified by our TA experiments. In fact, many parameters such as intermolecular distance at the interface,[28] the presence of interfacial dipoles[29] energy level bending at the interface, or molecular weight of the polymer impact the interfacial charge separation mechanism and efficiency.[30] We also note that a meaningful description of the dynamics of charges and triplets obtained by MCR analysis using a set of coupled rate equations based on a photophysical model was not possible, as too many parallel and sequential processes, such as geminate plus nongeminate recombination, triplet formation, decay, and annihilation, simply overparameterized any model.

Further TA experiments that we performed in the ns–μs time range show almost exclusively the triplet-induced absorption (see Figure 3b) indicating that the majority of the free charges have recombined and collapsed into the polymer's triplet state on this timescale. We also determined that the triplet-induced absorption in the PTDPP-TT:fullerene blend decays with a lifetime of 8 ns, which is similar to the 15 ns lifetime (see Figure S3, Supporting Information) obtained on the porphyrin-doped polymer film further supporting our assignment of this peak to triplet states and indicating that their recombination channel is not fundamentally different in the two samples.

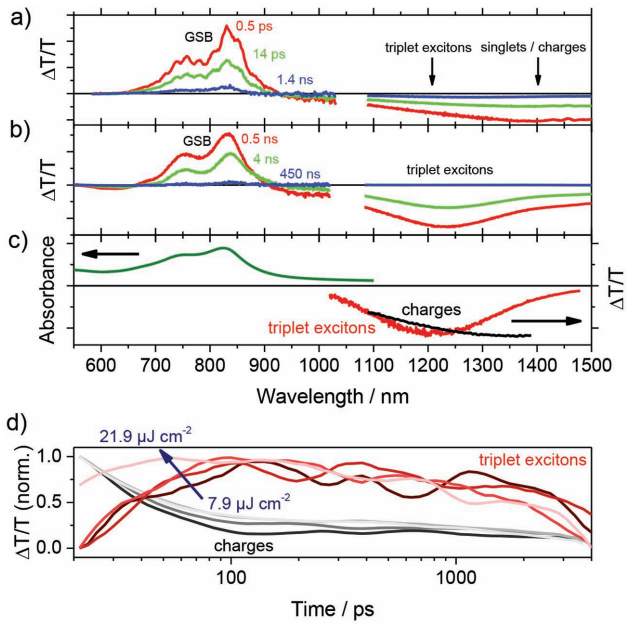

Figure 4. a) ps–ns vis–NIR transient absorption spectra of a 1:2 (w/w) PFDPP-TT:$PC_{71}BM$ blend at delay times of 0.5 ps (red), 14 ps (green), and 1.4 ns (blue). The pump fluence at 800 nm was 40.4 μJ cm^{-2} for the visible and 12.3 μJ cm^{-2} for the NIR measurements. b) ns–μs vis–NIR transient absorption spectra of a 1:2 (w/w) PFDPP-TT:$PC_{71}BM$ blend at delay times of 0.5 ns (red), 4 ns (green), and 450 ns (blue). The pump fluence at 532 nm was 70.4 μJ cm^{-2} for the visible and 61.6 μJ cm^{-2} for the NIR measurements. c) Absorption spectrum of a PFDPP-TT:$PC_{71}BM$ blend film (dark green), charge-induced absorption spectrum as obtained from MCR analysis (black), and triplet-induced absorption spectrum (red) obtained on a palladium–anthraporphyrin-doped polymer film. d) Fluence dependence of the dynamics of charges (black) and triplet excitons (red) obtained by MCR analysis using the separately determined triplet-induced absorption spectrum as input parameter (compare panel (c), red curve). The corresponding charge spectrum is shown in panel (c) (black curve). The data matrix was analyzed after 20 ps to exclude contributions from singlet excitons.

In case of the PFDPP-TT:$PC_{71}BM$ system we observed very similar phenomena as shown in Figure 4. Here, the EFA analysis also yielded two components on the ps–ns timescale. In line with the TA data obtained on PTDPP-TT:$PC_{71}BM$ the broad and unstructured photoinduced absorption evolves into a PA peaking at 1240 nm as shown in Figure 4a, which resembles the triplet-induced absorption obtained on a porphyrin-doped polymer film (see Figure 4c). The effect is even more pronounced for the ns–μs TA data, which already after 500 ps showed exclusively the triplet-induced absorption (see Figure 4b) likely due to the higher pump fluence used in these experiments. Interestingly, we observed the same lifetime of 11 ns (see Figure S4, Supporting Information) for triplets in the polymer:fullerene blend as we obtained in the porphyrin-doped PFDPP-TT polymer film, indicating that once triplets have been created in the photovoltaic blend their decay mechanism is similar to the porphyrin-doped polymer film. As in the case of PTDPP-TT we also observed a significant fraction of fast largely intensity-independent sub-ns recombination, as obtained by the MCR analysis shown in Figure 4d. The assignment of the triplet formation mechanism to a geminate or nongeminate recombination process is less clear than in the case of PTDPP-TT, as we only observed an earlier onset of triplet formation for the highest fluence. In fact, here the MCR analysis is likely affected by the limited signal-to-noise ratio, as indicated by the oscillations of the triplet exciton population in time. However, given the structural similarity of the two polymers, it appears reasonable that the photophysical processes are not fundamentally different.

The fast and almost quantitative triplet formation observed in both polymer:fullerene blends is rather astonishing and not compatible with the power conversion efficiencies of the respective photovoltaic devices, specifically the photocurrents and high fill factors. In fact, it appears that at the comparably high charge carrier concentrations obtained by pulsed laser excitation in our TA experiments triplet formation is enhanced likely due to the nongeminate, that is, intensity-dependent character of the triplet state formation mechanism. However, the only moderate short-circuit photocurrents, but rather high fill factors observed in devices may be explained by a considerable fraction of fast geminate recombination that can be deduced from the intensity-independent decay of component 1 in the MCR analysis of the TA data of both polymer:fullerene systems.

3. Conclusions

In this study, we investigated the exciton and charge carrier dynamics as well as the device performance of two DPP-based low bandgap polymers blended with $PC_{71}BM$ as acceptor in bulk heterojunction solar cell devices. The polymers differ in their chemical structure, namely, the replacement of the two thiophenes adjacent to the DPP unit in PTDPP-TT by furan in PFDPP-TT. The device performance of solar cells built with either of the polymers is at around 2.4%, while small differences in V_{OC}, J_{SC}, and FF were observed. We demonstrated that upon photon absorption singlet excitons are created in the pristine polymer films that are very short-lived and exhibit lifetimes of less than 20 ps. Nevertheless, triplet states are created as secondary photoproducts likely via fast singlet fission. In polymer:fullerene blends, we observed that a significant fraction of exciton dissociation creates charges, which rapidly recombine on a sub-ns timescale and thereby may limit the experimentally obtained photocurrent with respect to the maximum photocurrent that could theoretically be obtained from the photoactive layer. The

exact reason for the considerable fraction of this sub-ns recombination process requires further investigation in this series of materials. Finally, we demonstrate that under the measurement conditions applied in our TA experiments, that is, high fluence and thus high charge carrier density, the majority of charges recombines and successively populates the polymer triplet state. However, further experiments are required to unravel whether the triplet state formation observed in our TA experiments does also play a role in a device under solar illumination conditions which is different from the conditions used in TA experiments, as the charge carrier concentration is lower and the applied bias aids the extraction of charges from the photoactive layer.

Supporting Information

Supporting Information is available from the Wiley Online Library or from the author.

Acknowledgements: F.L. thanks the Max Planck Society for funding the Max Planck Research Group. J.R.O. thanks the IRTG 1404 for funding. H.A. thanks the DAAD for a RISE scholarship. D.W.G. acknowledges a Kekulé scholarship of the Fonds der Chemischen Industrie (FCI). K.-S.L. acknowledges funding from the NRF through the APCPI (ERC-2007-0056091) and from Hannam BK21 Plus Center for BT-IT Hybrid Nannomaterials. J.R.O., D.W.G and F.L. thank S. Baluschev for providing the palladium-anthraporphyrin.

Received: December 12, 2014; Revised: March 31, 2015; Published online: April 29, 2015; DOI: 10.1002/marc.201400714

Keywords: charge generation; DPP polymers; organic photovoltaics; transient absorption spectroscopy; triplet state formation

[1] D. Chandran, K.-S. Lee, *Macromol. Res.* **2013**, *21*, 272.
[2] J. C. Bijleveld, V. S. Gevaerts, D. Di Nuzzo, M. Turbiez, S. G. Mathijssen, D. M. de Leeuw, M. M. Wienk, R. A. Janssen, *Adv. Mater.* **2010**, *22*, E242.
[3] Y. N. Li, P. Sonar, L. Murphy, W. Hong, *Energy Environ. Sci.* **2013**, *6*, 1684.
[4] Z. Yi, X. Sun, Y. Zhao, Y. Guo, X. Chen, J. Qin, G. Yu, Y. Liu, *Chem. Mater.* **2012**, *24*, 4350.
[5] W. Li, W. S. Roelofs, M. M. Wienk, R. A. Janssen, *J. Am. Chem. Soc.* **2012**, *134*, 13787.
[6] W. Li, K. Hendriks, A. Furlan, A. Zhang, M. M. Wienk, R. A. J. Janssen, *Chem. Commun.* **2015**, *51*, 4290.
[7] D. Bartesaghi, M. Turbiez, L. J. A. Koster, *Org. Electron.* **2014**, *15*, 3191.
[8] D. H. Wang, A. K. K. Kyaw, J.-R. Pouliot, M. Leclerc, A. J. Heeger, *Adv. Energy Mater.* **2014**, *4*, 1300835.
[9] L. Ye, S. Zhang, W. Ma, B. Fan, X. Guo, Y. Huang, H. Ade, J. Hou, *Adv. Mater.* **2012**, *24*, 6335.
[10] J. C. Bijleveld, A. P. Zoombelt, S. G. J. Mathijssen, M. M. Wienk, M. Turbiez, D. M. de Leeuw, R. A. J. Janssen, *J. Am. Chem. Soc.* **2009**, *131*, 16616.
[11] W. Li, K. H. Hendriks, A. Furlan, W. S. C. Roelofs, M. M. Wienk, R. A. J. Janssen, *J. Am. Chem. Soc.* **2013**, *135*, 18942.
[12] K. H. Hendriks, G. H. L. Heintges, V. S. Gevaerts, M. M. Wienk, R. A. J. Janssen, *Angew. Chem. Int. Ed.* **2013**, *52*, 8341.
[13] W. Li, A. Furlan, K. H. Hendriks, M. M. Wienk, R. A. J. Janssen, *J. Am. Chem. Soc.* **2013**, *135*, 5529.
[14] K. H. Hendriks, G. H. L. Heintges, M. M. Wienk, R. A. J. Janssen, *J. Mater. Chem. A* **2014**, *2*, 17899.
[15] A. P. Zoombelt, S. G. J. Mathijssen, M. G. R. Turbiez, M. M. Wienk, R. A. J. Janssen, *J. Mater. Chem.* **2010**, *20*, 2240.
[16] V. S. Gevaerts, A. Furlan, M. M. Wienk, M. Turbiez, R. A. Janssen, *Adv. Mater.* **2012**, *24*, 2130.
[17] S. Kouijzer, S. Esiner, C. H. Frijters, M. Turbiez, M. M. Wienk, R. A. J. Janssen, *Adv. Energy Mater.* **2012**, *2*, 945.
[18] W. Li, K. H. Hendriks, W. S. Roelofs, Y. Kim, M. M. Wienk, R. A. Janssen, *Adv. Mater.* **2013**, *25*, 3182.
[19] S. D. Dimitrov, A. A. Bakulin, C. B. Nielsen, B. C. Schroeder, J. Du, H. Bronstein, I. McCulloch, R. H. Friend, J. R. Durrant, *J. Am. Chem. Soc.* **2012**, *134*, 18189.
[20] S. D. Dimitrov, C. B. Nielsen, S. Shoaee, P. S. Tuladhar, J. Du, I. McCulloch, J. R. Durrant, *J. Phys. Chem. Lett.* **2012**, *3*, 140.
[21] A. Rao, P. C. Chow, S. Gelinas, C. W. Schlenker, C. Z. Li, H. L. Yip, A. K. Jen, D. S. Ginger, R. H. Friend, *Nature* **2013**, *500*, 435.
[22] F. Etzold, I. A. Howard, N. Forler, A. Melnyk, D. Andrienko, M. R. Hansen, F. Laquai, *Energy Environ. Sci.* **2015**, DOI: 10.1039/C4EE03630A.
[23] S. D. Dimitrov, S. Wheeler, D. Niedzialek, B. C. Schroeder, H. Utzat, J. M. Frost, J. Yao, A. Gillett, P. S. Tuladhar, I. McCulloch, J. Nelson, J. R. Durrant, *Nat. Commun.* **2015**, *6*, 6501.
[24] Y. W. Soon, H. Cho, J. Low, H. Bronstein, I. McCulloch, J. R. Durrant, *Chem. Commun.* **2013**, *49*, 1291.
[25] I. A. Howard, R. Mauer, M. Meister, F. Laquai, *J. Am. Chem. Soc.* **2010**, *132*, 14866.
[26] F. Etzold, I. A. Howard, R. Mauer, M. Meister, T. D. Kim, K. S. Lee, N. S. Baek, F. Laquai, *J. Am. Chem. Soc.* **2011**, *133*, 9469.
[27] I. A. Howard, H. Mangold, F. Etzold, D. Gehrig, F. Laquai, *Ultrafast Dynamics in Molecules, Nanostructures and Interfaces*, World Scientific, Singapore **2013**.
[28] T. W. Holcombe, J. E. Norton, J. Rivnay, C. H. Woo, L. Goris, C. Piliego, G. Griffini, A. Sellinger, J.-L. Brédas, A. Salleo, J. M. J. Fréchet, *J. Am. Chem. Soc.* **2011**, *133*, 12106.
[29] C. Poelking, M. Tietze, C. Elschner, S. Olthof, D. Hertel, B. Baumeier, F. Würthner, K. Meerholz, K. Leo, D. Andrienko, *Nat. Mater.* **2015**, *14*, 434.
[30] R. C. Coffin, J. Peet, J. Rogers, G. C. Bazan, *Nat. Chem.* **2009**, *1*, 657.

Supporting Information

for *Macromol. Rapid Commun.,* DOI: 10.1002/marc.201400714

Triplet State Formation in Photovoltaic Blends of DPP-Type Copolymers and $PC_{71}BM$

Julian R. Ochsmann, Deepak Chandran, Dominik W. Gehrig, Husna Anwar, Pramod Kandoth Madathil, Kwang-Sup Lee,* Frédéric Laquai*

Supporting Information

DOI: 10.1002/marc.201400714

Triplet state formation in photovoltaic blends of DPP-type copolymers and $PC_{71}BM$

Julian Robert Ochsmann, Deepak Chandran, Dominik W. Gehrig, Husna Anwar, Pramod Kandoth Madathil, Kwang-Sup Lee,* and Frédéric Laquai*

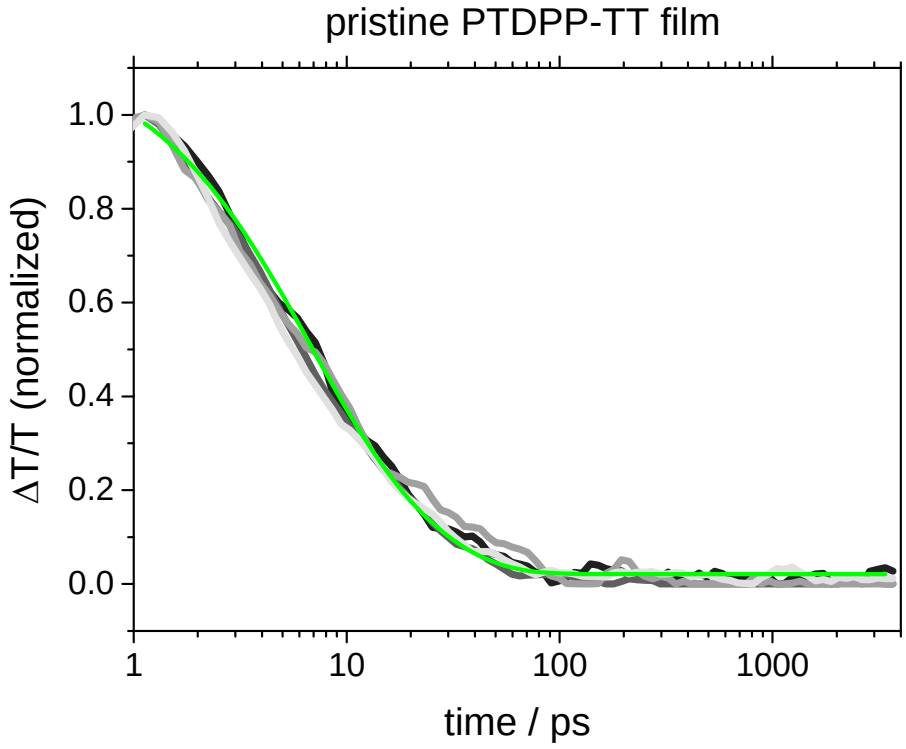

Figure S1. Normalized transient absorption kinetics of the singlet exciton absorption of a pristine PTDPP-TT film measured at four different fluences. The singlet exciton kinetics were obtained by MCR-ALS analysis. The green line represents a global fit with two exponentials to the kinetics of all fluences yielding inverse rates of ~3 ps and ~17 ps.

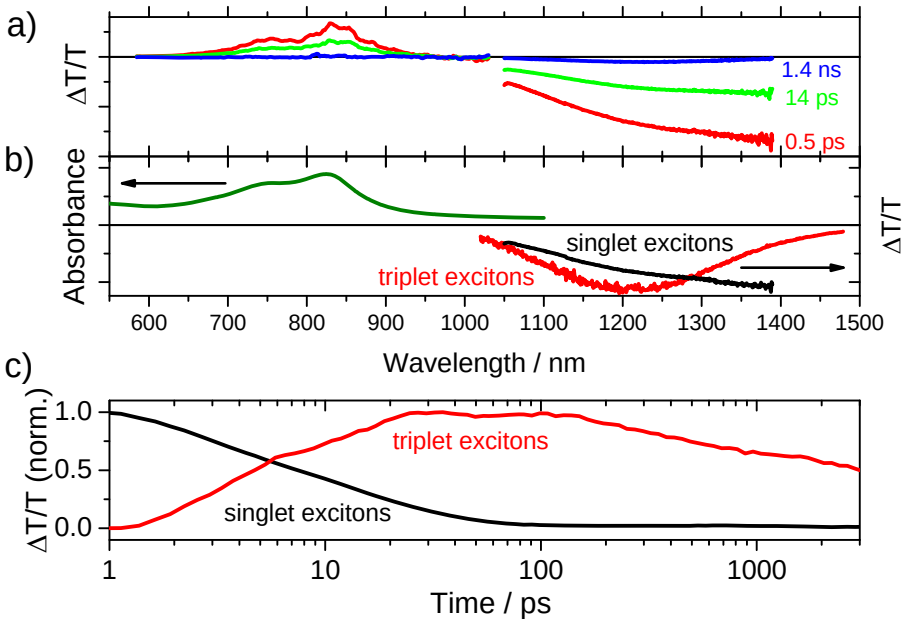

Figure S2. (a) Short delay transient absorption spectra of a pristine PFDPP-TT film measured in the visible (600-1040 nm) and NIR (1050-1400 nm) spectral region at delay times of 0.5 ps (red), 14 ps (green) and 1.4 ns (blue). The pump fluence at 800 nm was 14.2 µJ cm^{-2} for the visible and 5.3 µJ cm^{-2} for the NIR measurements.(b) Absorbance of the polymer film and singlet-induced absorption spectrum as obtained from MCR analysis (black) as well as triplet-induced absorption spectrum (red) obtained on a palladium-anthraporphyrin-doped polymer film. (c) Dynamics of singlet and triplet excitons obtained by MCR analysis using the separately determined triplet-induced absorption spectrum as input parameter (compare panel b, red curve).

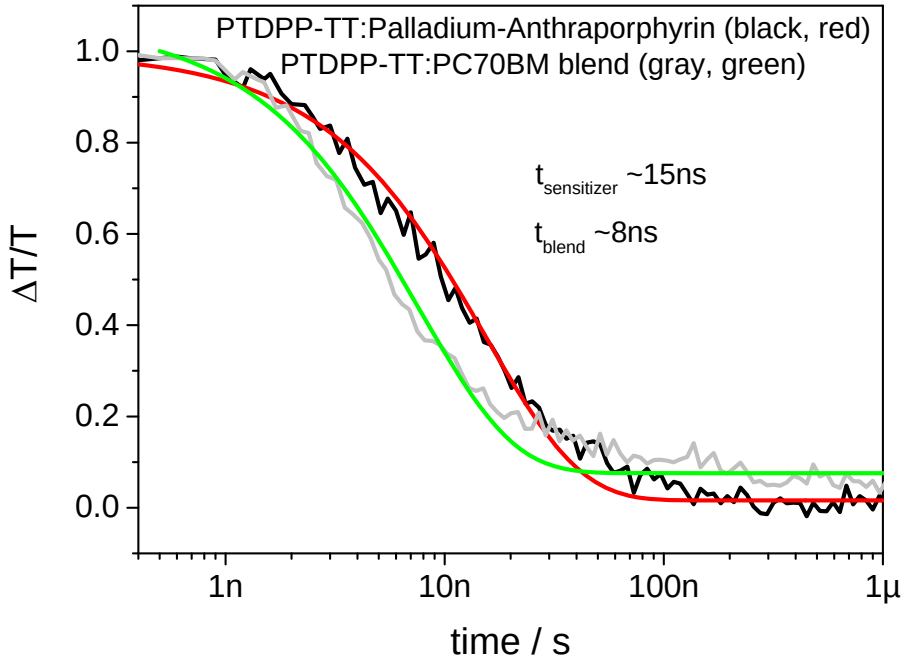

Figure S3. Comparison of the dynamics of the triplet-induced absorption integrated between 1020-1200 nm of PTDPP-TT:Pd-Anthraporphyrin (black) including a fit to a single exponential decay (red) with the dynamics of the photoinduced absorption of a PTDPP-TT:PC70BM film also including a fit to a single exponential decay process. Note that both fits, that is triplet- and photoinduced absorption, yield lifetimes of ~15 ns and 8 ns, respectively, supporting the assignment of the PA in the polymer:fullerene blend to triplet states.

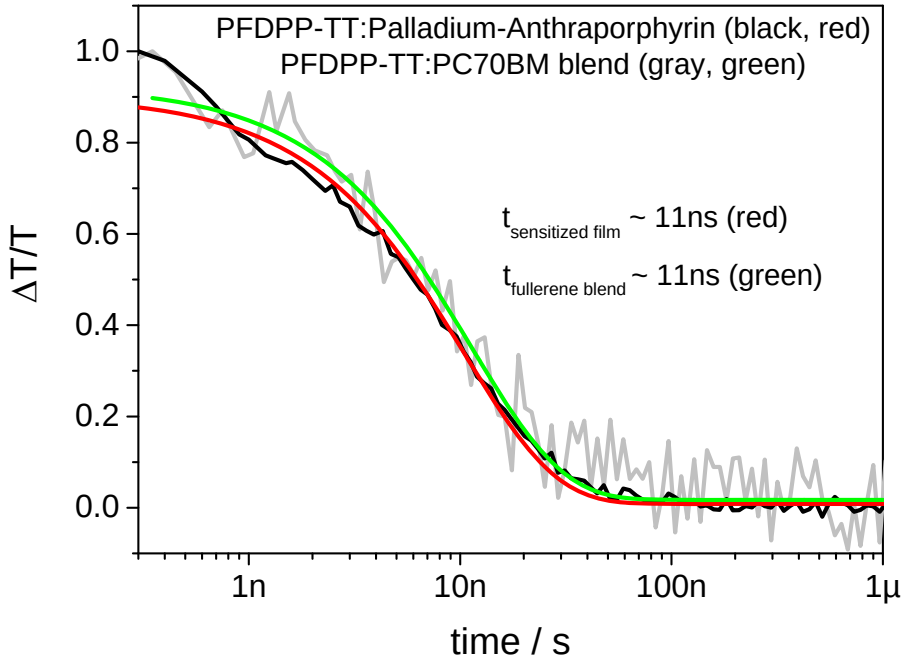

Figure S4. Comparison of the dynamics of the triplet-induced absorption integrated between 1100-1300 nm of PFDPP-TT:Pd-Anthraporphyrin (black) including a fit to a single exponential decay (red) with the dynamics of the photoinduced absorption of a PFDPP-TT:PC70BM film also including a fit to a single exponential decay process. Note that both fits, that is triplet- and photoinduced absorption, yield an inverse decay rate of ~11 ns supporting the assignment of the PA in the polymer:fullerene blend to triplet states.

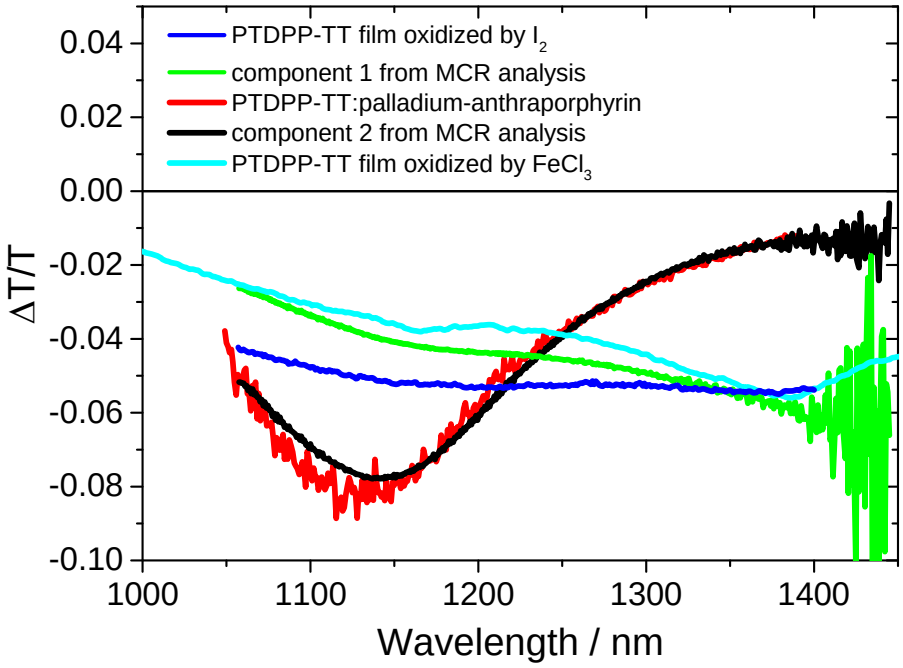

Figure S5. Spectrum of component 2 (black curve) as obtained by MCR analysis of the ps-ns-TA-measurements on a PTDPP-TT:$PC_{71}BM$ film without any spectral constraints as input parameters; Triplet induced absorption spectrum of a palladium-anthraporphyrin doped PTDPP-TT film (red curve); Spectrum of component 1 as obtained by MCR analysis of the ps-ns-TA-measurements on PTDPP-TT:$PC_{71}BM$ without any spectral constraints (green curve); Absorption spectrum of a PTDPP-TT film after oxidation with Iodine vapour (blue curve) and oxidation with $FeCl_3$ solution (cyan curve).

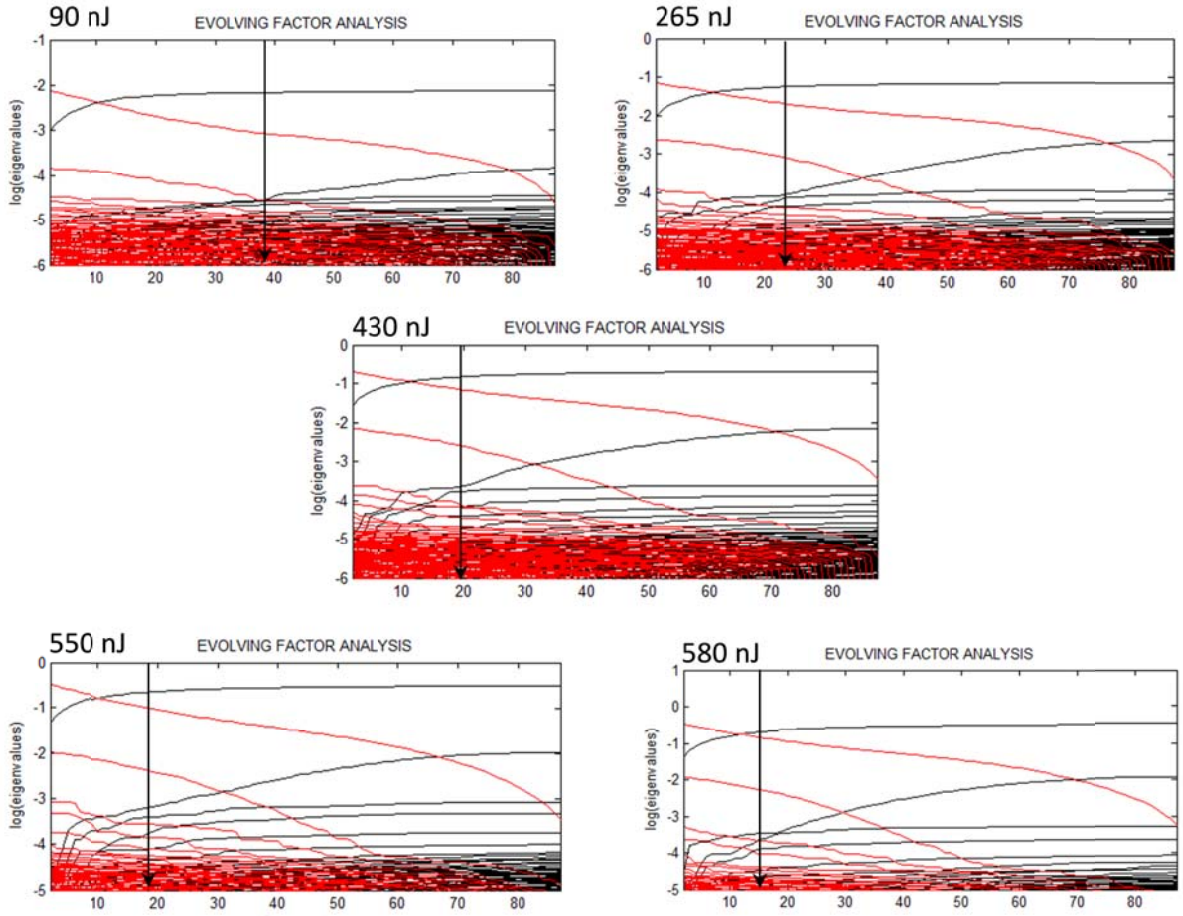

Figure S6. Evolving Factor Analysis (EFA) of the ps-ns NIR TA **d**ata of a PTDPP-TT:$PC_{71}BM$ film at increasing pump pulse energies. The analysis reveals two independent components. While the rise of the first component is largely intensity-independent, the onset of the rise of the second component **(**marked by the arrow) shifts to earlier time with increasing fluence, indicating a fluence-dependent generation mechanism.

5 PHOTOPHYSICS OF PDPP5T:$PC_{71}BM$ SOLAR CELLS

In this chapter the photovoltaic performance, surface morphology, and photophysics of the diketopyrrolopyrrole (DPP)-based donor-acceptor copolymer PDPP5T blended with $PC_{71}BM$ are investigated. Furthermore, the charge carrier mobility in neat PDPP5T films is determined by the time-of-flight (TOF) technique and in organic field effect transistors (OFETs).

We find, that the morphology of the photoactive PDPP5T:$PC_{71}BM$ blend films and hence the photovoltaic performance is greatly influenced by the preparation method, i.e. by using only chloroform as solvent versus adding the cosolvent *ortho*-dichlorobenzene (o-DCB) to the materials dissolved in chloroform. The exciton dynamics, charge generation and recombination mechanisms in the two different blend systems, prepared with and without o-DCB, are investigated with quasi-steady-state photoinduced absorption spectroscopy (PIA), time-resolved photoluminescence spectroscopy (TR-PL), and broad-band transient absorption (TA) pump-probe experiments covering the vis-NIR spectral range and fs-µs dynamic range. The raw TA data is further processed using multivariate curve resolution (MCR) analysis. In both PDPP5T:$PC_{71}BM$ blend systems, prepared with and without o-DCB we observe a significant population of the polymers' triplet state on the sub-ns timescale. Charge recombination and triplet state generation dynamics are both strongly intensity dependent, indicating that triplet states are formed by non-geminate recombination of free charges via triplet charge-transfer states (^{3}CT). This recombination of free charges into the triplet state opens up an additional loss channel in polymers where the triplet state is lower in energy than the ^{3}CT state. As PDPP5T films exhibit very high hole mobilities, we suggest that these high hole mobilities are, together with the nanoscale morphology and the high charge carrier density, responsible for the quick sub-ns recombination of free charge carriers in the blend films under open circuit conditions. However, in an OPV device under operating conditions the high charge carrier mobility might lead to an efficient sweep out of charges, minimizing the charge carrier losses by non-geminate recombination and formation of triplet states.

5.1 INTRODUCTION

DPP-based donor-acceptor copolymers are a promising class of low bandgap polymers for use in organic solar cells (OSCs) and organic field effect transistors (OFETs). Power conversion efficiencies (PCEs) as

high as 8 % have been achieved in bulk heterojunction OSCs based on DPP-polymers blended with PC$_{71}$BM.[126, 125] Applied in OFET devices DPP-based polymers reached record mobility values of 10.5 cm^2 V^{-1} s^{-1} for holes and 3 cm^2 V^{-1} s^{-1} for electrons.[127, 128]

In this work an alternating diketopyrrolopyrrole-quinquethiophene copolymer (PDPP5T) is used as a donor in conjunction with PC$_{71}$BM as acceptor for use in OSCs. The chemical structure of this polymer is shown in figure 39. Its molecular weight M_n was determined by gel permeation chromatography (GPC) to be 29 kg mol^{-1}.

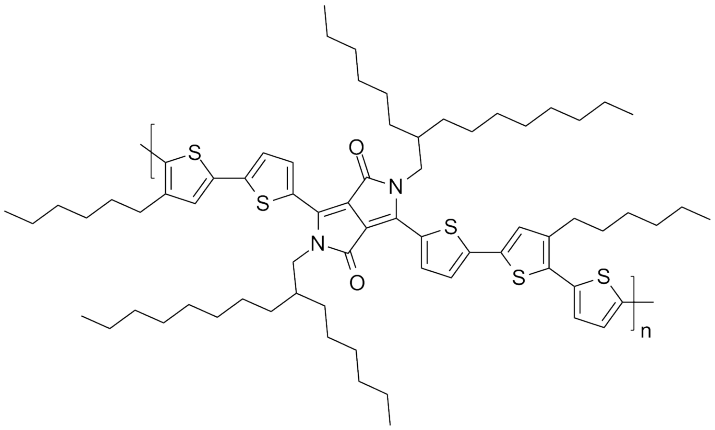

Figure 39: Chemical structure of PDPP5T.

Li et al. presented an OSC with a similar PDPP5T polymer blended with PC$_{71}$BM, yielding a PCE of 5.8 %. In OFET devices built with pristine PDPP5T a hole mobility of 1.5×10^{-2} cm^2 V^{-1} s^{-1} and an electron mobility 1.5×10^{-3} cm^2 V^{-1} s^{-1} were measured.[153] Gevaerts et al. applied the same polymer blended with PC$_{61}$BM as the back cell in a tandem device together with a PCDTBT:PC$_{71}$BM front cell, reaching a PCE of 7.0 %.[154]

As the PDPP5T polymer is commercially available on a multi-gram scale many studies have been published dealing with the potential of a large scale production of single- and multijunction PDPP5T-based photovoltaics.[155, 156, 157, 158, 159]

Furthermore, the influence of morphology on device performance[160] as well as the prediction[161] and the characterization of the morphology[162] and its real-time evolution[163] have been studied.

Despite the decent photovoltaic performance of PDPP5T and structurally related DPP-based polymers the short circuit current (J_{SC}) of these devices is often less than expected from the absorption characteristics. The fundamental loss mechanisms leading to a reduced internal quantum efficiency (IQE) and hence a reduced J_{SC} are not fully understood.[164] Bijleveld et al. studied the DPP-based polymer PDPPTPT with photoinduced absorption spectroscopy (PIA) and observed a population of the polymers triplet state in the PDPPTPT:PC$_{71}$BM blend system.[165] They argued that this triplet state is populated via

recombination of free charges, a process that constitutes a potential loss channel in a device, reducing the IQE.

Triplet state generation in polymer/fullerene blends for organic solar cells is a topic, that is currently being debated.[165, 166, 167, 168, 169, 170, 171, 172, 173, 152] In organic blend systems, where the polymers' triplet state is lower in energy than the charge-transfer state the population of the triplet state is energetically feasible and opens up an additional potential loss channel in an OPV device. Currently, two mechanisms of triplet state creation are being debated.

In the first mechanism the triplet state is populated via geminate recombination of interfacial charge-transfer (CT) states, which flip their spin from singlet (^{1}CT) to triplet (^{3}CT) character mediated by spin-state mixing on the ns-timescale. Such a mechanism was proposed by Dimitrov et al. for the triplet state formation in a photovoltaic blend of a silaindacenodithiophene copolymer and $PC_{71}BM$.[170] Also Di Nuzzo et al. argued on the basis of quasi-steady-state photoinduced absorption spectroscopy (PIA) measurements that in a PCPDTBT:$PC_{61}BM$ blend triplets are formed via geminate recombination and that by improving the morphology with solvent additives the yield of triplet formation can be minimized.[166]

The second mechanism of triplet state formation in an organic solar cell is similar to the situation in organic light-emitting diodes (OLEDs), where injected charges of opposite polarity meet at the recombination interface to form CT states with either triplet or singlet character in a ratio of 3:1, according to spin statistics. In an OSC these ^{3}CT and ^{1}CT states are formed via non-geminate recombination of free charges previously generated at the D/A interface by charge transfer from photoexcited singlet states. In contrast to the findings of Di Nuzzo et al. this second mechanism of triplet state formation via non-geminate recombination of free charges was proposed by Rao et al. and Chow et al. to describe the results of TA pump-probe spectroscopy on the PCPDTBT:$PC_{61}BM$ blend system.[168, 169] They found that the recombination of charges and the formation of triplet states were intensity dependent pointing to a non-geminate recombination mechanism of free charges. Rao et al. made similar observations for blends of PIDT-PhanQ in combination with several fullerene derivatives.[168] Etzold et al. found with TA spectroscopy that triplet state formation via non-geminate recombination occurs already on the sub-ns timescale in PSBTBT and PCPDTBT blended with fullerene derivatives.[171] However, triplet state formation is less in the blend with PSBTBT, explaining its better photovoltaic performance. Furthermore, Gehrig et al. observed sub-ns triplet state formation mediated by the recombination of free charges in a photovoltaic blend of the low bandgap polymer PBDTTT-C and $PC_{61}BM$.[172] Recently, we showed that sub-ns recombination of free charges followed by triplet state formation is also an

issue in blends based on DPP polymers, namely in PTDPP-TT and PFDPP-TT.[152]

Here, we show that in the PDPP5T:$PC_{71}BM$ blends prepared with and without o-DCB the recombination dynamics of charges and the triplet state formation dynamics occurring on the sub-ns timescale are clearly intensity dependent, pointing towards a non-geminate recombination mechanism of free charges and triplet state formation on the polymer via ^{3}CT states. The triplet states on the polymer then further decay on the ns-timescale either via triplet-triplet annihilation or via triplet-charge annihilation.

5.2 PHOTOVOLTAIC PERFORMANCE

Figure 40a shows the normalized steady-state absorption spectrum of a pristine PDPP5T film (blue curve) and PDPP5T in solution (green curve). The absorption spectrum of PDPP5T in solution has a maximum at 700 nm with a shoulder at 770 nm. A second smaller absorption band appears around 450 nm. The absorption spectrum of the thin film looks very similar, but the shoulder around 770 nm is more pronounced than in the solution and the absorption onset is slightly redshifted, which is probably due to an increased conjugation length of the polymer segments in the solid state.

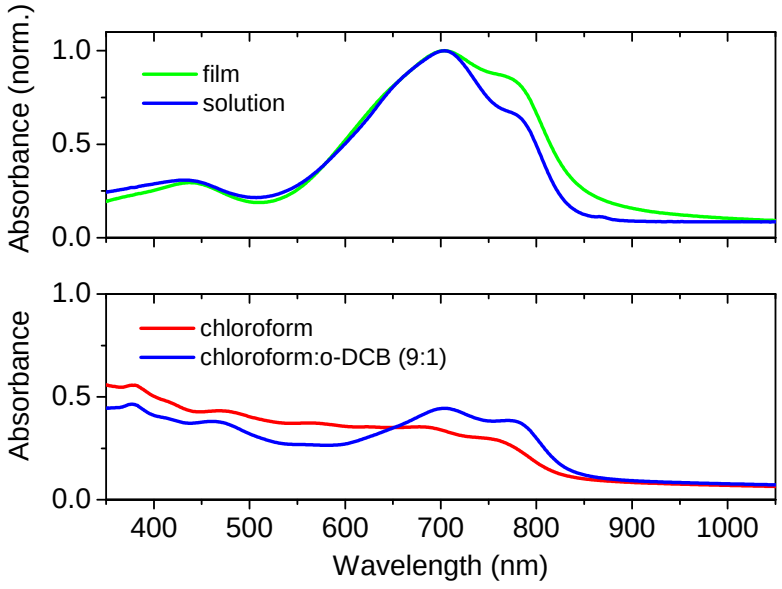

Figure 40: (a) Normalized steady-state absorption spectrum of a PDPP5T film (blue curve) and PDPP5T in solution (green curve) (b) Absorption spectra of a 1:2 by weight PDPP5T:$PC_{71}BM$ blend cast from chloroform and from a 9:1 by volume chloroform:*ortho*-dichlorobenzene solvent mixture (the film thickness for both films is ~120 nm).

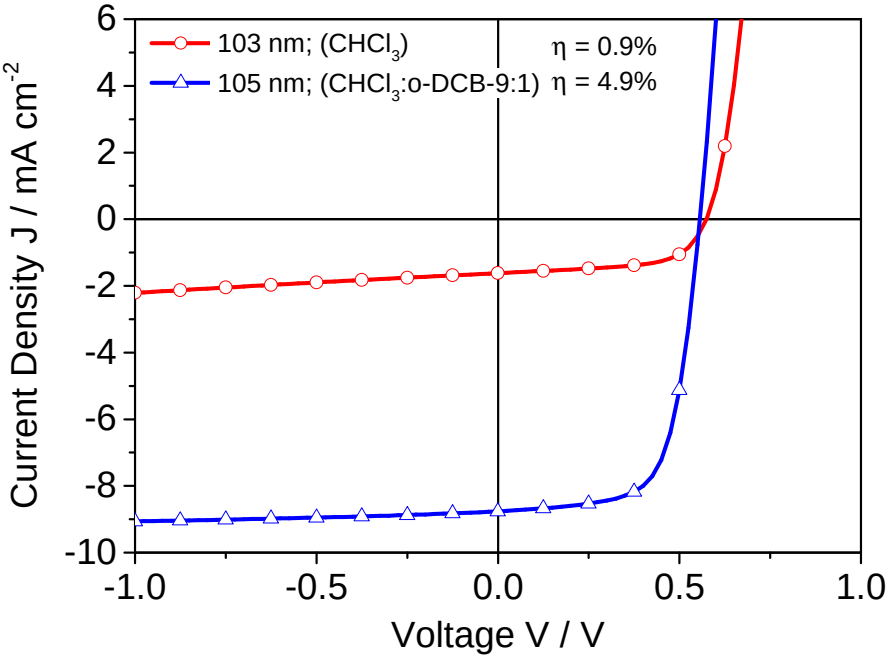

Figure 41: Current-Voltage ($J-V$) characteristics of BHJ solar cells made from 1:2 by weight PDPP5T:$PC_{71}BM$ blends cast from chloroform ($CHCl_3$) (red curve) and cast from a 9:1 by volume solution of $CHCl_3$:o-DCB (blue curve). η is the power conversion efficiency (PCE) under solar illumination of 67 mW cm^{-2}.

Figure 40b shows the absorption spectrum of two as cast 1:2 by weight PDPP5T:$PC_{71}BM$ blend films. One was cast from chloroform (red curve) and one from a solvent mixture of chloroform and *ortho*-dichlorobenzene (o-DCB) in a ratio of 9:1 by volume (blue curve). The absorption spectrum of the latter exhibits a more pronounced and red shifted absorption in the wavelength range from 650 to 800 nm compared to the former. This is an indication that the degree of crystallinity and the conjugation length of PDPP5T are higher in the blend film cast from the solvent mixture. In both absorption spectra there is an additional broad and unstructured absorption component, originating from $PC_{71}BM$ that extends from the visible- into the UV wavelength region.

The basic device architecture consists of the following layer structure: Glass/ITO/PEDOT:PSS/Active-Layer/Ca/Al. There is a drastic difference in photovoltaic performance between the two devices cast with or without o-DCB (see figure 41). While the device made without o-DCB has a short circuit current density (J_{SC}) of 1.6 mA cm^{-2}, a power conversion efficiency (PCE or η) of 0.9 % and a fill factor (FF) of 0.61, the device made with o-DCB is a much better performing device exhibiting a J_{SC} of 8.8 mA cm^{-2}, PCE of 4.9 % and a FF of 0.67. The open circuit voltage (V_{OC}) is similar for both devices and around 0.56 V.

Figure 42 shows the external quantum efficiency (EQE) for both devices. The difference in device performance of the two types of solar cells is also reflected in the EQE: While the EQE of the device without o-DCB is does not exceed 12 %, the maximum EQE value of the device with o-DCB is 54 %. The shape of both EQE curves are rather flat, only slightly reflecting the shape of the corresponding absorption spectra at wavelengths below the absorption onset.

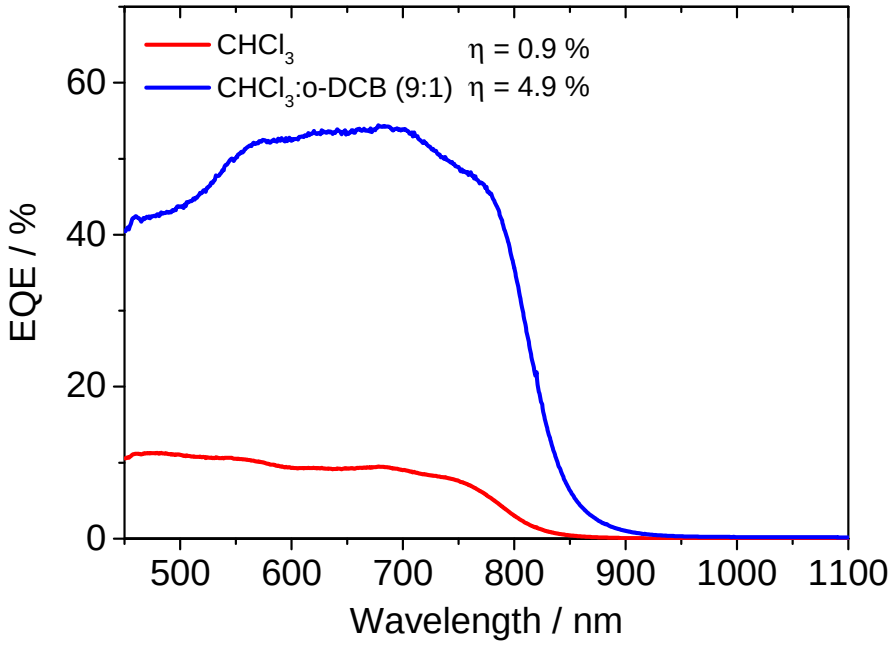

Figure 42: External Quantum Efficiencies (EQE) of BHJ solar cells made from 1:2 by weight PDPP5T:PC$_{71}$BM blends cast from chloroform (red curve) and cast from a 9:1 by volume solution of CHCl$_3$:o-DCB (blue curve).

5.3 SURFACE MORPHOLOGY OF PDPP5T:PC$_{71}$BM BLEND FILMS

The morphology of the active layer plays a crucial role in determining the device performance.[174, 175, 176] The intimacy of mixing of the donor and acceptor materials as well as size, composition and crystallinity of the phase separated domains are important factors that influence the charge carrier generation and the charge transport in the photoactive layer.[177, 178, 179] In addition, the presence and formation of percolation pathways have been considered important aspects in optimizing BHJ solar cells.[180] The donor/acceptor morphology can be controlled by varying the processing conditions of the materials.[139] The choice of the solvent, co-solvents, solvent additives, spin-coating speeds, drying time, thermal annealing or solvent vapour annealing are all heavily influencing the morphology of the photoactive layer.[181, 182, 183] Depending on the processing conditions the donor and acceptor materials of the photoactive layer in a

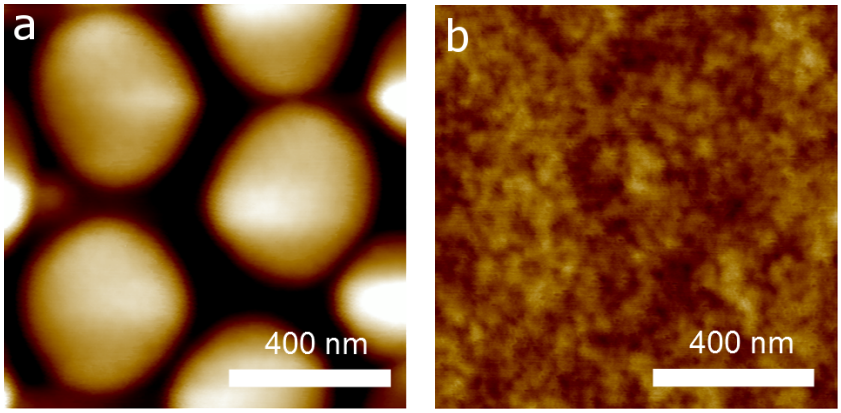

Figure 43: AFM surface scans of PDPP5T blended with PC$_{71}$BM in a ratio of 1:2 by weight (a) the solvent was chloroform (b) the solvent was chloroform and o-DCB in a ratio of 9:1 by volume.

BHJ solar cell can be intimately mixed or rather phase separated into bigger domains of the respective materials. Although the morphology of the active layer has such a huge impact on device performance, the understanding of the underlying mechanisms of the self-organizing of the materials and the interplay of the different processing conditions is only poorly understood and is rather phenomenological. Hence, the optimization of device morphology is rather based on trial and error than on a rational approach. However, recently S. Kouijzer et al. presented a model which seems to predict some morphological features of the PDPP5T:PC$_{71}$BM photovoltaic blend,[184] leading the way to further research which will help in the future design and morphological control of the donor/acceptor layer by rational means.

Because morphology is such an important factor in optimizing organic BHJ solar cells substantial research effort has been devoted to establish a quantitative relation between morphology and device performance.[185, 186, 187] A variety of experimental techniques have been applied to study the morphology of donor/acceptor blends, including transmission electron microscopy (TEM), scanning Kelvin probe microscopy (SKPM) and atomic force microscopy (AFM), while X-ray diffraction and neutron reflection measurements have been used to gather structural information about the blends.[188]

In our case the method of choice to study the influence of the different solvents on the surface morphology and to establish a relation between the blend morphology and the device performance was atomic force microscopy (AFM). Figure 43 displays the results of AFM scans of thin films of PDPP5T:PC$_{71}$BM spincast from chloroform or spincast from chloroform and *ortho*-dichlorobenzene in a ratio of 9:1 by volume. In picture 43a there are big circular shaped domains visible which have diameters of about 400 nm. These domains mainly consist of aggregates of PCBM which are embedded in a polymer rich matrix.

Figure 43b shows the surface structure of the sample prepared with the cosolvent o-DCB. The surface structure is rather fine grained and does not exhibit any clusters comparable to the ones we can see in the surface morphology of the sample prepared without any solvent additives. This enormous difference in surface morphology does most probably also explain the differences in device performance of the two solar cells. In the first sample quenching of excitons created on the large PCBM domains will most likely be incomplete. A significant amount of excitons will not reach the polymer:fullerene interface to undergo charge separation, whereas in the case of the rather intimately mixed blend structure where we used o-DCB, exciton diffusion to the interface and charge separation will be more efficient. In the next part we will show time-resolved photoluminescence (TR-PL) experiments which underline this hypothesis.

Kouijzer et al. also determined the morphology of two PDPP5T:PC$_{71}$BM blends which were prepared the same way, we prepared our samples. They analyzed the films by bright-field TEM and took additional TEM images of a thin cross section sample made with a focused ion beam.[184] Their observations of big PCBM 'blobs' embedded in a polymer rich phase are in line with our observations. From cross section images they make the additional observation that the big PCBM domains in the sample without o-DCB have a thin skin layer (> 5 nm) of PDPP5T rich phase on the top side between the PCBM and the aluminum contact, while on the bottom side some PCBM domains have thin skin layers and others seem to touch the PEDOT:PSS.

5.4 PCBM EXCITON DYNAMICS IN PDPP5T:PC$_{71}$BM BLEND FILMS

Figure 44 shows the decay kinetics (black curves) of PC$_{71}$BM excitons in PDPP5T:PC$_{71}$BM photovoltaic blends prepared without (a) and with o-DCB (b). The decay kinetics in (a) are well described by a single exponential yielding a lifetime of ~ 620 ps. The kinetics in (b) do not obey a single exponential decay. They are better described by a stretched exponential function, which describes the decay by a distribution of lifetimes. This description is taking into account that excitons created in different areas of the PCBM domains have different diffusion lengths until they reach the polymer:fullerene interface. The fit for the sample prepared with o-DCB with a stretched exponential yields a mean lifetime of ~ 205 ps. This result shows that exciton quenching from PCBM excitons in the sample prepared with o-DCB is much more efficient than in the blend prepared without o-DCB, since the mean exciton lifetime is much shorter. In fact, the lifetime of 620 ps approaches the fluorescence lifetime of pure PC$_{71}$BM determined experimentally by A. Fedorov et al. to be 630 ps.[189] This result indicates that the majority of excitons created on the big PCBM domains in the blend film prepared without o-DCB has decayed before reaching the inter-

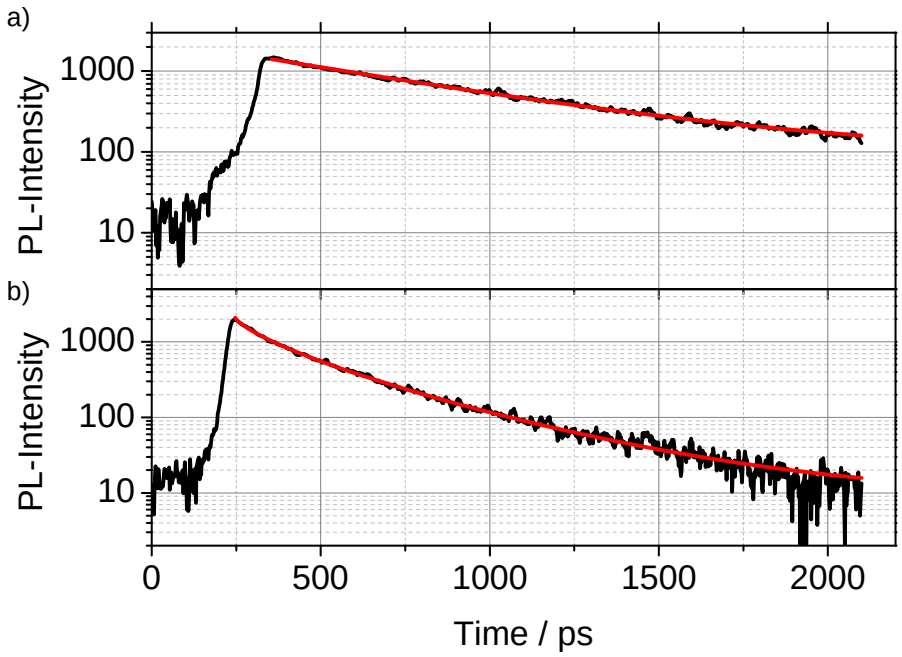

Figure 44: Photoluminescence kinetics of PC$_{71}$BM extracted from streak camera measurements (a) Kinetics of PC$_{71}$BM excitons in a PDPP5T:PC$_{71}$BM blend spincast from chloroform. (b) Fluorescent decay of excitons on PC$_{71}$BM in a PDPP5T:PC$_{71}$BM blend spincast from a solvent mixture of $CHCl_3$ and o-DCB in a ratio of 9:1 by volume. The red lines are fits to the black data curves.

face where efficient exciton quenching could occur. Therefore the decay kinetics can be well described by a single exponential, while in the blend prepared with o-DCB a distribution of lifetimes is necessary to account for a distribution of exciton diffusion lengths.

5.5 EXCITON DYNAMICS IN PRISTINE PDPP5T FILMS

Figure 45 shows the fluorescence decay of a pristine PDPP5T film obtained by a streak camera measurement (black line). A fit to the data with a single exponential (red line) yields a fluorescence lifetime of about 105 ps.

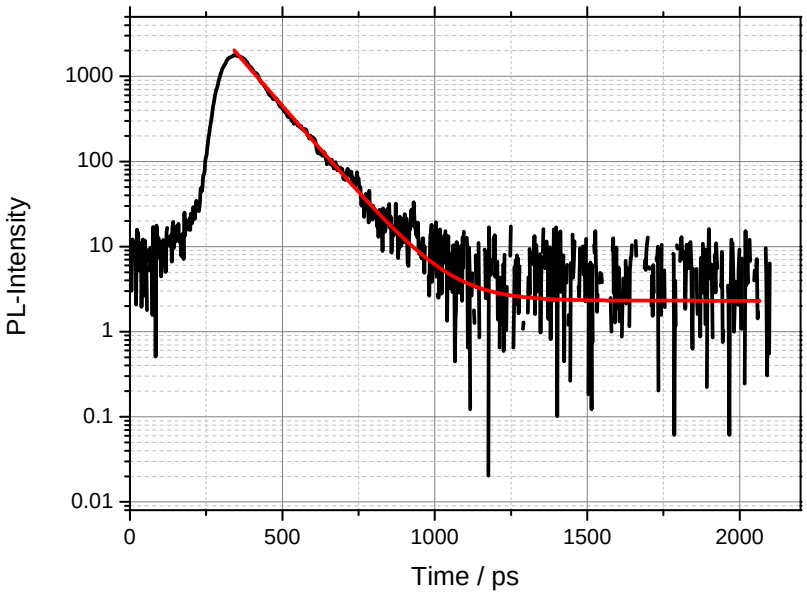

Figure 45: Fluorescence decay of a pristine PDPP5T film obtained by a streak camera experiment. The film was spincast from a solvent mixture of $CHCl_3$ and o-DCB in a ratio of 9:1 by volume. The laser excitation wavelength was 400 nm. The red line is a fit to the black data curve.

Figure 46 shows short delay (fs-ps, panel a) and long delay (ns-µs, panel b) transient absorption (TA) spectra in the visible and near infrared (NIR) spectral region as well as the steady-state absorption spectrum of a pristine polymer film (panel c). In the short and long-delay spectra we attribute the positive signal in the visible region which exhibits two distinct peaks at 700 and 780 nm to the ground state bleach, since it coincides with the structure of the absorption spectrum shown in panel c. The broad photoinduced absorption (PA) which starts at 800 nm and extends to longer wavelengths than were measured in this experiment originates from excitons created on the PDPP5T polymer.

We measured the pristine PDPP5T film at different laser fluences to see whether the observed kinetics are influenced by any higher order processes such as exciton-exciton annealing. The integrated kinetics of the exciton-induced absorption going from 1100 to 1500 nm measured at different laser fluences at an excitation wavelength of 700 nm are shown in figure 47. The laser excitation intensity was varied from 0.6 to 2.7 $\mu J\,cm^{-2}$. The kinetics are clearly fluence dependent

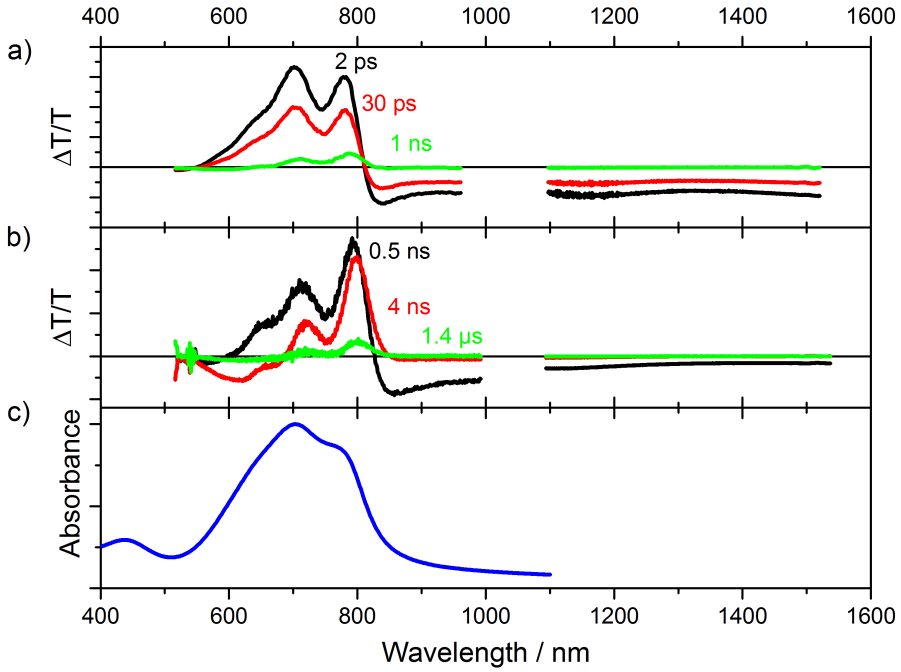

Figure 46: (a) Short delay (ps-ns) broadband transient absorption spectra of a pristine PDPP5T film excited at 420 nm measured in the visible (500-970 nm) and excited at 700 nm measured in the NIR (1100-1500 nm) spectral region at delay times of 2 ps (black), 30 ps (red) and 1 ns (green). The pump fluence at 420 nm was 13.1 µJ cm^{-2} for the visible and 1.6 µJ cm^{-2} at 700 nm for the NIR measurement. (b) Long delay (ns-µs) broadband transient absorption spectra of a pristine PDPP5T film excited at 532 nm and measured in the visible (500-1000 nm) and in the NIR (1100-1540 nm) spectral region at delay times of 0.5 ps (black), 4 ps (red) and 1.4 µs (green). The pump fluence at 532 nm was 92 µJ cm^{-2} for the visible and 11.4 µJ cm^{-2} at 532 nm for the NIR measurement. (c) Steady state absorption spectrum of a pristine PDPP5T film. The films were spincast from a solvent mixture of $CHCl_3$ and o-DCB in a ratio of 9:1 by volume.

with the kinetics at higher fluences (orange to red) exhibiting shorter lifetimes than the kinetics at lower fluences (cyan and blue). In fact at the two lowest fluences of 0.6 µJ cm^{-2} (blue curve) and 0.8 µJ cm^{-2} (cyan curve) the two corresponding decay curves are on top of each other, indicating that at these low fluences there are no higher order processes juggling with the pure singlet exciton decay dynamics. Hence, we did a global fit of the kinetics at the two lowest fluences with a single exponential in order to determine the exciton lifetime, yielding an inverse rate of ~ 78 ps. This inverse rate determined by TA spectroscopy in the NIR wavelength range is shorter than the inverse rate of ~ 105 ps determined by the photoluminescence measurement with the streak camera, but still within the experimental error of the two different methods.

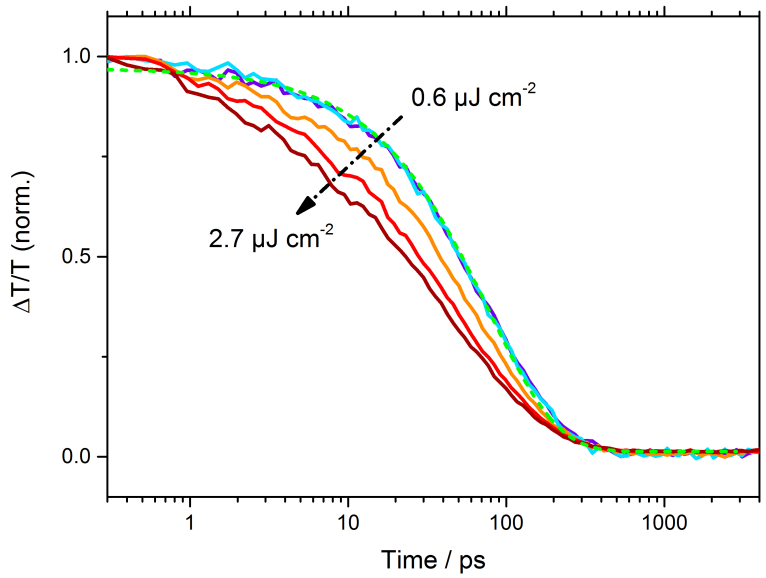

Figure 47: Integrated and normalized kinetics of the singlet exciton induced absorption from 1100 to 1500 nm extracted from short-delay (ps-ns) pump-probe measurements with laser excitation fluences going from 0.6 to 2.7 μJ cm^{-2} at an excitation wavelength of 700 nm. A fit to the kinetics at the two lowest fluences (cyan and blue curves) with a single exponential is also shown as a dashed green line.

In the long-delay spectra, shown in figure 46b, the shape of the PA at delay times bigger than one nanosecond differs from the shape of the singlet exciton spectrum obtained from the short delay measurement. As we will show later (section 5.6.2) this PA signal can be attributed to triplet excitons, since the shape of this spectrum is similar to a triplet spectrum obtained from TA spectroscopy by blending PDPP5T with the triplet sensitizer palladium-tetraanthraporphyrin.

The fluence dependent kinetics of the (ns-μs) pump-probe measurements of a pristine PDPP5T thin film integrated between 1100 and 1500 nm are displayed in figure 48. At early times between 1-2 ns there is a steep decay of the initial signal, which is due to singlet excitons decaying within the instrument response time of our setup. After 2 ns there is a residual signal which decays with a fluence dependence within one microsecond. We attribute this signal, as already mentioned earlier, to triplet excitons which are probably created by singlet fission. The signal lifetime of several nanoseconds is in line with our attribution to triplet excitons. The decay of the triplet exciton induced absorption is fluence dependent, which is an indication that higher order processes, such as triplet-triplet annihilation, occur in this sample at higher fluences (yellow to red curves). The kinetics at the two lowest fluences (blue and green curves) exhibit a similar decay behavior. A global fit with a single exponential to these two decay curves after 2 ns yields an inverse rate of ~ 81 ns.

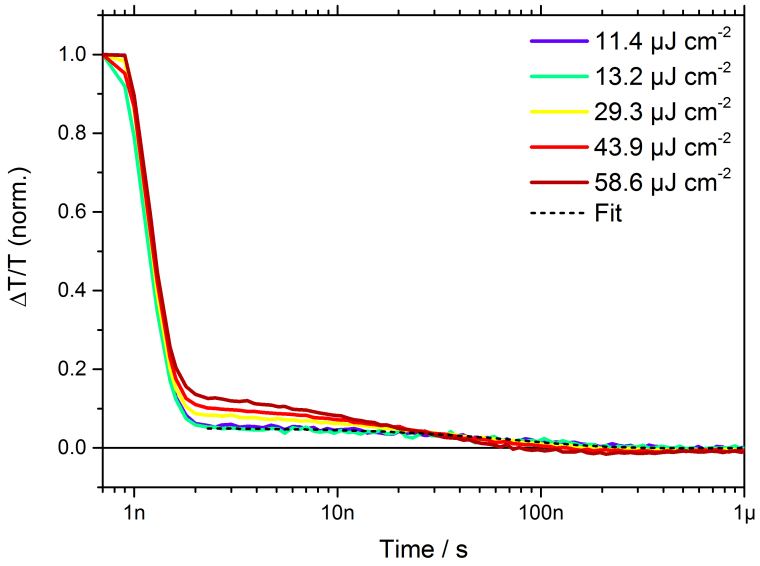

Figure 48: Integrated and normalized kinetics of the photoinduced absorption from 1100 to 1500 nm extracted from long-delay (ns-µs) pump-probe measurements with laser excitation fluences going from 11.4 to 58.6 µJ cm^{-2} at an excitation wavelength of 532 nm. A fit to the kinetics of the two lowest fluences (blue and green curves) after 2 ns with a single exponential is also shown as a dashed black line.

5.6 DETERMINING THE CHARGE- AND TRIPLET-INDUCED ABSORPTION SPECTRA OF PDPP5T

To facilitate the data analysis of the TA pump-probe spectra we did additional experiments to independently determine the spectral shape of the charge-induced and triplet exciton induced absorption features of PDPP5T. In the next two sections the corresponding results are presented.

5.6.1 *Oxidation Study on PDPP5T*

To determine the charge induced absorption or cation spectrum of the PDPP5T polymer we oxidized a thin pristine PDPP5T film by exposing it to an iodine atmosphere for 10 s, 2 min, and 15 min and measuring the steady-state absorption after every step. Figure 49 shows the corresponding spectra. For reasons of better comparability with the TA data, we plotted the results as change in transmission normalized by the transmission of the untreated sample, i.e. as $\Delta T/T$ versus wavelength in the same fashion as we plot our TA pump-probe spectra. Similar to the TA spectra of the pristine PDPP5T film described in section 5.5, here, we also observe a double peaked GSB feature between 600 and 800 nm. There is an additional GSB feature at lower wavelengths, between 300 and 500 nm, which we cannot observe with our TA setup, since our white light extends only to wavelengths above 500 nm. In the NIR spectral region there is a broad absorption feature with a peak at 1400 nm. This negative signal starts around 800 nm and extends to wavelengths longer than 1700 nm. This absorption peak which originates from the iodine having oxidized the polymer slightly blueshifts with exposure time of the polymer film to the iodine vapor, meaning that with an increasing number of positive charges on the polymer, the peak of the induced absorption shifts to higher energies.

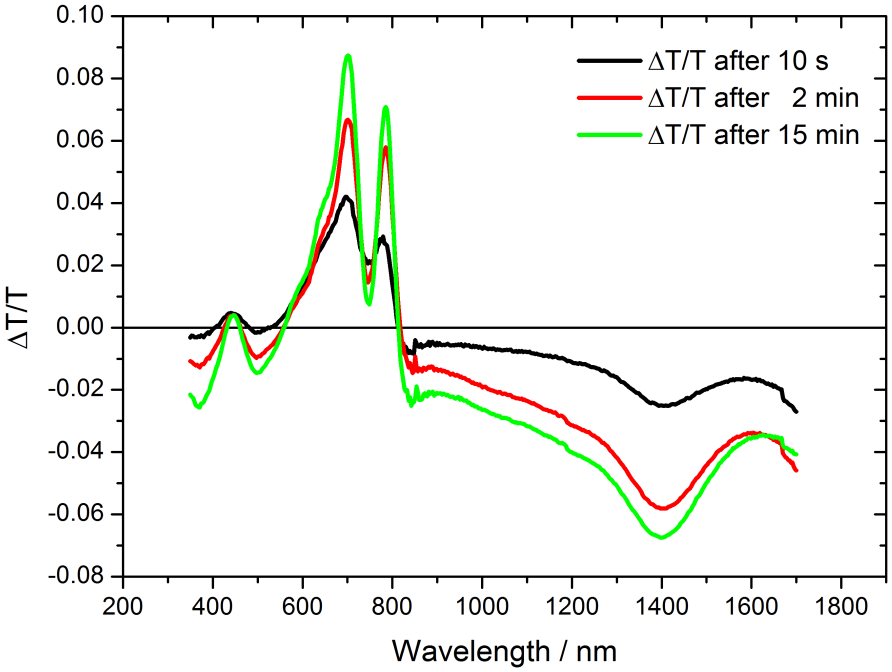

Figure 49: Cation spectra of a pristine PDPP5T film which was submersed into iodine vapor for 10 s, 2 min and 15 min. Before and after each treatment step steady-state absorption spectra were recorded. For better comparability with the TA pump-probe spectra we plotted the change in transmission normalized by the transmission of the untreated sample (ΔT/T).

5.6.2 *Triplet-state dynamics in a PDPP5T thin film doped with palladium-tetraanthraporphyrin*

In the long delay (ns-µs) pump-probe data of the pristine PDPP5T film, presented in section 5.5, we observed the formation of a long-lived species, which we interpreted as the polymer's first triplet state. In order to further support this assumption and to clearly distinguish between different species contributing to the PA features in our TA experiments, we measured a PDPP5T film doped with 5 weight % palladium-tetraanthraporphyrin (PdTAP)[190] as a triplet sensitizer with broadband TA spectroscopy in the NIR wavelength range. The results are shown in figure 50. The doped PDPP5T film was excited with a laser pulse at 532 nm, where the PDPP5T polymer has a decreased absorbance. Hence, the majority of excited states will be created on the triplet sensitizer PdTAP. The singlet excitons on PdTAP rapidly populate the sensitizers triplet state via intersystem crossing facilitated by the palladium atom. The PdTAP triplet energy level is at around 1.12 eV, while the triplet energy level of PDPP5T is estimated to be sufficiently low at around 0.9 eV to guarantee for an efficient downhill Dexter-type energy transfer from the triplet sensitizer PdTAP to the PDPP5T polymer. There might also be a small amount of Förster-type singlet energy transfer between PdTAP and PDPP5T and some singlet states on PDPP5T that where created with the excitation light at 532 nm, but since we have taken pump-probe spectra at delay times > 1 ns all the singlet excitons on the polymer should have decayed and their spectral contribution can be neglected. Thus, we get a pure spectrum of triplets on the PDPP5T polymer. Panel (a) in figure 50 displays these triplet spectra after 1.5 ns (black curve), 15 ns (red curve) and 146 ns (green curve). The shape of the measured spectrum with an absorption maximum at 1150 nm stays similar for all the presented delay times and the signal height decreases over time. However, the absorption maximum slightly red-shifts over time, indicative of a relaxation of triplet excitons within the density of states. Figure 50b presents the fluence dependence of the photoinduced absorption dynamics tracked between 1020 and 1200 nm with laser fluences going from 11.1 to 49.2 µJ cm^{-2}. The decay is clearly fluence dependent, with higher order processes, such as triplet-triplet or triplet-singlet annihilation, accelerating the decay dynamics at higher fluences. A fit (green curve) to the data of the decay dynamics at the lowest fluence of 11.1 µJ cm^{-2} (dark red curve) with a single exponential yields a life time of ~ 31 ns. This life time is smaller than the life time of ~ 81 ns determined from the PA dynamics of a pristine PDPP5T film in section 5.5. This might be the case, because in the measurement of the PdTAP doped PDPP5T film there are more higher order effects affecting the dynamics than in the measurement of the pristine PDPP5T film.

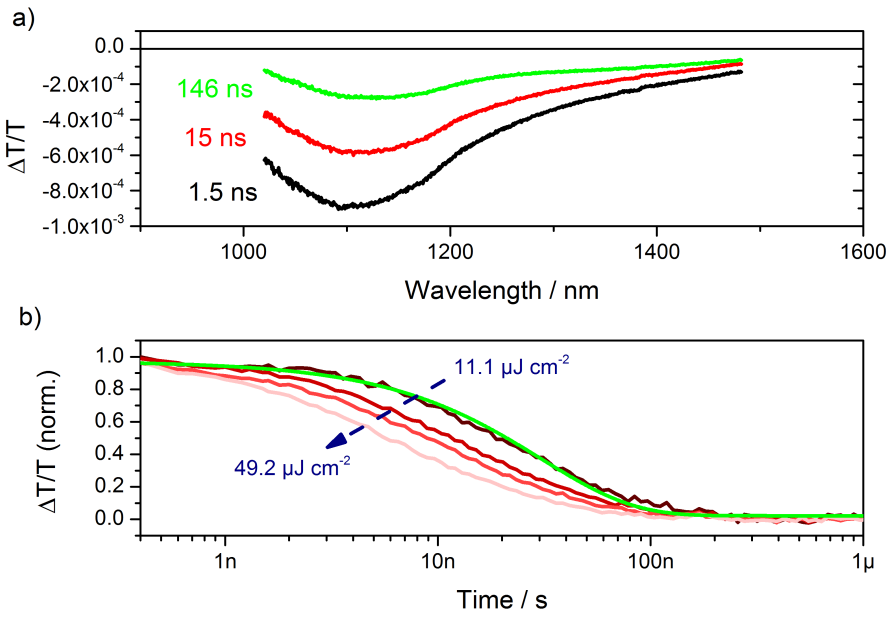

Figure 50: (a) Long delay (ns-µs) NIR pump-probe spectra of a thin PDPP5T film doped with 5 weigth % palladium-tetraanthraporphyrin excited at 532 nm with a fluence of 11.1 µJ cm^{-2} at delay times of 1.5 ns (black), 15 ns (red) and 146 ns (green curve) (b) Fluence dependence of the photoinduced absorption dynamics tracked between 1020 and 1200 nm. The green line is a fit with a single exponential to the dynamics measured with the lowest fluence of 11.1 µJ cm^{-2} yielding an inverse rate of ~ 31 ns.

5.7 CHARGE GENERATION AND TRIPLET-STATE FORMATION IN PDPP5T:$PC_{71}BM$

In this section we present the early time (ps-ns) vis-NIR pump-probe spectra and quasi-steady-state photoinduced absorption (PIA) spectra of 1:2 (w/w) PDPP5T:$PC_{71}BM$ blends prepared with and without o-DCB as a cosolvent. We measured the samples with different laser excitation wavelengths to either generate excited states mainly on the PDPP5T polymer or mainly on $PC_{71}BM$, in order to study the different charge carrier generation mechanisms from PDPP5T and PCBM excitons in the respective blend systems. In addition we analyzed the raw transient absorption pump-probe spectroscopy data by multivariate curve resolution (MCR) to get a clear picture of the dynamics of exciton decay, charge generation, early time recombination and triplet state formation in the PDPP5T:$PC_{71}BM$ blends.

5.7.1 *Charge generation and triplet-state formation on the sub-ns timescale*

The early time (ps-ns) pump-probe spectra as well as quasi-steady-state PIA, steady-state absorption, triplet-induced- and charge-induced absorption spectra of PDPP5T:$PC_{71}BM$ blends prepared without o-DCB can be found in figure 51, while the corresponding spectra for PDPP5T:$PC_{71}BM$ blends prepared with o-DCB are presented in figure 52. Figure 51a and 52a display the pump-probe vis-NIR spectra where we used 700 nm as excitation wavelength to create mainly excited states on the polymer. Figure 51b and 52b show the pump-probe vis-NIR spectra of the respective samples, where we created mainly excitons on PCBM. The excitation wavelengths were 420, 520 or 532 nm, depending on the experiment. Details are given in the respective captions. Panels c and d of figure 51 and 52 show the quasi-steady-state PIA, steady-state absorption, triplet-induced- and charge-induced absorption spectra of the respective PDPP5T:$PC_{71}BM$ blends for comparison. The early time (ps-ns) pump-probe spectra of both samples for all excitation wavelengths (figure 51a,b and 52a,b) exhibit two characteristic features: A positive double peaked signal in the shorter wavelength region from 500 to 800 nm and a negative signal after a zero crossing at 800 nm, which extends to 1500 nm and beyond. In line with the pump-probe spectra of pristine PDPP5T, presented in section 5.5, we attribute the positive signal to the ground state bleach (GSB) of the polymer. This double peaked structure is also apparent in the steady-state absorption spectra shown in figure 51d and 52d (blue curves). In the former case of the blend film prepared without o-DCB the double peaked absorption structure is slightly covered by the absorption of the fullerene derivative $PC_{71}BM$, but still recognizable.

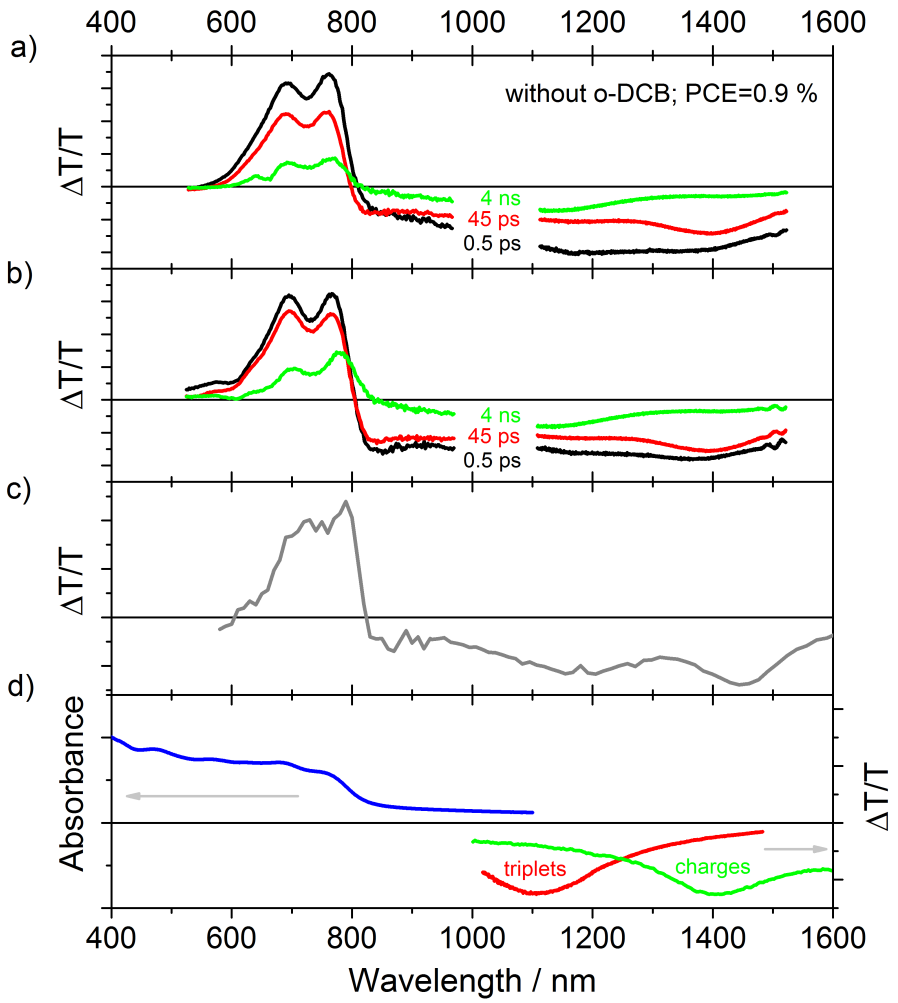

Figure 51: (a) ps-ns broadband transient absorption spectra of a 1:2 (w/w) PDPP5T:PC$_{71}$BM blend prepared without o-DCB excited at 700 nm and measured in the visible (500-1000 nm) and NIR (1100-1500 nm) at delay times of 0.5 ps (black), 45 ps (red) and 4 ns (green). The pump fluence at 700 nm was 7.3 µJ cm^{-2} for the visible and 3.1 µJ cm^{-2} for the NIR measurements. (b) ps-ns broadband transient absorption spectra of a 1:2 (w/w) PDPP5T:PC$_{71}$BM blend prepared without o-DCB excited at 420 nm and measured in the visible (500-1000 nm) and excited at 532 nm and measured in the NIR (1100-1500 nm) at delay times of 0.5 ps (black), 45 ps (red) and 4 ns (green). The pump fluence at 420 nm was 20.2 µJ cm^{-2} for the visible and 7.1 µJ cm^{-2} for the NIR measurements with an excitation wavelength of 532 nm. (c) Quasi-steady-state photoinduced absorption (PIA) spectrum of a 1:2 (w/w) PDPP5T:PC$_{71}$BM blend prepared without o-DCB at 80 K excited at 808 nm. (d) Steady-state absorption spectrum of a 1:2 (w/w) PDPP5T:PC$_{71}$BM blend prepared without o-DCB (blue), triplet-induced absorption spectrum (red) obtained on a palladium-tetraanthraporphyrin-doped PDPP5T film (compare section 5.6.2), charge-induced absorption spectrum (green) obtained on a PDPP5T film oxidized by iodine vapor (compare section 5.6.1).

We attribute the broad photoinduced absorption (PA) signal in the pump-probe spectra, which starts in the 'visible' measurements at around 800 nm and extends further to the window of the NIR pump-probe measurements going from 1100 to 1500 nm due to an overlay of the photoinduced absorption spectra of singlet excitons, charges and triplet excitons on the PDPP5T polymer. While singlet excitons are rather short lived on the time scale of several picoseconds, charges and triplet excitons exhibit usually longer lifetimes going from nanoseconds to microseconds. To get more information about the spectral shape of these long-lived species, we conducted PIA measurements at 80 K on both PDPP5T:$PC_{71}BM$ blends (figure 51c and 52c). The shape of the PIA spectra are similar for both blend systems. At shorter wavelengths from 600 to 800 nm we observe a GSB signal, followed by a broad PA signal extending to 1600 nm. In fact we measured PIA spectra until 4000 nm, but here we present the data until 1600 nm only. The PA signal extends to 4000 nm and further into the IR range to wavelengths longer than detected by our liquid nitrogen cooled InSb-based detector. Note that the PIA spectra are falsified around 808 nm, because of a substantial amount of scattered light from the 808 nm laser excitation. The PIA spectra of both blends show at longer wavelengths two PA peaks, one around 1200 nm and another around 1450 nm. From the PIA spectra alone it is neither clear which excited state causes the PA signal nor how many there are. However, by comparing the triplet-exciton-induced and charge-induced absorption spectra (figure 51d and figure 52d, red and green curves) with the PIA spectra, we come to the conclusion, that there are contributions from triplet excitons and charges in the PIA spectra, triplet excitons absorbing at shorter wavelengths around 1100 to 1200 nm and charges absorbing at larger wavelengths around 1400 to 1500 nm. Bearing this information in mind, we are able to understand the early time (ps-ns) vis-NIR pump-probe spectra.

Let us now take a more detailed look at the pump-probe spectra of the PDPP5T:$PC_{71}BM$ blend prepared without o-DCB where we excited at 700 nm for the visible and NIR measurements (figure 51a). After 0.5 ps the GSB and PA signals are the highest. We attribute the broad and rather unstructured PA signal after 0.5 ps to mainly singlet excitons on the polymer. It might be, that there is already some contribution from charges which are created on an ultrafast time scale as was observed in several polymer:PCBM systems, such as P3HT[191], PCBTDBT[192], PCDTBT[193] and pBTTT[194]. The contribution of charges in the NIR pump-probe spectra becomes apparent after 45 ps (red curve). This spectrum exhibits a pronounced absorption peak around 1400 nm, in the same region where the independently measured charge-induced absorption spectrum has its maximum (figure 51d, green curve). The visible pump-probe spectra show between 800 and 850 nm a negative signal that grows from 0.5 to 45 ps. This sig-

nal might be due to electro-absorption (EA), generated by interfacial charge-transfer (CT) states created between 0.5 and 45 ps, which induce an electric field across the polymer/PCBM-interface. After 4 ns (green curve) the EA signal and the charge-induced absorption signal have completely vanished, leaving behind a PA signal peaking around 1100 to 1200 nm, which we attribute to triplet excitons on the polymer, since it is similar in shape and spectral position to the separately determined triplet-induced absorption spectrum presented in figure 51d (red curve).

When we excite the PDPP5T:PC$_{71}$BM blend film prepared without o-DCB at 420 nm for the visible and at 532 nm for the NIR wavelength region (figure 51b), we observe after 0.5 ps a stronger EA signal in the visible compared to the EA signal 0.5 ps after the 700 nm excitation. The PA signal in the NIR region consists of contributions from singlet excitons and charges. This is an indication that charges in the blend prepared without o-DCB are created faster from PCBM excitons than from polymer excitons. This behavior can be understood by considering the morphological model proposed for the PDPP5T:PC$_{71}$BM blend prepared without o-DCB by S. Kouijzer et al.[184] They found that the big PCBM 'blobs' are embedded in a polymer rich matrix, but within this matrix are much smaller PCBM domains. The fast charge creation from PCBM excitons is probably due to these smaller PCBM domains and due to PCBM excitons created close to the surface of the big PCBM blobs. Most of the PCBM excitons created within the large PCBM domains will not contribute to charge generation, since the radii of the domains are much longer than the average exciton diffusion length of around 10 nm. As already discussed in section 5.4 time-resolved photoluminescence measurements on the two blend systems are also indicating that most of the PCBM excitons created in the big PCBM domains will not reach the polymer/PCBM interface to undergo charge transfer and they will hence not contribute to the observed TA signals. Thus, most of the charge-induced absorption signal most likely originates from charges created by charge transfer from excitons generated on the smaller PCBM domains within the polymer rich matrix. In the vis-NIR pump-probe spectrum of the blend prepared without o-DCB after 45 ps (figure 51b, red curve) the spectral shape coming from charge-induced absorption is quite pronounced. The GSB in the visible region has decayed less than in the pump-probe spectrum in figure 51a after 45 ps, where we excited at 700 nm. This is due to the fact that the GSB tracks the evolution of all excited states on the polymer. PCBM excitons which undergo charge separation at the interface will contribute not only ultrafast, but also with a time delay to the total number of excited states on the polymer by generating holes on the polymer via charge transfer at the D/A interface. Hence, the decay of the GSB will be delayed when the blend is excited at 420 nm, in contrast to the seemingly continuous decay of the GSB

when the blend is excited at 700 nm. After 4 ns (green curve) most of the excited states are triplet excitons. The spectrum after 4 ns is very similar to the spectrum obtained by 700 nm excitation after 4 ns presented in figure 51a.

Now, we will take a closer look at the early time (ps-ns) vis-NIR pump-probe spectra of the more efficient PDPP5T:PC$_{71}$BM blend prepared with o-DCB. Figure 52a depicts the pump-probe spectra upon excitation at 700 nm. It is striking, that in the visible pump-probe spectra the absorption peak between 800 and 850 nm that we attributed to electro-absorption (EA) is much more pronounced than in the less efficient blend prepared without o-DCB. Furthermore, the GSB is longer lived than in the blend prepared without o-DCB. After 4 ns (green curve) there is still around 60 % of the initial signal amplitude (black curve, after 0.5 ps) left. In addition, in the PIA measurement shown in figure 52c the EA feature around 825 nm is more pronounced than in the PIA measurement of the less efficient blend (compare figure 51c). These observations show that charge separation is more efficient in the blend prepared with o-DCB and that excited states live longer in this blend leading to a better device performance, because free charges have more time to be extracted in an organic solar cell device under operating conditions. The pump-probe vis-NIR spectrum after 0.5 ps (figure 52a) shows a broad and unstructured PA which we assign to singlet excitons. The feature originating from EA between 800 and 850 nm is already visible, but not as pronounced as after 45 ps (red curve). After 45 ps the PA in the NIR wavelength region shows mainly the spectral shape of charges, confirming our assignment of the absorption feature around 825 nm to EA. Furthermore, the GSB only slightly decays from 0.5 to 45 ps, indicating that most of the singlet excited states created on the PDPP5T polymer undergo efficient charge separation at the interface of the blend prepared with o-DCB. After 4 ns however, the GSB has decayed by around 40 % and also the charge peak around 1450 nm has decreased, but is still visible together with the triplet exciton peak around 1200 nm. Hence, we observe the formation of triplet excitons not only in the less efficient blend prepared without o-DCB, but also in the more efficient blend prepared with o-DCB, but it seems that charges are longer lived and probably also created in a higher yield in the blend prepared with o-DCB.

When we excite the PDPP5T:PC$_{71}$BM blend prepared with o-DCB mainly on the PCBM by using 420 nm for the visible and 520 nm for the NIR measurements (figure 52b) the spectral evolution differs clearly from the other pump-probe data that we discussed so far. Here, the GSB does not decay over time, but it is increasing from 0.5 to 45 ps and even up to 4 ns. This means, as mentioned earlier, that PCBM excitons first have to diffuse to the polymer/PCBM interface before

excited states such as charges can be created on the polymer that then will contribute to the GSB signal.

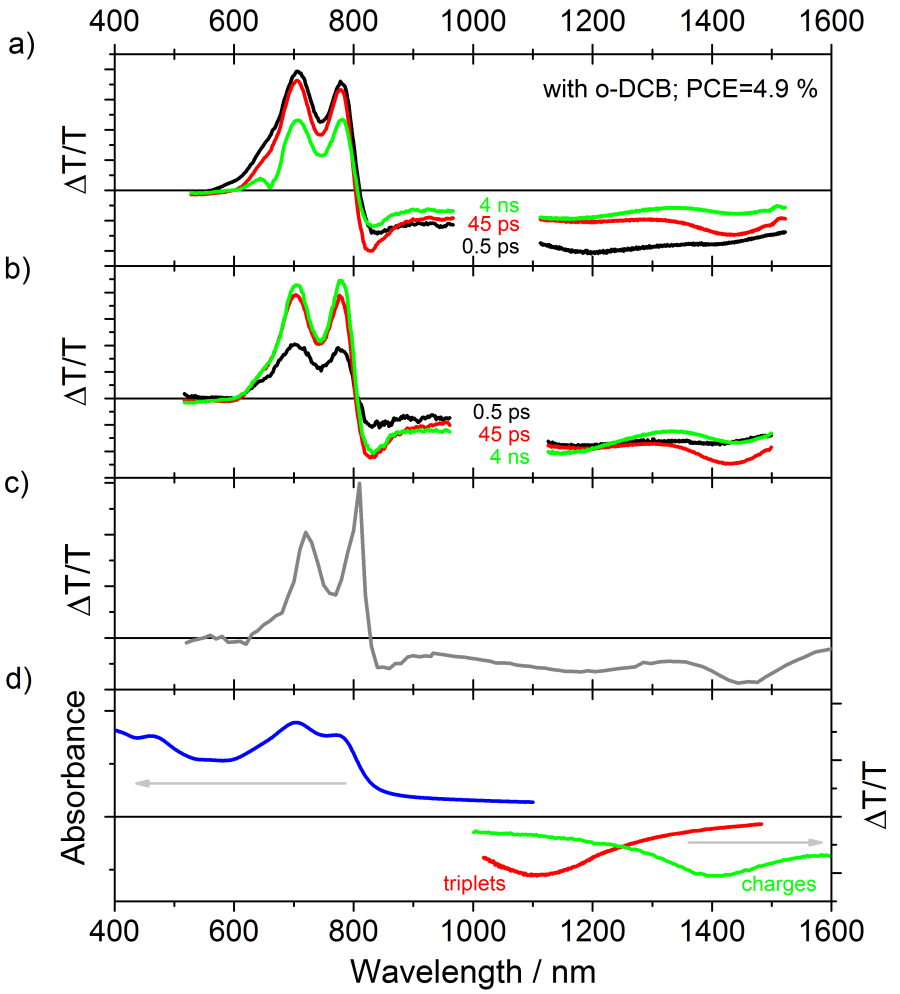

Figure 52: (a) ps-ns broadband transient absorption spectra of a 1:2 (w/w) PDPP5T:PC$_{71}$BM blend prepared with o-DCB excited at 700 nm and measured in the visible (500-1000 nm) and NIR (1100-1500 nm) at delay times of 0.5 ps (black), 45 ps (red) and 4 ns (green). The pump fluence at 700 nm was 5.5 µJ cm^{-2} for the visible and 3.1 µJ cm^{-2} for the NIR measurements. (b) ps-ns broadband transient absorption spectra of a 1:2 (w/w) PDPP5T:PC$_{71}$BM blend prepared with o-DCB excited at 420 nm and measured in the visible (500-1000 nm) and excited at 520 nm and measured in the NIR (1100-1500 nm) at delay times of 0.5 ps (black), 45 ps (red) and 4 ns (green). The pump fluence at 420 nm was 11.3 µJ cm^{-2} for the visible and 4.4 µJ cm^{-2} for the NIR measurements with an excitation wavelength of 520 nm. (c) Quasi-steady-state PIA spectrum of a 1:2 (w/w) PDPP5T:PC$_{71}$BM blend prepared with o-DCB at 80 K excited at 808 nm. (d) Steady-state absorption spectrum of a 1:2 (w/w) PDPP5T:PC$_{71}$BM blend prepared with o-DCB (blue), triplet-induced absorption spectrum (red) obtained on a palladium-tetraanthraporphyrin-doped PDPP5T film (compare section 5.6.2), charge-induced absorption spectrum (green) obtained on a PDPP5T film oxidized by iodine vapor (compare section 5.6.1).

After 0.5 ps the PA signal in the NIR wavelength range (figure 52b) exhibits the rather broad and unstructured shape that we already attributed to singlet excitons earlier. In line with the temporal evolution of the spectra in the visible, the spectra of the PA in the NIR measurements do not significantly decay, but stay rather constant. Nonetheless, there is a transformation from one species to the other perceptible as the spectral shapes change over time. From 0.5 to 45 ps there is a transformation from singlet excitons to charges and triplets apparent as the spectrum after 45 ps (figure 52b, red curve) holds spectral features of both charge-induced and triplet-induced absorption. After 4 ns the contribution of triplet excitons to the PA has risen, while the contribution of charge carriers has fallen. The conversion of charges to triplet-excited states seems to be an efficient process in this blend prepared with o-DCB as the height of the GSB, which is an indicator for the total number of excited states on the polymer, has only slightly decreased from 45 ps to 4 ns.

5.7.2 *Triplet-state formation by non-geminate recombination of charges on the sub-ns timescale*

After having discussed the early time (ps-ns) pump-probe spectra of PDPP5T:PC$_{71}$BM blends in the previous section, we will now focus on the dynamics of the excited states on the ps-ns timescale. We have seen that in the NIR pump-probe spectra there is always an overlay of spectra from different excited states, namely singlet excitons, charges and triplet excitons. Therefore, it is difficult to extract the pure kinetics of one of these excited states by just tracking the temporal evolution in a certain wavelength range, since there would always be an additional contribution from another excited state. In order to overcome this problem and to get as pure dynamics of the excited states as possible we conducted MCR analysis on the raw early time (ps-ns) pump-probe data. We did the MCR analysis on the whole fluence series using the separately determined charge-induced and triplet-induced absorption spectra as input parameters (compare section 5.6). The results of the MCR analysis are presented in figure 53 and 54 as the fluence dependence of the normalized dynamics of singlet excitons (black), charges (green) and triplet excitons (red) on the ps-ns time scale. Figure 53a shows the dynamics of the excited states in a PDPP5T:PC$_{71}$BM blend film after excitation at 700 nm. The dynamics are fluence dependent. At the highest laser fluence of 16.2 µJ cm^{-2} the decay of the singlet exciton signal is the fastest (light gray line), while at the lowest fluence of 1.6 µJ cm^{-2} (black line) the exciton decay is the slowest. Within one nanosecond all the singlet excitons in the sample have either decayed to the ground state (GS) or been quenched at the polymer/fullerene interface. The lifetime of the exciton signal seems to be similar to the lifetime of singlet excitons of around 78 ps deter-

mined from the mono-exponential fit of the singlet-exciton-induced absorption in the pristine PDPP5T blend (compare section 5.5). This indicates that the majority of singlet excitons is not quenched in the polymer:PCBM blend, but rather decays to the GS before reaching the interface.

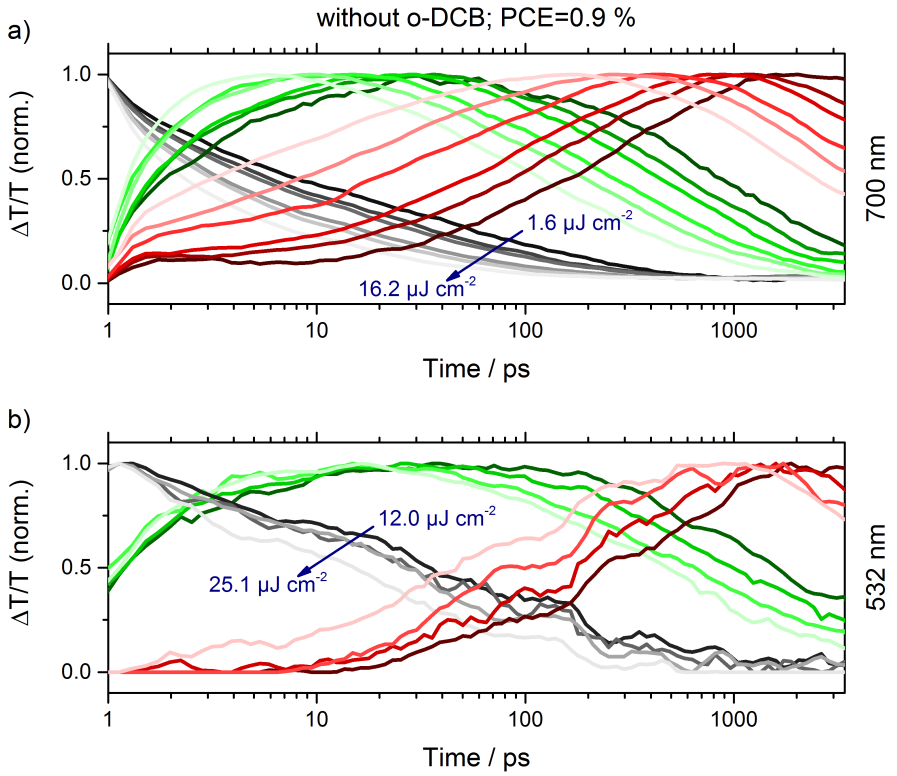

Figure 53: (a) Fluence dependence of the early time (ps-ns) dynamics of singlet excitons (black), charges (green) and triplet excitons (red) in a PDPP5T:PC$_{71}$BM blend prepared without o-DCB after excitation at 700 nm obtained by MCR analysis using the separately determined charge-induced and triplet-induced absorption spectra as input parameters (compare section 5.6). (b) Fluence dependence of the early time (ps-ns) dynamics of singlet excitons (black), charges (green) and triplet excitons (red) in a PDPP5T:PC$_{71}$BM blend prepared without o-DCB after excitation at 532 nm obtained by MCR analysis using the separately determined charge-induced and triplet-induced absorption spectra as input parameters (compare section 5.6).

The dynamics of charges (green) are also fluence dependent. The charge generation is fastest at the highest fluence, where the maximum value of created charges is reached at around 6 ps. At the lowest fluence the maximum value of created charges is reached after roughly 30 ps. From the maximum values onward charges recombine and the decay dynamics are fluence dependent, indicating that charges recombine to a great extent non-geminately. Already at early times, within 1 ps after laser excitation, there is a triplet exciton sig-

nal (red curves). These signals grow over time and reach their maximum values between 200 and 1100 ps depending on the respective fluences. The rise of the triplet signals is not as sharp as the rise of the charge signal and the maximum population of triplets is reached a few hundred picoseconds after the maximum population of charges is reached. These findings indicate that there are two mechanisms leading to the formation of triplet-excited states on the polymer: A) Triplets are created on the fs-ps timescale probably via singlet fission or intersystem crossing. B) Triplet states are created on the ps-ns timescale via non-geminate recombination of free charges. At the end of our measurement window at delay times longer than 1 ns there is the onset of a fluence dependent decay of triplet excitons visible. Due to the high number of excited states in the sample and the multitude of generation and recombination events it is not possible to globally fit the data with a consistent model. From a detailed qualitative analysis of the data it is however possible to extract sufficient information about the nature of the excited state dynamics.

Upon excitation of the PDPP5T:PC$_{71}$BM blend prepared without o-DCB at 532 nm a higher fraction of ultrafast charge carrier generation is observed as there is already 50 % of the total population of charges present immediately after excitation (green curves, figure 53b). This finding goes in line with the observations we made from the corresponding pump-probe spectra in the previous subsection. The rise of the charge signal does not exhibit a very pronounced dependence on fluence, but this might also be the case, because the laser fluence was only varied between 12.0 and 25.1 µJ cm^{-2} in these experiments. The decay of charges however is clearly fluence dependent, as is the rise of triplet excitons (red curves). Upon excitation at 532 nm, when we create mainly excited states on the PCBM domains, no triplet excitons are present shortly after excitation as was the case upon excitation at 700 nm. These findings support the assumption of the two mechanisms of triplet state creation presented in the previous paragraph: When we create mainly PCBM excitons we do not see an early onset of triplet state creation via fast singlet fission, simply because we did not create sufficient excitons on the polymer to observe this effect. However, the majority of triplet states seems to be created via non-geminate recombination of charges, since both the charge recombination and the triplet formation dynamics are fluence dependent and occur on a similar timescale from tens to hundreds of picoseconds.

Figure 54a displays the fluence dependent dynamics of the excited states in the PDPP5T:PC$_{71}$BM blend prepared with o-DCB upon excitation at 700 nm. Also in these measurements the decay of singlet excitons is fluence dependent, but the decay of excitons is one order of magnitude faster than in the blend prepared without o-DCB, with all excitons having decayed within 100 ps. Quenching of excitons cre-

ated on the polymer is much more efficient in the blend prepared with o-DCB, which also leads to more efficient solar cell devices. It seems that after 200 ps the signal of singlet excitons is rising again. This might be caused by an artefact from the MCR analysis, due to the shape of the triplet-induced absorption spectrum in the spectrum of the singlet-induced absorption intermingling with the dynamics of the singlet excitons.

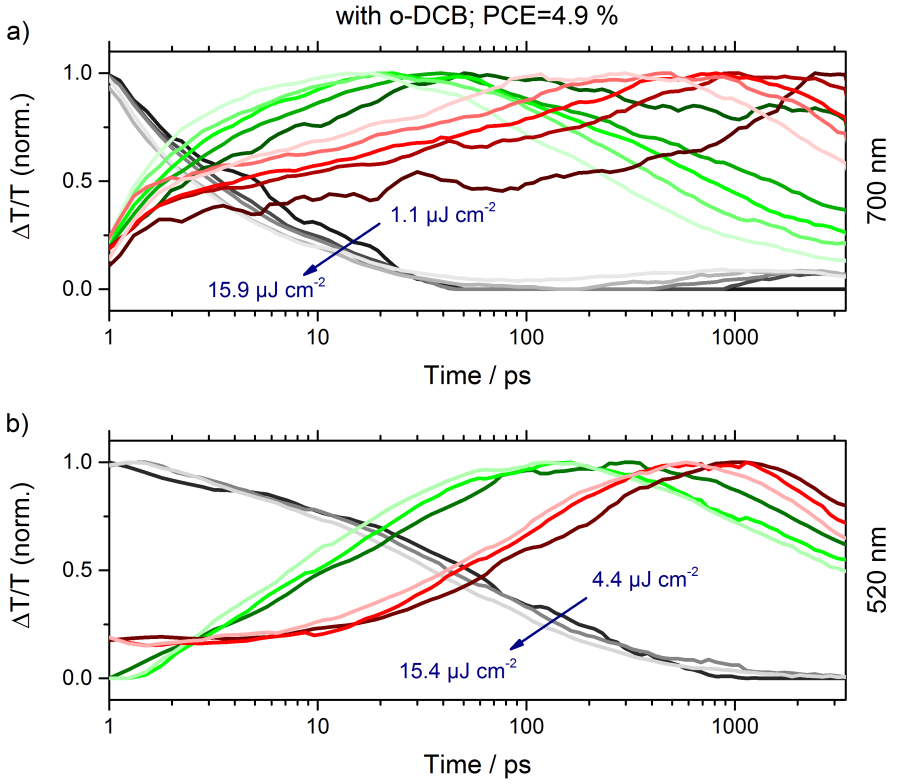

Figure 54: (a) Fluence dependence of the early time (ps-ns) dynamics of singlet excitons (black), charges (green) and triplet excitons (red) in a PDPP5T:PC$_{71}$BM blend prepared with o-DCB after excitation at 700 nm obtained by MCR analysis using the separately determined charge-induced and triplet-induced absorption spectra as input parameters (compare section 5.6). (b) Fluence dependence of the early time (ps-ns) dynamics of singlet excitons (black), charges (green) and triplet excitons (red) in a PDPP5T:PC$_{71}$BM blend prepared with o-DCB after excitation at 520 nm obtained by MCR analysis using the separately determined charge-induced and triplet-induced absorption spectra as input parameters (compare section 5.6).

The dynamics of charges and triplet excitons look similar to the dynamics observed in the blend prepared without o-DCB. Some amount of charges and triplet excitons are created on an ultrafast timescale within less than 1 ps. The majority of charges however is created within 10 to 50 ps after excitation depending on the laser fluence. The fluence dependent signals of triplet excitons reach their maximum

values within 200 ps to 2 ns after photoexcitation. The complete process of charge and triplet recombination cannot be monitored on the ps-ns timescale. We will discuss long delay (ns-µs) pump-probe data showing the complete charge and triplet recombination dynamics in the next section.

The excited state dynamics of a PDPP5T:PC$_{71}$BM blend prepared with o-DCB upon laser excitation at 520 nm is shown in figure 54b. Immediately after laser excitation a triplet-induced absorption signal is observed, but no charge-induced absorption signal is present. The charge signals rise slowly and reach their respective maximum values depending on the fluences within 100 to 300 ps after laser excitation, that is 90 to 250 ps later than upon laser excitation at 700 nm, confirming our observation already made in the previous subsection on the ps-ns pump-probe spectra, that charge generation from PCBM excitons is delayed by diffusion. The fluence dependent rise of the triplet-induced absorption signal is, as a result, also slower and the corresponding maximum values are reached between 600 ps and 1 ns. These observations are confirming our prior hypothesis that triplet state formation on the PDPP5T polymer is a result of fast singlet fission, intersystem crossing and non-geminate recombination of free charges. Interestingly, in this measurement there is already a contribution from triplet excitons immediately after excitation, a feature that we did not observe in the measurements of the blend prepared without o-DCB upon excitation at 532 nm (compare figure 53b). It might be that the fraction of PDPP5T excitation and hence also the triplet state formation via singlet fission and intersystem crossing is higher in the blend prepared with o-DCB. This observation is consistent with the steady-state absorption spectra of the two blend systems (compare figure 51d and 52d, blue curves), which show a higher PCBM absorbance in relation to the PDPP5T absorbance in the PDPP5T:PC$_{71}$BM blend prepared without o-DCB compared to the absorbance of the PDPP5T:PC$_{71}$BM blend prepared with o-DCB.

5.8 CHARGE AND TRIPLET EXCITON RECOMBINATION ON THE NS-TIMESCALE

After having discussed the transient absorption pump-probe spectra and the exciton and charge carrier dynamics on the ps-ns time scale in the previous section, we will now turn to the long delay (ns-µs) TA data to get a complete picture of the charge and triplet exciton recombination dynamics occurring on the nanosecond timescale. Figure 55a and 56a display the ns-µs vis-NIR transient absorption spectra of the PDPP5T:PC$_{71}$BM blend systems prepared with and without o-DCB respectively, while figure 55b and 56b show the corresponding fluence dependent kinetics of charges (green) and triplet excitons (red) obtained by MCR analysis.

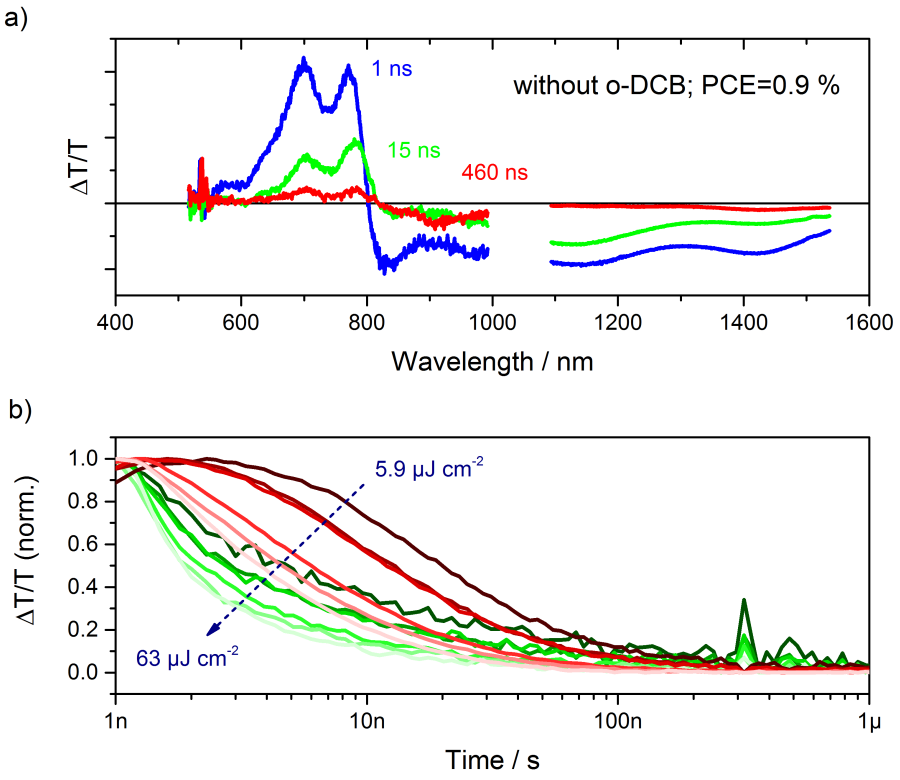

Figure 55: (a) ns-µs broadband transient absorption spectra of a 1:2 (w/w) PDPP5T:PC$_{71}$BM blend prepared without o-DCB excited at 532 nm and measured in the visible (500-1000 nm) and NIR (1100-1500 nm) at delay times of 1 ns (blue), 15 ns (green) and 460 ns (red). The pump fluence at 532 nm was 20.7 µJ cm^{-2} for the visible and 5.9 µJ cm^{-2} for the NIR measurements. (b) Fluence dependence of the ns-µs dynamics of charges (green) and triplet excitons (red) in a PDPP5T:PC$_{71}$BM blend prepared without o-DCB after excitation at 532 nm obtained by MCR analysis without any spectra constraints.

The shape of the ns-µs vis-NIR pump-probe spectra of the PDPP5T:PC$_{71}$BM blends depicted in figure 55a and 56a is similar to the shape

of the early time (ps-ns) vis-NIR pump-probe spectra discussed in the previous section. There is a positive GSB signal from 600 to 800 nm and a negative PA signal which extends from 800 nm to 1500 nm and to longer wavelengths than measured in these experiments. In the TA spectrum of the less efficient blend prepared without o-DCB (figure 55a) after 1 ns (blue) there is, in addition to the GSB, a pronounced EA feature around 825 nm. As we have discussed earlier this is an indication of charge-transfer states being present in the sample. In the NIR region there are two pronounced absorption peaks discernible at around 1150 and 1400 nm. We attributed these absorption features to triplet states and charges, respectively. Both absorption peaks as well as the GSB and the EA feature decay over time. After 15 ns more than 50 % of the initial GSB signal has decayed and the EA feature has almost completely vanished. This is an indication that most of the interfacial charge-transfer states have decayed after 15 ns and that the remaining charges are mostly free charges, which do not give rise to a Stark-Effect (EA) signal. The charge-induced absorption feature has decayed more in relation to the triplet-induced absorption feature. After 460 ns (red) almost all the signals have vanished. There is only a small GSB signal and a residual charge-induced absorption signal left. The fluence dependent dynamics of charges and triplet states obtained by MCR analysis depicted in figure 55b complement our observations made from the pump-probe spectra. Charges (green) and triplet-excited states (red) show fluence dependent decays. The decay of charges is steeper at the beginning, while for the lowest fluence of $5.9\,\mu J\,cm^{-2}$ the triplet state signal still rises until 2 ns. The decay of triplet states is also highly fluence dependent, but not as steep as the decay of charge carriers. That is, because triplet states are continuously created from the recombination of free charge carriers as long as there are still free charge carriers present in the sample. In contrast, the pool of free charges is not refilled after all excitons have decayed to the GS or been quenched into charges after 1 ns. We assume, as mentioned earlier, that on the ps-ns timescale triplet states are created via non-geminate recombination of free charges. The triplet states in turn are most likely to decay via triplet-triplet annihilation and triplet-charge annihilation, since the decay of the triplet-induced absorption is fluence dependent and cannot be described by a single exponential or power law decay. After 1 µs all the signals have completely vanished.

The ns-µs TA data of the more efficent PDPP5T:$PC_{71}BM$ blend prepared with o-DCB shown in figure 56 are similar to the TA data of the blend prepared without o-DCB. In the spectrum after 1 ns (blue curve, figure 56a) we observe the two distinct PA peaks from triplets around 1150 nm and charges around 1450 nm which both decay over time, leaving a residual charge signal after 460 ns (red) behind. The GSB and the EA signals decay from 1 to 460 ns, but the EA feature is still

visible after 15 ns (green), which was not the case for the less efficient blend, indicating that charge-transfer states live longer in the more efficient blend.

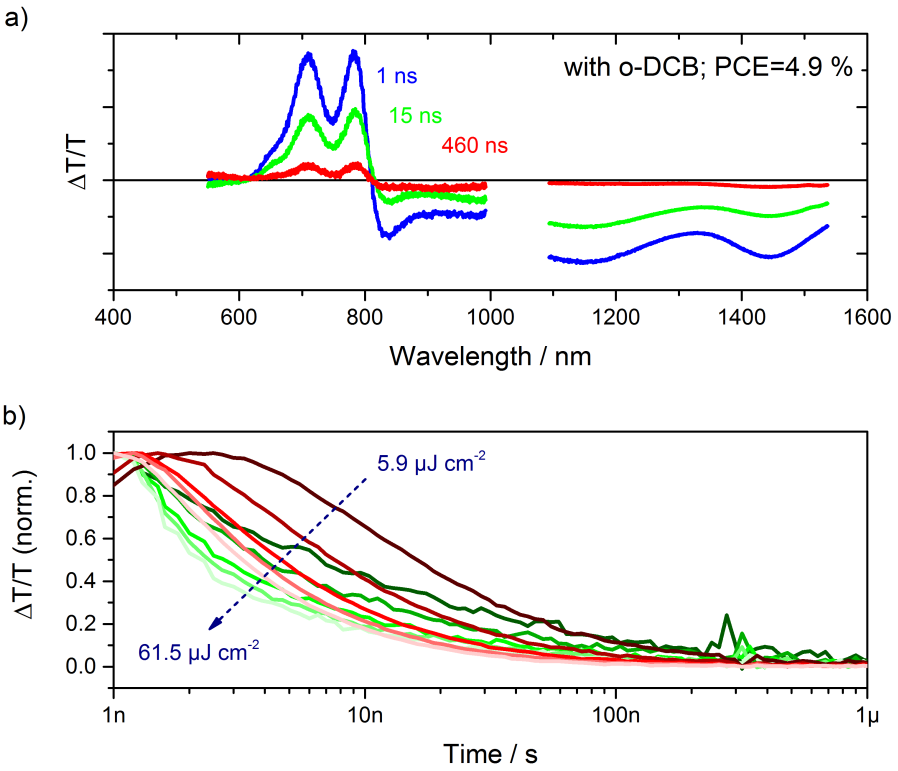

Figure 56: (a) ns-µs broadband transient absorption spectra of a 1:2 (w/w) PDPP5T:PC$_{71}$BM blend prepared with o-DCB excited at 532 nm and measured in the visible (500-1000 nm) and NIR (1100-1500 nm) at delay times of 1 ns (blue), 15 ns (green) and 460 ns (red). The pump fluence at 532 nm was 10.4 µJ cm^{-2} for the visible and 5.9 µJ cm^{-2} for the NIR measurements. (b) Fluence dependence of the ns-µs dynamics of charges (green) and triplet excitons (red) in a PDPP5T:PC$_{71}$BM blend prepared with o-DCB after excitation at 532 nm obtained by MCR analysis without any spectra constraints.

The dynamics of charges and triplet states in the PDPP5T:PC$_{71}$BM blend prepared with o-DCB are also fluence dependent (figure 56b). Interestingly, the charge carriers in this more efficient blend are not considerably longer lived than charge carriers in the less efficient blend. Also in the blend prepared with o-DCB the charge and triplet state signals have vanished within 1 µs, which is quite fast for a blend system that exhibits power conversion efficiencies of around 5 % in a photovoltaic device. In other polymer:PCBM systems charges are rather long lived with charge signals extending to 10 µs.[191, 193, 192] It might be that this efficient triplet state creation that we observe in the PDPP5T:PC$_{71}$BM blend systems is not an issue in a solar cell device under solar illumination of 1 sun, because charge pairs might be extracted before they can recombine at the interface and subsequently

form triplet states on the polymer. Furthermore the short charge carrier lifetimes in combination with the high FF of 0.67 and the high power conversion efficiency of 4.9 % is an indication that charge carrier mobility is high in the PDPP5T:$PC_{71}BM$ blend system. It might be that in a device under operating conditions the competition of charge recombination at the interface and extraction of charges at the electrodes shifts in favor of the latter, leading to well performing solar cell devices. In the next section we will show experiments to determine the charge carrier mobility in the PDPP5T polymer, which are indeed pointing to a comparably high hole mobility in this DPP-type polymer.

In summary, charge generation and triplet state formation as well as charge recombination and triplet-state recombination dynamics in the PDPP5T:$PC_{71}BM$ systems prepared with and without o-DCB are quite similar. Although, these excited-state dynamics are similar the power conversion efficiencies diverge with 0.9 % for the device prepared without o-DCB and with 4.9 % for the device prepared with o-DCB. This apparent discrepancy will be discussed in more detail in the final discussion (section 8.2) by looking in more detail at the morphologies of both blend systems.

5.9 CHARGE CARRIER MOBILITY IN THE PDPP5T POLYMER

In the following two subsections we will discuss experimental results obtained by the time-of-flight (TOF) technique and by building and measuring organic field-effect transistors (OFET). We will see that the hole mobilities in the pristine PDPP5T polymer determined from the TOF and OFET measurements are high in comparison to other well studied polymers such as P3HT,[195, 187] PCPDTBT[196] or PTB7.[197] It has been shown previously for other DPP-based polymers that hole mobilities are rather high.[198, 129] This is potentially beneficial for the performance of OPV devices, since charge carrier separation and extraction might be enhanced by a higher charge carrier mobility.

5.9.1 *Field dependence of the hole mobility in pristine PDPP5T determined by the time-of-flight technique*

Figure 57 displays time-of-flight hole transients parametric in laser excitation intensity. Charge carriers, i.e. holes in the PDPP5T film were created with light intensities of $I = I_0$ (black), $I/I_0 = 73$ % (blue) and $I/I_0 = 15$ % (red).

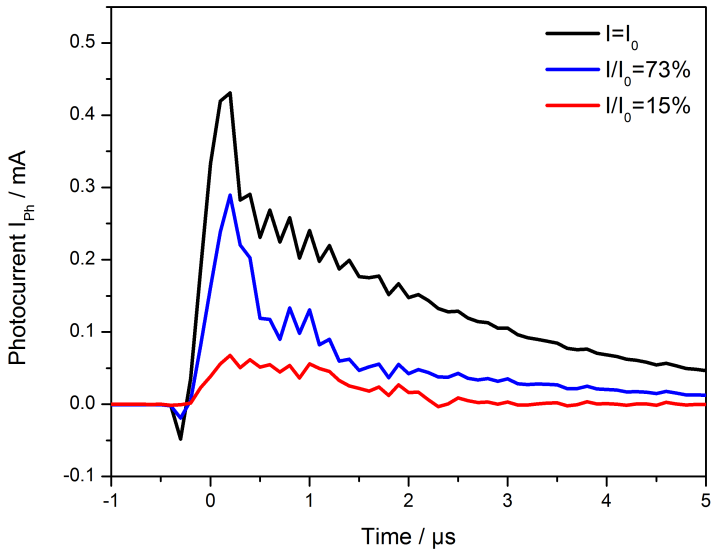

Figure 57: Light intensity dependence of Time-of-flight hole transients in pristine PDPP5T. Charge carriers in the sample were created with a maximum laser excitation intensity of I_0 (black curve) and with less intense excitations of 73 % (blue) and 15 % (red) of I_0.

The shape of the hole transients does not change for the two highest light intensities. In both cases there is an initial current spike caused by the photogeneration of charges close to the positively charged anode, followed by a current decay caused by the holes traveling through the bulk layer to the negatively charged cathode. The hole

transient for the lowest light intensity ($I/I_0 = 15$ %, red) does not exhibit such a sharp initial current spike, probably due to a lesser amount of photogenerated charges. The signals at all light intensities do not show a plateau after the initial charge-generation peak, meaning that charge transport in the PDPP5T polymer is dispersive. This is an indication that due to high structural disorder, charge transport is trap-limited in this polymer. Because of the dispersive trap-limited nature of the charge transport it is best to determine the transit time t_T of the charge carrier package by plotting the time-of-flight hole transients on a double logarithmic scale and to obtain t_T from the kink of the photocurrent transient. An exemplary TOF measurement in a double logarithmic presentation of photocurrent versus time at an electric field of $15 \cdot 10^4$ V cm^{-1} is shown in figure 58.

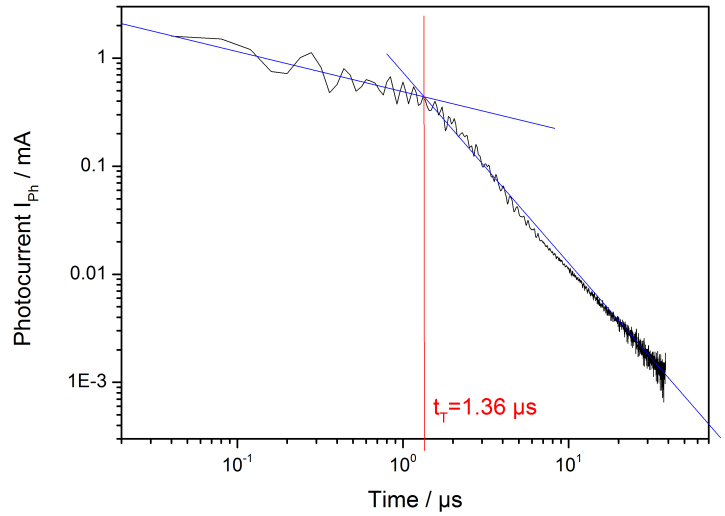

Figure 58: Exemplary Time-of-flight hole transients in pristine PDPP5T at an applied field of $15 \cdot 10^4$ V cm^{-1}.

The position of the kink from which we obtain the transit time was determined by fitting two lines to the data and taking the transit time from the crossing point of the two lines. In this case the transit time was determined to be 1.36 µs. In all the measurements at various electric fields there was a defined kink in the double-logarithmic representation, from which it was possible to determine t_T. From the transit-time t_T the charge-carrier mobility can be calculated, using the following relation

$$\mu = \frac{d^2}{V \times t_T} \tag{54}$$

where d is the diode layer thickness and V is the voltage applied at the diode's electrodes. Table 2 gives an overview of the obtained hole mobilities at different applied voltages. In addition the resulting electric field F in the diode, its square root $F^{1/2}$ and the transit time t_T are given in this table.

Table 2: Applied voltage V, electric field F, its squareroot $F^{1/2}$, transit time t_T and the hole-mobility μ_H obtained for a 3.7 µm thick sample.

Voltage (V)	F (V cm^{-1})	$F^{1/2}$ (V$^{1/2}$ cm$^{-1/2}$)	t_T (µs)	μ_H (cm^2 V^{-1}s^{-1})
15	4.09×10^4	202.2	192	4.67×10^{-5}
20	5.45×10^4	233.5	71	9.47×10^{-5}
25	6.82×10^4	261.1	24	2.24×10^{-4}
30	8.18×10^4	286	8.8	5.1×10^{-4}
35	9.54×10^4	309	4.8	7.94×10^{-4}
40	10.91×10^4	330.2	3.2	1.1×10^{-3}
45	12.27×10^4	350.3	2.4	1.23×10^{-3}

The dependence of the obtained hole mobilities on the applied electric field is plotted in figure 59. At small electric fields (200-290 V cm^{-1}) the dependence of the hole mobility on the electric field is linear in the semi-logarithmic plot, showing a Poole-Frenkel-type field dependence $\ln\mu_H \propto F^{1/2}$ as expected for charge carrier transport in an amorphous solid, whereas at higher electric fields (300-360 V cm^{-1}) the data does not show a linear behavior anymore. The reason for this non-linear behavior at high electric fields might be, that at higher electric fields and hence shorter transit times we approach the RC-limit of this TOF-setup.

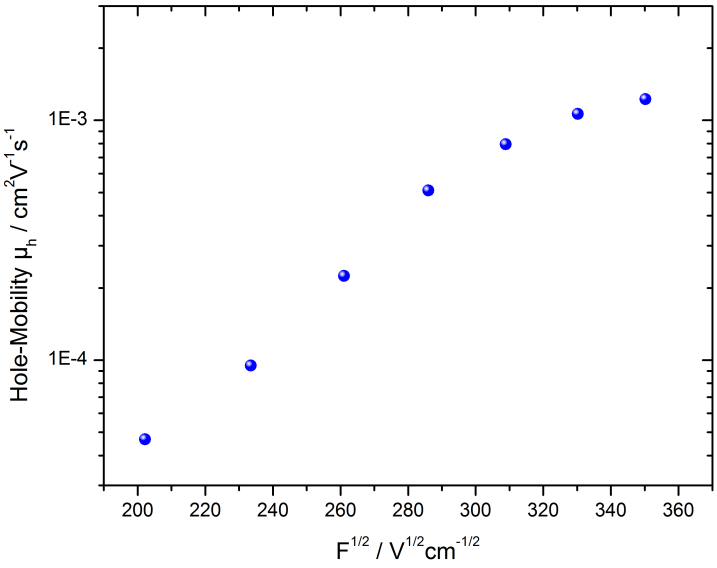

Figure 59: Field dependence of the hole mobility in pristine PDPP5T.

The values for the hole-mobility vary between 4.67×10^{-5} for the lowest and 1.23×10^{-3} cm^2 V^{-1}s^{-1} for the highest applied electric field. The sample was not annealed for any of the measurements. The values determined for the hole-mobility are significantly higher than the values determined for regioregular P3HT by Mauer et al.[187], which

do not exceed $5 \times 10^{-4}\,cm^2\,V^{-1}s^{-1}$. Furthermore the hole-mobilities of P3HT were shown to be independent of the electric field, whereas hole-mobilities in PDPP5T are field dependent.

5.9.2 *Influence of the annealing temperature on the field-effect mobility in pristine PDPP5T*

Organic field-effect transistors (OFET) have been built to study the field effect mobility in pristine PDPP5T. The schematic layout of such an OFET device is shown in figure 60.

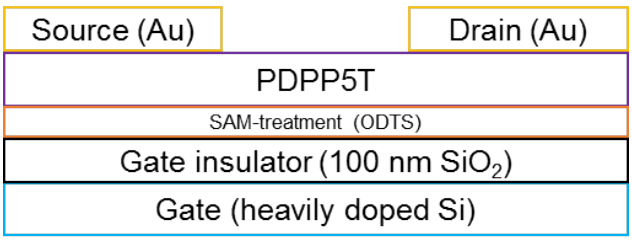

Figure 60: Schematic layout of the organic field-effect transistor devices.

A heavily doped silicon wafer covered by a 100 nm thermally grown SiO_2 dielectric layer was used as the gate substrate. The substrate was successively cleaned in piranha solution, deionized water, acetone, and propyl alcohol for 30, 15, 10, and 10 min, respectively. After the cleaning process and drying, the sample was covered by a self-assembled mono-layer (SAM) of octadecyltrichlorosilane (ODTS). In order to create the SAM, the substrate and a small vial containing 15 mg ODTS were put into a petri dish, which was covered by aluminum foil and put into a vacuum oven. The pressure of the vacuum oven was carefully adjusted to the boiling point of ODTS and the temperature was set to 100 °C for two hours. Subsequently the temperature was slowly cooled down to room temperature. The polymer PDPP5T was spincoated onto the substrates under nitrogen atmosphere from a 7 mg/mL solution of chloroform at 1000 rpm. Samples were either not annealed or annealed for 30 min at 80, 120, 160, and 200 °C, respectively. As source and drain electrodes 70 nm thin Au layers were evaporated through a shadow mask at a rate of 1 Å/s. The channel width was 2600 µm and the channel length was 200 µm. The samples were measured under nitrogen atmosphere with a semiconductor parametric analyzer (Agilent 4155C) in the saturation regime, where the drain-source voltage V_{DS} was −30 V. In the saturation regime, where $V_{DS} > V_{GS} - V_{th}$, with V_{GS} being the gate-source voltage and V_{th} being the threshold voltage, the following relation between the drain-source current I_{DS} and V_{GS} is valid:

$$I_{DS} = \frac{W}{2L} C_i \mu (V_{GS} - V_{th})^2 \tag{55}$$

Where W and L are the channel width and length, respectively, C_i is the capacitance and μ is the mobility. Equation 55 can be rewritten in the form

$$I_{DS}^{1/2} = \left(\frac{W}{2L} C_i \mu\right)^{1/2} V_{GS} - \left(\frac{W}{2L} C_i \mu\right)^{1/2} V_{th} \tag{56}$$

that establishes a simple linear relation between $I_{DS}^{1/2}$ and V_{GS} from which the mobility μ can be obtained.

Figure 61 shows the drain-source current I_{DS} versus gate-source voltage V_{GS} transfer characteristics of as cast and annealed OFET devices based on PDPP5T (dots and lines) and their $I_{DS}^{1/2}$ versus V_{GS} characteristics (dashed lines) with the corresponding fits (solid red lines) to the data.

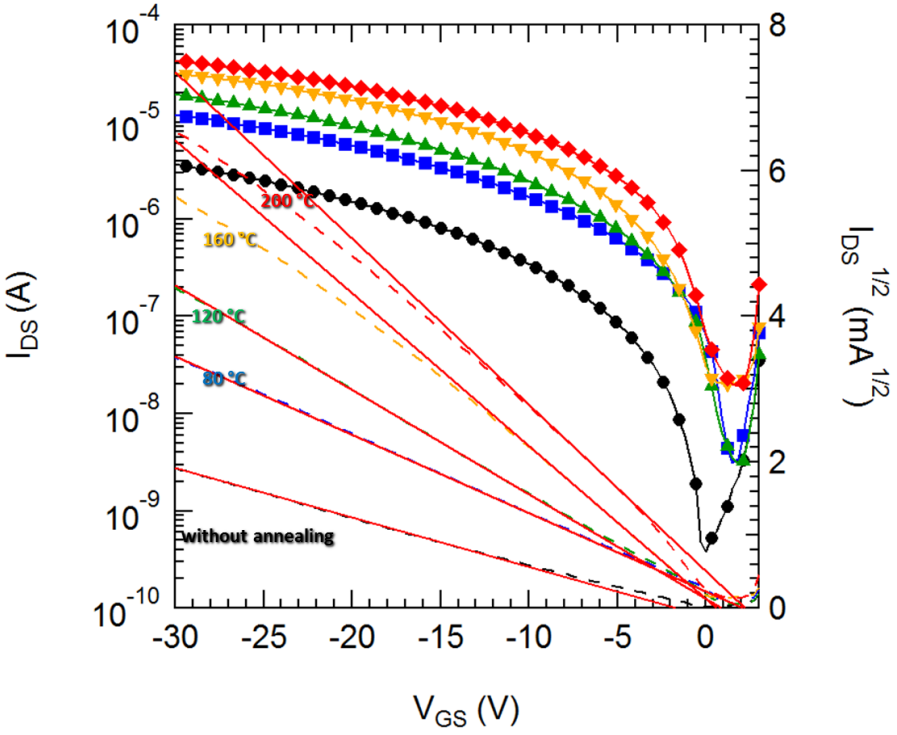

Figure 61: Drain-source current I_{DS} versus gate-source voltage V_{GS} transfer characteristics of as cast and annealed OFET devices based on PDPP5T (dots and lines) and their $I_{DS}^{1/2}$ versus V_{GS} characteristics (dashed lines) together with the corresponding fits (red lines) to the data. The data of the as-cast device is shown in black. The annealing temperatures were 80 °C (blue), 120 °C (green), 160 °C (yellow), and 200 °C (red).

The effect of the annealing temperature on the transfer characteristics is obvious: with increasing annealing temperature the drain-source current I_{DS} increases. Also the slope of the data in the $I_{DS}^{1/2}$ versus V_{GS}-representation and hence the mobility values increase. Table 3 lists the values of the hole-mobility μ_H, the threshold volt-

Table 3: Hole-mobility μ_H, threshold voltage V_{th}, and on-off ratio I_{on}/I_{off} determined for OFET devices in the saturation regime at a drain-source Voltage V_{DS} of −30 V before and after annealing for 30 min at 80, 120, 160, and 200 °C.

annealing temperature	μ_H ($cm^2\,V^{-1}s^{-1}$)	V_{th} (V)	I_{on}/I_{off}
RT	0.02	-1.70	1.06×10^4
80	0.05	2.13	2.66×10^4
120	0.09	0.86	1.59×10^4
160	0.20	0.61	6.32×10^4
200	0.23	2.21	4.51×10^4

age V_{th}, and the on-off ratio I_{on}/I_{off} for the OFET devices in dependence of the annealing temperature. The values for the hole-mobility increase from 0.02 $cm^2\,V^{-1}s^{-1}$ for the as-cast device to 0.23 $cm^2\,V^{-1}s^{-1}$ for the OFET device annealed at 200 °C. The increase in mobility with each step of increase in annealing temperature is enormous. With every step from room temperature to 160 °C the mobility values are increased by a factor of about two. However, in the last step from 160 °C to 200 °C the mobility is increased by 15 % only. It seems that by thermally annealing the thin PDPP5T polymer film, the polymer transforms from an amorphous to a more crystalline state and hence the mobility increases with increasing crystallinity. However, at annealing temperatures higher than 160 °C the degree of crystallinity of the polymer probably reaches its maximum and hence the mobility does not significantly increase anymore. The obtained values for the field effect mobility of holes are quite high. But we note, that Yi et al. obtained even higher hole-mobilities of 0.36 to 1.24 $cm^2\,V^{-1}s^{-1}$ for a structurally similar polymer with a similar molecular weight of $M_n = 44$ kg mol^{-1}, but with β-unsubstituted quinquethiophene (5T) units.[199]

5.10 CONCLUSIONS

We have demonstrated, that the photovoltaic performance of PDPP5T:$PC_{71}BM$ bulk heterojunction solar cells are strongly influenced by the processing conditions. When the active layer is spincast from chloroform as the only solvent a PCE of 0.9 % is obtained. However, when a solvent mixture of chloroform and o-DCB (9:1 v/v) is used the PCE drastically increases to 4.9 %. The change in photovoltaic performance is reflected in the surface morphology determined by AFM. In the samples prepared without o-DCB big PCBM domains are formed embedded in a polymer rich matrix, while when o-DCB is added as a cosolvent the surface morphology is rather fine grained, indicating that the polymer and the PCBM are more intimately mixed forming a nanoscale morphology that is favorable for device performance.

Time-resolved photoluminescence (TR-PL) measurements have shown that the majority of excitons created on the big PCBM domains in the sample prepared without o-DCB do not reach the D/A interface, since the fitted lifetime of ~ 620 ps approaches the mean lifetime of pure PCBM (~ 630 ps). However, in the sample prepared with o-DCB a mean PCBM lifetime of ~ 205 ps was determined, indicating that more of the excitons are quenched at the interface.

The exciton lifetime in pristine PDPP5T is rather small with an inverse rate of ~ 105 ps determined from TR-PL measurements and ~ 78 ps determined from TA pump-probe spectroscopy. In pristine PDPP5T we observed the formation of triplet states, which decay with an inverse rate of ~ 81 ns as determined by TA spectroscopy. These triplet states are probably created via singlet fission.

With a combination of PIA spectroscopy, vis-NIR transient absorption spectroscopy and multivariate curve resolution analysis of the raw TA data we further studied the photophysics of the PDPP5T:$PC_{71}BM$ blends prepared with and without o-DCB. Although the solar cells built with these blends differ substantially in their photovoltaic efficiency, we observe in both blends the formation of triplet states on the sub-ns timescale. The recombination of charge carriers and the formation of triplets are both strongly intensity dependent. Hence, we suggest that triplet state formation in the PDPP5T:$PC_{71}BM$ upon laser excitation occurs via non-geminate recombination of charges into the ^{3}CT state and subsequent relaxation to the triplet state T_1 on the polymer. Since, we observe an almost quantitative triplet state formation in both the less well and the better performing blend systems, we assume that triplet-state formation is rather a small issue in solar cell devices under operating conditions. In an operating solar cell with electrodes, the recombination of charges is in kinetic competition with the extraction of charges. Most likely under AM 1.5G conditions, this competition is shifted in favor of the latter.

In addition, the high hole mobilities observed in the pristine PDPP5T polymer most likely enhance the probability of electron-hole encounter at the interface, leading to fast sub-ns non-geminate recombination of free charges. At the same time a high charge carrier mobility is also beneficial for device performance, as charges can efficiently diffuse and drift to the applied electrodes in order to contribute to the photocurrent.

6

TUNING REDUCTIVE AND OXIDATIVE PHOTOINDUCED ELECTRON TRANSFER IN AMIDE-LINKED ANTHRAQUINONE-PORPHYRIN-FERROCENE ARCHITECTURES

The following article was published in *European Journal of Inorganic Chemistry* and is reprinted with permission from Melomedov et al.[14]

My contribution to this work are pages 125-127 (pp 1997-1999), presenting the results of time-resolved transient absorption spectroscopy of selected compounds.

EurJIC European Journal of Inorganic Chemistry
ChemPubSoc Europe
FULL PAPER

DOI:10.1002/ejic.201400118

Tuning Reductive and Oxidative Photoinduced Electron Transfer in Amide-Linked Anthraquinone–Porphyrin–Ferrocene Architectures

Jascha Melomedov,[a] Julian Robert Ochsmann,[b] Michael Meister,[b] Frédéric Laquai,[b] and Katja Heinze*[a]

Keywords: Electron transfer / Density functional calculations / Substituent effects / Porphyrinoids / Quinones

Porphyrin amino acids **3a**–**3h** with *meso* substituents Ar of tunable electron-donating power (Ar = 4-C_6H_4O*n*Bu, 4-C_6H_4OMe, 4-C_6H_4Me, Mes, C_6H_5, 4-C_6H_4F, 4-$C_6H_4CF_3$, C_6F_5) have been linked at the N terminus to anthraquinone Q as electron acceptor through amide bonds to give Q-P^{Ar} dyads **4a**–**4h**. These were conjugated to ferrocene Fc at the C terminus as electron donor to give the acceptor-chromophore-donor Q-P^{Ar}-Fc triads **6a**–**6h**. To further modify the energies of the electronically excited and charge-separated states, the triads **6a**–**6h** were metallated with zinc(II) to give the corresponding Q-(Zn)P^{Ar}-Fc triads **Zn-6a**–**Zn-6h**. The Q-P^{Ar1} dyad (Ar^1 = C_6H_5) was further extended with a second porphyrin P^{Ar2} (Ar^2 = 4-C_6H_4Me) as well as appended to a ferrocene to give the tetrad Q-P^{Ar1}-P^{Ar2}-Fc **9**. Almost all the conjugates show strongly reduced fluorescence quantum yields and excited-state lifetimes, which has been interpreted as photoinduced electron transfer (PET) either from the excited porphyrin to the quinone (oxidative PET) or from the ferrocene to the excited porphyrin (reductive PET). Electrochemical data, absorption spectroscopy, steady-state emission, time-resolved fluorescence, transient absorption pump-probe spectroscopy as well as DFT calculations have been used to elaborate the preferred PET pathway (reductive vs. oxidative PET) in these architectures with systematically varied electron-donating substituents at the central chromophore.

Introduction

Photoinduced electron transfer (PET) is a key step in natural photosynthesis.[1] For a deeper understanding of photosynthetic processes such as sunlight energy collection, light-energy storage, light-to-chemical energy conversion, electron-transport pathways and finally the efficient utilisation of sunlight, a number of elegant functional artificial reaction centres have been designed and intensively investigated to gain an increasingly clear picture of the important processes.[2–7] The rational design of reaction centres to mimic the multistep downhill electron transfer is theoretically based on the Marcus theory of electron transfer (ET)[8] and experimentally relies on the availability of suitable building blocks that can be assembled at will. Artificial reaction centres consist of non-covalently or covalently linked donor–acceptor units with quinones (natural acceptors),[3] porphyrins[4] or fullerenes[5] acting as electron acceptors and porphyrins,[6] ferrocene[5e–5i,7] or carotenoid polyenes[6] acting as electron donors. A variety of quinone–porphyrin[3] (Q-P) and porphyrin–ferrocene (P-Fc) systems[5e–5i,7] have been investigated with respect to PET, proving very useful for fundamental PET research and potential applications. Furthermore, several other metal complexes have been attached to porphyrins as electron-accepting units.[9] Variation of Q has allowed the effect of exothermicity on the rates of electron transfer to be studied in considerable detail[3c,3e] and variation of Fc substituents has shown that energy- and electron-transfer pathways depend on the oxidation potential of the ferrocene.[10] Elaborated C_{60}-P_n-Fc architectures feature long-lived charge-separated states.[5e–5h] In C_{60}-(Zn)P_n-Fc conjugates with C_{60} as the electron acceptor, the first PET typically is the thermodynamically favourable oxidative quenching of the excited porphyrin by the fullerene followed by a thermal shift of charge from the ferrocene to the central porphyrin.[5e–5h] The effect of the number of porphyrins sandwiched between C_{60} and ferrocene has also been thoroughly investigated.[5e–5h] In systems containing both Fc and Q, the preference of the initial photoinduced electron-transfer step is ambiguous as the free energies for both steps are of a similar magnitude.

To the best of our knowledge, systems combining the electron-accepting features of quinones, the light-absorbing properties of porphyrin chromophores and the electron-donating properties of ferrocene derivatives have not yet been studied with respect to either the preferred PET pathways

[a] Institute of Inorganic and Analytical Chemistry, Johannes Gutenberg University of Mainz,
Duesbergweg 10–14, 55128 Mainz, Germany
E-mail: katja.heinze@uni-mainz.de
http://www.ak-heinze.chemie.uni-mainz.de/
[b] Max Planck Institute for Polymer Research,
Ackermannweg 10, 55128 Mainz, Germany
Supporting information for this article is available on the WWW under http://dx.doi.org/10.1002/ejic.201400118.

EurJIC European Journal of Inorganic Chemistry www.eurjic.org FULL PAPER

or the tuning of PET pathways by modifying the excited-state energies of the central chromophore in a systematic manner with Fc donor and Q acceptor levels held at a fixed energy.

Linking reaction centre components through amide bonds has considerable advantages, namely a rather rigid connectivity of the building blocks,[11,12] a defined directional design in linear arrays (N terminus→C terminus) and a simple orthogonal modification at the termini with electron donors and acceptors. Furthermore, oligoamide synthesis can be conveniently accomplished by using solid-phase synthesis methods.[13]

We have previously reported suitable building blocks for directional oligoporphyrin amides, namely porphyrin amino acids with a *trans*-AB_2C substitution pattern (Scheme 1).[11,14] These porphyrin amino acids feature electron-donating mesityl, phenyl and electron-withdrawing fluorinated aryl groups at the *meso* positions (Ar = Mes, C_6H_5, 4-C_6H_4F, 4-$C_6H_4CF_3$, C_6F_5).[6c,11,14] More strongly electron-donating substituents such as Ar = 4-C_6H_4OR have not been studied. The key building blocks used in this study are porphyrin amino acids P^{Ar} and their esters with a full range of Ar substituents, anthraquinone-2-carboxylic acid Q as the electron acceptor and aminoferrocene Fc-NH_2 as the electron donor.[15]

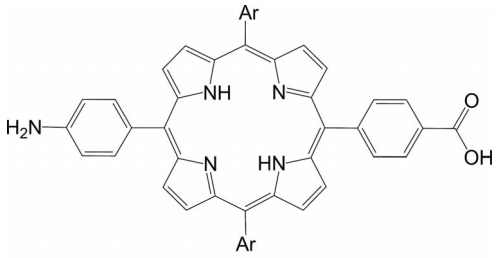

Ar = 2,4,6-$C_6H_2Me_3$, C_6H_5, 4-C_6H_4F, 4-$C_6H_4CF_3$, C_6F_5

Scheme 1. Porphyrin amino acid building blocks.

Herein we report 1) the synthesis and properties of new *trans*-AB_2C-substituted porphyrin amino acid esters with electron-donating *meso* substituents Ar = 4-C_6H_4O*n*Bu, 4-C_6H_4OMe, 4-C_6H_4Me and C_6H_5[14] (**3a**, **3b**, **3d**, **3e**) and their corresponding *N*-acetyl-protected derivatives (**Ac-3a**, **Ac-3b**, **Ac-3d**, **Ac-3e**) as building blocks and reference compounds, 2) the coupling of eight *trans*-AB_2C-substituted porphyrin amino acid building blocks P^{Ar} with varying electron-withdrawing power (Ar = 4-C_6H_4O*n*Bu, 4-C_6H_4OMe, 4-C_6H_4Me, Mes, C_6H_5, 4-C_6H_4F, 4-$C_6H_4CF_3$, C_6F_5) to anthraquinone-2-carboxylic acid Q to give Q-P^{Ar} dyads (**4a**–**4h**), 3) the amide coupling of Fc-NH_2 to Q-P^{Ar} to give Q-P^{Ar}-Fc triads (**6a**–**6h**) and metallation with zinc(II) to give Q-(Zn)P^{Ar}-Fc triads (**Zn-6a**–**Zn-6h**), 4) the (formal) extension of the triad Q-P^{Ar1}-Fc (Ar^1 = C_6H_5) with an additional porphyrin amino acid P^{Ar2} (Ar^2 = 4-C_6H_4Me) to furnish the tetrad Q-P^{Ar1}-P^{Ar2}-Fc (**9**) and 5) the examination of initial charge separation pathway preferences in dyads **4**, triads **6** and **Zn-6** as well as in tetrad **9** with fixed acceptor (Q) and donor (Fc) levels, namely oxidative (P^{Ar} to Q) versus reductive (Fc to P^{Ar}) PET with respect to the substituent Ar, by electrochemical methods, absorption spectroscopy, steady-state emission, time-resolved fluorescence, transient absorption spectroscopy as well as by DFT calculations.

The results of this work will be of considerable value to the rational design of artificial photosynthetic systems that feature multistep electron transfer by well-defined efficient single-electron transfer and charge-shift steps. Through our design strategy it is easy to tune the individual energy levels of the chromophore radical ions relative to the acceptor and donor levels. This versatile modular design will allow the construction of even larger arrays with predefined sequences and excited-state energy levels.

Results and Discussion

Synthesis and Characterisation of Building Blocks 3, Dyads 4, Triads 6 and Zn-6, and Tetrad 9

In addition to the recently reported *trans*-AB_2C porphyrin amino acids P^{Ar}[11,14] with Ar = Mes (**3c**), C_6H_5 (**3e**), 4-C_6H_4F (**3f**), 4-$C_6H_4CF_3$ (**3g**) and C_6F_5 (**3h**), substituents with a greater electron-donating power are required for a comprehensive study. Hence, three novel *trans*-AB_2C-substituted porphyrin[16] amino acid esters[11,14] with electron-releasing *meso* substituents [Ar = 4-C_6H_4O*n*Bu (**3a**), 4-C_6H_4OMe (**3b**), 4-C_6H_4Me (**3d**)] were synthesised following a Lindsey-type 2+2 condensation procedure[17] employing nitro- and ester-substituted phenyldipyrromethanes.[18] The nitro functional group was reduced to the amine by reduction with tin(II) chloride in hydrochloric acid to obtain the porphyrin amino acid esters **3a**, **3b** and **3d** (see the Supporting Information). As the optical properties of amines are strongly pH-dependent and the oxidation of amines is often irreversible, *N*-acetyl-protected reference compounds **Ac-3a**, **Ac-3b**, **Ac-3d** and **Ac-3e** as well as their corresponding Zn^{II} complexes **Zn-Ac-3a**, **Zn-Ac-3b**, **Zn-Ac-3d** and **Zn-Ac-3e** were synthesised following established procedures (see the Supporting Information).[11,19]

The eight porphyrin amino acid esters **3a**–**3h**, with Ar exhibiting increasing electron-withdrawing power, were coupled to anthraquinone-2-carboxylic acid (as electron acceptor) after activating the latter as the acid chloride by reaction with thionyl chloride to give the Q-P^{Ar} dyads **4a**–**4h** (Scheme 2). Cleavage of the methyl ester by using aqueous KOH in methanol/THF delivered the quinone-porphyrin acids **5a**–**5g**, respectively (Scheme 2). The base-catalysed cleavage of dyad **4h** also led to the nucleophilic aromatic substitution of fluoride in the electron-poor aryl substituents by methoxide (Ar = C_6F_5→Ar = 4-C_6F_4OMe) to give acid **5i**. Therefore to obtain **5h** from **4h**, an acid-catalysed hydrolysis protocol needed to be employed (Scheme 2). Quinone-porphyrin-ferrocene triads Q-P^{Ar}-Fc (**6a**–**6i**) were assembled by activation of the acid groups in **5a**–**5i** as acid chlorides by using thionyl chloride and coupling with aminoferrocene[15] (as electron donor). The quin-

EurJIC European Journal of Inorganic Chemistry www.eurjic.org FULL PAPER

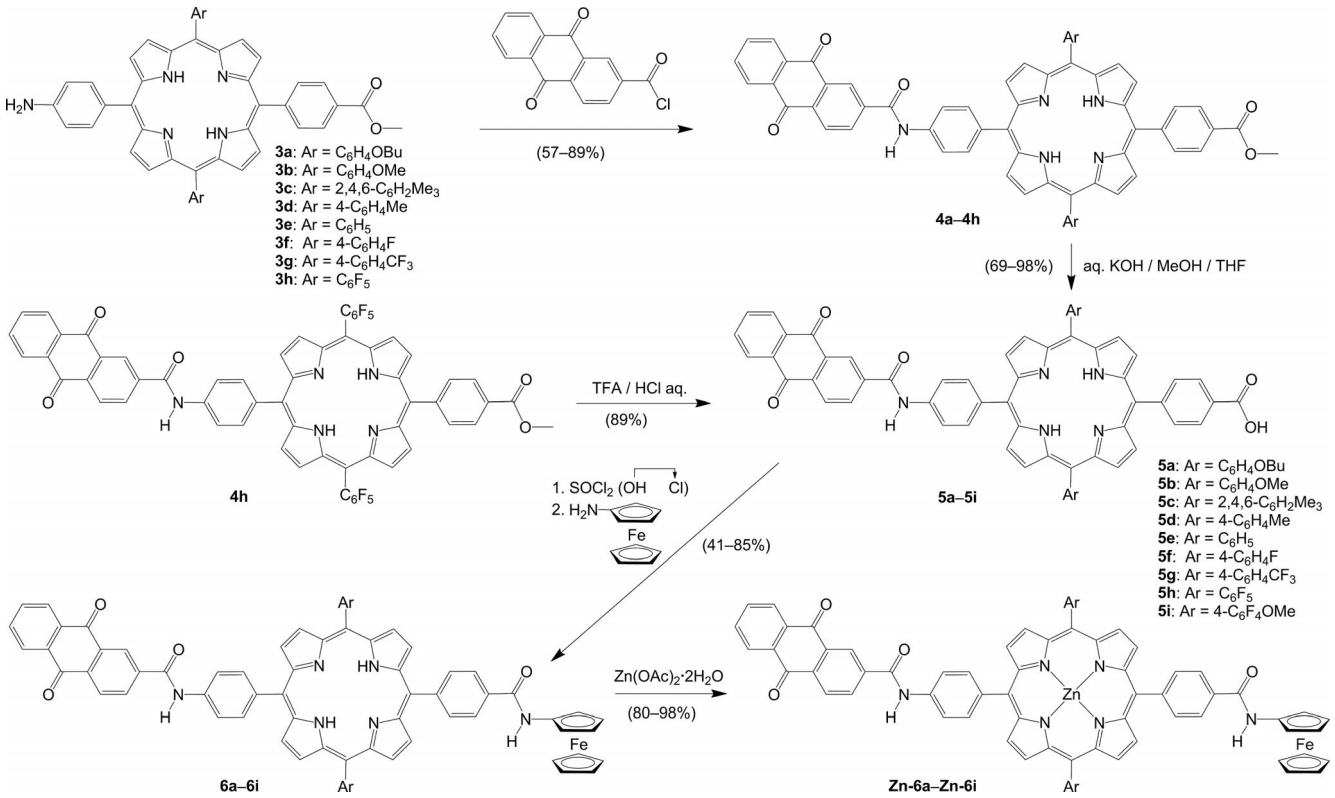

Scheme 2. Synthesis of dyads **4a**–**4h** and triads **6a**–**6i** and **Zn-6a**–**Zn-6i**.

one-(Zn)porphyrin-ferrocene triads Q-(Zn)P^{Ar}-Fc (**Zn-6a**–**Zn-6i**) were obtained from the free base triads **6a**–**6i** by metallation with zinc(II) acetate dihydrate (Scheme 2).

The construction of the Q-P^{C6H5}-P^{C6H4Me}-Fc tetrad **9** is depicted in Scheme 3. Q-P acid **5e** was coupled to porphyrin amino acid ester **3d** (activated as the acid chloride by using thionyl chloride) to give the Q-P^{C6H5}-P^{C6H4Me} triad **7**. The ferrocene entity was attached to **7** through an amide bond after base-catalysed methyl ester cleavage (to give free acid **8**, see the Supporting Information). Subsequent formation of the acid chloride and coupling with aminoferrocene gave the target tetrad **9**. The quinone reference *N*-ethylanthraquinone-2-carboxylic acid amide **10** as well as the bis(porphyrin) reference P^{C6H5}-P^{C6H4Me} **11** were synthesised as described in the Supporting Information.

The correct formation of all monoporphyrins **3**, the dyads **4**, the triads **6**, **Zn-6** and **7**, the tetrad **9**, the quinone reference compound **10** and the bis(porphyrin) reference **11** was substantiated by multinuclear NMR spectroscopy (^{1}H, ^{13}C, ^{19}F), IR and UV/Vis spectroscopy as well as (high-resolution) mass spectrometry (see the Supporting Information). In all cases the mass spectra show the signals expected for the intact porphyrin and porphyrin conjugates. In the ^{1}H NMR spectra, successful amide formation is clearly indicated by the disappearance of the amine proton resonances of **3a**–**3h** at δ = 4.99 ppm and the appearance of the amide resonances of dyads **4a**–**4h** at δ = 10.30–10.40 ppm. The covalent attachment of the ferrocene by amide coupling to the dyads **4** was confirmed by observing a second amide proton resonance at δ = 9.19–9.29 ppm in the ^{1}H NMR spectra of **6a**–**6h**. The presence of three NH amide resonances at δ = 9.21, 10.21 and 10.33 ppm demonstrates the successful synthesis of tetrad **9**. The resonances corresponding to the quinone and ferrocene moieties in the dyads, triads and tetrads further prove the integrity of the oligoamides. Metallation of triads **6** with Zn^{II} resulted in the expected changes in the porphyrin resonances, such as the disappearance of the pyrrole NH resonances. For the Q-(Zn)P dyads featuring an azomethine linker, the quinone proton resonances are reported to be shifted to a higher field. This has been rationalised by the coordination of the quinone carbonyl oxygen atom to the Zn^{II} centre.[3m] The Q proton resonances of the Q-Zn(P)-Fc triads **Zn-6** are not shifted, and hence a Zn···O=C interaction in **Zn-6** can be excluded. Possibly for the reported Q-Zn(P) dyads, a Zn···$N_{azomethine}$ interaction seems to be more likely than Zn···$OC_{quinone}$ coordination.[3m]

Absorption and Emission of Dyads 4, Triads 6 and Zn-6, and Tetrad 9

The absorption data for the dyads, triads, tetrad and reference compounds are presented in Table 1. The absorption spectra of **4a**–**4h**, **6a**–**6h** and **Zn-6a**–**Zn-6h** are essentially identical to those of the corresponding reference porphyrins **Ac-3a**–**Ac-3h** and **Zn-Ac-3a**–**Zn-Ac-3h**. As a result of the low extinction coefficients of *N*-ethylanthraquinone-2-carb-

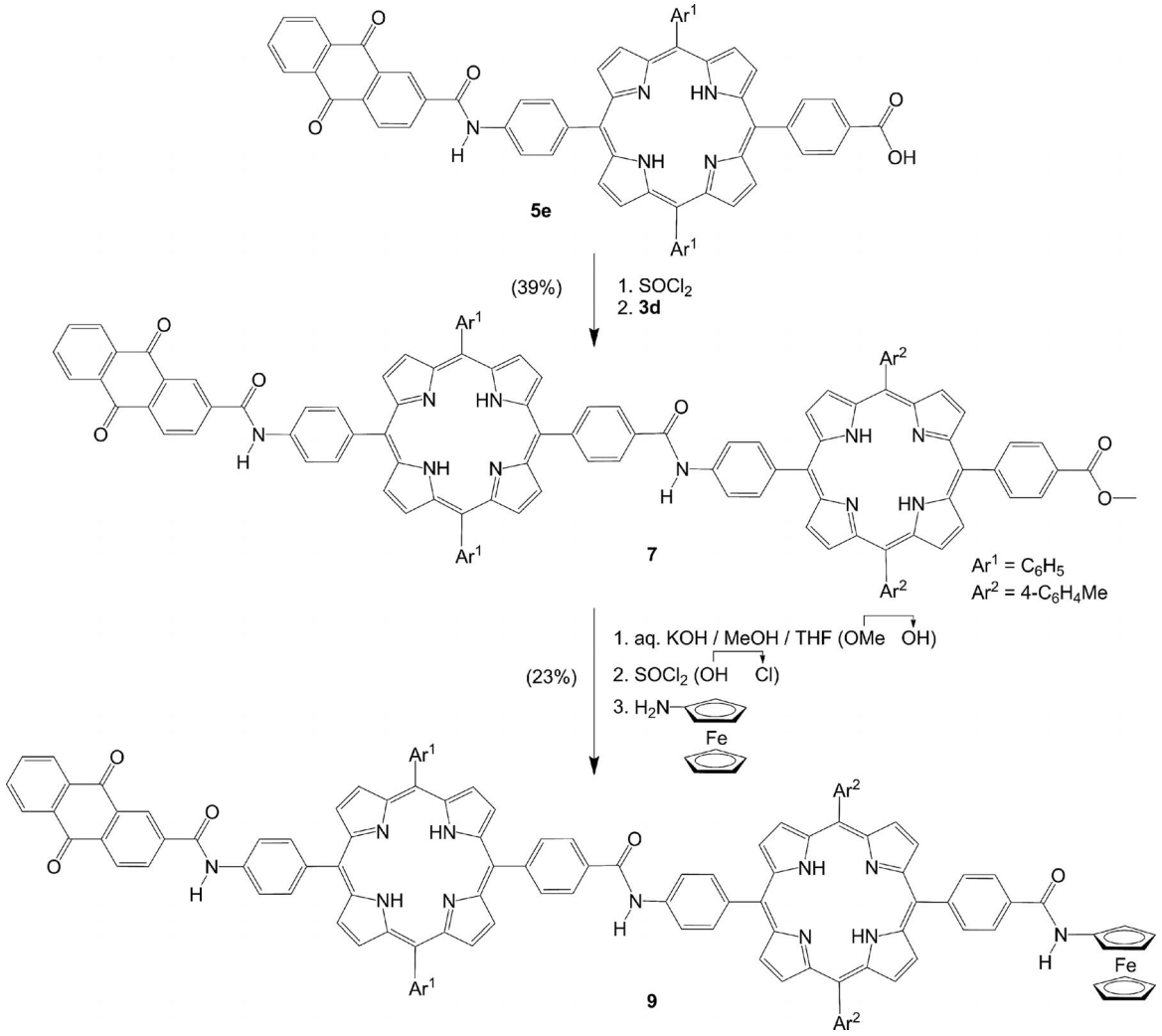

Scheme 3. Synthesis of tetrad **9**.

oxylic acid amide **10** (λ_{max} = 328 nm, ε = 5300 $M^{-1}cm^{-1}$) and 1-(acetylamino)ferrocene (Fc-NHAc; λ_{max} = 441 nm, ε = 215 $M^{-1}cm^{-1}$),[15] no absorption bands from these chromophores are discernible in the absorption spectra of the dyads and triads. The shapes and intensities of the Soret bands relative to their Q bands remain unaffected after the linking of quinone and ferrocene to the porphyrin core (Figure 1 and the Supporting Information). A slight blue shift of the porphyrin Soret and porphyrin Q bands is observed within the Q-P series **4a**→**4h** and Q-P-Fc series **6a**→**6h** due to the increasing electron-withdrawing character of *meso*-aryl substituents Ar. Neither new charge-transfer bands[20] nor perturbations of the porphyrin absorption bands were detected, which indicates only a weak ground-state electronic interaction between the quinone or the ferrocene with the central porphyrin. The Q-(Zn)P^{Ar}-Fc triads **Zn-6a**–**Zn-6h** show a small bathochromic shift (1–4 nm) of porphyrin absorbance bands in comparison with the corresponding reference porphyrins **Zn-Ac-3a**–**Zn-Ac-3h** (Figure 1 and Table 1).

Figure 2 shows the absorption spectra of triad Q-P^{C6H5}-P^{C6H4Me} (**7**), tetrad Q-P^{C6H5}-P^{C6H4Me}-Fc (**9**) and reference dyad P^{C6H5}-P^{C6H4Me} (**11**). Appending a quinone or a ferrocene to the bis(porphyrin) core does not alter the absorption spectrum, similarly to the monoporphyrin conjugates. Furthermore, the absorption spectra of the bis(porphyrins) **7**, **9** and **11** are nearly identical to those of the constituent porphyrins **Ac-3d** and **Ac-3e** and exhibit no splitting of the Soret or Q bands.[11] In summary, the absorption spectra are essentially a superposition of the individual unperturbed spectra of the building blocks.

The fluorescence data, quantum yields and the excited-state lifetimes of the new porphyrin amino acid esters **3a**, **3b**, **3d** and **3e**, and the reference porphyrins **Ac-3a**, **Ac-3b**, **Ac-3d**, **Ac-3e**, **Zn-Ac-3a**, **Zn-Ac-3b**, **Zn-Ac-3d**, **Zn-Ac-3e** and bis(porphyrin) **11** are collected in Table 2. As discussed previously[11] for related porphyrins, a small hypsochromic shift of the emission band is observed in the series **Ac-3a**→**Ac-3b**→**Ac-3d**→**Ac-3e** and **Zn-Ac-3a**→**Zn-Ac-3b**→**Zn-Ac-3d**→**Zn-Ac-3e**.

EurJIC European Journal of Inorganic Chemistry www.eurjic.org FULL PAPER

Table 1. Absorption data for **Ac-3a**–**Ac-3h**, **Zn-Ac-3a**–**Zn-Ac-3h**, **4a**–**4h**, **6a**–**6i**, **Zn-6a**–**Zn-6i**, **7**, **9** and **11** in CH_2Cl_2 at room temperature.

	Ar	λ [nm] (ε [10^{-4} м$^{-1}$ cm^{-1}])				
		Soret	$Q_y(1,0)$	$Q_y(0,0)$	$Q_x(1,0)$	$Q_x(0,0)$
Ac-3a	C_6H_4O*n*Bu	422 (30.03)	517 (1.14)	555 (0.73)	593 (0.63)	649 (0.65)
4a	C_6H_4O*n*Bu	422 (32.44)	518 (1.36)	555 (0.84)	593 (0.49)	649 (0.47)
6a	C_6H_4O*n*Bu	422 (36.31)	518 (1.35)	555 (0.89)	593 (0.36)	650 (0.39)
Zn-Ac-3a	C_6H_4O*n*Bu	424 (40.10)	552 (1.75)	594 (0.65)	–	–
Zn-6a	C_6H_4O*n*Bu	425 (47.78)	552 (1.33)	594 (0.78)	–	–
Ac-3b	C_6H_4OMe	421 (35.40)	517 (1.38)	554 (0.87)	593 (0.45)	648 (0.42)
4b	C_6H_4OMe	421 (39.59)	517 (1.40)	554 (0.89)	593 (0.33)	649 (0.35)
6b	C_6H_4OMe	422 (39.19)	518 (1.67)	554 (1.11)	593 (0.69)	649 (0.53)
Zn-Ac-3b	C_6H_4OMe	424 (48.62)	551 (1.90)	593 (0.63)	–	–
Zn-6b	C_6H_4OMe	424 (51.07)	552 (1.96)	594 (0.73)	–	–
Ac-3c	Mes	420 (36.29)	516 (1.24)	550 (0.37)	593 (0.28)	652 (0.55)
4c	Mes	421 (36.33)	516 (1.55)	551 (0.68)	592 (0.34)	651 (0.56)
6c	Mes	421 (36.18)	516 (1.51)	552 (0.60)	592 (0.30)	648 (0.25)
Zn-Ac-3c	Mes	423 (45.12)	551 (1.92)	592 (0.45)	–	–
Zn-6c	Mes	424 (49.71)	552 (1.88)	594 (0.18)	–	
Ac-3d	C_6H_4Me	420 (33.60)	516 (1.27)	552 (0.71)	592 (0.39)	647 (0.35)
4d	C_6H_4Me	420 (39.00)	517 (1.93)	552 (1.26)	591 (0.85)	647 (0.82)
6d	C_6H_4Me	420 (44.69)	517 (1.72)	553 (1.57)	591 (1.12)	647 (0.61)
Zn-Ac-3d	C_6H_4Me	421 (45.15)	549 (1.82)	588 (0.46)	–	–
Zn-6d	C_6H_4Me	423 (47.02)	551 (2.02)	593 (0.75)	–	–
Ac-3e	C_6H_5	419 (32.60)	515 (1.34)	551 (0.68)	591 (0.43)	646 (0.34)
4e	C_6H_5	419 (32.25)	515 (1.34)	551 (0.69)	591 (0.42)	646 (0.36)
6e	C_6H_5	419 (35.06)	516 (1.56)	551 (0.84)	591 (0.49)	646 (0.42)
Zn-Ac-3e	C_6H_5	420 (36.10)	549 (1.63)	589 (0.48)	–	–
Zn-6e	C_6H_5	423 (38.89)	551 (1.63)	592 (0.46)	–	–
Ac-3f	C_6H_4F	419 (50.42)	515 (2.16)	551 (1.07)	591 (0.72)	647 (0.61)
4f	C_6H_4F	419 (46.25)	515 (1.96)	551 (0.98)	591 (0.59)	647 (0.45)
6f	C_6H_4F	419 (41.79)	515 (2.22)	551 (1.38)	589 (1.00)	646 (0.86)
Zn-Ac-3f	C_6H_4F	420 (41.45)	548 (1.87)	587 (0.50)	–	–
Zn-6f	C_6H_4F	422 (47.69)	551 (2.05)	593 (0.63)	–	–
Ac-3g	$C_6H_4CF_3$	419 (41.40)	515 (1.78)	550 (0.79)	590 (0.57)	646 (0.40)
4g	$C_6H_4CF_3$	419 (31.57)	515 (1.45)	549 (0.69)	591 (0.47)	649 (0.41)
6g	$C_6H_4CF_3$	419 (32.42)	515 (1.54)	551 (0.78)	590 (0.53)	646 (0.41)
Zn-Ac-3g	$C_6H_4CF_3$	420 (28.30)	548 (1.17)	588 (0.21)	–	–
Zn-6g	$C_6H_4CF_3$	423 (34.13)	552 (1.59)	593 (0.48)	–	–
Ac-3h	C_6F_5	418 (39.31)	512 (2.38)	545 (0.84)	587 (0.93)	642 (0.56)
4h	C_6F_5	418 (34.69)	512 (2.15)	546 (0.70)	588 (0.79)	642 (0.44)
6h	C_6F_5	417 (41.02)	511 (2.20)	545 (0.42)	588 (0.49)	642 (0.48)
Zn-Ac-3h	C_6F_5	422 (51.09)	552 (2.01)	593 (0.36)	–	–
Zn-6h	C_6F_5	422 (47.51)	551 (1.68)	594 (0.65)	–	–
6i	C_6F_4OMe	419 (37.03)	512 (1.87)	546 (0.45)	589 (0.48)	644 (0.11)
Zn-6i	C_6F_4OMe	423 (43.97)	552 (1.86)	592 (0.32)	–	–
11	C_6H_5/C_6H_4Me	422 (73.50)	516 (3.53)	552 (2.05)	591 (1.19)	647 (1.06)
7	C_6H_5/C_6H_4Me	422 (76.62)	516 (3.57)	552 (2.06)	591 (1.15)	647 (1.04)
9	C_6H_5/C_6H_4Me	422 (77.48)	517 (3.74)	553 (2.14)	591 (1.14)	647 (1.02)

The emission spectra of selected dyads, triads, tetrad **9** and reference porphyrins are shown in Figures 1 and 2. Linking anthraquinone to porphyrins **3** and **Zn-3** as well as to (bis)porphyrin **11** leads to a significant decrease in the fluorescence intensity of quinone conjugates **4** and **7** (see Tables 2 and 3). The quenching efficiency varies between 10 and 92%, which indicates the presence of a new non-radiative decay channel in the dyads, namely oxidative PET. The strongest decrease in fluorescence intensity is found for dyad **4a** with Ar = 4-C_6H_4O*n*Bu (92%, Figure 1), whereas almost no quenching at all is seen for dyad **4h** with Ar = C_6F_5 (10%, Table 2 and Table 3). As anticipated, the nature of the *meso*-aryl substituent Ar controls the efficiency of fluorescence quenching by oxidative PET. Electron-rich substituents induce stronger quenching than electron-withdrawing substituents. Only dyad **4c** with sterically demanding mesityl groups (Ar = Mes) at the *meso* positions deviates from the described trend. DFT geometry optimisations of **4c** revealed a 90° dihedral angle between the mesityl and porphyrin planes in contrast to the smaller angles observed for all other substituents (Ar = C_6F_5: 79°; all other Ar: 63–66°; see the Supporting Information). Furthermore, full rotation of a mesityl group connected to a porphyrin has an activation barrier of around 74 kJ mol^{-1} in solu-

EurJIC European Journal of Inorganic Chemistry www.eurjic.org FULL PAPER

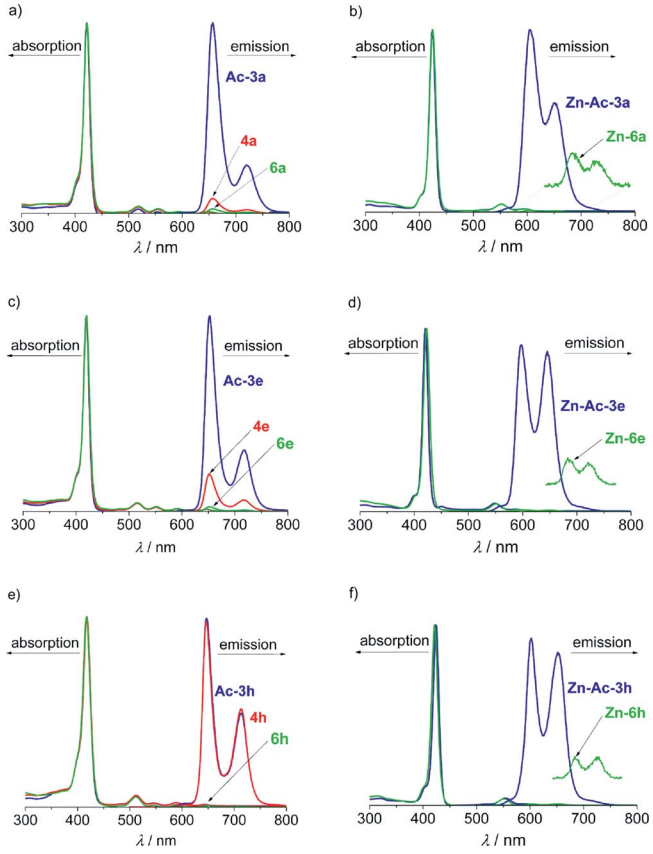

Figure 1. Normalised absorption and emission spectra of a) **Ac-3a**, **4a**, **6a**, b) **Zn-Ac-3a**, **Zn-6a**, c) **Ac-3e**, **4e**, **6e**, d) **Zn-Ac-3e**, **Zn-6e**, e) **Ac-3h**, **4h**, **6h** and f) **Zn-Ac-3h**, **Zn-6h** in CH_2Cl_2 at room temperature.

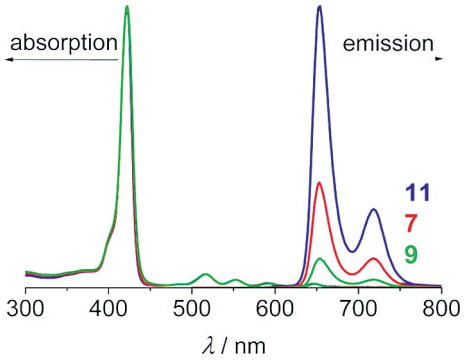

Figure 2. Normalised absorption and emission spectra of the reference compound P^{C6H5}-P^{C6H4Me} (**11**), triad Q-P^{C6H5}-P^{C6H4Me} (**7**) and tetrad Q-P^{C6H5}-P^{C6H4Me}-Fc (**9**) in CH_2Cl_2 at room temperature.

tion,[21] which also prevents the population of intermediate more co-planar conformations. Therefore the rather fixed orthogonal arrangement of the Mes substituent precludes the strong electronic influence expected from the trialkylated aryl group.

In quinone-bis(porphyrin) **7**, the emission is quenched by only 64% due to the attached quinone. From the extinction

Table 2. Emission data for porphyrins **3** and bisporphyrin **11** in CH_2Cl_2 at room temperature.

	Ar	λ [nm]		Φ	τ [ns] [a]
		Q(0,0)	Q(0,1)		
3a	C_6H_4OnBu	660	723	0.1631	n.d.[b]
Ac-3a	C_6H_4OnBu	657	720	0.1594	9.28
Zn-Ac-3a	C_6H_4OnBu	606	651	0.1003	1.71
3b	C_6H_4OMe	659	721	0.1448	n.d.[b]
Ac-3b	C_6H_4OMe	657	719	0.1348	9.49
Zn-Ac-3b	C_6H_4OMe	606	651	0.0940	1.81
3d	C_6H_4Me	657	721	0.0878	n.d. [b]
Ac-3d	C_6H_4Me	654	719	0.1311	9.69
Zn-Ac-3d	C_6H_4Me	600	646	0.0884	1.91
Ac-3e	C_6H_5	652	717	0.1167	9.88
Zn-Ac-3e	C_6H_5	597	645	0.1037	1.99
11	C_6H_5/C_6H_4Me	654	718	0.1284	9.70

[a] All decays are monoexponential; excitation wavelength λ_{exc} = 400 or 550 nm. [b] n.d.: not determined.

coefficients of the constituent porphyrins **Ac-3d** and **Ac-3e** (Table 1), it is reasonable to assume that both porphyrins in **7** are excited with nearly equal probability [ε(**Ac-3d**)/ε(**Ac-3e**) ≈ 1.03:1.00]. If energy transfer between the two porphyrins was absent, approximately 80%(**4e**)/2 = 40% quenching would be expected. The larger quenching observed suggests rapid energy transfer from the Ar = C_6H_4Me-substituted porphyrin to the Ar = C_6H_5-substituted porphyrin in **7**. The latter excited porphyrin undergoes oxidative PET to the appended quinone.

The fluorescence studies of the ferrocene conjugates **6** and **Zn-6** revealed an even stronger reduction of the emission quantum yield compared with the corresponding reference compounds **Ac-3** and **Zn-Ac-3** (Figure 1, Tables 2 and 4). The quenching of triads **6a**–**6h** and metallated triads **Zn-6a**–**Zn-6h** is almost quantitative and most of them are essentially non-fluorescent. Therefore a further efficient non-radiative decay pathway is enabled, namely reductive PET with ferrocene acting as electron donor and/or triplet energy transfer to the ferrocene.[7a,10]

To distinguish between electron and energy transfer, the emission spectra of **Ac-3a**, **4a** and **6a** (Figure 3) as well as **Ac-3h**, **4h** and **6h** were exemplarily recorded at low temperatures (300→77 K). Indeed, upon cooling, the integrated emission intensity of **6a** (×5.0) increases much more strongly than that of **Ac-3a** (×1.3) or **4a** (×1.7) (Figure 3). A similar trend is observed for the **Ac-3h** (×1.8), **4h** (×1.4), **6h** (×3.3) series. Even more pronounced is the gain in fluorescence intensity in the zinc triads **Zn-6a** (×17.5) and **Zn-6h** (×16.4) at low temperature. This supports the existence of PET pathways in triads **6** and **Zn-6** that are impeded at low temperatures.[3i] However, some residual quenching by energy transfer to ferrocene cannot be fully excluded on the basis of these data alone.

Tetrad **9** essentially shows similar emission behaviour to the triads **6**. The quantum yield of the Q-P^{C6H5}-P^{C6H4Me}-Fc conjugate **9** is decreased by 89% with respect to the

EurJIC European Journal of Inorganic Chemistry www.eurjic.org FULL PAPER

Table 3. Emission data for Q-P^{Ar} dyads **4a**–**4h** and triad **7** in CH_2Cl_2 at room temperature.

	Ar	λ [nm]		Φ	τ [ns][a]	Quenching [%]	k_{ET} [10^9 s^{-1}][d]	Φ_{ET}[e]
		Q(0,0)	Q(0,1)					
4a	C_6H_4OnBu	657	720	0.0125	0.613	92[b]	1.524	0.93
4b	C_6H_4OMe	656	720	0.0140	0.700	90[b]	1.323	0.93
4c	Mes	653	719	0.0532	1.820	32[b]	0.458	0.83
4d	C_6H_4Me	654	719	0.0161	0.942	78[b]	0.958	0.90
4e	C_6H_5	652	717	0.0230	1.370	80[b]	0.629	0.86
4f	C_6H_4F	652	717	0.0281	2.970	72[b]	0.233	0.69
4g	$C_6H_4CF_3$	652	717	0.0548	4.810	49[b]	0.108	0.52
4h	C_6F_5	647	712	0.0628	9.550	10[b]	0.003	0.03
7	C_6H_5/C_6H_4Me	653	718	0.0458	4.070	64[c]	0.143	0.58

[a] All decays are monoexponential; excitation wavelength λ_{exc} = 400 or 550 nm. [b] Relative to reference compound **Ac-3**. [c] Relative to reference compound **11**. [d] $k_{ET} = 1/\tau - 1/\tau_{ref}$. [e] $\Phi = k_{ET}\tau$.

Table 4. Emission data for triads **6a**–**6i**, **Zn-6a**–**Zn-6i** and tetrad **9** in CH_2Cl_2 at room temperature.

	Ar	λ [nm]		Φ	τ_1 [ps] (A_1 [%]); τ_2 [ps] (A_2 [%])[a,b]	Quenching [%]	k_{ET} [10^9 s^{-1}][d]	Φ_{ET}[e]
		Q(0,0)	Q(0,1)					
6a	C_6H_4OnBu	656	720	0.0042	214.99 (100)	97	4.544	0.98
6b	C_6H_4OMe	657	720	0.0034	240.54 (100)	97	4.052	0.97
6c	Mes	652	718	0.0041	272.83 (100)	94	3.574	0.97
6d	C_6H_4Me	655	720	0.0036	229.37 (100)	97	4.247	0.98
6e	C_6H_5	651	717	0.0030	164.02 (86); 644.23 (14)	97	5.996	0.98
6f	C_6H_4F	652	718	0.0025	148.07 (94); 586.62 (6)	98	6.650	0.98
6g	$C_6H_4CF_3$	652	717	0.0063	94.96 (86); 467.65 (14)	94	10.43	0.99
6h	C_6F_5	648	712	0.0029	26.39 (96); 274.57 (4)	96	37.79	1.00
6i	C_6F_4OMe	650	714	0.0006	39.30 (93); 398.03 (7)	n.d.[c]	n.d.[c]	n.d.[c]
Zn-6a	C_6H_4OnBu	607	652	0.0011	23.04 (87); 139.15 (13)	99	42.82	0.99
Zn-6b	C_6H_4OMe	606	651	0.0005	33.34 (92); 182.80 (8)	99	29.39	0.98
Zn-6c	Mes	604	653	0.0014	25.92 (77); 184.51 (13)	98	38.12	0.99
Zn-6d	C_6H_4Me	607	653	0.0012	27.13 (83); 189.38 (17)	99	36.34	0.99
Zn-6e	C_6H_5	601	647	0.0009	29.53 (88); 107.63 (12)	99	33.36	0.99
Zn-6f	C_6H_4F	602	649	0.0049	133.53 (73); 281.39 (27)	99	6.948	0.93
Zn-6g	$C_6H_4CF_3$	605	653	0.0028	35.20 (75); 285.80 (25)	97	27.93	0.98
Zn-6h	C_6F_5	602	654	0.0025	20.65 (94); 215.88 (6)	96	47.91	0.99
Zn-6i	C_6F_4OMe	602	651	0.0020	15.33 (90); 142.73 (10)	n.d.[c]	n.d.[c]	n.d.[c]
9	C_6H_5/C_6H_4Me	654	718	0.0145	361.77 (67); 2152.55 (33)	89	2.661; 0.363	

[a] Decays are mono- or biexponential; excitation wavelength λ_{exc} = 400 or 550 nm. [b] The relative amplitudes A were calculated from fitting the data by the equations $Y = A_1e^{-k/\tau 1} + A_2e^{-k/\tau 2}$ and $A_1 + A_2 = 100\%$. [c] n.d.: not determined. [d] $k_{ET} = 1/\tau - 1/\tau_{ref}$. [e] $\Phi_{ET} = k_{ET}\tau$; $\tau = \tau_1$ with the largest amplitude used in the equations.

bis(porphyrin) reference **11**. When we neglect interporphyrin energy transfer, approximately 50% of the decay should occur oxidatively through Q-P^{C6H5} and 50% reductively through P^{C6H4Me}-Fc. The observed intermediate quenching of **9** (89%) between that of **4e** (80%) and **6d** (97%) is in accord with the concept of two decay pathways. Therefore both PET pathways appear possible in **9**.

Kinetics of Photoinduced Electron Transfer by Time-Resolved Fluorescence Decay

The fluorescence lifetimes τ of dyads, triads, tetrad **9** and reference compounds are presented in Tables 2–4 and the fluorescence decay curves of selected conjugates and reference porphyrins are shown in Figure 4.

The fluorescence lifetimes of the free-base reference porphyrins and P^{Ph}-P^{PhMe} (**11**) are $\tau \approx 10$ ns and those of the zinc(II) porphyrins are $\tau \approx 2$ ns, as expected.[11] All the excited states of the reference porphyrins **Ac-3**, **Zn-Ac-3**, reference dyad **11** and Q-P dyads **4a**–**4h** decay with a single rate constant. The PET from the porphyrin to the anthraquinone in the Q-P dyads **4** opens a new deactivation pathway for the excited singlet state and reduces its lifetime generating the $Q^{\bullet-}$-$P^{\bullet+}$ charge-separated state (CS state). Other pathways (e.g., originating from adventitiously reduced anthraquinone to the hydroquinone[31]) are not detected in dyads **4**. The fluorescence lifetimes of **4** are in the range of $\tau = 0.613$ ns (**4a**, Ar = 4-C_6H_4OnBu) to $\tau = 9.55$ ns (**4h**, Ar = C_6F_5). A clear trend (with the exception of **4c**, Ar = Mes, see above) is observed with the more electron-rich porphyrins featuring shorter lifetimes (Table 3). From these data, rate constants k_{ET} for oxidative PET were calculated (Table 3). The rate constants of the electron-rich porphyrins **4a**, **4b** and **4d** (1.5×10^9–0.9×10^9 s^{-1}) are fully compatible with those of the reported Q-P dyads consisting of electron-rich porphyrins and quinones.[3] The much lower rates of

EurJIC European Journal of Inorganic Chemistry
www.eurjic.org
FULL PAPER

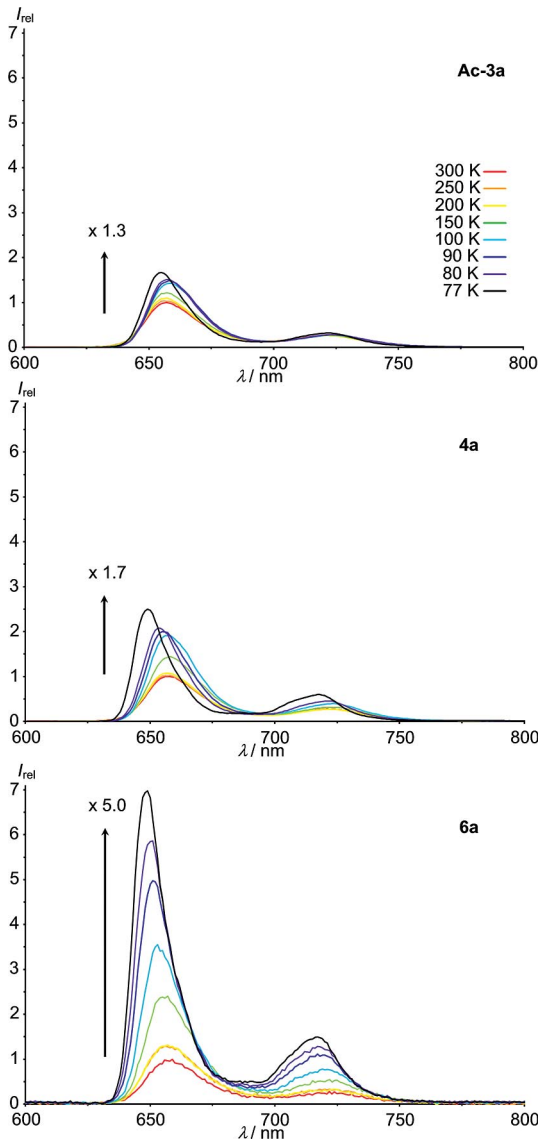

Figure 3. Normalised emission spectra of **Ac-3a**, **4a** and **6a** in 2-methyltetrahydrofuran at $T = 300 \rightarrow 77$ K.

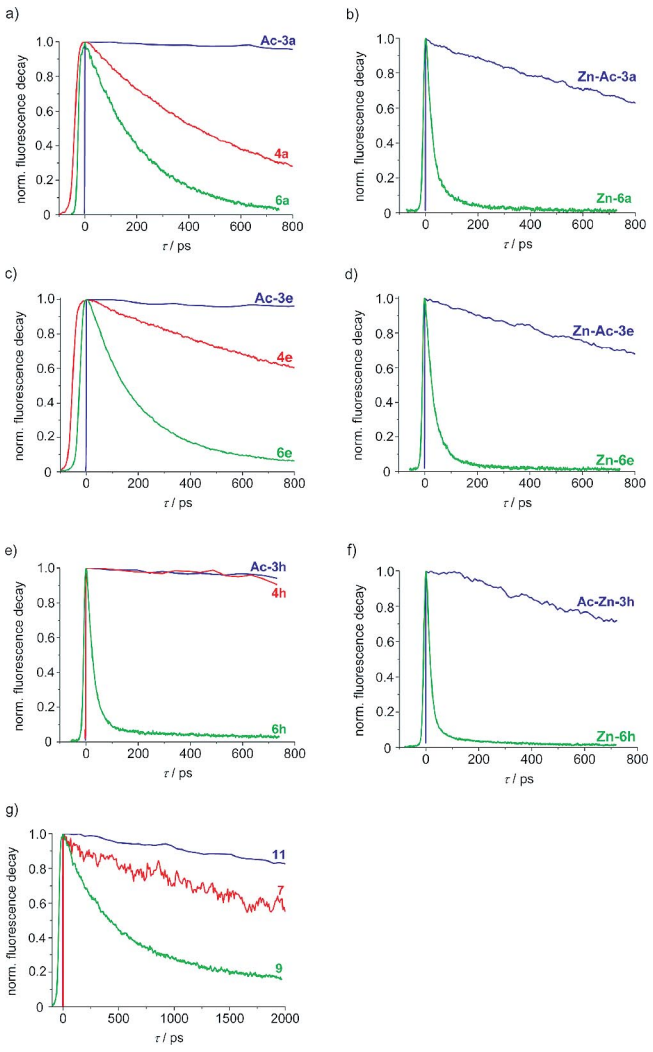

Figure 4. Fluorescence decay profiles of a) **Ac-3a**, **4a**, **6a**, b) **Zn-Ac-3a**, **Zn-6a**, c) **Ac-3e**, **4e**, **6e**, d) **Zn-Ac-3e**, **Zn-6e**, e) **Ac-3h**, **4h**, **6h**, f) **Zn-Ac-3h**, **Zn-6h** and g) **11**, **7**, **9** in CH_2Cl_2 (λ_{exc} = 400 and 550 nm).

ET observed for the electron-withdrawing porphyrin dyads **4f**–**4h** are related to the lower thermodynamic driving force for the ET (see Electrochemical Studies below).

Triads **6a**–**6d** feature a monoexponential decay whereas the decays of all other dyads have to be fitted by biexponential decay curves (Table 4). The minor component (τ_2, A_2) could be due to additional quenching by the heavy-atom effect of the ferrocene,[7c] population of the ferrocene triplet state,[10] the presence of ferrocene/amide conformations that are less suitable for ET or intermolecular Zn···O=C(quinone) interactions in **Zn-6**.[3m] The latter path, however, seems to be less pronounced based on NMR spectroscopic data for **Zn-6** (see above). Rate constants were estimated from the fluorescence lifetimes with the largest amplitude (τ_1, A_1; Table 4). These rate constants for **6a**–**6h** are larger than those of the corresponding **4a**–**4h** lacking ferrocene (Table 3 and Table 4). Whereas k_{ET} decreases for Q-P^{Ar} dyads **4** with electron-withdrawing substituents (Table 3), the reverse trend is observed for Q-P^{Ar}-Fc triads **6** (Table 4). The latter observation would be expected for reductive PET from ferrocene to the excited porphyrin as the dominant pathway. Indeed, k_{ET} is minimal for **6b**–**6d**, increases slightly for electron-rich **6a** favouring PET to the quinone and increases dramatically for electron-poor **6e**–**6h** favouring PET from ferrocene. Hence reductive PET seems to be favourable in **6e**–**6h** whereas oxidative and reductive pathways are both accessible in **6a**–**6d**.

In the zinc(II) porphyrin triads **Zn-6**, the rate constants k_{ET} are large (30×10^9–40×10^9 s^{-1}; except for **Zn-6f**, which is unexplained at the moment) and ET is basically quantitative. No clear correlation between k_{ET} and the nature of the porphyrin substituents can be discerned (Table 4). This might be explained by the larger driving force [$\Delta(\Delta G_{ET}) \approx 0.17$ eV] of both PET pathways in zinc(II) porphyrin donor/acceptor assemblies due to the higher energy of the singlet excited state of zinc(II) porphyrins and the lower oxidation potential of zinc(II) porphyrins relative to free-base por-

EurJIC European Journal of Inorganic Chemistry www.eurjic.org FULL PAPER

phyrins (Table 4; see Electrochemical Studies below). Other scenarios would be accelerated quenching via ^{3}ZnP states due to the heavy-atom effect of ferrocene[7c] or via ferrocene triplet states.[10]

As suggested from the quantum yield data, the singlet excited states of tetrad **9** can be quenched by PET from the C_6H_5-substituted porphyrin to its adjacent quinone and/or by PET from ferrocene to its adjacent C_6H_4Me-substituted porphyrin. The two fluorescence lifetimes of **9** [τ_1 = 362 ps (67%) and τ_2 = 2153 ps (33%)] roughly correspond to the lifetimes of Q-P^{C6H4Me}-Fc **6d** (τ = 229 ps) and Q-P^{C6H5} **4e** (τ = 1370 ps). This suggests that indeed both initial PET pathways are conceivable in **9** with the reductive PET being more probable than the oxidative PET. On the basis of this interpretation, the rate constants were estimated to be 2.66×10^9 s^{-1} (reductive PET) and 0.36×10^9 s^{-1} (oxidative PET). The thermodynamic feasibility of reductive and oxidative PET will be discussed in the next sections.

Electrochemical Studies

Cyclic voltammograms of porphyrins typically show two reversible oxidation and two reversible reduction waves. Porphyrins **3a**–**3h** with amine substituents are only quasi-reversibly or even irreversibly oxidised.[11,14] As the amino porphyrins do not qualify as references, their *N*-acetylated analogues **Ac-3a**–**Ac-3h** were used instead. The redox potentials of the new amino porphyrins **3a**, **3b**, **3e** and **3d** and the porphyrin reference compounds **Ac-3a**, **Ac-3b**, **Ac-3d** and **Ac-3e** are presented in Table 5. As described previously, the *meso*-aryl substituents cause a stepwise anodic shift of porphyrin oxidation and reduction.[11] The new *N*-acetylated porphyrins **Ac-3a**, **Ac-3b**, **Ac-3d** and **Ac-3e** confirm and complete the trend in the full series Ar = 4-C_6H_4O*n*Bu → 4-C_6H_4OMe → 4-C_6H_4Me → Mes → C_6H_5 → 4-C_6H_4F → 4-$C_6H_4CF_3$ → C_6F_5. The shifts observed amount to 0.34 V for the first oxidation and 0.25 V for the first reduction from **Ac-3a** (Ar = C_6H_4O*n*Bu) to **Ac-3h** (Ar = C_6F_5[11]).

In Q-P dyads **4a**–**4h** an additional redox event at a rather constant potential of $E_{1/2}$ = –1.20 V corresponding to the first reversible reduction of the quinone to the semiquinonate is observed. For dyad **4c** even the second reduction of anthraquinone at $E_{1/2}$ = –1.72 V has been detected. The individual redox potentials of the porphyrins **Ac-3** are essentially unperturbed by the appended quinone in **4** (Table 6 and Figure 5).

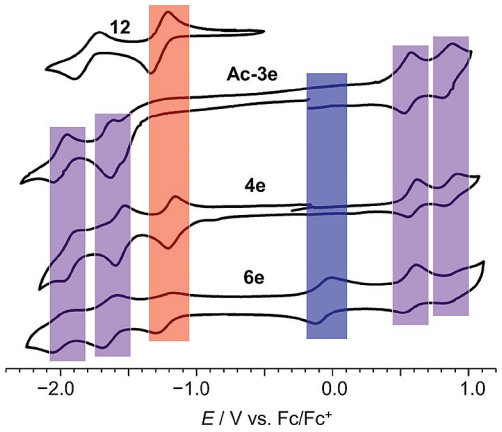

Figure 5. Cyclic voltammograms of quinone reference **12**, porphyrin **Ac-3e**, dyad **4e** and triad **6e** in (nBu$_4$N)(PF$_6$)/CH$_2$Cl$_2$.

Attachment of a ferrocene unit (**6a**–**6h**, **Zn-6a**–**Zn-6h**) yields a further oxidation process at a rather constant potential of $E_{1/2}$ = –0.08 V corresponding to the oxidation of ferrocene to ferrocenium (Table 6 and Figure 5). Only minor effects of ferrocene on the porphyrin and anthraquinone redox potentials are observed. Likewise only minor effects of the Ar substituent on the Fc and Q potentials are noted, which indicates a weak interchromophore interaction in the ground state. The quinone in the zinc porphyrins **Zn-6** is slightly easier to reduce than in the free-base porphyrins **6** (Table 6).

The redox data for bis(porphyrins) **11**, **7** and **9** are presented in Table 6. The additional porphyrin superimposes its redox waves onto those of the respective partner mono-

Table 5. Redox potentials of monoporphyrins **3**, **Ac-3**, **Zn-Ac-3** and (bis)porphyrin **11** vs. Fc/Fc$^+$ in (nBu$_4$N)(PF$_6$)/CH$_2$Cl$_2$ at room temperature.

	Ar	C$_6$H$_4$–R′	$E_{1/2}$(ox^1) [V]	$E_{1/2}$(ox^2) [V]	$E_{1/2}$(red^1) [V]	$E_{1/2}$(red^2) [V]
3a	C$_6$H$_4$O*n*Bu	NH$_2$	0.420	0.590	–1.660[a]	–2.010[a]
Ac-3a	C$_6$H$_4$O*n*Bu	NHAc	0.480	0.730	–1.640	–1.980
Zn-Ac-3a	C$_6$H$_4$O*n*Bu	NHAc	0.300	0.720	–1.790	–2.160
3b	C$_6$H$_4$OMe	NH$_2$	0.540[a]	n.o.[b]	–1.660	–1.990
Ac-3b	C$_6$H$_4$OMe	NHAc	0.510	0.750	–1.630	–1.970
Zn-Ac-3b	C$_6$H$_4$OMe	NHAc	0.310	0.710	–1.780	n.o.[b]
3d	C$_6$H$_4$Me	NH$_2$	0.440	0.550	–1.640[a]	–1.980[a]
Ac-3d	C$_6$H$_4$Me	NHAc	0.520	0.830	–1.610	–1.950
Zn-Ac-3d	C$_6$H$_4$Me	NHAc	0.361	0.800	–1.720	–2.090
Ac-3e	C$_6$H$_5$	NHAc	0.550	0.840	–1.630	–2.000
Zn-Ac-3e	C$_6$H$_5$	NHAc	0.360	0.780	–1.750	–2.110
11	C$_6$H$_5$/C$_6$H$_4$Me	NHAc	0.540 (2e)	0.860	–1.660 (2e)	–2.010

[a] Irreversible. [b] n.o.: not observed.

EurJIC European Journal of Inorganic Chemistry www.eurjic.org FULL PAPER

Table 6. Redox potentials of **4**, **6**, **Zn-6**, **11**, **7** and **9** in V vs. Fc/Fc^+ in $(nBu_4N)(PF_6)/CH_2Cl_2$ at room temperature.

	Ar	$E(P)_{1/2}(ox^1)$ [V]	$E(P)_{1/2}(ox^2)$ [V]	$E(Fc)_{1/2}(ox)$ [V]	$E(Q)_{1/2}(red)$ [V]	$E(P/Q)_{1/2}(red^1)$ [V]	$E(P)_{1/2}(red^2)$ [V]
4a	C_6H_4OnBu	0.500	0.750	–	–1.230	–1.640	–2.000
4b	C_6H_4OMe	0.500	0.760	–	–1.230	–1.660	–1.990
4c	Mes	0.560	0.960	–	–1.230	–1.720 (2e)	–2.070
4d	C_6H_4Me	0.540	0.840	–	–1.210	–1.600	–1.980
4e	C_6H_5	0.580	0.870	–	–1.190	–1.560	–1.940
4f	C_6H_4F	0.600	0.880	–	–1.210	–1.580	–1.930
4g	$C_6H_4CF_3$	0.670	0.960	–	–1.200	–1.530	–1.870
4h	C_6F_5	0.830	1.050	–	–1.240	–1.420	–1.850
6a	C_6H_4OnBu	0.510	0.770	–0.070	–1.210	–1.650	–2.010[a]
6b	C_6H_4OMe	0.500	0.770	–0.079	–1.220	–1.650	–2.010[a]
6c	Mes	0.560	0.990	–0.070	–1.230	–1.710 (2e)	–2.070
6d	C_6H_4Me	0.550	0.855	–0.075	–1.190	–1.605	–1.965
6e	C_6H_5	0.560	0.925	–0.090	–1.260	–1.670	–2.060
6f	C_6H_4F	0.585	0.945[a]	–0.085	–1.235	–1.625	–2.015[a]
6g	$C_6H_4CF_3$	0.640	0.990	–0.080	–1.230	–1.570	–1.930
6h	C_6F_5	0.800	1.040	–0.100	–1.270	–1.430	–1.900
6i	C_6F_4OMe	0.770	1.075	–0.050	–1.240	–1.420	–1.890
Zn-6a	C_6H_4OnBu	0.370	0.670	–0.070	–1.170	–1.620	–2.200[a]
Zn-6b	C_6H_4OMe	0.360	0.670	–0.080	–1.150	–1.590[a]	n.o.[b]
Zn-6c	Mes	0.410	0.750	–0.060	–1.180[c]	–1.620[a]	–2.220[a]
Zn-6d	C_6H_4Me	0.390	0.710	–0.089	–1.190[c]	–1.630[a]	–2.230[a]
Zn-6e	C_6H_5	0.430	0.740	–0.080	–1.120	–1.580[a]	–2.190[a]
Zn-6f	C_6H_4F	0.440	0.750	–0.080	–1.120	–1.590	–2.180[a]
Zn-6g	$C_6H_4CF_3$	0.480	0.770	–0.100	–1.240[a]	–1.610[a]	n.o.[b]
Zn-6h	C_6F_5	0.630	0.910	–0.090	–1.180	n.o.[b]	–2.000[a]
Zn-6i	C_6F_4OMe	0.600	0.880	–0.090	–1.160	–1.610[a]	–2.040[a]
11	C_6H_5/C_6H_4Me	0.540 (2e)	0.860 (2e)	–	–	–1.650 (2e)	–2.010 (2e)
7	C_6H_5/C_6H_4Me	0.570 (2e)	0.890	–	–1.200	–1.600 (2e)	–1.970
9	C_6H_5/C_6H_4Me	0.590 (2e)	0.870	–0.060	–1.190	–1.600 (2e)	–1.980

[a] Irreversible, E_p given. [b] n.o.: not observed. [c] Quasi-reversible.

porphyrin, and two-electron reversible redox waves for the first oxidation and first reduction of both porphyrins at around –0.59 and –1.60 V are detected. Tetrad **9** additionally shows the one-electron reduction of the quinone at $E_{1/2}$ = –1.190 V and the one-electron oxidation of the ferrocene at $E_{1/2}$ = –0.060 V.

Thermodynamic Driving Force for Photoinduced Electron Transfer

The energies of the porphyrin first excited singlet states $E(S_0 \rightarrow S_1)$ of **4a**–**4h** were obtained from the average values of the $Q_x(0,0)$ absorption and Q(0,0) emission bands (Tables 1–4). The energies of the CS states $Q^{\cdot-}$-$P^{\cdot+}$ were evaluated from the first oxidation potential of the porphyrin $E_{1/2}(P/P^{\cdot+})$, the first reduction potential of the quinone $E_{1/2}(Q/Q^{\cdot-})$ and the Coulomb term $e_0^2/[4\pi\varepsilon_0\varepsilon(CH_2Cl_2)r_{AD}]$ (Table 6). From these data the thermodynamic driving forces for PET were calculated according to the Rehm–Weller equation:[22] $\Delta G_{ET} = E_{1/2}(D/D^{\cdot+}) - E_{1/2}(A/A^{\cdot-}) - e_0^2/[4\pi\varepsilon_0\varepsilon(CH_2Cl_2)r_{AD}] - E(S_0 \rightarrow S_1)$ with ε_0 = 8.85519×10^{-12} F m^{-1}, $\varepsilon(CH_2Cl_2)$ = 8.93 and r_{AD} = 15.5 Å, as determined by DFT models (see below), to give a Coulomb term of 0.104 eV in CH_2Cl_2 . The data are presented in Table 7. Figure 6 shows the energy level diagram for all Q-P dyads **4a**–**4h**. This series of compounds displays a $k_{ET}/\Delta G_{ET}$ correlation in the normal Marcus region (Table 3 and Table 7) with k_{ET} increasing the more negative ΔG_{ET} is (except for the mesityl derivative **4c**, see above). For **4h**, the ET is even calculated to be slightly endergonic, which accounts for the observed weak fluorescence quenching.

Table 7. Energies of the porphyrin S_1 and CS states for dyads **4a**–**4h** and the driving forces ΔG_{ET}.

	Ar	$E(S_0 \rightarrow S_1)$ [eV]	$E(Q^{\cdot-}\text{-}P^{\cdot+})$[a] [eV]	ΔG_{ET} [eV]
4a	C_6H_4OnBu	1.89	1.63	–0.26
4b	C_6H_4OMe	1.89	1.63	–0.26
4c	Mes	1.90	1.69	–0.21
4d	C_6H_4Me	1.90	1.65	–0.25
4e	C_6H_5	1.91	1.67	–0.24
4f	C_6H_4F	1.91	1.71	–0.20
4g	$C_6H_4CF_3$	1.91	1.77	–0.14
4h	C_6F_5	1.93	1.97	+0.04

[a] Including Coulomb term of 0.104 eV.

As suggested above, two different PET pathways exist in triads **6a**–**6h** and **Zn-6a**–**Zn-6h**. The first one is the oxidative pathway, as is also found in Q-P dyads **4**, leading to the $Q^{\cdot-}$-$P^{\cdot+}$-Fc and $Q^{\cdot-}$-(Zn)$P^{\cdot+}$-Fc CS states, respectively (Table 8, Figures 7 and 8). The second one is the reductive pathway leading to the Q-$P^{\cdot-}$-$Fc^{\cdot+}$ and Q-(Zn)$P^{\cdot-}$-$Fc^{\cdot+}$ CS states, respectively (Table 8, Figures 7 and 8). The final CS states are described by $Q^{\cdot-}$-P-$Fc^{\cdot+}$ and $Q^{\cdot-}$-(Zn)P-$Fc^{\cdot+}$, respectively. The free energies of the initial and final CS states were estimated from the Rehm–Weller equation[22] and are

EurJIC European Journal of Inorganic Chemistry www.eurjic.org FULL PAPER

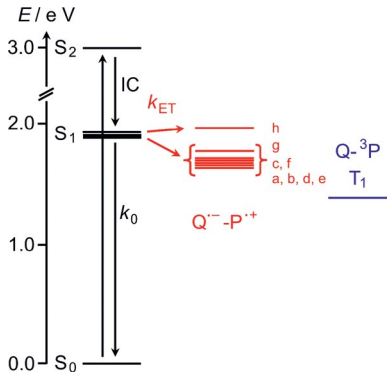

Figure 6. Energy level diagram for Q-P dyads **4a**–**4h** (IC = internal conversion; the porphyrin triplet state T_1 is estimated to be 1.43 eV[3f]).

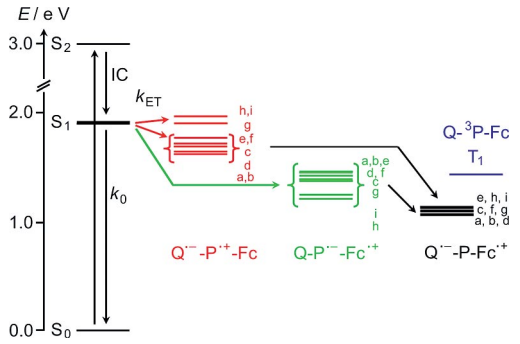

Figure 7. Energy level diagram for Q-P-Fc triads **6a**–**6i** (the porphyrin triplet state T_1 is estimated to be 1.43 eV[3f]).

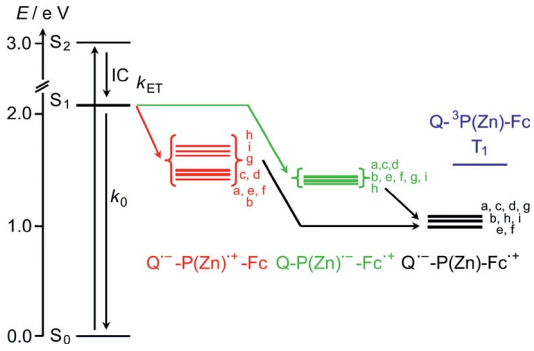

Figure 8. Energy level diagram for Q-(Zn)P-Fc triads **Zn-6a**–**Zn-6i** (the zinc porphyrin triplet state T_1 is estimated to be 1.53 eV.[5b]).

given in Table 8 (quinone-porphyrin centre-to-centre distance r_{AD} = 15.5 Å; Coulomb term for Q•−-P•+-Fc 0.104 eV; porphyrin centre to iron distance r_{AD} = 13.0 Å; Coulomb term for Q-P•−-Fc•+ 0.124 eV; quinone-centre to iron distance r_{AD} = 28.3 Å; Coulomb term for Q•−-P-Fc•+ 0.057 eV).

In the free-base porphyrin triads **6a**–**6i**, the reductive PET to give Q-P•−-Fc•+ as the initial CS state is clearly favoured over the oxidative PET that gives the Q•−-P•+-Fc initial CS state (Figure 7). This is especially pronounced in **6g**–**6i** with strongly electron-withdrawing substituents. In the zinc(II) porphyrin triads **Zn-6**, oxidative PET becomes competitive with reductive PET with respect to the driving force ΔG_{ET} (Table 8 and Figure 8). The final Q•−-(Zn)P-Fc•+ CS states of **Zn-6** are slightly lower than the final Q•−-P-Fc•+ CS states of **6** due to the slightly preferred reduction of Q in the zinc porphyrins **Zn-6** (see above, Table 6).

In bis(porphyrin) **11**, the conceivable $P_1^{\bullet+}$-$P_2^{\bullet-}$ and $P_1^{\bullet-}$-$P_2^{\bullet+}$ CS states are located 0.15 and 0.16 eV (including the Coulomb term of 0.08 eV; porphyrin-porphyrin centre-to-centre distance 19.3 Å) above the excited singlet state S_1 and are thus less relevant for excited-state decay (Figure 9 and Table 9). This is also reflected in the unchanged lifetime of **11** (τ = 9.70 ns) with respect to reference porphyrins **Ac-3d** (τ = 9.69 ns) and **Ac-3e** (τ = 9.88 ns). The thermodynamic driving forces for ET in tetrad **9** were again calculated from the Rehm–Weller equation[22] (see above) and are given in

Table 8. Energies of porphyrin S_1 and CS states for **6** and **Zn-6** and driving forces ΔG_{ET}.

	Ar	$E(S_0 \rightarrow S_1)$ [eV]	E(Q•−-P•+-Fc)[a] [eV]	E(Q-P•−-Fc•+)[b] [eV]	E(Q•−-P-Fc•+)[c] [eV]	ΔG_{ET}(Q•−-P•+-Fc) [eV]	ΔG_{ET}(Q-P•−-Fc•+) [eV]	ΔG_{ET}(Q•−-P-Fc•+) [eV]
6a	C_6H_4OnBu	1.90	1.62	1.46	1.08	–0.28	–0.44	–0.82
6b	C_6H_4OMe	1.90	1.62	1.45	1.08	–0.28	–0.45	–0.82
6c	Mes	1.91	1.69	1.39	1.10	–0.22	–0.52	–0.81
6d	C_6H_4Me	1.91	1.64	1.41	1.06	–0.27	–0.50	–0.84
6e	C_6H_5	1.91	1.72	1.46	1.11	–0.19	–0.45	–0.79
6f	C_6H_4F	1.91	1.72	1.42	1.09	–0.19	–0.49	–0.82
6g	$C_6H_4CF_3$	1.91	1.77	1.37	1.09	–0.04	–0.54	–0.82
6h	C_6F_5	1.92	1.97	1.21	1.11	+0.05	–0.71	–0.81
6i	C_6F_4OMe	1.92	1.91	1.25	1.13	–0.01	–0.67	–0.79
Zn-6a	C_6H_4OnBu	2.07	1.44	1.43	1.04	–0.63	–0.64	–1.03
Zn-6b	C_6H_4OMe	2.07	1.41	1.39	1.01	–0.66	–0.66	–1.06
Zn-6c	Mes	2.07	1.49	1.44	1.06	–0.58	–0.63	–1.01
Zn-6d	C_6H_4Me	2.07	1.48	1.42	1.04	–0.59	–0.65	–1.03
Zn-6e	C_6H_5	2.08	1.45	1.38	0.98	–0.63	–0.70	–1.10
Zn-6f	C_6H_4F	2.08	1.46	1.39	0.98	–0.62	–0.69	–1.10
Zn-6g	$C_6H_4CF_3$	2.07	1.62	1.39	1.08	–0.45	–0.68	–0.99
Zn-6h	C_6F_5	2.07	1.71	1.37[d]	1.03	–0.36	–0.70	–1.04
Zn-6i	C_6F_4OMe	2.08	1.66	1.40	1.01	–0.42	–0.68	–1.07

[a] Including Coulomb term of 0.104 eV. [b] Including Coulomb term of 0.124 eV. [c] Including Coulomb term of 0.057 eV. [d] Calculated with $E(P)_{1/2}(red^1)$ = –1.58 eV from reference porphyrin **Ac-3h**, see ref.[10].

EurJIC European Journal of Inorganic Chemistry www.eurjic.org FULL PAPER

Table 9. Reductive PET (ΔG_{ET} = –0.48 eV) to give Q–P_1–$P_2^{\bullet-}$-$Fc^{\bullet+}$ is thermodynamically favoured in **9** over oxidative PET (ΔG_{ET} = –0.26 eV) similarly to **6d** and **6e** (Tables 8, 9 and Figure 9). This excellently supports the kinetic analysis of ET in **9** (see above). The shift of charge from P_2 to P_1 to give Q-$P_1^{\bullet-}$-P_2-$Fc^{\bullet+}$ is slightly endergonic (0.09 eV) whereas the following thermal ET to give $Q^{\bullet-}$-P_1-P_2-$Fc^{\bullet+}$ is again exergonic by 0.42 eV (Figure 9).

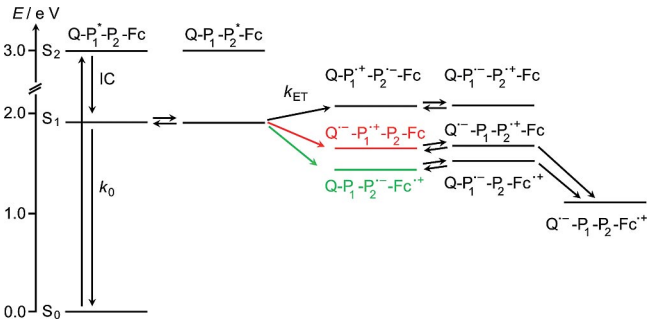

Figure 9. Energy level diagram for Q–P_1–P_2-Fc tetrad **9**.

Table 9. Energies of porphyrin S_1 and CS states for **9** and driving forces ΔG_{ET}.

State	E [eV][a]	r_{AD} [Å]	Coulomb term [eV]
$E_{P1}(S_0 \rightarrow S_1)$	1.91	–	–
$E_{P2}(S_0 \rightarrow S_1)$	1.91	–	–
E(Q-$P_1^{\bullet+}$-$P_2^{\bullet-}$-Fc) or E(Q-$P_1^{\bullet-}$-$P_2^{\bullet+}$-Fc)[b,c,d,e]	2.07/2.08	19.3	0.084
E($Q^{\bullet-}$-$P_1^{\bullet+}$- P_2-Fc)[b]	1.65	15.5	0.104
E($Q^{\bullet-}$-P_1-$P_2^{\bullet+}$-Fc)[c]	1.67	34.8	0.046
E(Q-P_1-$P_2^{\bullet-}$-$Fc^{\bullet+}$)[d]	1.43	13.0	0.124
E(Q-$P_1^{\bullet-}$-P_2-$Fc^{\bullet+}$)[e]	1.52	32.3	0.050
E($Q^{\bullet-}$-P_1-P_2-$Fc^{\bullet+}$)	1.10	47.8	0.033
Driving force	**ΔG_{ET} [eV]**		
ΔG_{ET}($Q^{\bullet-}$-$P_1^{\bullet+}$-P_2-Fc)	–0.26		
ΔG_{ET}($Q^{\bullet-}$-P_1-$P_2^{\bullet+}$-Fc)	–0.24		
ΔG_{ET}(Q–P_1-$P_2^{\bullet-}$-$Fc^{\bullet+}$)	–0.48		
ΔG_{ET}(Q-$P_1^{\bullet-}$-P_2-$Fc^{\bullet+}$)	–0.39		
ΔG_{ET}($Q^{\bullet-}$-P_1-P_2-$Fc^{\bullet+}$)	–0.81		

[a] Including Coulomb terms. [b] Calculated with $E(P_1)_{1/2}(ox^1)$ = 0.550 V from reference porphyrin **Ac-3e**. [c] Calculated with $E(P_2)_{1/2}(ox^1)$ = 0.520 V from reference porphyrin **Ac-3d**. [d] Calculated with $E(P_1)_{1/2}(red^1)$ = –1.630 V from reference porphyrin **Ac-3e**. [e] Calculated with $E(P_2)_{1/2}(red^1)$ = –1.610 V from reference porphyrin **Ac-3d**.

Densitiy Functional Calculations on Ground and CS States

To estimate distances between redox sites (Q–P centre-to-centre; P centre to Fe, Q centre to Fe, P–P centre-to-centre) and to visualise frontier molecular orbitals, the ground states of dyads and triads with electron-donating and -withdrawing substituents were optimised by DFT (B3LYP/LANL2DZ, PCM, CH_2Cl_2)[23] methods (see the Supporting Information). Figure 10 exemplarily depicts the frontier molecular orbitals of dyads **4b** and **4h** showing the typical Gouterman four orbital scheme for porphyrins (nomenclature adopted from D_{4h} local point symmetry to describe the node structure of the orbitals[24]) and the lowest π* orbital of the quinone located between the HOMOs and LUMOs of the porphyrin. Two points are immediately evident: 1) electron-withdrawing Ar substituents reduce the energy gap between the LUMO of the porphyrin and the π* orbital of the quinone (Figure 11), which disfavours oxidative PET, and 2) the symmetry of the local porphyrin LUMO in **4h** (Figure 10, b; LUMO+1; Ar = C_6F_5) is different to that in all the other dyads and features a node at the *meso* carbon atoms in the amide direction. This orbital inversion is typically observed in porphyrins with strongly electron-withdrawing substituents.[11,25] Naturally, small orbital coefficients at the bridging unit between redox centres

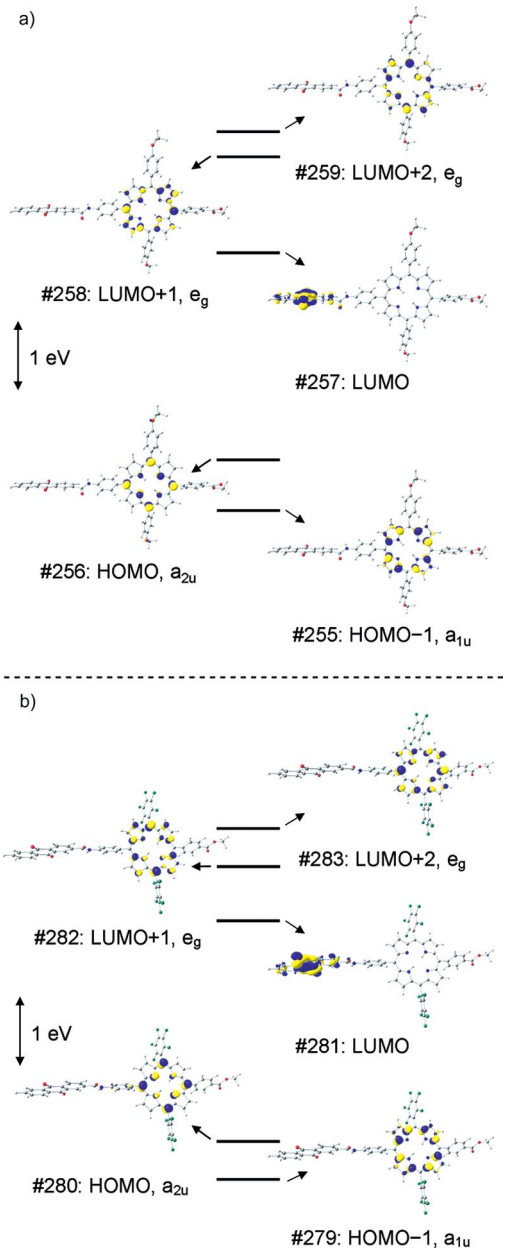

Figure 10. B3LYP/LANL2DZ, PCM-calculated frontier orbitals for a) **4b** and b) **4h** (isosurface value 0.05 a.u.).

EurJIC European Journal of Inorganic Chemistry www.eurjic.org FULL PAPER

disfavours ET. Hence, PET in **4h** is not only thermodynamically slightly uphill (Figure 6), but probably also kinetically hindered due to the unfavourable orbital symmetry.

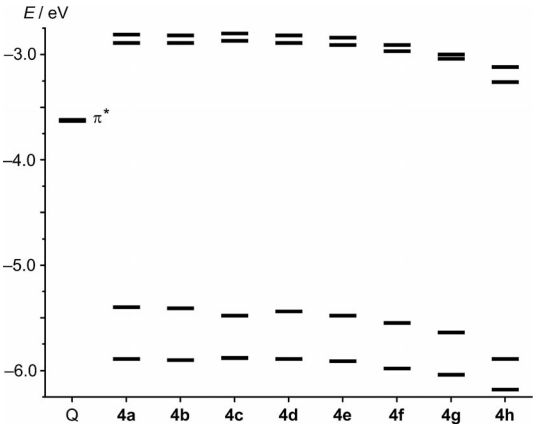

Figure 11. B3LYP/LANL2DZ, PCM-calculated molecular orbital energy diagram for dyads **4**.

A similar picture with respect to the quinone π* orbital arises for the triads **6** (Figure 12) and **Zn-6**. The porphyrin LUMO inversion is also observed for **6g** (Figure 13) and **6h**. In addition, the occupied ferrocene-based δ orbitals (d_{xy}, $d_{x^2-y^2}$) are close in energy to the local porphyrin HOMOs (Figure 12). For electron-rich **6a**–**6f**, the δ(Fc) orbitals are below the porphyrin a_{2u} orbital, in **6g** the a_{2u} orbital is lowered in energy and mixes with a δ(Fc) orbital (Figure 13, HOMO) and in **6h** the porphyrin a_{2u} orbital is located even below the δ(Fc) orbitals. Naturally, this simple orbital picture cannot account for quantitative relationships, but it clearly demonstrates the lowering of the porphyrin HOMOs relative to the essentially constant ferrocene HOMOs (Figure 12), which should favour reductive PET in triads with electron-withdrawing substituents (see Tables 4 and 8). The near degeneracy of porphyrin and ferrocene HOMOs in terms of energy also allows for orbital mixing (Figure 13) and mixing of states, which should also allow energy-transfer processes between porphyrin and ferrocene. These energy-transfer processes might be assigned to the second decay (τ_2, A_2) in **6e**–**6i** and **Zn-6a**–**Zn-6i**

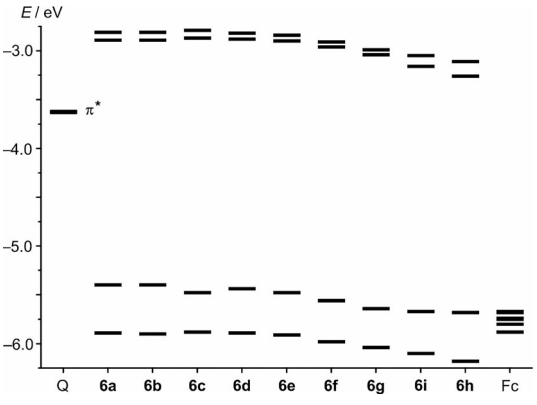

Figure 12. B3LYP/LANL2DZ, PCM-calculated molecular orbital energy diagram for triads **6**.

(Table 4; for the molecular orbitals of **Zn-6**, see the Supporting Information).

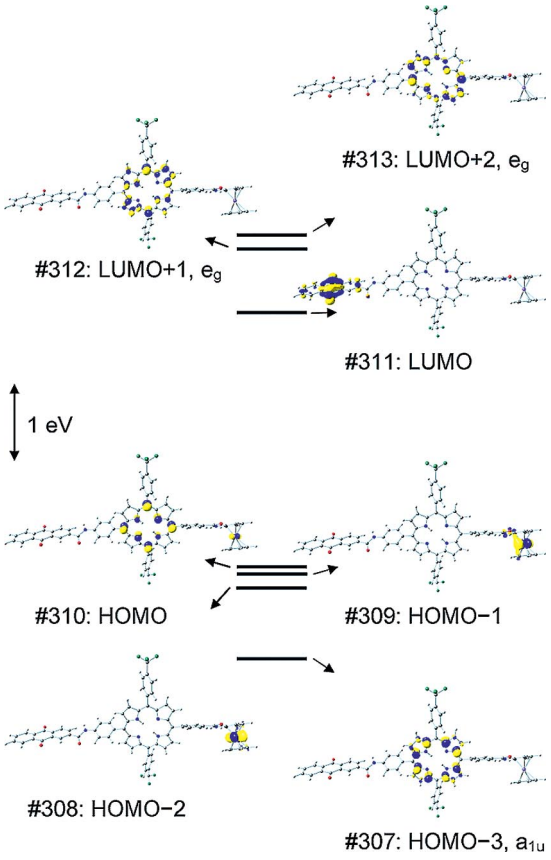

Figure 13. B3LYP/LANL2DZ, PCM-calculated frontier orbitals for triad **6g** (isosurface value 0.05 a.u.).

Tetrad **9** features a double nearly degenerate set of Gouterman orbitals as well as the quinone π* and the occupied ferrocene d orbitals, as expected from the constituent building blocks (see the Supporting Information). The porphyrin HOMOs are of local a_{2u} symmetry with large coefficients at the connecting *meso* carbon atoms. This should allow for energy and electron transfer between the two porphyrins[11] based on orbital symmetry arguments, as suggested in Figure 9.

For dyad **4b** (Ar = 4-C_6H_4OMe) we succeeded in optimising the $Q^{\cdot-}$-$P^{\cdot+}$ CS triplet state by DFT methods (Figure 14, a). The calculated spin density is clearly distributed over the porphyrin radical cation and quinone radical anion, as expected from the molecular orbital scheme (Figure 10). The quinone CO bond lengths were calculated to be 1.26 Å in the ground state and 1.30 Å in the CS state, clearly reflecting the semiquinone character. The analogous DFT optimisation of **4d** (Ar = 4-C_6H_4Me) resulted in the porphyrin triplet state T_1 (Figures 6 and 14, b), which suggests a close proximity of the CS (1.65 eV, Table 7) and local triplet states in terms of energy. Indeed, the porphyrin triplet state of H_2TPP has been reported to have an energy of 1.43 eV.[3f]

To gain an impression of the spin density and charge distribution in the final $Q^{\cdot-}$-P-$Fc^{\cdot+}$ and $Q^{\cdot-}$-(Zn)P-$Fc^{\cdot+}$ CS

EurJIC European Journal of Inorganic Chemistry
www.eurjic.org FULL PAPER

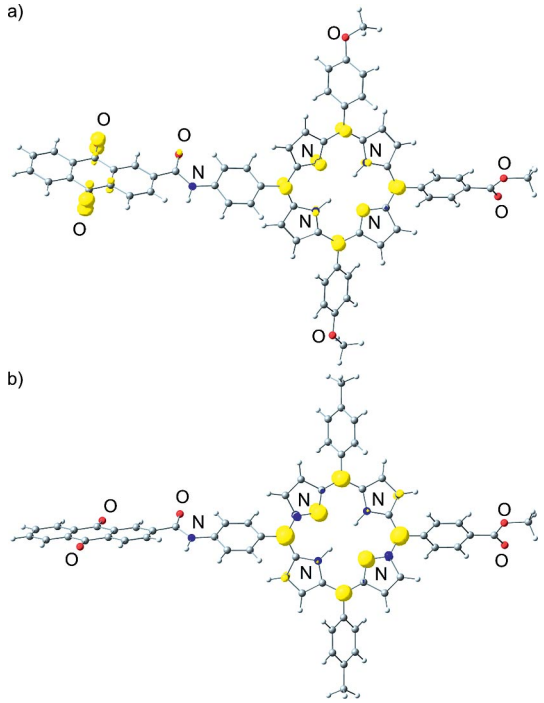

Figure 14. DFT-calculated spin density of a) the $Q^{\cdot-}$-$P^{\cdot+}$ CS triplet state of **4b** and b) the porphyrin triplet state of **4d** (isosurface value 0.01 a.u.).

states of the triads we tried to optimise this (triplet) state, but all attempts yielded only the optimised ferrocene triplet state with a Mulliken spin density of 2.03 at the iron centre (Figure 15, a). The calculated Fe···Cp(centroid) distances are increased significantly from 1.73 to 1.91 Å. The energy of the triplet state of unsubstituted ferrocene has been reported to be 1.16 eV,[10] which is clearly close to the energies of the $Q^{\cdot-}$-P-$Fc^{\cdot+}$ and $Q^{\cdot-}$-(Zn)P-$Fc^{\cdot+}$ CS states (cf. Table 8). To artificially stabilise the $Q^{\cdot-}$-P-$Fc^{\cdot+}$ and $Q^{\cdot-}$-(Zn)P-$Fc^{\cdot+}$ CS states relative to the ferrocene triplet we placed two Lewis acidic[26] BF_3 molecules at the quinone oxygen atoms, which allowed optimisation of the CS states of **6e**(·2BF_3) and **Zn-6e**(·2BF_3) as the lowest-energy triplet states (Figure 15, b,c). The calculated spin densities are clearly at both the ferrocenium and semiquinonato radicals. Again, the quinone CO bond lengths are elongated from 1.26 to 1.30 Å. Furthermore, the Fe···Cp(centroid) distances are elongated from 1.73 to 1.80 Å, which indicates the ferrocenium state.

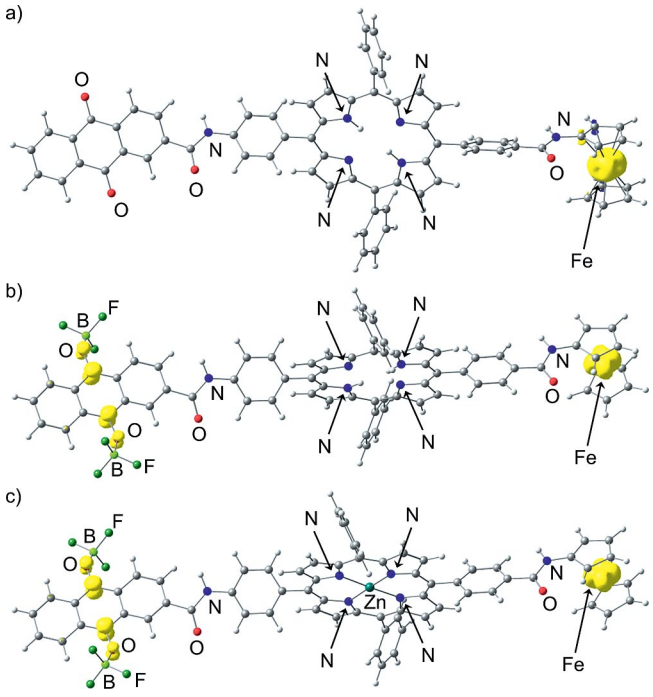

Figure 15. DFT-calculated spin densities of a) the ferrocene triplet state of **6e**, b) the $Q^{\cdot-}$-P-$Fc^{\cdot+}$ triplet CS state of **6e**(·2BF_3) and c) the $Q^{\cdot-}$-(Zn)P-$Fc^{\cdot+}$ triplet CS state of **Zn-6e**(·2BF_3) (isosurface value 0.01 a.u.).

Transient Absorption Spectroscopy of Selected Compounds

Compared with the porphyrin bands, the absorptions of the semiquinone radical anion $Q^{\cdot-}$ and ferrocenium cation $Fc^{\cdot+}$ are rather weak. Chemical reduction of the reference *N*-ethylanthraquinone-2-carboxylic acid amide with decamethylcobaltocene [$CoCp^*_2$][27] (see the Supporting Information) generated the semiquinone radical anion $Q^{\cdot-}$ with an absorption maximum at 618 nm and ε_{618} = 750 $M^{-1}\,cm^{-1}$ (THF). The ferrocenium reference $[Fc\text{-}NHAc]^+$ absorbs at 759 nm with ε_{759} = 350 $M^{-1}\,cm^{-1}$ (CH_2Cl_2).[28] Owing to the low extinction coefficients, that is, small absorption cross-sections, these bands are difficult to detect in transient absorption (TA) pump-probe experiments as they are overwhelmed by the excited-state absorptions of the strongly absorbing porphyrin excited states. Hence all transient absorption spectra are largely dominated by features of the porphyrin radical(s) and porphyrin triplet states.

The pico- to nanosecond TA spectra of compounds **4a** and **6a** in THF are presented in Figure 16. The spectra show multiple peaked features that correspond to ground-

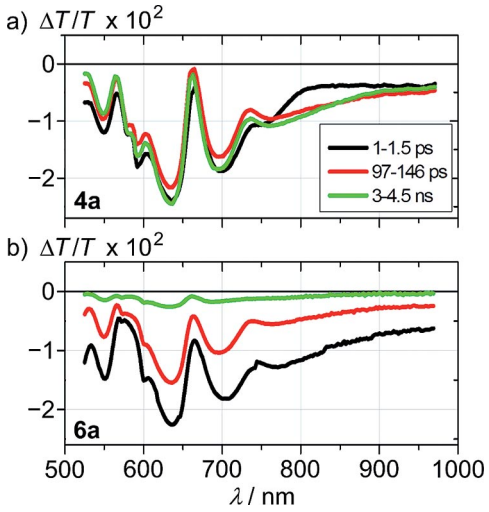

Figure 16. ps–ns transient absorption spectra of a) **4a** and b) **6a** in THF after excitation at λ_{exc} = 420 nm. Note the significantly faster decay of the TA signal for compound **6a**.

EurJIC European Journal of Inorganic Chemistry www.eurjic.org FULL PAPER

state bleaching and stimulated emission overlapped by the excited-state absorption of the porphyrin. The spectra do not change much during the observed period of time, except for compound **4a**, for which there is an increase in the intensity of the photoinduced absorption in the spectral region between 750–900 nm. This spectral evolution may be related to electron transfer from the porphyrin to the quinone, but a clear assignment is difficult.

As a consequence of the superposition of several bands corresponding to porphyrin radical ions, namely the excited-state absorption, the ground-state bleaching and stimulated emission bands, and the low extinction coefficients of the $Q^{\cdot-}$ and $Fc^{\cdot+}$ radicals, the transient spectra of intermediate CS states are not observed for dyad **4a** and triad **6a**. However, very clearly a much more rapid decay of the entire TA spectrum is observed for the ferrocenyl derivative **6a**. The decay is well fitted by a single exponential with an inverse rate of 220 ps, which is essentially the same as the 215 ps determined for the fluorescence lifetime of **6a**. This fast decay is likely due to the fast reductive quenching of the porphyrin excited state by the ferrocene, parallel oxidative quenching by the quinone (Figure 7) and/or heavy atom quenching by the ferrocene to give the porphyrin triplet state. For the two PET pathways, porphyrin radical anions and radical cations could be simultaneously present and would create superimposed excited-state absorption spectra that are difficult to analyse. After charge transfer from $P^{\cdot-}$ to Q or from Fc to $P^{\cdot+}$, the final CS state should show no features arising from porphyrin, but only weak bands corresponding to $Q^{\cdot-}$ and $Fc^{\cdot+}$ radicals. These latter would be difficult to detect, especially if the final CS state is only formed in low yields. However, the significant decrease in the TA signal intensity on the nanosecond timescale observed for **6a** in comparison with **4a** indicates that in the former a large fraction of the porphyrin excited states are rapidly quenched and that the ground state of the porphyrin in **6a** is quickly recovered after photoexcitation. This is in line with the experimentally observed faster photoluminescence decay of **6a**, the much lower fluorescence quantum yield and the predicted higher driving force for photoinduced electron transfer from the ferrocene to the porphyrin in comparison with electron transfer from the porphyrin to the quinone moiety, all of which indicate that the charge-transfer process from ferrocenium to the porphyrin is efficient.

As the pico- to nanosecond TA spectra are rather difficult to interpret due to the multitude of features and potentially parallel photophysical processes, we had a closer look at the nano- to microsecond spectra and dynamics. On the nanosecond timescale, the shapes of the transient absorption spectra of **Ac-3a**, **4a** and **6a** are rather similar (see the Supporting Information). The decay of the TA signals on this timescale should largely reflect the recombination dynamics of the triplet and CS states in these compounds. In fact, the dynamics of the TA signals of all three compounds **Ac-3a**, **4a** and **6a** can be well described by the sum of two exponentials with a nano- and microsecond component indicating two processes, as shown in Figure 17. In the case of the reference porphyrin **Ac-3a**, we obtained inverse rate constants of 12 ns and 7 µs.

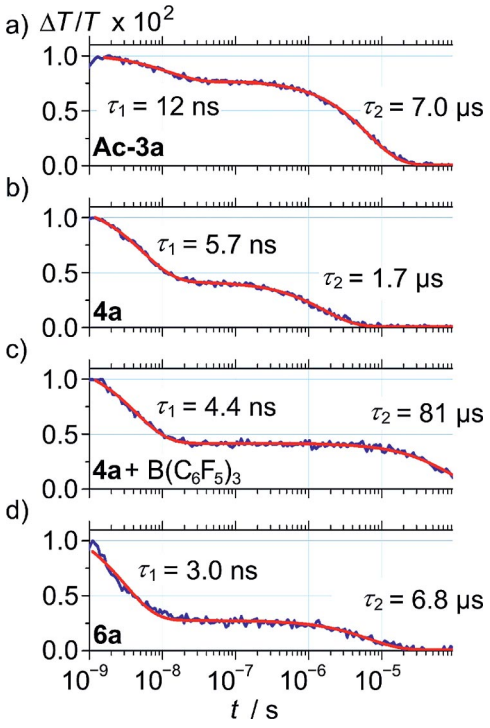

Figure 17. ns–µs transient absorption dynamics of a) **Ac-3a**, b) **4a**, c) **4a** plus 100 equiv. $B(C_6F_5)_3$ and d) **6a** in THF solution after excitation at λ_{exc} = 532 nm. The dynamics were monitored in the spectral region 550–620 nm. The solid red lines represent exponential fits to the data and the inverse decay rates are also shown. Note the significantly slower TA signal decay for compound **4a** plus additive indicating the stabilisation of the CS state by the Lewis acid.

The nanosecond lifetime τ_1 corresponds approximately to the measured fluorescence lifetime of around 10 ns within the error that can be expected between the two different experimental techniques. The microsecond lifetime τ_2 can be assigned to the decay of the porphyrin triplet T_1 state generated by intersystem crossing from the porphyrin singlet S_1 state due to its significantly longer lifetime in the range typical for the decay of triplets. Fitting the signal dynamics of **4a** yields inverse rate constants of 5.7 ns and 1.7 µs. The former is shorter than the lifetime observed for the reference porphyrin **Ac-3a**, indicating additional decay channels, but longer than the observed fluorescence lifetime of compound **4a** (in CH_2Cl_2), which might be a solvent effect. However, in this case we most probably approached the temporal resolution of our ns–µs TA set-up, which is about several nanoseconds. The second longer-lived component has a considerably shorter lifetime than the porphyrin triplet-state lifetime observed for compound **Ac-3a** and thus appears to originate from a state other than the T_1 triplet. Given that the efficiency of ET obtained by analysis of the fluorescence quenching is Φ_{ET} = 0.93, we assign this component to the decay of the $Q^{\cdot-}$-$P^{\cdot+}$ CS state, which is formed in high yield in the case of compound **4a**. The dynamics of the TA signals of compound **6a** can be fitted with inverse rates of τ_1 = 3 ns and τ_2 = 6.8 µs. Although the former is

EurJIC European Journal of Inorganic Chemistry www.eurjic.org FULL PAPER

certainly limited by the temporal resolution of our set-up and represents the sub-nanosecond dynamics of the PET processes, the latter component is close to the triplet lifetime observed for compound **Ac-3a**. This appears reasonable as in this compound no features of porphyrin radicals should be observed from the final $Q^{\bullet-}$-P-$Fc^{\bullet+}$ CS state after electron transfer to Q and from Fc are complete. Therefore we observe the decay of a fraction of porphyrin triplet states created either by ISC from the porphyrin singlet state directly after photoexcitation or, which is more likely, by a transition of the initial Q-$P^{\bullet-}$-$Fc^{\bullet+}$ CS state (1.46 eV, Table 8 and Figure 7) into the T_1 state of the porphyrin (1.43 eV[3f]).

As suggested by the DFT calculations, a CS state involving the quinone can be stabilised by coordinating a Lewis acid to the quinone carbonyl groups. Excess tris(pentafluorophenyl)boron was added to **4a** and **6a** in THF and the ps–ns as well as ns–µs transient absorption spectra and dynamics were studied (see Figure 17 and the Supporting Information). Some spectral but mostly temporal differences were observed with respect to the spectra and dynamics of **4a** and **6a** in the absence of the Lewis acid. The most striking observation is a pronounced decrease in the decay rate, in other words, increase in the lifetime of the $Q^{\bullet-}$-$P^{\bullet+}$ CS state observed for compound **4a**. In fact, the ns–µs TA experiments showed that the lifetime of the CS state is significantly increased from τ_2 = 1.7 µs to τ_2 = 80 µs upon addition of $B(C_6F_5)_3$ (cf. Figure 17, b,c). This suggests that the $Q^{\bullet-}$-$P^{\bullet+}$ CS state is significantly stabilised by the Lewis acid, as suggested by the DFT calculations, and further supports our assignment of the dynamics to the recombination of the charge-separated state. Although the effect is pronounced for **4a**, it is much less obvious for **6a**. This appears reasonable as we assigned the dynamics in the latter to the recombination of the porphyrin triplet state, which should not be affected by the presence of the Lewis acid.

Conclusions

Anthraquinone–porphyrin dyads (Q-P, **4**), anthraquinone–porphyrin–ferrocene triads (Q-P-Fc, **6**) and zincated triads [Q-(Zn)P-Fc, **Zn-6**] with *meso* substituents Ar of increasing electron-withdrawing character in the porphyrin component have been designed and synthesised by amide coupling (Ar = 4-C_6H_4O*n*Bu, 4-C_6H_4OMe, Mes, 4-C_6H_4Me, C_6H_5, 4-C_6H_4F, 4-$C_6H_4CF_3$ and C_6F_5). Based on this modular amide-coupling approach, a Q-P^{C6H5}-P^{C6H4Me}-Fc tetrad (**9**) was constructed. In the ground states of **4**, **6**, **Zn-6** and **9**, only marginal interactions between the individual building blocks Q, P and Fc are observed, and energy transfer between the two porphyrins in **9** is possible. The fluorescence of dyads **4** is quenched by oxidative photoinduced electron transfer (PET). The rate of ET increases by several orders of magnitude with increasing electron-donating power of the *meso* substituent Ar (k_{ET} = 0.003×10^9 to 1.5×10^9 s^{-1}) due to the increased driving force $\Delta(\Delta G_{ET})$ = –0.3 eV. In triads **6** an additional reductive PET pathway is thermodynamically feasible. This ET pathway is favoured by electron-withdrawing *meso* substituents Ar [k_{ET} = 4×10^9 to 38×10^9 s^{-1}; $\Delta(\Delta G_{ET})$ = –0.2 eV]. Comparable rates and driving forces for reductive and oxidative quenching are found for Ar = 4-C_6H_4O*n*Bu, 4-C_6H_4OMe and 4-C_6H_4Me in triads **6**. The zinc porphyrins **Zn-6** are basically non-fluorescent. If the major deactivation in zinc conjugates indeed occurs by PET, both pathways feature similar driving forces for Ar = 4-C_6H_4O*n*Bu, 4-C_6H_4OMe, Mes, 4-C_6H_4Me and C_6H_5. In tetrad **9**, both pathways are also feasible, although reductive PET (ΔG_{ET} = –0.48 eV; k_{ET} = 2.66×10^9 s^{-1}) is preferred over oxidative PET (ΔG_{ET} = –0.26 eV; k_{ET} = 0.363×10^9 s^{-1}). With these preparative, spectroscopic, electrochemical and theoretical results in hand, more complex architectures with well-defined excited-state energies in a structurally precisely organised manner can be envisaged.

Supporting Information (see footnote on the first page of this article): Experimental and analytical details, normalised absorption and emission spectra of selected Q-P dyads, Q-P-Fc triads and reference porphyrins in CH_2Cl_2n DFT (B3LYP/LANL2DZ, PCM) calculated frontier orbitals of **Zn-6b**, **Zn-6g**, **Zn-6h** and **9**, absorption spectra of *N*-ethylanthraquinone-2-carboxamide treated with $CoCp^*_2$ in THF; ns to µs transient absorption spectra of **Ac-3a**, **4a**, **4a** + $B(C_6F_5)_3$, **6a** and **6a** + $B(C_6F_5)_3$ in THF; after excitation at λ_{exc} = 532 nm, energies (eV) of relevant frontier molecular orbitals of the Q-P dyads **4a**–**4h** determined by DFT (B3LYP/LANL2DZ, PCM), energies (eV) of relevant frontier molecular orbitals of the Q-P-Fc triads **6a**–**6i** and Q-P-Fc triads **Zn-6a**–**Zn-6i** determined by DFT (B3LYP/LANL2DZ, PCM), Cartesian coordinates of DFT-optimised geometries.

Acknowledgments

This work was supported by the Deutsche Forschungsgemeinschaft (DFG) (He 2778-6/1). J. R. O. and M. M. thank the Max Planck Graduate Center for support and F. L. (all Max Planck Institute for Polymer Research of Mainz, Germany) thanks the Max Planck Society for funding the Max Planck Research group.

[1] a) M. G. Rockley, M. W. Windsor, R. J. Cogdellt, W. W. Parsont, H. Neurath, *Proc. Natl. Acad. Sci. USA* **1975**, *72*, 2251–2255; b) K. J. Kaufmann, P. L. Dutton, T. L. Netzel, J. S. Leigh, P. M. Rentzepis, *Science* **1975**, *188*, 1301–1304; c) J. J. Katz, J. R. Norris, L. L. Shipman, M. C. Thurnauer, M. R. Wasielewski, *Ann. Rev. Biophys. Bioeng.* **1978**, *7*, 393–434; d) J. Deisenhofer, O. Epp, K. Miki, R. Huber, H. Michel, *J. Mol. Biol.* **1984**, *180*, 385–398.

[2] a) M. R. Wasielewski, *Chem. Rev.* **1992**, *92*, 435–461; b) A. Harriman, J.-P. Sauvage, *Chem. Soc. Rev.* **1996**, *25*, 41–48; c) D. Gust, T. A. Moore, A. L. Moore, *Acc. Chem. Res.* **2001**, *34*, 40–48; d) L. Sun, L. Hammarström, B. Åkermark, S. Styring, *Chem. Soc. Rev.* **2001**, *30*, 36–49; e) S. Fukuzumi, *Org. Biomol. Chem.* **2003**, *1*, 609–620.

[3] a) A. R. McIntosh, A. Siemiarczuk, J. R. Bolton, M. J. Stillman, T.-F. Ho, A. C. Weedon, *J. Am. Chem. Soc.* **1983**, *105*, 7215–7223; b) A. Siemiarczuk, A. R. McIntosh, T.-F. Ho, M. J. Stillman, K. J. Roach, A. C. Weedon, J. R. Bolton, J. S. Connolly, *J. Am. Chem. Soc.* **1983**, *105*, 7224–7230; c) M. R. Wasielewski, M. P. Niemczyk, W. A. Svec, E. B. Pewitt, *J. Am. Chem. Soc.* **1985**, *107*, 1080–1082; d) D. Gust, T. A. Moore, P. A. Liddell, G. A. Nemeth, L. R. Makings, A. L. Moore, D. Barrett, P. J. Pessiki, R. V. Bemasson, M. Rougée, C. Chachaty, F. C.

De Schryver, M. Van der Auweraer, A. R. Holzwarth, J. S. Connolly, *J. Am. Chem. Soc.* **1987**, *109*, 846–856; e) A. D. Joran, B. A. Leland, P. M. Felker, A. H. Zewail, J. J. Hopfield, P. B. Dervan, *Nature* **1987**, *327*, 508–511; f) J. A. Schmidt, A. R. McIntosh, A. C. Weedon, J. R. Bolton, J. S. Connolly, J. K. Hurley, M. R. Wasielewski, *J. Am. Chem. Soc.* **1988**, *110*, 1733–1740; g) J. von Gersdorff, M. Huber, H. Schubert, D. Niethammer, B. Kirste, M. Plato, K. Möbius, H. Kurreck, R. Eichberger, R. Kietzmann, F. Willig, *Angew. Chem. Int. Ed. Engl.* **1990**, *29*, 670–672; *Angew. Chem.* **1990**, *102*, 690–692; h) J. Zimmermann, J. Von Gersdorff, H. Kurreck, B. Ridder, *J. Photochem. Photobiol. B: Biology* **1997**, *40*, 209–217; i) J. P. Sumida, P. A. Liddell, S. Lin, A. N. Macpherson, G. R. Seely, A. L. Moore, T. A. Moore, D. Gust, *J. Phys. Chem. A* **1998**, *102*, 5512–5519; j) O. Korth, A. Wiehe, H. Kurreck, B. Röder, *Chem. Phys.* **1999**, *246*, 363–372; k) Y. K. Kang, I. V. Rubtsov, P. M. Iovine, J. Chen, M. J. Therien, *J. Am. Chem. Soc.* **2002**, *124*, 8275–8279; l) J. Springer, G. Kodis, L. De Garza, A. L. Moore, T. A. Moore, D. Gust, *J. Phys. Chem. A* **2003**, *107*, 3567–3575; m) P. P. Kumar, G. Premaladha, B. G. Maiya, *J. Chem. Sci.* **2005**, *117*, 193–201.

[4] a) A. M. Brun, A. Harriman, V. Heitz, J.-P. Sauvage, *J. Am. Chem. Soc.* **1991**, *113*, 8657–8663; b) V. Heitz, S. Chardon-Noblat, J.-P. Sauvage, *Tetrahedron Lett.* **1991**, *32*, 197–198; c) E. K. L. Yeow, P. J. Sintic, N. M. Cabral, J. N. H. Reek, M. J. Crossley, K. P. Ghiggino, *Phys. Chem. Chem. Phys.* **2000**, *2*, 4281–4291; d) K. Kilså, J. Kajanus, A. N. Macpherson, J. Mårtensson, B. Albinsson, *J. Am. Chem. Soc.* **2001**, *123*, 3069–3080; e) S. Fukuzumi, K. Ohkubo, W. E. Z. Ou, J. Shao, K. M. Kadish, J. A. Hutchison, K. P. Ghiggino, P. J. Sintic, M. J. Crossley, *J. Am. Chem. Soc.* **2003**, *125*, 14984–14985; f) J. H. Jang, H. J. Kim, H.-J. Kim, C. H. Kim, T. Joo, D. Won Cho, M. Yoon, *Bull. Korean Chem. Soc.* **2007**, *28*, 1967–1972; g) J. Fortage, J. Boixel, E. Blart, L. Hammarström, H. C. Becker, F. Odobel, *Chem. Eur. J.* **2008**, *14*, 3467–3480; h) J. Fortage, A. Scarpaci, L. Viau, Y. Pellegrin, E. Blart, M. Falkenstrçm, L. Hammarström, I. Asselberghs, R. Kellens, W. Libaers, K. Clays, M. P. Eng, F. Odobel, *Chem. Eur. J.* **2009**, *15*, 9058–9067; i) J. Fortage, J. Boixel, E. Blart, H. C. Becker, F. Odobel, *Inorg. Chem.* **2009**, *48*, 518–526.

[5] a) D. Kuciauskas, S. Lin, G. R. Seely, A. L. Moore, T. A. Moore, T. Drovetskaya, C. A. Reed, P. D. W. Boyd, *J. Phys. Chem.* **1996**, *100*, 15926–15932; b) C. Luo, D. M. Guldi, H. Imahori, K. Tamaki, Y. Sakata, *J. Am. Chem. Soc.* **2000**, *122*, 6535–6551; c) H. Imahori, N. V. Tkachenko, V. Vehmanen, K. Tamaki, H. Lemmetyinen, Y. Sakata, S. Fukuzumi, *J. Phys. Chem. A* **2001**, *105*, 1750–1756; d) V. Vehmanen, N. V. Tkachenko, H. Imahori, S. Fukuzumi, H. Lemmetyinen, *Spectrochim. Acta Part A* **2001**, *57*, 2229–2244; e) H. Imahori, D. M. Guldi, K. Tamaki, Y. Yoshida, C. Luo, Y. Sakata, S. Fukuzumi, *J. Am. Chem. Soc.* **2001**, *123*, 6617–6628; f) H. Imahori, K. Tamaki, Y. Araki, Y. Sekiguchi, O. Ito, Y. Sakata, S. Fukuzumi, *J. Am. Chem. Soc.* **2002**, *124*, 5165–5174; g) H. Imahori, Y. Sekiguchi, Y. Kashiwagi, T. Sato, Y. Araki, O. Ito, H. Yamada, S. Fukuzumi, *Chem. Eur. J.* **2004**, *10*, 3184–3196; h) M. U. Winters, E. Dahlstedt, H. E. Blades, C. J. Wilson, M. J. Frampton, H. L. Anderson, B. Albinsson, *J. Am. Chem. Soc.* **2007**, *129*, 4291–4297; i) C. Wijesinghe, M. E. El-Khouly, M. E. Zandler, S. Fukuzumi, F. D′Souza, *Chem. Eur. J.* **2013**, *19*, 9629–9638.

[6] a) D. Gust, T. A. Moore, A. L. Moore, F. Cao, D. Luttrul, J. M. Degraziano, X. C. Ma, L. R. Makings, S. Lee, T. T. Trier, E. Bittersmann, G. R. Seely, S. Woodward, R. V. Bensasson, M. Roug, F. C. De Schryver, M. Van der Auweraer, *J. Am. Chem. Soc.* **1991**, *113*, 3638–3649; b) D. Gust, T. A. Moore, A. L. Moore, A. N. Macpherson, A. Lopez, J. M. DeGraziano, I. Gouni, E. Bittersmann, G. R. Seely, F. Gao, R. A. Nieman, X. C. Ma, L. J. Demanche, S. Hung, D. K. Luttrull, S. Lee, P. K. Kerrigan, *J. Am. Chem. Soc.* **1993**, *115*, 11141–11152; c) S. L. Gould, G. Kodis, R. E. Palacios, L. De La Garza, A. Brune, D. Gust, T. A. Moore, A. L. Moore, *J. Phys. Chem. B* **2004**, *108*, 10566–10580.

[7] a) R. Ciasson, E. J. Lee, X. Zbao, M. S. Wrighton, *J. Phys. Chem.* **1993**, *97*, 2596–2601; b) M. Kubo, Y. Mori, M. Otani, M. Murakami, Y. Ishibashi, M. Yasuda, K. Hosomizu, H. Miyasaka, H. Imahori, S. Nakashima, *Chem. Phys. Lett.* **2006**, *429*, 91–96; c) H. Mansour, M. E. El-khouly, S. Y. Shaban, O. Ito, N. Jux, *J. Porphyrins Phthalocyanines* **2007**, *11*, 719–728; d) V. S. Shetti, M. Ravikanth, *Eur. J. Org. Chem.* **2010**, 494–508.

[8] a) R. A. Marcus, *J. Chem. Phys.* **1956**, *24*, 979–989; b) R. A. Marcus, *Annu. Rev. Phys. Chem.* **1964**, *15*, 155–196; c) R. A. Marcus, *Angew. Chem. Int. Ed. Engl.* **1993**, *32*, 1111–1121; *Angew. Chem.* **1993**, *105*, 1161–1172.

[9] a) S. Fukuzumi, K. Ohkubo, W. E. Z. Ou, J. Shao, K. M. Kadish, *J. Am. Chem. Soc.* **2003**, *125*, 14984–14985; b) M. Linke-Schaetzel, C. E. Anson, A. K. Powell, G. Buth, E. Palomares, J. D. Durrant, T. Silviu Balaban, J.-M. Lehn, *Chem. Eur. J.* **2006**, *12*, 1931–1940; c) B. M. J. M. Suijkerbuijk, R. J. M. Klein Gebbink, *Angew. Chem.* **2008**, *120*, 7506–7532; d) J. Fortage, J. Boixel, E. Blart, L. Hammarström, *Chem. Eur. J.* **2008**, *14*, 3467–3480; e) K. Kiyosawa, N. Shiraishi, T. Shimada, D. Masui, H. Tachibana, *J. Phys. Chem. C* **2009**, *113*, 11667–11673; f) J. Fortage, A. Scarpaci, L. Viau, Y. Pellegrin, E. Blart, M. Falkenström, L. Hammarström, I. Asselberghs, R. Kellens, W. Libaers, K. Clays, M. P. Eng, F. Odobel, *Chem. Eur. J.* **2009**, *15*, 9058–9067; g) A. C. Benniston, A. Harriman, P. Li, *J. Am. Chem. Soc.* **2010**, *132*, 26–27; h) H. Kon, T. Nagata, *Chem. Eur. J.* **2012**, *18*, 1781–1788.

[10] Y. Araki, Y. Yasumura, O. Ito, *J. Phys. Chem. B* **2005**, *109*, 9843–9848.

[11] J. Melomedov, A. Wünsche Von Leupoldt, M. Meister, F. Laquai, K. Heinze, *Dalton Trans.* **2013**, *42*, 9727–9739.

[12] a) A. Breivogel, K. Hempel, K. Heinze, *Inorg. Chim. Acta* **2011**, *374*, 152–162; b) D. Siebler, M. Linseis, T. Gasi, L. M. Carrella, R. F. Winter, C. Förster, K. Heinze, *Chem. Eur. J.* **2011**, *17*, 4540–4551; c) J. Dietrich, U. Thorenz, C. Förster, K. Heinze, *Inorg. Chem.* **2013**, *52*, 1248–1264; d) J. Dietrich, A. Wünsche von Leupoldt, M. Grabolle, U. Resch-Genger, K. Heinze, *Eur. J. Inorg. Chem.* **2013**, 3009–3019.

[13] a) K. Heinze, U. Wild, M. Beckmann, *Eur. J. Inorg. Chem.* **2007**, 617–623; b) K. Heinze, M. Beckmann, K. Hempel, *Chem. Eur. J.* **2008**, *14*, 9468–9480; c) K. Heinze, K. Hempel, *Chem. Eur. J.* **2009**, *15*, 1346–1358; d) G. Dirscherl, B. König, *Eur. J. Org. Chem.* **2008**, 597–634; e) D. Siebler, C. Förster, K. Heinze, *Dalton Trans.* **2011**, *40*, 3558–3575.

[14] K. Heinze, A. Reinhart, *Dalton Trans.* **2008**, 469–480.

[15] a) B. Bildstein, M. Malaun, H. Kopacka, K. Wurst, M. Mitterböck, K. Ongania, G. Opromolla, P. Zanello, *Organometallics* **1999**, *18*, 4325–4336; b) K. Heinze, M. Schlenker, *Eur. J. Inorg. Chem.* **2004**, 2974–2988.

[16] a) P. D. Rao, S. Dhanalekshmi, B. J. Littler, J. S. Lindsey, *J. Org. Chem.* **2000**, *65*, 7323–7344; b) A. K. Burrell, D. L. Officer, P. G. Plieger, D. C. W. Reid, *Chem. Rev.* **2001**, *101*, 2751–2796; c) J. S. Lindsey, *Acc. Chem. Res.* **2010**, *43*, 300–311; d) M. O. Senge, *Chem. Commun.* **2011**, *47*, 1943–1960.

[17] C. M. Carcel, J. K. Laha, R. S. Loewe, P. Thamyongkit, K. Schweikart, V. Misra, D. F. Bocian, J. S. Lindsey, N. Carolina, *J. Org. Chem.* **2004**, *69*, 6739–6750.

[18] a) B. J. Littler, Y. Ciringh, J. S. Lindsey, *J. Org. Chem.* **1999**, *64*, 2864–2872; b) K. Heinze, A. Reinhart, *Z. Naturforsch. B* **2005**, *60*, 758–762; c) T. Rohand, E. Dolusic, T. H. Ngo, W. Maes, W. Dehaen, *ARKIVOC* **2007**, *x*, 307–324.

[19] K. Phukan, M. Ganguly, N. Devi, *Synth. Commun.* **2009**, *39*, 2694–2701.

[20] S. B. Colbran, S. T. Lee, D. G. Lonnon, F. J. D. Maharaj, A. M. McDonagh, K. A. Walker, R. D. Young, *Organometallics* **2006**, *25*, 2216–2224.

[21] P. Heier, C. Förster, D. Schollmeyer, N. Boscher, P. Choquet, K. Heinze, *Dalton Trans.* **2013**, *42*, 906–917.

[22] A. Weller, *Z. Phys. Chem. (Muenchen Ger.)* **1982**, *133*, 93–98.
[23] M. J. Frisch, G. W. Trucks, H. B. Schlegel, G. E. Scuseria, M. A. Robb, J. R. Cheeseman, G. Scalmani, V. Barone, B. Mennucci, G. A. Petersson, H. Nakatsuji, M. Caricato, X. Li, H. P. Hratchian, A. F. Izmaylov, J. Bloino, G. Zheng, J. L. Sonnenberg, M. Hada, M. Ehara, K. Toyota, R. Fukuda, J. Hasegawa, M. Ishida, T. Nakajima, Y. Honda, O. Kitao, H. Nakai, T. Vreven, J. A. Montgomery Jr., J. E. Peralta, F. Ogliaro, M. Bearpark, J. J. Heyd, E. Brothers, K. N. Kudin, V. N. Staroverov, R. Kobayashi, J. Normand, K. Raghavachari, A. Rendell, J. C. Burant, S. S. Iyengar, J. Tomasi, M. Cossi, N. Rega, J. M. Millam, M. Klene, J. E. Knox, J. B. Cross, V. Bakken, C. Adamo, J. Jaramillo, R. Gomperts, R. E. Stratmann, O. Yazyev, A. J. Austin, R. Cammi, C. Pomelli, J. W. Ochterski, R. L. Martin, K. Morokuma, V. G. Zakrzewski, G. A. Voth, P. Salvador, J. J. Dannenberg, S. Dapprich, A. D. Daniels, O. Farkas, J. B. Foresman, J. V. Ortiz, J. Cioslowski, D. J. Fox, *Gaussian 09*, revision A.02, Gaussian, Inc., Wallingford, CT, **2009**.
[24] M. Gouterman, *J. Chem. Phys.* **1959**, *30*, 1139–1161.
[25] D. Holten, D. F. Bocian, J. S. Lindsey, *Acc. Chem. Res.* **2002**, *35*, 57–69.
[26] For the use of Lewis acidic metal ions to stabilise a CS state, see: a) S. Fukuzumi, K. Okamoto, H. Imahori, *Angew. Chem. Int. Ed.* **2002**, *41*, 620–622; *Angew. Chem.* **2002**, *114*, 642–644; b) S. Fukuzumi, K. Okamoto, Y. Yoshida, H. Imahori, Y. Araki, O. Ito, *J. Am. Chem. Soc.* **2003**, *125*, 1007–1013.
[27] N. G. Connelly, W. E. Geiger, *Chem. Rev.* **1996**, *96*, 877–910.
[28] D. Siebler, C. Förster, K. Heinze, *Eur. J. Inorg. Chem.* **2010**, 3986–3992.

Received: January 28, 2014
Published Online: February 27, 2014

7

AMINOFERROCENE AND FERROCENE AMINO ACID AS ELECTRON DONORS IN MODULAR PORPHYRIN-FERROCENE AND PORPHYRIN-FERROCENE-PORPHYRIN CONJUGATES

The following article was published in *European Journal of Inorganic Chemistry* and is reprinted with permission from Melomedov et al.[200]

My contribution to this work are pages 141-143 (pp 2911-2912), presenting the results of time-resolved transient absorption spectroscopy of selected compounds.

EurJIC European Journal of Inorganic Chemistry
ChemPubSoc Europe
FULL PAPER

DOI:10.1002/ejic.201402138

Aminoferrocene and Ferrocene Amino Acid as Electron Donors in Modular Porphyrin–Ferrocene and Porphyrin–Ferrocene–Porphyrin Conjugates

Jascha Melomedov,[a] Julian Robert Ochsmann,[b] Michael Meister,[b] Frédéric Laquai,[b] and Katja Heinze*[a]

Keywords: Artificial photosynthesis / Energy transfer / Electron transfer / Metallocenes / Porphyrins

New amide-linked porphyrin–ferrocene conjugates [M(P^{Ar})–Fc] were prepared from aminoferrocene and a carboxy-substituted *meso*-tetraaryl-porphyrin [M = 2H, Zn; Ar = mesityl (Mes), C_6F_5: **3a**, **3e**, **Zn-3a**, **Zn-3e**]. A further porphyrin building block was attached to the second cyclopentadienyl ring of the ferrocene moiety to give the metallopeptides M(P^{Mes})–Fc–M(P^{Ar}) (M = 2H, Zn; Ar = C_6H_5, 4-C_6H_4F: **6b**, **6c**, Zn-**6b**, Zn-**6c**). The effects of the Ar substituents, the porphyrin central atom M and the presence of the second porphyrin at the ferrocene hinge on the excited-state dynamics was studied by optical absorption spectroscopy, electrochemistry, steady-state emission, time-resolved fluorescence measurements and transient absorption pump–probe spectroscopy in addition to density functional theory calculations. In the ground state, only weak interactions were revealed between the ferrocene and porphyrin units by optical absorption spectroscopy and electrochemical measurements. However, the porphyrin emission is strongly quenched with respect to that of the reference porphyrins without the ferrocene moieties. Fluorescence is partially recovered at lower temperatures, which suggests an activated excited-state decay process. All excited-state lifetimes are reduced with respect to those of the reference porphyrins. The quantum yields and lifetimes correlate with the porphyrin and ferrocene redox potentials. All observations point to photoinduced electron transfer from ferrocene to the porphyrin in the normal Marcus region as the dominant excited-state reactivity. The resulting charge-separated states of selected conjugates were studied by ns–µs transient absorption pump–probe spectroscopy. Hints for the feasibility of singlet–singlet energy transfer between cofacial porphyrins were found in tweezers **6** and **Zn-6**.

Introduction

To mimic the light-harvesting and charge-separating processes in natural photosynthesis, a plethora of model compounds have been designed and thoroughly investigated.[1–4,6] These artificial photosynthetic reaction centres typically consist of electron-donor and electron-acceptor units combined with a chromophore. Porphyrins and metalloporphyrins are highly suited and well-established building elements for biomimetic model compounds[1–4,6] owing to their favourable photophysical properties and their outstanding role in plant and bacterial photosynthesis. In artificial reaction centres, porphyrins can act as electron donors[2] or acceptors.[3] Typically, porphyrins function as electron acceptors in porphyrin–ferrocene arrays [M(P)–Fc], and the organometallic ferrocene acts as an electron donor.[4,6]

Many ferrocene derivatives are stable, feature well-defined Fc/Fc^+ redox states and are able to reduce the S_1 excited state of the porphyrin.[4,5] This renders ferrocene highly suitable as an electron donor in model compounds for artificial charge separation and molecular electronic devices.[1,4,6,7]

Recently, we reported a modular synthetic strategy for amide-linked architectures with porphyrin amino acids as chromophores, quinones as electron acceptors and ferrocenes as electron donors. In these conjugates, both oxidative photoinduced electron transfer (PET), that is, excited porphyrin to quinone, and reductive PET pathways, namely, ferrocene to excited porphyrin, have been identified (Scheme 1).[1f]

The core building block of these artificial reaction centres is a *trans*-AB_2C-substituted *meso*-tetraaryl porphyrin amino acid,[9,10] and different aryl groups of varying electron-donating or -withdrawing power at the *meso* positions dictate the preferred PET pathway. To specifically focus on the reductive pathway, new porphyrin–ferrocene conjugates and porphyrin–ferrocene–porphyrin tweezers[6] with tuneable electronic properties of the porphyrin electron acceptor as well as of the ferrocene electron donor have been designed in the present study. Aminoferrocene[5a] and

[a] Institute of Inorganic Chemistry and Analytical Chemistry, Johannes Gutenberg-University of Mainz, Duesbergweg 10-14, 55128 Mainz, Germany
E-mail: katja.heinze@uni-mainz.de
http://www.ak-heinze.chemie.uni-mainz.de/
[b] Max Planck Institute for Polymer Research, Ackermannweg 10, 55128 Mainz, Germany
Supporting information for this article is available on the WWW under http://dx.doi.org/10.1002/ejic.201402138.

EurJIC European Journal of Inorganic Chemistry
www.eurjic.org FULL PAPER

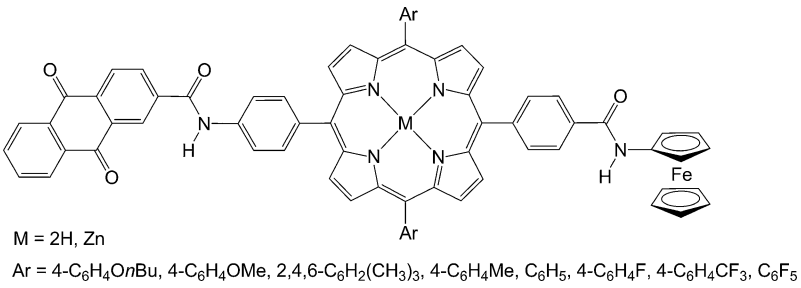

Scheme 1. Artificial photosynthetic reaction centres assembled through amide bonds and based on *trans*-AB_2C-substituted porphyrin amino acids, anthraquinone carboxylic acid and aminoferrocene.[1f]

ferrocene amino acid (*N*-Fmoc-protected; Fmoc = 9-fluorenylmethoxycarbonyl)[5a] were employed as electron donors with different redox potentials. Furthermore, the orthogonal amine/acid substitution pattern of the latter allows straightforward access to unsymmetric 1,1′-disubstituted ferrocenes with two different porphyrins. We report the synthesis of M(P^{Ar})–Fc dyads [M = 2H, Zn; Ar = mesityl (Mes), C_6F_5: **3a**, **3e**, **Zn-3a**, **Zn-3e**) by amide coupling of a porphyrin monoacid with aminoferrocene. *N*-Fmoc-protected conjugates *N*-Fmoc–Fc–P^{Ar} (Ar = C_6H_5, 4-C_6H_4F, 4-$C_6H_4CF_3$, C_6F_5: **5b**–**5e**) were introduced as versatile building blocks by coupling porphyrin amino acid esters with *N*-Fmoc-protected ferrocene amino acid. Finally, bis(porphyrin) tweezers P^{Mes}–Fc–P^{Ar} (**6b** and **6c**) are accessible from building blocks **5b** and **5c** and a porphyrin acid by amide coupling. Metallation yields the corresponding zinc(II) porphyrins Zn(P^{Mes})–Fc–Zn(P^{Ar}) (Zn-**6b** and Zn-**6c**). All new compounds were fully characterised by standard techniques in addition to detailed photophysical and redox chemical characterisation. Density functional calculations were employed to further underscore the experimental results.

Results and Discussion

The porphyrin starting materials and reference compounds **1a**, **2a**, Zn-**1a**, **1e**, **2e**, **4b**–**4e**, Ac-**4b**–Ac-**4e**, Zn-Ac-**4b** and Zn-Ac-**4c** were prepared according to literature procedures.[8,10] The synthesis and characterisation of reference porphyrin [10,20-bis(pentafluorophenyl)-5,15-bis(4-methoxycarbonylphenyl)porphyrinato]zinc(II) (Zn-**1e**) is described in the Experimental Section. All analytical data are collected in the Supporting Information.

The new porphyrin–ferrocene (P^{Ar}–Fc) conjugates **3a** and **3e** were prepared in a two-step procedure from *trans*-A_2B_2 porphyrin diesters **1a**/**1e** (Ar = Mes,[1f,2d,8,10] C_6F_5)[1f,10] by partial hydrolysis to give monoacids **2a**/**2e**, followed by in situ acid activation with thionyl chloride and coupling with aminoferrocene.[5a] Metallation of the dyads

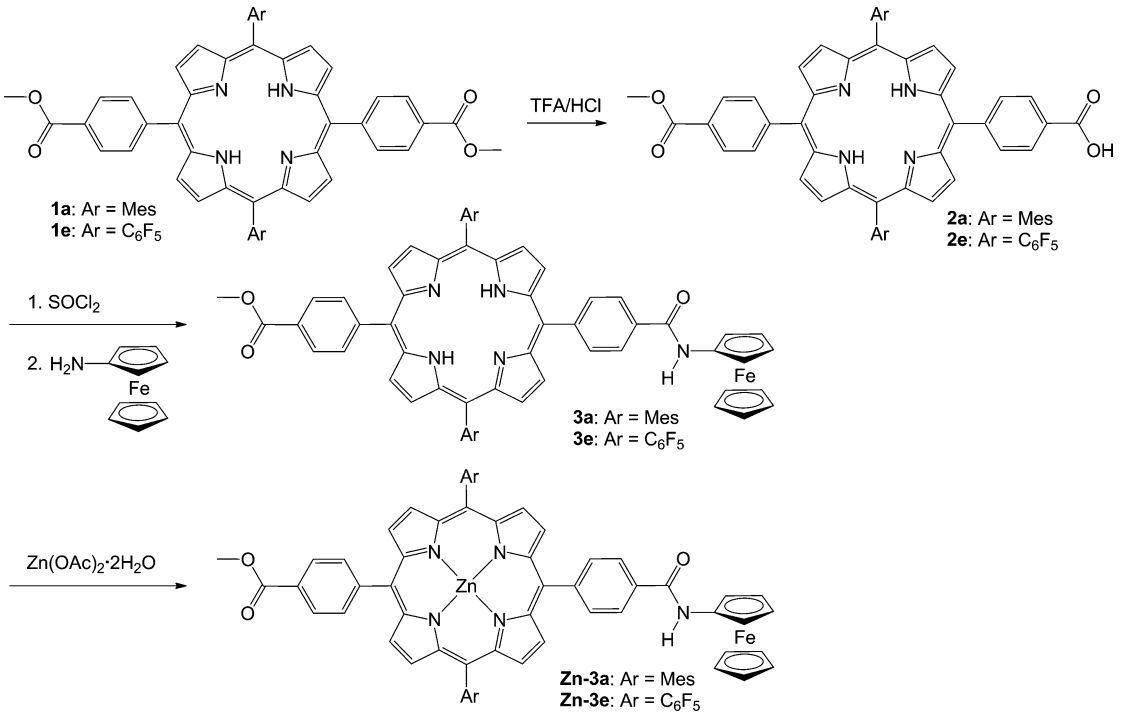

Scheme 2. Syntheses of **3** and Zn-**3** from aminoferrocene.

EurJIC European Journal of Inorganic Chemistry www.eurjic.org FULL PAPER

3 with zinc(II) acetate dihydrate gave the corresponding ferrocenylzinc(II) porphyrins [Zn(P^{Ar})–Fc] Zn-**3a** and Zn-**3e** (Scheme 2).[1f,9,10]

The key building block of 1,1′-ferrocenylenebis(porphyrins) **6** is the *N*-Fmoc-protected ferrocene amino acid.[5a] It was convenient to first couple a porphyrin amino ester **4b**–**4e**[1f,9,10] to the C terminus of the central ferrocene unit to give *N*-Fmoc–Fc–P^{Ar} (Ar = C_6H_5, 4-C_6H_4F, 4-$C_6H_4CF_3$, C_6F_5: **5b**–**5e**). To prove the synthetic concept of adding a further porphyrin to **5**, the *N*-Fmoc protecting groups of **5b** and **5c** were removed with tris(2-aminoethyl)amine, and finally the second porphyrin was attached to the N terminus after activation of the porphyrin acid **2a** with 1-chloro-*N*,*N*,2-trimethyl-1-propenylamine (Ghosez's reagent),[11] similar to the synthesis of conjugates **3** (Scheme 3). Again, metallation of **6b** or **6c** with zinc(II) acetate dihydrate yielded the corresponding trimetallic Zn–Fe–Zn complexes Zn-**6b** and Zn-**6c**.[1f,9,10]

The correct compositions of all of the new compounds **3**, Zn-**3**, **5**, **6** and Zn-**6** were established by multinuclear NMR spectroscopy (^1H, ^{13}C and ^{19}F), IR and UV/Vis spectroscopy, as well as (high-resolution) mass spectrometry. The appearance of the amide proton resonances of **3**, Zn-**3** and **5** in $CDCl_3$ at $\delta \approx 9.20$ ppm indicates the successful formation of the amide bonds. For tweezers **6** in [D_8]tetrahydrofuran ([D_8]THF), two amide proton resonances were found at $\delta \approx 9.75$ ppm for the FcNH amide proton and δ = 10.21–10.42 ppm for the P^{Ar}NH amide proton, which suggests that there are NH···O hydrogen bonds to the THF solvent. Interestingly, all tweezers **6** display only a single amide resonance at $\delta > 9$ ppm in $CDCl_3$, which indicates that only one NH group forms hydrogen bonds. This finding suggests that an intramolecular hydrogen bond (IHB) across the ferrocene moiety might be present in $CDCl_3$ solution. Such IHBs have been frequently observed for 1,1′-disubstituted ferrocenes with amide arms in weakly coordinating solvents.[5] The IR spectra of Zn-**6b** in CH_2Cl_2 were recorded, and indeed two NH absorption bands were found at 3430 and 3299 cm^{-1}; these bands clearly indicate the simultaneous presence of free and hydrogen-bonded NH groups, respectively. The intramolecular nature of the hydrogen bond is shown by the retention of the NH_{free}/NH_{bonded} ratio as the samples are diluted (Figure 1, a). An optimised DFT model of Zn-**6b** (B3LYP, LANL2DZ, IEFPCM CH_2Cl_2) is displayed in Figure 1 (b), and the proposed NH···O IHB is illustrated. This type of IHB with an eight-membered ring is the most stable one according to literature precedent for other amide substituents at the 1,1′-disubstituted ferrocene.[5] The IHB results in a V-shape of the tweezers (Figure 1, b).

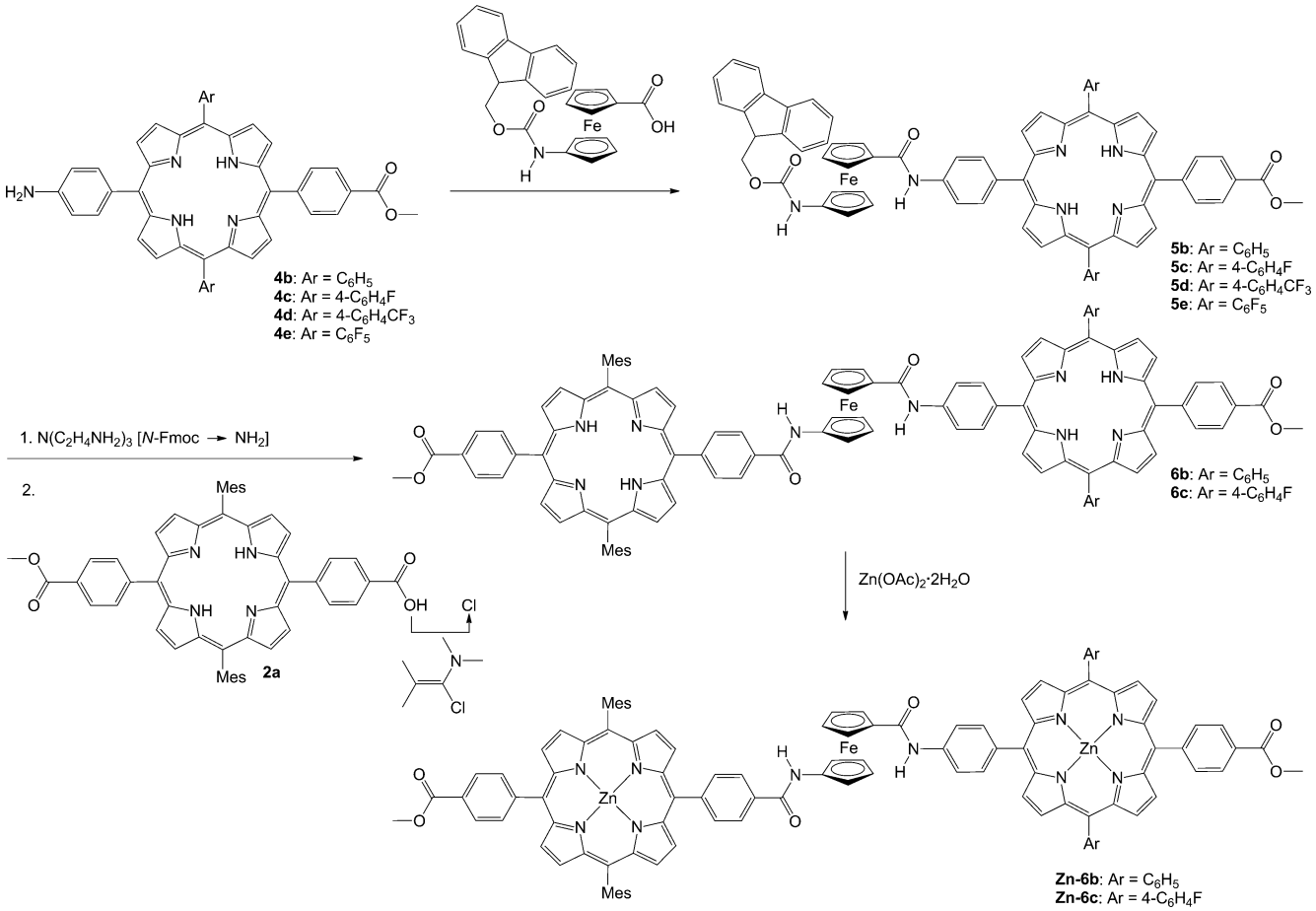

Scheme 3. Syntheses of **5**, **6** and Zn-**6** from *N*-Fmoc-protected ferrocene amino acid.

EurJIC European Journal of Inorganic Chemistry
www.eurjic.org
FULL PAPER

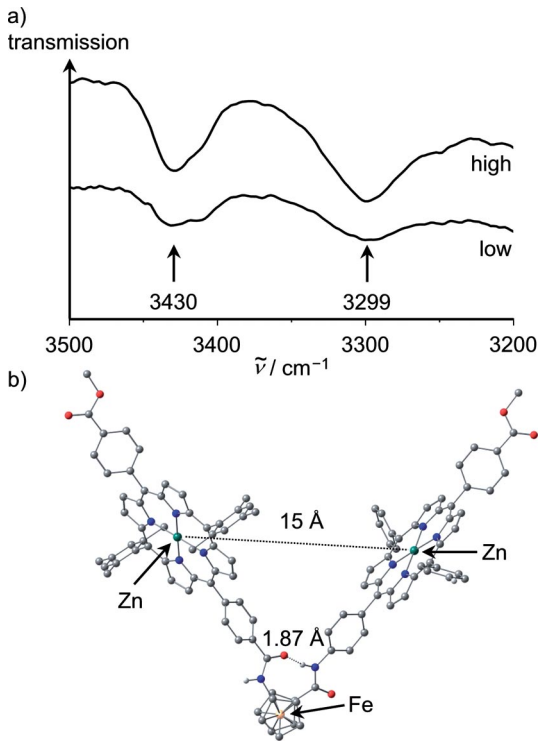

Figure 1. (a) IR spectra of Zn-**6b** at high and low concentrations in CH_2Cl_2 at room temperature. (b) Calculated (B3LYP/LANL2DZ, IEFPCM) V-shape structure of Zn-**6b** featuring an NH···O IHB (CH hydrogen atoms omitted for clarity).

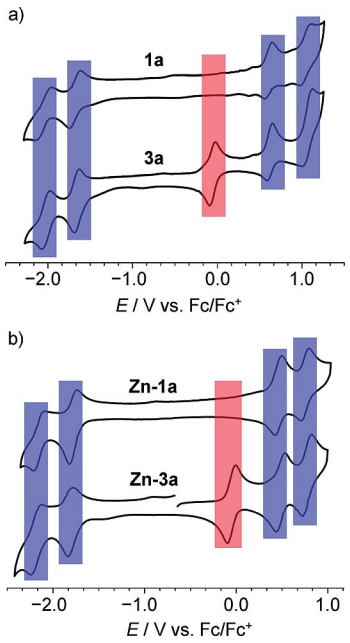

Figure 2. Cyclic voltammograms of **3a**, Zn-**3a**, **1a** and Zn-**1a** in $[n\text{Bu}_4\text{N}][\text{PF}_6]/\text{CH}_2\text{Cl}_2$.

All cyclic voltammograms of dyads **3**, Zn-**3** and **5** exhibit two reversible oxidation and two reversible reduction processes of the porphyrin moieties and a reversible wave for the ferrocene/ferrocenium couple. For instance, the cyclic voltammograms of **3a**, Zn-**3a** and the corresponding ferrocene-free reference porphyrins **1a** and Zn-**1a** are depicted in Figure 2. Hence, the Fc–P conjugates **3**, Zn-**3** and **5** can store and release up to five electrons. With increasing electron-withdrawing power of the *meso*-aryl substituents, an anodic shift of the porphyrin redox potentials was detected for **3**, **5** and Zn-**3**, as expected (Table 1).[1f,10] The ferrocene/ferrocenium wave was detected at $E_{1/2} \approx -0.09$ V for **3** and Zn-**3**, whereas the oxidation of the ferrocene amino acid building block in **5** is shifted by ca. 230 mV to $E_{1/2} = 0.13$–0.14 V, as expected from the additional carbonyl substituent at the ferrocene hinge (Figure 2, a and b).[5b]

In tweezers **6** and Zn-**6**, the redox waves of both porphyrins and the ferrocene unit ($E_{1/2} = 0.15$–0.16 V) are superimposed (Table 1). In all cases, reversible two-electron waves are observed for the first oxidations of the porphyrins. Zinc porphyrins Zn-**6** show a further 2e oxidation wave, whereas this wave is split into two 1e waves for the free-base bis(porphyrins) **6**. In the reductive region, free-base conjugates **6** show a 2e and a further 1e wave, whereas Zn-**6** feature only a single 1e reduction under our conditions. The Fc/Fc$^+$ potential remains essentially unaffected by the appendage of the second porphyrin to **5**. Vice versa, the influence of the ferrocene moiety on the redox features of the porphyrin is marginal.[1f] In essence, the redox properties are described by the properties of the individual building blocks, and the electronic interactions in the ground state between the building blocks of the dyads and tweezers is considered as very weak. This is exemplified by

Table 1. Redox potentials [V] of **3**, Zn-**3**, **5**, **6** and Zn-**6** vs. Fc/Fc$^+$ in $[n\text{Bu}_4\text{N}][\text{PF}_6]/\text{CH}_2\text{Cl}_2$ at room temperature.

	Ar	$E_{1/2}$(P, ox^3)	$E_{1/2}$(P, ox^2)	$E_{1/2}$(P, ox^1)	$E_{1/2}$(Fc, ox)	$E_{1/2}$(P, red^1)	$E_{1/2}$(P, red^2)
3a	Mes	–	1.040	0.590	–0.090	–1.690	–2.060
3e	C_6F_5	–	n.o.	0.890	–0.090	–1.430	–1.820
Zn-**3a**	Mes	–	0.730	0.440	–0.090	–1.830	–2.230
Zn-**3e**	C_6F_5	–	0.920	0.680	–0.100	–1.570	–1.980
5b	C_6H_5	–	0.890	0.580	0.140	–1.610	–1.980
5c	4-C_6H_4F	–	0.880	0.590	0.130	–1.620	–1.960
5d	4-$C_6H_4CF_3$	–	0.940	0.660	0.140	–1.570	–1.900
5e	C_6F_5	–	1.050	0.820	0.130	–1.400	–1.820
6b	C_6H_5	1.070[a]	0.880	0.600 (2e)	0.160	–1.640 (2e)	–2.000
6c	4-C_6H_4F	1.080[a]	0.880	0.610 (2e)	0.150	–1.630 (2e)	–1.960
Zn-**6b**	C_6H_5	–	0.740 (2e)	0.420 (2e)	0.160	–1.830	n.o.[b]
Zn-**6c**	4-C_6H_4F	–	0.730 (2e)	0.400 (2e)	0.150	–1.910	n.o.[b]

[a] Only clearly observed in the square-wave voltammogram. [b] Not observed.

EurJIC European Journal of Inorganic Chemistry www.eurjic.org FULL PAPER

the cyclic voltammograms of **5c** and **6c** and of their corresponding ferrocene-free reference porphyrins **1a** and Ac-**4c** in Figure 3. Bis(porphyrins) **6** and Zn-**6** can store and release up to eight and six electrons ($[\mathbf{6}]^{3-}\cdots[\mathbf{6}]^{5+}$; $[\text{Zn-}\mathbf{6}]^{-}\cdots[\text{Zn-}\mathbf{6}]^{5+}$), respectively; hence, these polyamides can be considered as multielectron stores.

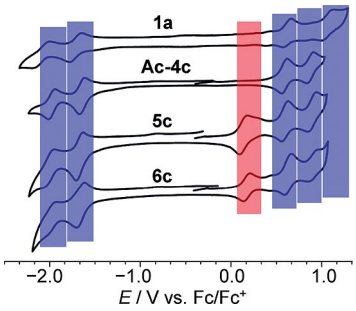

Figure 3. Cyclic voltammograms of **5c** and **6c** and reference porphyrins **1a** and Ac-**4c** in $[n\text{Bu}_4\text{N}][\text{PF}_6]/\text{CH}_2\text{Cl}_2$.

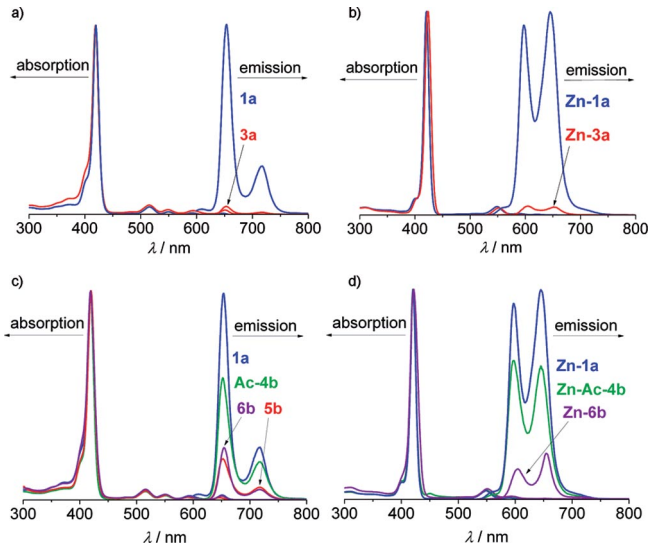

Figure 4. Normalised absorption and emission spectra of (a) **1a** and **3a**; (b) Zn-**1a** and Zn-**3a**; (c) **1a**, Ac-**4b**, **5b** and **6b** and (d) Zn-**1a**, Zn-Ac-**4b** and Zn-**6b** in CH_2Cl_2 at room temperature.

The electronic absorption spectra of **3**, Zn-**3**, **5**, **6** and Zn-**6** are essentially superpositions of the electronic transitions of the porphyrin constituents (Table 2). The absorption spectra of selected compounds and their references are shown in Figure 4. Fully analogous observations were made previously concerning the absorption data of amide-linked porphyrins[10] and anthraquinone–porphyrin–ferrocene triads.[1f] The characteristic absorption bands of the ferrocene moieties are not detectable in the absorption spectra of the dyads and tweezers because of the much lower absorptivities of (acetylamino)ferrocene (λ_{max} = 441 nm, ε = 215 $\text{M}^{-1}\text{cm}^{-1}$)[5a] and 1-(acetylamino)ferrocene-1′-carboxylic acid (λ_{max} = 441 nm, ε = 350 $\text{M}^{-1}\text{cm}^{-1}$)[5a] compared with those of the porphyrins (ε = 4–10 × 10^5 $\text{M}^{-1}\text{cm}^{-1}$). A comparison of the absorption spectra of the dyads and tweezers with those of the corresponding reference porphyrins indicates neither new bands nor appreciable shifts of porphyrin bands and, thus, a very weak electronic interaction between the chromophores in the ground state.[1f,10]

The emission spectroscopic data of the dyads and tweezers are summarised in Table 3. The typical porphyrin fluorescence is strongly quenched in the ferrocene porphyrins **3**, Zn-**3**, **5**, **6** and Zn-**6** relative to those of the respective reference compounds (Figure 4). Thus, the presence of ferrocene opens up new nonradiative pathways for the first excited singlet state (S_1) decay of the porphyrins. In particular, electron transfer from ferrocene to porphyrin should account for this observation, but energy transfer to ferrocene is also feasible.[4e,12] Notably, the most efficient fluorescence quenching in the series **3**, Zn-**3** and **5** was observed in dyads **3e**, Zn-**3e** and **5e** with the strongly electron-withdrawing C_6F_5 substituent, and the weakest decrease of fluorescence intensity was detected in the dyads with less electron-withdrawing substituents Mes, 4-C_6H_4F and C_6H_5 (Table 3). Similarly, the lower Fc/Fc^+ potential of **3e** ($E_{1/2}$ = –0.09 V) compared with that of **5e** ($E_{1/2}$ = +0.13 V) results in a stronger fluorescence quenching in **3e** (Φ = 0.0014) than in **5e** (Φ = 0.0094). These electronic influences already clearly

Table 2. Absorption data of **3**, **5**, **6** and Zn-**6** in CH_2Cl_2 at room temperature.

	Ar	Soret λ_{max} [nm] (ε/$\text{M}^{-1}\text{cm}^{-1}$)	$Q_y(1,0)$ λ_{max} [nm] (ε/10^4 $\text{M}^{-1}\text{cm}^{-1}$)	$Q_y(0,0)$ λ_{max} [nm] (ε/10^4 $\text{M}^{-1}\text{cm}^{-1}$)	$Q_x(1,0)$ λ_{max} [nm] (ε/10^4 $\text{M}^{-1}\text{cm}^{-1}$)	$Q_x(0,0)$ λ_{max} [nm] (ε/10^4 $\text{M}^{-1}\text{cm}^{-1}$)
3a	Mes	420 (44.69)	516 (1.77)	550 (0.79)	591 (0.61)	647 (0.57)
3e	C_6F_5	416 (33.50)	511 (1.69)	544 (0.30)	587 (0.42)	642 (0.54)
Zn-**3a**	Mes	424 (30.18)	552 (1.03)	594 (0.38)	–	–
Zn-**3e**	C_6F_5	421 (50.07)	552 (2.65)	583 (1.03)	–	–
5b	C_6H_5	420 (38.93)	516 (1.68)	552 (0.88)	591 (0.53)	647 (0.43)
5c	4-C_6H_4F	420 (39.89)	516 (1.56)	552 (0.97)	591 (0.56)	647 (0.46)
5d	4-$C_6H_4CF_3$	420 (29.14)	516 (1.46)	551 (0.77)	592 (0.51)	649 (0.43)
5e	C_6F_5	417 (66.61)	512 (4.26)	546 (1.37)	588 (1.45)	643 (0.73)
6b	C_6H_5	419 (78.60)	516 (3.99)	551 (2.09)	592 (1.30)	650 (1.46)
6c	4-C_6H_4F	420 (53.00)	516 (2.83)	552 (1.44)	591 (0.94)	647 (0.97)
Zn-**6b**	C_6H_5	422 (109.44)	551 (5.48)	593 (1.62)	–	–
Zn-**6c**	4-C_6H_4F	420 (82.95)	549 (5.68)	588 (2.81)	–	–

EurJIC European Journal of Inorganic Chemistry www.eurjic.org FULL PAPER

Table 3. Emission data of **3**, Zn-**3**, **5**, **6** and Zn-**6** in CH_2Cl_2 at room temperature.

	Ar	Q(0,0) [nm]	Q(0,1) [nm]	Φ	τ [ns] (A_1/%); τ [ns] (A_2/%)[a]	Quenching [%][b]	k_{ET} [10^9 s^{-1}][c,d]	Φ_{ET} [e,f]
3a	Mes	653	717	0.0122	0.201 (80); 3.52 (20)	84	4.87	98
3e	C_6F_5	646	714	0.0014	0.022 (91); 2.00 (9)	97	45.36	100
Zn-**3a**	Mes	605	651	0.0096	0.139 (82); 1.56 (18)	90	6.80	95
Zn-**3e**	C_6F_5	598	649	0.0006	0.013 (84); 1.11 (16)	99	76.41	99
5b	C_6H_5	652	717	0.0416	2.00 (75); 5.97 (25)	64	0.40	80
5c	4-C_6H_4F	652	717	0.0449	2.05 (76); 5.48 (24)	55	0.39	80
5d	4-$C_6H_4CF_3$	655	716	0.0255	1.87 (100)	76	0.43	80
5e	C_6F_5	649	716	0.0094	0.332 (72); 1.49 (28)	87	2.91	97
6b	C_6H_5	654	717	0.0475	3.17 (100)	59[g]	0.43	82
						37[h]	0.42	80
6c	4-C_6H_4F	655	718	0.0451	3.07 (100)	55[i]	0.23	71
						42[h]	0.22	68
Zn-**6b**	C_6H_5	603	655	0.0198	0.63 (84); 1.87 (16)	81[j]	1.08	68
						81[k]	1.19	75
Zn-**6c**	4-C_6H_4F	597	653	0.0203	0.74 (73); 3.23 (27)	64[l]	0.87	64
						80[k]	0.95	70

[a] The relative amplitudes A were calculated from fitting the data with the equations $Y = A_1e^{-k/\tau 1} + A_2e^{-k/\tau 2}$ and $A_1 + A_2 = 100\%$. [b] Φ_{ref} = 0.0774 (**1a**), 0.1001 (Zn-**1a**), 0.0520 (**1e**), 0.0788 (Zn-**1e**), 0.1003 (Ac-**4c**), 0.0569 (Zn-Ac-**4c**), 0.1167 (Ac-**4b**), 0.1037 (Zn-Ac-**4b**), 0.1080 (Ac-**4d**), 0.0696 (Ac-**4e**).[10] [c] $k_{ET} = 1/\tau - 1/\tau_{ref}$. [d] τ_{ref} = 9.87 (**1a**), 2.53 (Zn-**1a**), 10.05 (**1b**), 1.95 (Zn-**1b**), 9.88 (**4b**), 1.99 (Ac-Zn-**4b**), 9.98 (Ac-**4c**), 2.07 (Ac-Zn-**4c**), 9.64 (Ac-**4d**), 9.83 (Ac-**4e**) ns.[10] [e] $\Phi_{ET} = k_{ET}\tau$. [f] To calculate Φ_{ET}, τ_1 with the largest amplitude was used. [g] Relative to Ac-**4b**. [h] Relative to **1a**. [i] Relative to Ac-**4c**. [j] Relative to Zn-Ac-**4b**. [k] Relative to Zn-**1a**. [l] Relative to Zn-Ac-**4c**.

point to a significant contribution of the reductive PET pathway to the excited-state decay.

The linkage of the second porphyrin unit to dyads **5b** and **5c** leads to no significant change of the fluorescence quantum yield in **6b** and **6c** (Table 3). Both porphyrin components in **6b** and **6c** feature similar extinction coefficients at the excitation wavelength, which results in essentially equal excitation probability. The reduction potentials of the different porphyrins in the tweezers **6b** and **6c** (references **1a**/Ac-**4b** and **1a**/Ac-**4c**) are rather similar and, hence, a similar PET rate to both excited porphyrins might be expected. The complexation of tweezers **6** to zinc(II) leads to a further reduction of the porphyrin fluorescence quantum yield in Zn-**6** by enhancing the intersystem crossing (ISC) rate to the porphyrin triplet state T_1(P).

To substantiate that the emission quenching essentially results from PET rather than from energy transfer to ferrocene, the low-temperature fluorescence spectra of **1e**, **3e**, Zn-**1e** and Zn-**3e** were recorded (Figure 5). As 2-methyltetrahydrofuran solutions of references **1e** and Zn-**1e** were cooled to 77 K, there were small increases of the integrated fluorescence intensities by factors of 1.83 and 1.29, respectively. On the other hand, the ferrocene dyads **3e** and Zn-**3e** enjoy fluorescence increases by factors of 2.88 and 3.38, respectively. Upon cooling, the corresponding absorption bands of **1e** and **3e** sharpen, and the Soret bands increase by a factor of 1.7 in both cases (see Supporting Information). Hence, one part of the fluorescence increase is due to the increase of absorptivity (**1e** and **3e**), whereas an additional process is present for the ferrocenyl porphyrin **3e**. These results support an activated process, such as electron transfer requiring inner- and outer-sphere reorganisation energy,[13] as the major decay path for the porphyrin S_1 states in ferrocenyl porphyrins in addition to fluorescence, internal conversion (IC) to the ground state, ISC to the T_1(P) state promoted by the heavy-atom effect and energy transfer to give the ferrocene triplet state T_1(Fc).[4e,12]

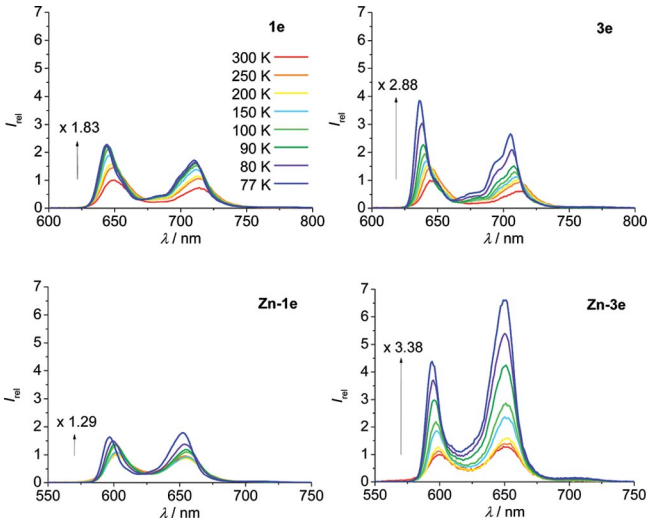

Figure 5. Normalised emission spectra of **1e**, **3e**, Zn-**1e** and Zn-**3e** in 2-methyltetrahydrofuran at T = 300→77 K (λ_{exc} = 420 nm).

The results of fluorescence lifetime measurements in CH_2Cl_2 are summarised in Table 3, and representative decay profiles of the dyads and tweezers are displayed in Figure 6. Dyad **5d** features a monoexponential decay, whereas all decays of dyads **3** and **5** were best fitted by biexponential rate laws (Figure 4). We assign the major component (τ_1, A_1) to the PET pathway, and the minor component (τ_2, A_2) is probably caused by ISC to T_1(P) or energy transfer to generate T_1(Fc) (vide supra).[4e,12] All lifetimes τ_1 are signifi-

EurJIC European Journal of Inorganic Chemistry www.eurjic.org FULL PAPER

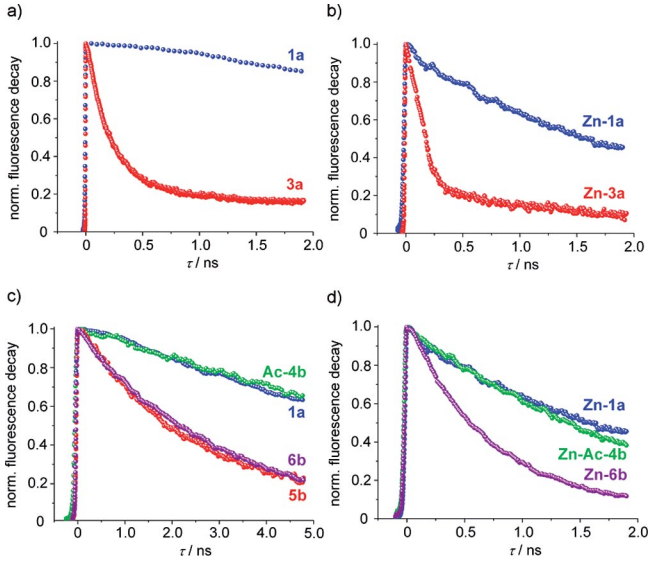

Figure 6. Fluorescence decay profiles of (a) **1a** and **3a**; (b) Zn-**1a** and Zn-**3a**; (c) **1a**, Ac-**4b**, **5b**, **6b** and (d) Zn-**1a**, Zn-Ac-**4b** and Zn-**6b** in CH_2Cl_2 (λ_{exc} = 400 and 550 nm).

cantly reduced compared with those of the reference compounds. Similar to the quantum yields Φ, the lifetimes τ_1 clearly depend on the electron-withdrawing power of the porphyrin substituents Ar (Table 3, e.g., **3a**/**3e**, Zn-**3a**/Zn-**3e** and **5b**/**5e**) and the Fc/Fc^+ potential in **3e** (τ_1 = 0.022 ns) and **5e** (τ_1 = 0.332 ns).[1f]

Depending on the initial excitation at either the N-terminal mesityl or C-terminal aryl-substituted porphyrin (Ar = 4-C_6H_5, 4-C_6H_4F: **6b**, **6c**), the reductive PET in **6** and Zn-**6** can occur from the central ferrocene to the N or C terminus. In free-base tweezers **6**, the decays are monoexponential with lifetimes $\tau \approx 3$ ns. This suggests that both PET paths P^{Mes}←Fc/Fc→P^{C6H5} (**6b**) and P^{Mes}←Fc/Fc→P^{C6H4F} (**6c**) are conceivable with nearly the same rates or rapid singlet–singlet energy transfer between the porphyrins before ET (Table 3). Both are consistent with the quantum yields of **5b**/**6b** and **5c**/**6c** (Table 3). The zincated tweezers Zn-**6** feature biexponential decays. The dominant component (τ_1 = 0.63 ns for Zn-**6b** and τ_1 = 0.74 ns for Zn-**6c**) is again assigned to reductive PET to the N- and C-terminal porphyrins, and the minor one (τ_2) is due to ISC to produce the porphyrin triplet state T_1(P) or energy transfer to produce the ferrocene triplet state T_1(Fc).

From the lifetimes, the rate constants for the electron transfer (k_{ET}) and quantum efficiencies (Φ_{ET}) were estimated (Table 3). To correlate the rates with thermodynamic driving forces, the energies of the $P^{\bullet-}$–$Fc^{\bullet+}$ and *N*-Fmoc–$Fc^{\bullet+}$–$P^{\bullet-}$ charge-separated (CS) states were estimated from the oxidation potential of the ferrocene $E_{1/2}$(Fc,ox) and the first reduction potential of the porphyrin moiety $E_{1/2}$(P,red^1) including the Coulomb term $e_0^2/[4\pi\varepsilon_0\varepsilon$-$(CH_2Cl_2)r_{AD}]$. The energies of the porphyrin S_1 excited states $E(S_0 \rightarrow S_1)$ were estimated as the average value of the $Q_x(0,0)$ absorption bands and Q(0,0) emission bands (Tables 2 and 3). The thermodynamic driving forces ΔG_{ET} were then estimated according to the Rehm–Weller equation,[14] $\Delta G_{ET} = E_{1/2}(Fc,ox) - E_{1/2}(P,red^1) - e_0^2/[4\pi\varepsilon_0\varepsilon(CH_2Cl_2)r_{AD}] - E(S_0 \rightarrow S_1)$ with $\varepsilon_0 = 8.85519 \times 10^{-12}$ F m^{-1}, $\varepsilon(CH_2Cl_2) = 8.93$ and r_{AD} = 13.0 Å for **3a**, **3e**, Zn-**3a**, Zn-**3e** and **5e** and 12.9 Å for **5b**–**5d** (Table 4). The Coulomb terms in CH_2Cl_2 are 0.124 eV for **3a**, **3e**, Zn-**3a**, Zn-**3e** and **5e** and 0.125 eV for **5b**–**5d**. The centre-to-centre distances (r_{AD}) were obtained from geometry-optimised DFT models (vide supra). With $\Delta G_{ET} \approx 0.27$–0.72 eV, the PET in the dyads occurs in the normal Marcus region.[15] As expected from Marcus theory, the electron-transfer rate increases with increasing driving force in dyads **3** and **5** (Tables 3 and 4, Figures 7 and 8).

The ferrocene–porphyrin centre-to-centre distances in tweezers **6** and Zn-**6** are ca. 13.0 Å, and the Coulomb term in CH_2Cl_2 is estimated as 0.124 eV. As the first reduction potentials of the different porphyrins in Zn-**6** are not individually resolved in the cyclic voltammograms, the energies of the CS states of Zn-**6** were estimated from the first reduction potentials of suitable reference porphyrins Zn-**1a**,[10] Zn-Ac-**4b**[1f] and Zn-Ac-**4c**.[10] The estimated energies for N- and C-terminal CS states of tweezers $M(P^{Mes\bullet-})$–$Fc^{\bullet+}$–$M(P^{Ar})$ and $M(P^{Mes})$–$Fc^{\bullet+}$–$M(P^{Ar\bullet-})$ (M = 2H, Zn) and the driving forces ΔG_{ET} estimated from the Rehm–Weller equation[14] are essentially identical, as expected from

Table 4. Energies [eV] of porphyrin S_1 and CS states for **3**, Zn-**3**, **5**, **6** and Zn-**6** and driving forces ΔG_{ET}.

	Ar	$E(S_0 \rightarrow S_1)$	$E(P^{\bullet-}$–$Fc^{\bullet+})$ or $(P^{Mes\bullet-}$–$Fc^{\bullet+}$–$P^{Ar})/(P^{Mes}$–$Fc^{\bullet+}$–$P^{Ar\bullet-})$	$\Delta G_{ET}(P^{\bullet-}$–$Fc^{\bullet+})$ o r $(P_{Mes}^{\bullet-}$–$Fc^{\bullet+}$–$P^{Ar})/(P_{Mes}$–$Fc^{\bullet+}$–$P_2^{\bullet-})$
3a	Mes	1.90	1.48	–0.42
3e	C_6F_5	1.92	1.22	–0.70
Zn-**3a**	Mes	2.05	1.62	–0.43
Zn-**3e**	C_6F_5	2.07	1.35	–0.72
5b	C_6H_5	1.90	1.63	–0.27
5c	4-C_6H_4F	1.90	1.63	–0.27
5d	4-$C_6H_4CF_3$	1.90	1.59	–0.31
5e	C_6F_5	1.91	1.41	–0.50
6b	C_6H_5	1.90	1.68	–0.22
6c	4-C_6H_4F	1.89	1.66	–0.23
Zn-**6b**	C_6H_5	2.05	1.82[a]/1.79[b]	–0.23/–0.26
Zn-**6c**	4-C_6H_4F	2.08	1.81[a]/1.78[b]	–0.27/–0.30

[a] Calculated with the first reduction potential of Zn-**1a** $E_{1/2}$(P,red^1) = –1.78 V. [b] Calculated with the first reduction potential $E_{1/2}$-(P,red^1) = –1.75 V of Zn-Ac-**4b** and Zn-Ac-**4c**.[10]

EurJIC European Journal of Inorganic Chemistry
www.eurjic.org FULL PAPER

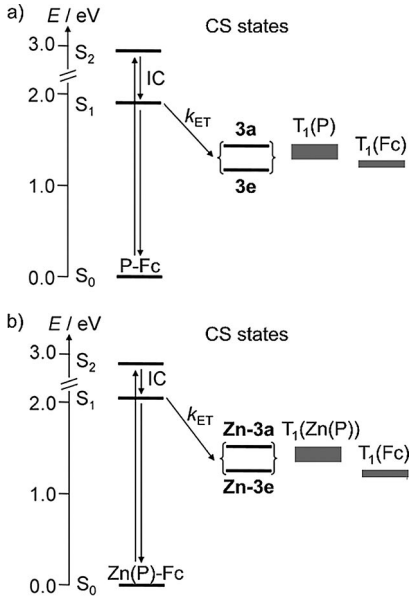

Figure 7. Energy level diagrams of (a) **3a**/**3e** and (b) Zn-**3a**/Zn-**3e** with the estimated porphyrin triplet state T_1(P) at ca. 1.43 eV,[16] the zinc porphyrin triplet state T_1[Zn(P)] at ca. 1.53 eV[17] and the ferrocene triplet state T_1(Fc) at ca. 1.16 eV.[12] The energies of the triplet states certainly vary with the substituents, as is qualitatively reflected in the diagram by the thicker energy level bars of the triplet states.

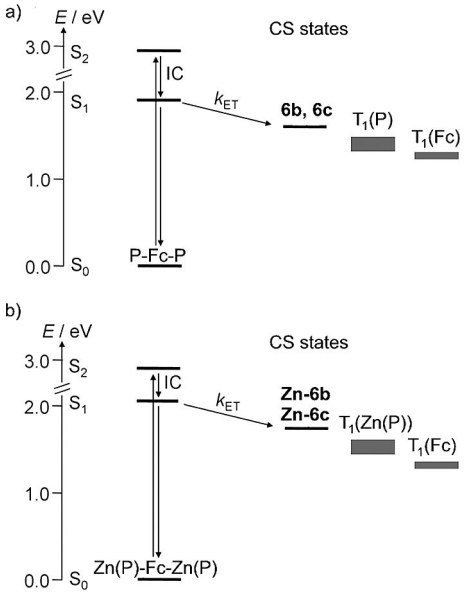

Figure 9. Energy level diagrams of (a) **6b**/**6c** and (b) Zn-**6b**/Zn-**6c** with the estimated porphyrin triplet state T_1(P) at ca. 1.43 eV,[16] the zinc porphyrin triplet state T_1[Zn(P)] at ca. 1.53 eV[17] and the ferrocene triplet state T_1(Fc) at ca. 1.16 eV.[12] The energies of the triplet states certainly vary with the substituents, as is qualitatively reflected in the diagram by the thicker energy level bars of the triplet states.

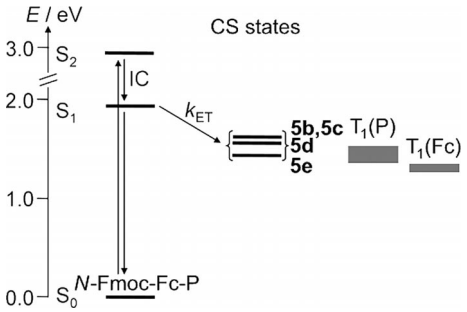

Figure 8. Energy level diagram of **5b**–**5e** with the estimated porphyrin triplet state T_1(P) at ca. 1.43 eV[15] and the ferrocene triplet state T_1(Fc) at ca. 1.16 eV.[12] The energies of the triplet states certainly vary with the substituents, as is qualitatively reflected in the diagram by the thicker energy level bars of the triplet states.

the similar optical and redox properties of the constituent porphyrins (Table 4 and Figure 9).

The geometric and electronic structures of the amide-linked dyads and tweezers were studied by DFT (B3LYP, LANL2DZ, IEFPCM CH_2Cl_2)[18] approaches. Although approximate exchange-correlation potentials might not yield orbital energies compatible with the experiment, orbital symmetry and the trends imposed by electronic substituent effects will be correctly reproduced. Hence, no attempts to optimise the amount of Hartree–Fock exchange for a better agreement with experimental values were pursued, and the orbital energies given (especially the relative position of the Fc orbitals with respect to the porphyrin orbitals) shall only be used as a rough guide. The typical four Gouterman frontier molecular orbitals of porphyrins[19] and the highest occupied ferrocene-based nearly degenerate δ orbitals (d_{xy}, $d_{x^2-y^2}$) for dyads **3a** and **3e** are shown in Figure 10. As typically observed, the strongly electron-withdrawing C_6F_5 substituents lead to a local lowest unoccupied molecular orbital (LUMO) inversion, and the porphyrin LUMO in **3a** features large orbital coefficients at the linking *meso*-carbon atoms, whereas nodes are observed at the linking *meso*-carbon atoms in **3e**.[1f,19,20] The porphyrin highest occupied molecular orbitals (HOMOs) are located below the ferrocene HOMOs in **3e**, whereas one porphyrin HOMO is found above the ferrocene HOMOs in **3a**. The same picture was observed for zincated dyads Zn-**3a** and Zn-**3e** (see Supporting Information). In the series **5a**–**5e**, the increasing electron-withdrawing power of the porphyrin substituents lowers the energy of the porphyrin frontier orbitals (Figure 11), whereas the ferrocene orbitals remain invariant in energy, as expected from the invariant Fc/Fc^+ redox potentials (Table 1). Note that the Fc δ orbital energies of **5** are below those of **3**/Zn-**3** owing to the electron-withdrawing CO substituent at ferrocene, which is consistent with the different Fc/Fc^+ redox potentials of **5** and **3**/Zn-**3** (Table 1).

Representatively for all tweezers **6** and Zn-**6**, the calculated frontier orbitals of **6b**, which consist of a twin set of four Gouterman orbitals[19] and two occupied ferrocene δ orbitals (d_{xy}, $d_{x^2-y^2}$), are depicted in Figure 12. The local porphyrin HOMOs and LUMOs as well as the ferrocene δ orbitals are essentially pairwise degenerate (Figure 12). The accidental degeneracy of the porphyrin frontier orbitals is caused primarily by cancellation of substituent effects at the different porphyrins (Mes/C_6H_4CONHR vs. C_6H_5/

EurJIC European Journal of Inorganic Chemistry www.eurjic.org FULL PAPER

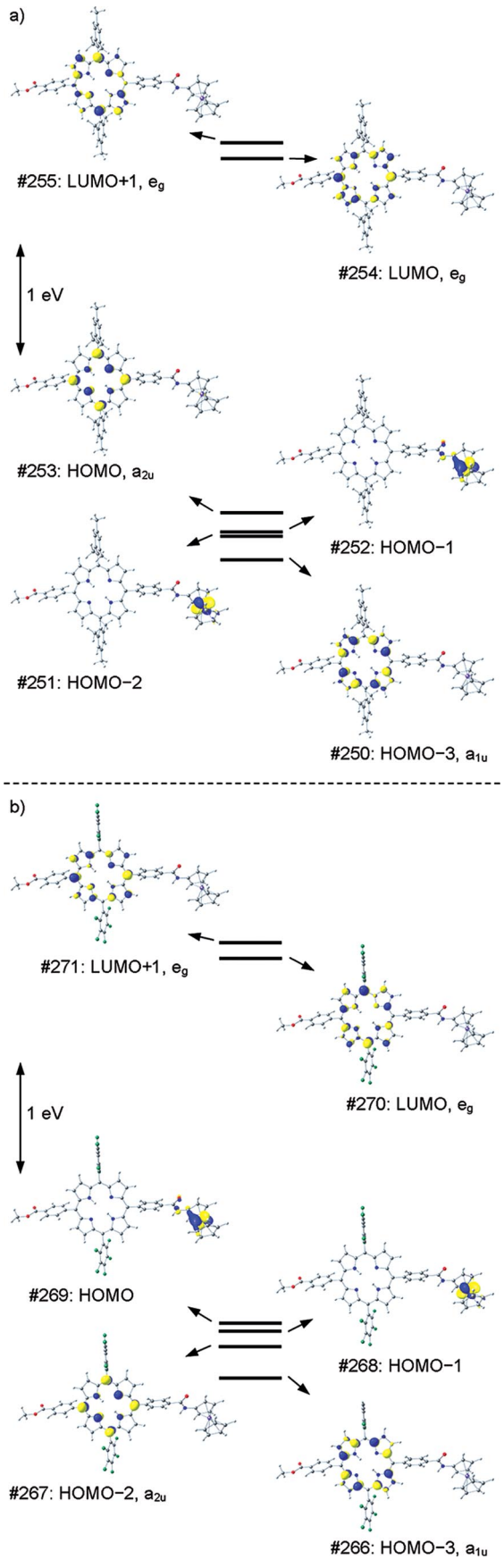

Figure 10. Calculated (B3LYP/LANL2DZ, IEFPCM) frontier orbitals of (a) **3a** and (b) **3e** (isosurface value 0.05 a.u.).

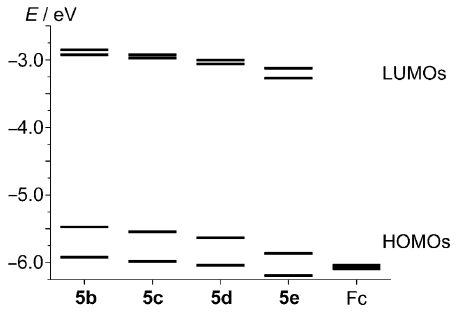

Figure 11. Calculated (B3LYP/LANL2DZ, IEFPCM) molecular orbital energy diagram of dyads **5b**–**5e**. The LUMOs of ferrocene are outside the window shown.

C_6H_4NHCOR or C_6H_4F/C_6H_4NHCOR). In the tweezers, the porphyrin local LUMOs feature nonzero orbital coefficients at the *meso*-carbon bridging atoms. The porphyrin local HOMOs possess a_{2u} symmetry with large orbital coefficients at the *meso*-carbon bridging atoms. This symmetry allows both reductive PET pathways to generate the N-terminal $P^{Mes\cdot-}$–$Fc^{\cdot+}$–P^{Ar} or C-terminal P^{Mes}–$Fc^{\cdot+}$–$P^{Ar\cdot-}$ charge-separated state depending on the initial local excitation of the N-terminal or C-terminal porphyrin.

Furthermore, in addition to the extended tweezers structure shown in Figure 12, a hydrogen-bonded V-shaped conformer is conceivable for **6** and Zn-**6** (Figure 1, b).[5a–5d] The IR spectra suggested the presence of such V-shaped tweezers in solutions of non-coordinating solvents. In the V-shaped conformers, a slight energy decrease of the P^{Mes} frontier orbitals and a slight energy increase of the P^{Ar} frontier orbitals were calculated, as expected for a NH···O hydrogen bond from the P^{Ar} porphyrin to the P^{Mes} porphyrin (see Supporting Information). The H···O hydrogen bond distance is 1.87 Å, and the centre-to-centre distance of the porphyrins is calculated as ca. 15 Å. This distance is too large to find evidence for a V-shape structure by optical absorption spectroscopy, and indeed no shift of Soret and Q bands owing to π–π interactions between the porphyrin macrocycles was observed. However, a through-space singlet–singlet energy transfer in V-shaped **6** and Zn-**6** by a Förster resonance energy transfer mechanism might well occur over this distance.[21] The emission energies of the individual porphyrins in **6** and Zn-**6** are too similar to be distinguished. However, the relative intensities of the Q(0,0) and Q(0,1) emission bands are slightly different in the respective reference compounds. With this phenomenological comparison, the emission seems to be favoured from the mesityl-substituted porphyrin in all cases of **6** and Zn-**6** discussed. This is clearly seen in Figure 4 (d), in which the band shape of Zn-**6b** resembles more the band shape of Zn-**1a** than that of Zn-Ac-**4b**. This interpretation is also consistent with findings for analogous ferrocene-free amide-linked bis(porphyrins) P^{Mes}–P^{Ar}.[10] Further experimental verification of energy transfer between the porphyrins within tweezers of type **6** and Zn-**6** must await the synthesis of analogous tweezers featuring more distinct porphyrins such as mixed free-base and metallated porphyrins; this has

EurJIC European Journal of Inorganic Chemistry www.eurjic.org FULL PAPER

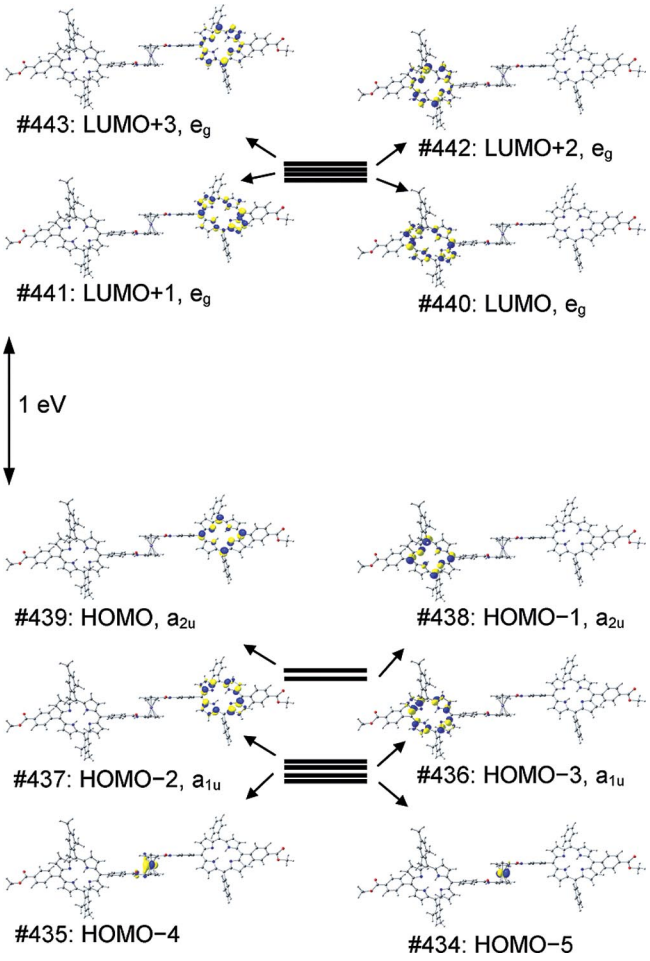

Figure 12. Calculated (B3LYP/LANL2DZ, IEFPCM) frontier orbitals of **6b** (isosurface value 0.05 a.u.).

also been unambiguously demonstrated in amide-linked bis(porphyrins).[10]

The proposed V-shaped tweezers structure[22] prompted us to attempt to prepare host–guest complexes of **6b** and Zn-**6b** with 7,7,8,8-tetracyanoquinodimethane ($E_{1/2}$ = –0.30 V in CH_3CN)[23] and *N*-ethylanthraquinone-2-carboxamide ($E_{1/2}$ = –1.28 V in CH_2Cl_2)[1f] as electron acceptors. These acceptors could be bound by hydrogen bonds in the ground state and could give rise to proton-coupled electron transfer in the excited state of the porphyrin.[24] Titration of the tweezers with more than 1000 equiv. of the putative electron acceptors in CH_2Cl_2 did not appreciably change the absorption and emission spectra. Hence, significant electron transfer of the excited porphyrins or the porphyrin radical anions (in the CS state) to the external acceptor is not observed. This might either be because of unfavourable steric interactions between the potential host and guest or a too rapid excited-state decay through ferrocene-mediated channels (triplet formation).

Indeed, attempts to calculate $P^{\bullet-}$–$Fc^{\bullet+}$, $Zn(P^{\bullet-})$–$Fc^{\bullet+}$ and *N*-Fmoc–$Fc^{\bullet+}$–$P^{\bullet-}$ CS states by DFT methods lead to ferrocene triplet states as the lowest triplet state with the spin density localised on the ferrocene moieties (see Supporting Information). This is consistent with the similar or even lower estimated energies for T_1(Fc) than those of the CS states (Figures 7–9).

To monitor the excited-state and charge-transfer kinetics, we performed ns–µs transient absorption (TA) pump–probe experiments on porphyrins **1e** and Zn-**1e** and ferrocenyl porphyrins **3e** and Zn-**3e**. The ns–µs TA spectra of the parent porphyrins **1e** and Zn-**1e** are characterised by a broad excited-state absorption that covers almost the entire probe wavelength range. However, the ground-state bleaching and stimulated emission of the porphyrin (Figure 13) can be identified as distinct peak features superimposed on the broad and featureless excited-state absorption. The corresponding kinetics tracked at different wavelength regions are shown in Figure 14. The data can be well described by a sum of two exponentials with lifetimes for **1e** of τ_1 = 12.5 ns and τ_2 = 105.8 µs. The short component agrees well with the fluorescence lifetime of ca. 10 ns[10] as determined by streak camera experiments within the experimental uncertainty of the two different measurement techniques. The longer-lived component τ_2, which has a microsecond lifetime, can be assigned to the recombination of the triplet state of the porphyrin T_1(P), generated by ISC from the S_1 state. For Zn-**1e**, we obtained inverse rate constants of τ_1 = 2.4 ns and τ_2 = 147.5 µs by fitting the experimental data to a sum of two exponentials. Likewise, we assigned the nanosecond lifetime τ_1 to the fluorescence decay and the microsecond lifetime τ_2 to the recombination of the triplet state of the porphyrin. In fact, τ_1 is essentially similar to the experimentally measured fluorescence lifetime of 2 ns. However, we note that here we approach the temporal resolution of our ns–µs TA setup.

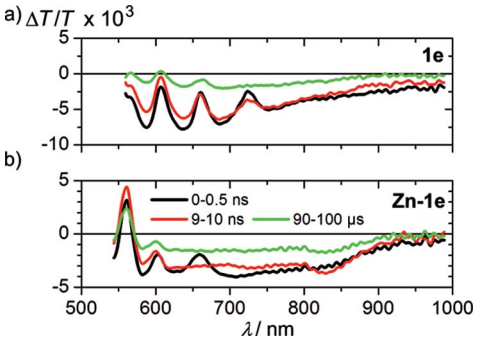

Figure 13. Selected ns–µs TA spectra of (a) **1e** and (b) Zn-**1e** in THF after excitation at 532 nm. The delay times are 500 ps (black), 10 ns (red) and 100 µs (green).

Interestingly, a photoinduced absorption (PA) feature emerged after 10 ns in the 800 to 850 nm wavelength range for Zn-**1e**. We assigned this photoinduced absorption to the triplet state of Zn-**1e** T_1[Zn(P)], as similar PA features have been reported for triplet states of metallated porphyrins.[25] The kinetics of this particular wavelength region are shown in Figure 14 (b, green curve). Clearly, the signal grows in at early times and reaches its maximum after ca. 10 ns. The accumulation of the triplet state of the porphyrin in the first 10 ns is in line with the decay of its S_1 state, which occurs on the same timescale.

EurJIC European Journal of Inorganic Chemistry www.eurjic.org FULL PAPER

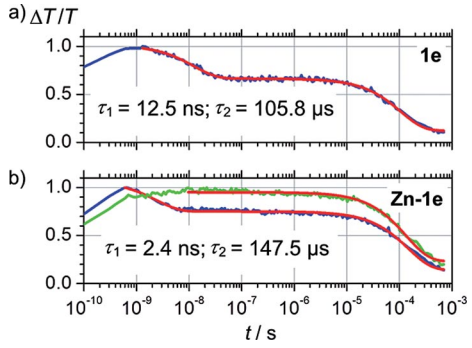

Figure 14. Integrated TA kinetics (750–950 nm) of (a) **1e** and (b) **Zn-1e** (blue: 700–800 nm; green: 825–850 nm). The red curves are exponential or biexponential fits to the experimental data.

The ns–μs TA spectra of ferrocenyl-substituted porphyrins **3e** and Zn-**3e** are depicted in Figure 15. As the extinction coefficient of the ferrocenium cation is very small, the TA spectra are dominated by the excited-state absorption of the porphyrin, which extends over the entire spectral range from approximately 500 to 1000 nm. According to reports by Kubo et al.[4d] and Pandey et al.,[26] a photoinduced absorption band in the 700 to 900 nm wavelength range can be assigned to the porphyrin radical anion. They found radical anion absorption bands in a series of fluorinated porphyrins with maxima between 799–813 nm by chemical reduction and steady-state absorption. The integrated TA kinetics of the compounds in the wavelength region above 700 nm are shown in Figure 16. A fit of the kinetics for **3e** to a sum of three exponentials yields inverse rate constants of τ_1 = 6 ns, τ_2 = 1.1 μs and τ_3 = 88.1 μs. The inverse rate constant τ_1 can be attributed to the decay of singlet excitons, which are quenched faster than for **1e** owing to the additional PET decay channel. We attribute τ_2 to the lifetime of the CS state, which appears to undergo ISC to the first triplet excited state T_1(P) of the porphyrin, as the shape of the spectra after 3 μs resembles the spectral shape of the T_1(P) state that we also observed for porphyrin **1e**. Interestingly, the T_1(P) state of **3e** is not as long-lived as the T_1 state of reference porphyrin **1e**. It is conceivable that the triplet state of the porphyrin transfers to the triplet excited state of the ferrocene T_1(Fc) or alternatively that the porphyrin T_1 state returns faster to the ground state because of the heavy-atom effect induced by the presence of the iron atom in the ferrocene moiety. The integrated TA kinetics of **Zn-3e** monitored in the wavelength regions 700–800 nm (blue curve) and 825 to 850 nm (green curve) are shown in Figure 16 (b); the main absorption originates from the zinc porphyrin T_1[Zn(P)] state. For Zn-**3e**, the data can be described by a sum of two exponentials. The obtained lifetimes are τ_1 = 1.9 ns and τ_2 = 2.3 μs. We assume that we cannot observe the kinetics of the CS state of Zn-**3e** because the photoinduced absorption signal of the porphyrin radical anion is superimposed by the signal of the zinc porphyrin T_1[Zn(P)] state, which indicates that the latter has a larger cross section than the porphyrin radical anion. The nanosecond component τ_1 describes the kinetics of singlet excitons, which transfer into the CS state that is not observed in the TA spectra of Zn-**3e**. We assign τ_2 to the decay of the zinc porphyrin T_1[Zn(P)] state into either the ground state or the ferrocene T_1(Fc) state, which successively decays to the ground state. However, the latter is a process that we cannot directly observe in our TA experiments. In contrast to the inverse rate constant of τ_3 = 88.1 μs observed for **3e**, the inverse rate constant τ_2 = 2.3 μs for Zn-**3e** is significantly smaller. Hence, it appears that either of the two processes (or both), namely, triplet state decay into the ground state and energy transfer from the porphyrin T_1[Zn(P)] state to the ferrocene T_1(Fc) state, is facilitated by the zinc atom in Zn-**3e**.

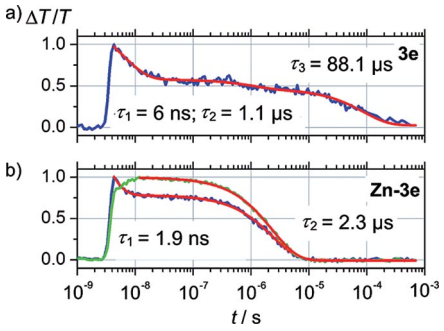

Figure 16. Integrated TA kinetics of (a) **3e** (750–950 nm) and (b) **Zn-3e** (blue: 700–800 nm; green: 825–850 nm). The red curves are fits to the experimental data.

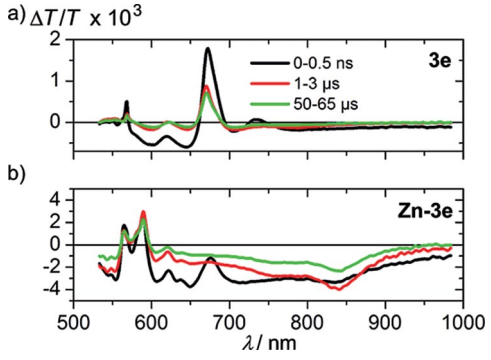

Figure 15. Selected ns–μs TA spectra of (a) **3e** after 0.5 ns, 3 μs and 65 μs and (b) **Zn-3e** after 0.5 ns, 10 ns and 1 μs in THF solution after excitation at 532 nm.

Conclusions

The amide-linked porphyrin–ferrocene dyads P^{Ar}–Fc (**3**), Zn(P^{Ar})–Fc (Zn-**3**; Ar = Mes, C_6F_5) and *N*-Fmoc–Fc–P^{Ar} (**5**; Ar = C_6H_5, 4-C_6H_4F, 4-$C_6H_4CF_3$, C_6F_5) were prepared from the corresponding ferrocene and porphyrin building blocks by amide formation. Two *N*-Fmoc–Fc–P^{Ar} dyads (Ar = C_6H_5, 4-C_6H_4F) were further extended to porphyrin–ferrocene–porphyrin tweezers **6**, which were subsequently metallated with zinc(II) to give Zn-**6**.

All dyads and tweezers show only weak interactions between the porphyrin and ferrocene moieties in their ground states, but there is strong fluorescence quenching and ex-

EurJIC European Journal of Inorganic Chemistry www.eurjic.org FULL PAPER

cited-state lifetime reduction with respect to the corresponding ferrocene-free reference compounds. Porphyrin and ferrocene substituent effects as well as low-temperature experiments substantiate a reductive photoinduced electron transfer as the major deactivation pathway of the porphyrin S_1 excited state. The final lowest electronically excited states are porphyrin and ferrocene triplet states as shown by DFT calculations and transient absorption measurements. Additionally, hints for a singlet–singlet energy-transfer pathway between the different porphyrins in **6** and Zn-**6** were found and suggested to occur through a hydrogen-bonded V-shaped structure of the tweezers.

Experimental Section

Instrumentation: NMR spectra were recorded with a Bruker Avance DRX 400 spectrometer at 400.31 (^{1}H), 100.05 (^{13}C{^{1}H}) and 367.67 MHz (^{19}F). Chemical shifts (δ) are reported in ppm relative to the solvent signal as an internal standard {[D_8]THF (^{1}H: δ = 1.73, 3.58 ppm; ^{13}C: δ = 25.5, 67.7 ppm), $CDCl_3$ (^{1}H: δ = 7.24 ppm; ^{13}C: δ = 77.0 ppm), CD_2Cl_2 (^{1}H: δ = 5.32 ppm; ^{13}C: δ = 54.0 ppm)} or external $CFCl_3$ (^{19}F: δ = 0 ppm); s = singlet, d = doublet, pt = pseudotriplet (unresolved doublet of doublets), dd = doublet of doublets, ddd = doublet of doublet of doublets, br s = broad singlet. IR spectra were recorded with a BioRad Excalibur FTS 3100 spectrometer with samples as CsI disks. Signal intensities: vs = very strong, s = strong, m = medium, w = weak. ESI and high-resolution (HR) ESI mass spectra were recorded with a Micromass Q-TOF-Ultima spectrometer. Field desorption (FD) mass spectra were obtained with a FD Finnigan MAT95 spectrometer. Cyclic voltammetry (CV) and square-wave voltammetry measurements were performed with a BioLogic SP-50 voltammetric analyser with samples in CH_2Cl_2 containing 0.1 M [nBu$_4$N][PF_6] as supporting electrolyte at a glassy carbon working electrode with a platinum wire counter electrode and a 0.01 M $Ag/AgNO_3$ reference electrode. All cyclic voltammetric measurements were recorded at 100 mV s^{-1} scan speed. Ferrocene was employed as an internal reference redox system.

UV/Vis/NIR absorption spectra were measured with a Varian Cary 5000 spectrometer with samples in CH_2Cl_2 in 1.0 cm cells (Hellma, suprasil). Steady-state emission spectra were recorded with a Varian Cary Eclipse spectrometer with samples in CH_2Cl_2 in 1.0 cm cells (Hellma, suprasil). Quantum yields Φ were determined by comparing the areas under the emission spectra on an energy scale [cm^{-1}] recorded for optically matched solutions (absorption intensity under 0.05) of the samples and the reference [Φ(H_2TPP) = 0.13 in benzene][27] and using the equation[28] $\Phi = \Phi_{ref} \times I/I_{ref} \times \eta^2/\eta^2_{ref}$ with η(benzene) = 1.5011, η(CH_2Cl_2) = 1.4242 and η(THF) = 1.4070; experimental uncertainty 15%. Fluorescence decay measurements were performed with ca. 1×10^{-5} M solutions by the time-correlated single photon counting method with a Hamamatsu streak camera system. Two time modes were used for the measurements: one with a resolution down to a few picoseconds and a maximum time range of two nanoseconds [fast sweep, mononuclear zinc(II) porphyrins, P–Fc, Zn(P)–Fc dyads and *N*-Fmoc–Fc–P^{Ar} with Ar = C_6F_5], and a second time mode with a time resolution down to a few hundred picoseconds and a maximum time range limited by the repetition rate of the excitation source [slow sweep, all free-base porphyrins, *N*-Fmoc–Fc–P^{Ar} dyads, P^{Mes}–Fc–P^{Ar} and Zn(P^{Mes})–Fc–Zn(P^{Ar}) tweezers]. Excitation was provided depending on the measuring mode. For fast-sweep experiments, a Ti:sapphire ultrafast laser system (Coherent Mira 900 Dual fs–ps Oscillator) with a repetition rate of 80 MHz and a pulse length of 100 fs pumped by a diode-pumped solid-state laser (Coherent Verdi V8) was used. The 800 nm output was frequency doubled by using a barium borate (BBO) crystal to achieve the excitation wavelength of 400 nm. For the slow sweep measurements, we used a Fianium fibre laser supercontinuum source (SC450–2), which provides a white laser light (460–2200 nm) with a pulse width of 6 ps and a fundamental repetition rate of 20 MHz, which was typically derated by an implemented pulse picker to 1 MHz. The desired excitation wavelength (550 nm) was filtered out of the white light by using an acousto-optical modulator (AOM, Fianium AOTF).[29] Transient absorption measurements were performed with a home-built pump–probe setup.[29] To measure a time range up to 3 ns with a resolution of ca. 100 fs, the output of a commercial titanium:sapphire amplifier (Coherent LIBRA HE, 3.5 mJ, 1 kHz, 100 fs) was split; one portion was used to generate a 515 nm excitation pulse by using an optical parametric amplifier (Coherent OPerA Solo), and the other was used to generate a 1300 nm seed pulse [output of an optical parametric amplifier (Coherent OPerA Solo)] for white-light generation in the visible to NIR (500–1000 nm) in a c-cut 3 mm thick sapphire window. The variable delay of up to 3 ns between pump and probe was introduced by a broadband retroreflector mounted on a mechanical delay stage. The excitation pulse was chopped at 500 Hz, and the white light pulses were dispersed onto linear silicon (Hamamatsu NMOS linear image sensor S3901 photodiode). The array was read out at 1 kHz. Adjacent diode readings corresponding to the transmission of the sample after an excitation pulse and without an excitation pulse were used to calculate $\Delta T/T$. Samples were excited with fluences of ca. 100 μJ cm^{-2}.

Density functional calculations were performed with the Gaussian09 series[18] of programs. The B3LYP formulation of density functional theory was used, and the LANL2DZ basis set was employed. To include solvent effects, the integral equation formalism polarisable continuum model (IEFPCM, CH_2Cl_2) was employed. No symmetry constraints were imposed on the molecules. The presence of energy minima of the ground states was checked by analytical frequency calculations.

Materials: Unless otherwise noted, all chemical reagents were used without any further purification as received from suppliers (Sigma–Aldrich, Acros, Alfa Aesar). THF was freshly distilled from sodium. CH_2Cl_2 and 1,2-dichloroethane were freshly distilled from calcium hydride. Porphyrins **1a**, **2a**, Zn-**1a**, **1e**, **2e**, **4b**–**4e**, Ac-**4b**–Ac-**4e**, Zn-Ac-**4b**, Zn-Ac-**4c**, aminoferrocene and *N*-Fmoc-protected ferrocene amino acid were prepared by published procedures.[2d,5a,8–10,30–33]

General Procedure for the Preparation of 3a and 3e: 5-(4-Carboxyphenyl)-15-(4-methoxycarbonylphenyl)-10,20-bis(2,4,6-trimethylphenyl)porphyrin (**2a**) or 5-(4-carboxyphenyl)-15-(4-methoxycarbonylphenyl)-10,20-bis(2,3,4,5,6-pentafluorophenyl)porphyrin (**2e**; 1 equiv.) and pyridine (1 mL) were dissolved in anhydrous toluene (20 mL). Thionyl chloride (5 equiv.) was added, and the reaction mixture was stirred under nitrogen for 3 h at room temperature. The excess thionyl chloride and solvent were removed under reduced pressure. The residue was redissolved in toluene (20 mL) and pyridine (1 mL) in an ultrasonic bath. Aminoferrocene (1.3 equiv.) dissolved in toluene (20 mL) and pyridine (1 mL) were added. The mixture was stirred overnight, and the solvent was removed by evaporation under reduced pressure. The residue was purified by chromatography [silica, toluene/ethyl acetate (20:1)].

General Procedure for the Preparation of Zn-3a and Zn-3e: Dyad **3a** or **3e** (1 equiv.) and zinc(II) acetate dihydrate (5 equiv.) were

EurJIC European Journal of Inorganic Chemistry www.eurjic.org FULL PAPER

stirred overnight in CH_2Cl_2 (5 mL). After concentration under reduced pressure, the product was isolated by column chromatography.

General Procedure for the Preparation of 5b, 5c, 5d and 5e: *N*-Fmoc-protected ferrocene amino acid *N*-Fmoc-Fca-OH (H-Fca-OH = 1-amino-1′-ferrocene carboxylic acid; Fmoc = 9-fluorenylmethoxycarbonyl) and one drop of pyridine were dissolved in anhydrous CH_2Cl_2 (40 mL). Oxalyl chloride was added, and the reaction mixture was stirred under nitrogen for 1 h at room temperature. The excess oxalyl chloride and solvent were removed by evaporation under reduced pressure. The residue was dissolved in CH_2Cl_2 (10 mL), and the solvent was removed under reduced pressure. The acid chloride was dissolved in CH_2Cl_2 (40 mL). To this solution, a solution of the porphyrin amino component in CH_2Cl_2 (40 mL with one drop of pyridine) was added. The reaction mixture was stirred for 18 h at room temperature and washed with water, and the organic phase was concentrated under reduced pressure. The product was isolated by column chromatography.

General Procedure for the Preparation of 6b and 6c: Compound **5b** or **5c** and tris(2-aminoethyl)amine were dissolved in anhydrous CH_2Cl_2 (20 mL), and the reaction mixture was stirred under nitrogen for 3 h at room temperature and washed with saturated brine (2× 10 mL) and phosphate buffer (pH 5.5). The solution was dried with Na_2SO_4, and the solvent was removed under reduced pressure. 5-(4-Carboxyphenyl)-15-(4-methoxycarbonylphenyl)-10,20-bis(2,4,6-trimethylphenyl) porphyrin (**2a**) was dissolved in anhydrous CH_2Cl_2 (30 mL), 1-chloro-*N*,*N*,2-trimethylpropenylamine (Ghosez's reagent) was added, and the reaction mixture was stirred under nitrogen for 1 h at room temperature. After the acid chloride formed (TLC control), the excess Ghosez's reagent and solvent were removed by evaporation under reduced pressure. To remove the *N*,*N*-dimethylamide byproduct, anhydrous CH_2Cl_2 (20 mL) was added, and the volatiles were again removed by evaporation. The acid chloride was dissolved in CH_2Cl_2 (30 mL with 0.05 mL of triethylamine), and this solution was added dropwise to a solution of the amino component prepared from **5b** or **5c** in CH_2Cl_2. The reaction mixture was stirred for 18 h at room temperature and washed with water, and the organic phase was concentrated under reduced pressure. After column chromatography, **6b** and **6c** were isolated.

General Procedure for the Preparation of Zn-6b and Zn-6c: Compound **6b** or **6c** (1 equiv.) and zinc(II) acetate dihydrate (12 equiv.) were stirred overnight in CH_2Cl_2 (10 mL). After concentration under reduced pressure, the product was isolated by column chromatography [silica, toluene/ethyl acetate 50:1].

[10,20-Bis(pentafluorophenyl)-5,15-bis(4-methoxycarbonylphenyl)porphyrinato]zinc(II) (Zn-1e): Porphyrin **1e** (50 mg, 0.054 mmol) and zinc(II) acetate dihydrate (61 mg, 0.27 mmol) were stirred overnight in CH_2Cl_2 (10 mL). After concentration under reduced pressure, the product was isolated by column chromatography [silica, CH_2Cl_2, R_f = 0.50], yield 49.9 mg (0.051 mmol, 94%), purple-red powder. $C_{48}H_{22}F_{10}N_4O_4Zn$ (974.1067).

Supporting Information (see footnote on the first page of this article): Complete analytical data; absorption spectra of **1e** and **3e** in 2-methyltetrahydrofuran at T = 300→77 K; B3LYP/LANL2DZ, IEFPCM calculated frontier orbitals of Zn-**3a**, Zn-**3e**, **5d**, **5e**, **6c**, Zn-**6b** and Zn-**6c**; B3LYP/LANL2DZ, IEFPCM calculated molecular orbital energy diagrams of **3a**, **3e**, Zn-**3a**, Zn-**3e**, **6b**, **6c**, Zn-**6b** and Zn-**6c**; B3LYP/LANL2DZ, IEFPCM calculated spin densities of the lowest triplet state of **3e** and **5e**; Cartesian coordinates of all DFT-optimised geometries.

Acknowledgments

This work was supported by the Deutsche Forschungsgemeinschaft (DFG) (He 2778-6/1). J. R. O. thanks the International Research Training Group (IRTG 1404) "Self Organized Materials for Optoelectronics" for funding, M. M. thanks the Max Planck Graduate Center with the Johannes Gutenberg University (MPGC) for support and F. L. thanks the Max Planck Society for funding a Max Planck Research group.

[1] a) H. Imahori, D. M. Guldi, K. Tamaki, Y. Yoshida, C. Luo, Y. Sakata, S. Fukuzumi, *J. Am. Chem. Soc.* **2001**, *123*, 6617–6628; b) H. Imahori, K. Tamaki, Y. Araki, Y. Sekiguchi, O. Ito, Y. Sakata, S. Fukuzumi, *J. Am. Chem. Soc.* **2002**, *124*, 5165–5174; c) H. Imahori, Y. Sekiguchi, Y. Kashiwagi, T. Sato, Y. Araki, O. Ito, H. Yamada, S. Fukuzumi, *Chem. Eur. J.* **2004**, *10*, 3184–3196; d) M. U. Winters, E. Dahlstedt, H. E. Blades, C. J. Wilson, M. J. Frampton, H. L. Anderson, B. Albinsson, *J. Am. Chem. Soc.* **2007**, *129*, 4291–4297; e) C. Wijesinghe, M. E. El-Khouly, M. E. Zandler, S. Fukuzumi, F. D'Souza, *Chem. Eur. J.* **2013**, *19*, 9629–9638; f) J. Melomedov, J. R. Ochsmann, M. Meister, F. Laquai, K. Heinze, *Eur. J. Inorg. Chem.* **2014**, 1984–2001.

[2] a) D. Gust, T. A. Moore, A. L. Moore, F. Cao, D. Luttrull, J. M. DeGraziano, X. C. Ma, L. R. Makings, S. Lee, T. T. Trier, E. Bittersmann, G. R. Seely, S. Woodward, R. V. Bensasson, M. Roug, F. C. De Schryver, M. Van der Auweraer, *J. Am. Chem. Soc.* **1991**, *113*, 3638–3649; b) D. Gust, T. A. Moore, A. L. Moore, A. N. Macpherson, A. Lopez, J. M. DeGraziano, I. Gouni, E. Bittersmann, G. R. Seely, F. Gao, R. A. Nieman, X. C. Ma, L. J. Demanche, S. Hung, D. K. Luttrull, S. Lee, P. K. Kerrigan, *J. Am. Chem. Soc.* **1993**, *115*, 11141–11152; c) M. D. Meijer, G. P. M. van Klink, G. van Koten, *Coord. Chem. Rev.* **2002**, *230*, 141–163; d) S. L. Gould, G. Kodis, R. E. Palacios, L. De La Garza, A. Brune, D. Gust, T. A. Moore, A. L. Moore, *J. Phys. Chem. B* **2004**, *108*, 10566–10580.

[3] a) A. M. Brun, A. Harriman, V. Heitz, J.-P. Sauvage, *J. Am. Chem. Soc.* **1991**, *113*, 8657–8663; b) V. Heitz, S. Chardon-Noblat, J.-P. Sauvage, *Tetrahedron Lett.* **1991**, *32*, 197–198; c) E. K. L. Yeow, P. J. Sintic, N. M. Cabral, J. N. H. Reek, M. J. Crossley, K. P. Ghiggino, *Phys. Chem. Chem. Phys.* **2000**, *2*, 4281–4291; d) K. Kilså, J. Kajanus, A. N. Macpherson, J. Mårtensson, B. Albinsson, *J. Am. Chem. Soc.* **2001**, *123*, 3069–3080; e) S. Fukuzumi, K. Ohkubo, W. E, Z. Ou, J. Shao, K. M. Kadish, J. A. Hutchison, K. P. Ghiggino, P. J. Sintic, M. J. Crossley, *J. Am. Chem. Soc.* **2003**, *125*, 14984–14985; f) J. Hee Jang, H. J. Kim, H.-J. Kim, C. H. Kim, T. Joo, D. Won Cho, M. Yoon, *Bull. Korean Chem. Soc.* **2007**, *28*, 1967–1972; g) J. Fortage, J. Boixel, E. Blart, L. Hammarström, H. C. Becker, F. Odobel, *Chem. Eur. J.* **2008**, *14*, 3467–3480; h) J. Fortage, A. Scarpaci, L. Viau, Y. Pellegrin, E. Blart, M. Falkenström, L. Hammarström, I. Asselberghs, R. Kellens, W. Libaers, K. Clays, M. P. Eng, F. Odobel, *Chem. Eur. J.* **2009**, *15*, 9058–9067; i) J. Fortage, J. Boixel, E. Blart, H. C. Becker, F. Odobel, *Inorg. Chem.* **2009**, *48*, 518–526.

[4] a) R. Giasson, E. J. Lee, X. Zhao, M. S. Wrighton, *J. Phys. Chem.* **1993**, *97*, 2596–2601; b) N. B. Thornton, H. Wojtowicz, T. Netzel, D. W. Dixon, *J. Phys. Chem. B* **1998**, *102*, 2101–2110; c) V. A. Nadtochenko, N. N. Denisov, V. Yu. Gak, N. V. Abramova, N. M. Loim, *Russ. Chem. Bull.* **1999**, *40*, 1900–1903; d) M. Kubo, Y. Mori, M. Otani, M. Murakami, Y. Ishibashi, M. Yasuda, K. Hosomizu, H. Miyasaka, H. Imahori, S. Nakashima, *Chem. Phys. Lett.* **2006**, *429*, 91–96; e) H. Mansour, M. E. El-khouly, S. Y. Shaban, O. Ito, N. Jux, *J. Porphyrins Phthalocyanines* **2007**, *10*, 719–728; f) P. K. Poddutoori, A. S. D. Sandanayaka, T. Hasobe, O. Ito, A. van der Est, *J. Phys. Chem. B* **2010**, *114*, 14348–14357; g) M. A. Bakar, N. N. Sergeeva, T. Juillard, M. O. Senge, *Organometallics* **2011**, *30*, 3225–3228; h) B. M. J. M. Suijkerbuijk, R. J. M. Klein Geb-

bink, *Angew. Chem. Int. Ed.* **2008**, *47*, 7396–7421; *Angew. Chem.* **2008**, *120*, 7506–7532; i) S. J. Dammer, P. V. Solntsev, J. R. Sabin, V. N. Nemykin, *Inorg. Chem.* **2013**, *52*, 9496–9510; j) L. Lvova, P. Galloni, B. Floris, I. Lundström, R. Paolesse, C. Di Natale, *Sensors* **2013**, *13*, 5841–5856; k) V. N. Nemykin, P. Chen, P. V. Solntsev, A. A. Purchel, K. M. Kadish, *J. Porphyrins Phthalocyanines* **2012**, *16*, 793–801; l) A. Vecchi, E. Gatto, B. Floris, V. Conte, M. Venanzi, V. N. Nemykin, P. Galloni, *Chem. Commun.* **2012**, *48*, 5145–5147; m) V. N. Nemykin, G. T. Rohde, C. D. Barrett, R. G. Hadt, J. R. Sabin, G. Reina, P. Galloni, B. Floris, *Inorg. Chem.* **2010**, *49*, 7497–7509; n) V. N. Nemykin, G. T. Rohde, C. D. Barrett, R. G. Hadt, C. Bizzarri, P. Galloni, B. Floris, I. Nowik, R. H. Herber, A. G. Marrani, R. Zanoni, N. M. Loim, *J. Am. Chem. Soc.* **2009**, *131*, 14969–14978.

[5] a) K. Heinze, M. Schlenker, *Eur. J. Inorg. Chem.* **2004**, 2974–2988; b) K. Heinze, D. Siebler, *Z. Anorg. Allg. Chem.* **2007**, *633*, 2223–2233; c) D. Siebler, M. Linseis, T. Gasi, L. M. Carrella, R. F. Winter, C. Förster, K. Heinze, *Chem. Eur. J.* **2011**, *17*, 4540–4551; d) D. Siebler, C. Förster, K. Heinze, *Dalton Trans.* **2011**, *40*, 3558–3575; e) H. Huesmann, C. Förster, D. Siebler, T. Gasi, K. Heinze, *Organometallics* **2012**, *31*, 413–427.

[6] A. K. Burrell, W. Campbell, D. L. Officer, *Tetrahedron Lett.* **1997**, *38*, 1249–1252.

[7] K. Heinze, K. Hempel, M. Beckmann, *Eur. J. Inorg. Chem.* **2006**, 2040–2050.

[8] C. M. Carcel, J. K. Laha, R. S. Loewe, P. Thamyongkit, K. Schweikart, V. Misra, D. F. Bocian, J. S. Lindsey, N. Carolina, *J. Org. Chem.* **2004**, *69*, 6739–6750.

[9] K. Heinze, A. Reinhart, *Dalton Trans.* **2008**, 469–480.

[10] J. Melomedov, A. Wünsche von Leupoldt, M. Meister, F. Laquai, K. Heinze, *Dalton Trans.* **2013**, *42*, 9727–9739.

[11] A. Devos, J. Remiona, A.-M. Frisque-Hesbain, A. Colens, L. Ghosez, *J. Chem. Soc., Chem. Commun.* **1979**, 1180–1181.

[12] Y. Araki, Y. Yasumura, O. Ito, *J. Phys. Chem. B* **2005**, *109*, 9843–9848.

[13] E. D. German, A. M. Kuznetso, *Electrochim. Acta* **1981**, *26*, 1595–1608.

[14] A. Weller, *Z. Phys. Chem. (Muenchen Ger.)* **1982**, *133*, 93–98.

[15] a) R. A. Marcus, *J. Chem. Phys.* **1956**, *24*, 979–989; b) R. A. Marcus, *Annu. Rev. Phys. Chem.* **1964**, *15*, 155–196; c) R. A. Marcus, *Angew. Chem. Int. Ed. Engl.* **1993**, *32*, 1111–1121; *Angew. Chem.* **1996**, *105*, 1161–1172.

[16] J. A. Schmidt, A. R. McIntosh, A. C. Weedon, J. R. Bolton, J. S. Connolly, J. K. Hurley, M. R. Wasielewski, *J. Am. Chem. Soc.* **1988**, *110*, 1733–1740.

[17] C. Luo, D. M. Guldi, H. Imahori, K. Tamaki, Y. Sakata, *J. Am. Chem. Soc.* **2000**, *122*, 6535–6551.

[18] M. J. Frisch, G. W. Trucks, H. B. Schlegel, G. E. Scuseria, M. A. Robb, J. R. Cheeseman, G. Scalmani, V. Barone, B. Mennucci, G. A. Petersson, H. Nakatsuji, M. Caricato, X. Li, H. P. Hratchian, A. F. Izmaylov, J. Bloino, G. Zheng, J. L. Sonnenberg, M. Hada, M. Ehara, K. Toyota, R. Fukuda, J. Hasegawa, M. Ishida, T. Nakajima, Y. Honda, O. Kitao, H. Nakai, T. Vreven, J. A. Montgomery Jr., J. E. Peralta, F. Ogliaro, M. Bearpark, J. J. Heyd, E. Brothers, K. N. Kudin, V. N. Staroverov, R. Kobayashi, J. Normand, K. Raghavachari, A. Rendell, J. C. Burant, S. S. Iyengar, J. Tomasi, M. Cossi, N. Rega, J. M. Millam, M. Klene, J. E. Knox, J. B. Cross, V. Bakken, C. Adamo, J. Jaramillo, R. Gomperts, R. E. Stratmann, O. Yazyev, A. J. Austin, R. Cammi, C. Pomelli, J. W. Ochterski, R. L. Martin, K. Morokuma, V. G. Zakrzewski, G. A. Voth, P. Salvador, J. J. Dannenberg, S. Dapprich, A. D. Daniels, O. Farkas, J. B. Foresman, J. V. Ortiz, J. Cioslowski, D. J. Fox, *Gaussian 09*, revision A.02, Gaussian Inc., Wallingford CT, **2009**.

[19] M. Gouterman, *J. Chem. Phys.* **1959**, *30*, 1139–1161.

[20] D. Holten, D. F. Bocian, J. S. Lindsey, *Acc. Chem. Res.* **2002**, *35*, 57–69.

[21] J.-M. Camus, S. M. Aly, C. Stern, R. Guilard, P. D. Harvey, *Chem. Commun.* **2011**, *47*, 8817–8819.

[22] a) S. Brahma, S. A. Ikbal, S. P. Rath, *Inorg. Chem.* **2014**, *53*, 49–62; b) H. Yoon, C.-H. Lee, W.-D. Jang, *Chem. Eur. J.* **2012**, *18*, 12479–12486; c) A. Chaudhary, S. P. Rath, *Chem. Eur. J.* **2012**, *18*, 7404–7417; d) A. Chaudhary, S. P. Rath, *Chem. Eur. J.* **2011**, *17*, 11478–11487; e) B. Habermeyer, A. Takai, C. P. Gros, M. El Ojaimi, J.-M. Barbe, S. Fukuzumi, *Chem. Eur. J.* **2011**, *17*, 10670–10681; f) J.-M. Barbe, B. Habermeyer, T. Khoury, C. P. Gros, P. Richard, P. Chen, K. M. Kadish, *Inorg. Chem.* **2010**, *49*, 8929–8940.

[23] N. G. Connelly, W. E. Geiger, *Chem. Rev.* **1996**, *96*, 877–910.

[24] O. S. Wenger, *Chem. Eur. J.* **2011**, *17*, 11692–11702.

[25] J. Rodriguez, C. Kirmaier, D. Holten, *J. Am. Chem. Soc.* **1989**, *111*, 6500–6506.

[26] S. K. Pandey, A. L. Gryshuk, A. Graham, K. Ohkubo, S. Fukuzumi, M. P. Dobhal, G. Zheng, Z. Ou, R. Zhan, K. M. Kadish, A. Oseroff, S. Ramaprasade, R. K. Pandey, *Tetrahedron* **2003**, *59*, 10059–10073.

[27] A. Rosa, G. Ricciardi, E. J. Baerends, A. Romeo, L. Monsu, *J. Phys. Chem. A* **2003**, *107*, 11468–11482.

[28] J. R. Lakowicz, *Principles of Fluorescence Spectroscopy*, 3rd ed., Springer, New York, **2006**.

[29] F. Etzold, I. A. Howard, N. Forler, D. M. Cho, M. Meister, H. Mangold, J. Shu, M. R. Hansen, K. Müllen, F. Laquai, *J. Am. Chem. Soc.* **2012**, *134*, 10569–10583.

[30] D. T. Gryko, M. Tasior, B. Koszarna, *J. Porphyrins Phthalocyanines* **2003**, *7*, 239–248.

[31] T. Rohand, E. Dolusic, T. H. Ngo, W. Maes, W. Dehaen, *ARKIVOC* **2007**, *10*, 307–324.

[32] B. J. Littler, Y. Ciringh, J. S. Lindsey, *J. Org. Chem.* **1999**, *64*, 2864–2872.

[33] K. Heinze, A. Reinhart, *Z. Naturforsch. B* **2005**, *60*, 758–762.

Received: March 5, 2014
Published Online: May 26, 2014

8 DISCUSSION

In this work the photovoltaic performance of three DPP-based low bandgap donor-acceptor copolymers, namely PTDPP-TT, PFDPP-TT, and PDPP5T blended with $PC_{71}BM$ were investigated. Organic bulk heterojunction (BHJ) solar cells were fabricated under different processing conditions. In comparison to mid-bandgap polymers, such as P3HT or PCDTBT, one would expect a higher short circuit current density J_{SC} and hence a higher device performance from OSCs based on low bandgap polymers, due to their increased photon harvesting properties. However, the observed values for J_{SC} are often much smaller than expected. In order to identify the loss channels in devices, responsible for the reduction in J_{SC} we investigated the photophysics of the DPP-polymer/fullerene blends with different experimental methods such as PIA, TA spectroscopy, TR-PL, and the TOF technique (see chapter 3 Methods).

8.1 FACTORS LIMITING THE DEVICE EFFICIENCY IN PTDPP-TT AND PFDPP-TT BASED SOLAR CELLS

Table 4 summarizes the results of the PTDPP-TT: $PC_{71}BM$ and PFDPP-TT: $PC_{71}BM$ solar cells. In addition, the field effect hole mobilities of neat PTDPP-TT and PFDPP-TT as recently determined by Chandran et al. are listed.[201]

Table 4: Comparison of the figures of merit of PTDPP-TT and PFDPP-TT solar cells together with the theoretical short-circuit current J_{sc}^{th}, obtained from integrating the convolution of the absorption spectrum with the AM 1.5G spectrum, assuming 100 % IQE. Furthermore, the active layer thickness d, the optical bandgap E_g, and the hole mobility μ_H determined in OFET devices prepared with the neat polymers[201] are listed.

	PTDPP-TT	PFDPP-TT
J_{SC} / mA cm^{-2}	3.4	4.7
V_{OC} / V	0.67	0.59
FF	0.62	0.58
PCE / %	1.9	2.2
J_{sc}^{th} / mA cm^{-2}	14	15.8
d / nm	75	82
E_g / eV	1.38	1.31
μ_H / cm^2 V^{-1}s^{-1}	9×10^{-2}	4×10^{-2}

Although, the optical bandgaps of the materials are optimal for a good device performance (compare section 2.7.3) and the high hole mobilities are potentially beneficial for efficient charge separation at the interface and transport of positive charges to the electrodes, the observed PCE and J_{SC} values are rather low. In fact, the measured values of J_{SC} are much lower than the theoretical short-circuit current values J_{sc}^{th} obtained from integrating the convolution of the absorption spectrum with the AM 1.5G spectrum assuming 100 % IQE. This is a clear indication that a significant part of the collected photons is not being converted into extracted charges. These losses can be quantified to roughly 76 and 70 % for the PTDPP-TT:$PC_{71}BM$ and PFDPP-TT:$PC_{71}BM$ solar cells, respectively.

The better FF of the PTDPP-TT device might be explained by the higher hole mobility of this material and the thinner active layer in the solar cell device, which are both factors facilitating the extraction of charges and hence reducing the field dependence of the photocurrent. The higher J_{SC} of the PFDPP-TT device can be explained by the enhanced absorption of the photoactive layer, due to the smaller bandgap of this material and the thicker active layer.

Apart from the small differences in photovoltaic device performance, the observed photophysics of the two blend systems are virtually the same. TA spectroscopy on neat polymer films, showed that the singlet exciton lifetime in both polymers is very short, probably due to fast internal conversion, with values around 17 and 19 ps for PTDPP-TT and PFDPP-TT, respectively. These short exciton lifetimes might constitute one of the loss channels leading to a reduced photocurrent, since this lifetime might not be long enough for excitons to reach the D/A-interface, where they could undergo charge separation. Furthermore, we found that a substantial fraction of charges is recombining geminately on a sub-ns timescale. This means, that a substantial fraction of charges created at the interface is not being separated into spatially-separated charges which could potentially be extracted at the electrodes, but is bound at the interface where they recombine, and is hence representing an additional loss channel. However, with our TA experiments we cannot further determine the reasons for this fast recombination process.

Another loss channel observed in the PTDPP-TT:$PC_{71}BM$ and PFDPP-TT:$PC_{71}BM$ systems is the formation of triplet excitons on the respective polymers on the sub-ns timescale by nongeminate recombination of free charges. Triplet state formation in polymer/fullerene systems will be discussed in more detail further below in section 8.3.

It has to be noted, that Li et al. presented a solar cell with a significantly higher efficiency of 6.9 % with their polymer DT-PDPP-TT having the same chemical structure as the PTDPP-TT polymer investigated by us.[202] This high PCE might be due to the significantly higher molecular weight of $M_n = 447\,kg\,mol^{-1}$ compared to $M_n = 47\,kg\,mol^{-1}$

in our case. High molecular weights are generally considered to be helpful in forming well interconnected nanometer-sized, semi-crystalline polymer and fullerene domains, which are beneficial for photovoltaic device performance.[125, 143] These semi-crystalline domains extend the conjugation length of the polymer backbone and enhance the wavefunction delocalization of charges, hence facilitating charge carrier separation and collection.[202, 203] Li et al. also found a significantly higher hole mobility of 0.8 cm^2 V^{-1} s^{-1} determined in an OFET device. Furthermore, Loh and coworkers synthesized the polymer PDBF-*co*-TT, which has a similar chemical structure as the PFDPP-TT polymer investigated by us.[204] However, PDBF-*co*-TT has smaller alkyl side chains (octyldodecyl) attached to the DPP-moiety. Applied in an OSC device they obtained a PCE of 4.4 % and in an OFET device they obtained a hole mobility of 0.53×10^{-1} cm^2 V^{-1} s^{-1}. Again, the reason for the better performance of this polymer might be the higher molecular weight M_n = of 132 kg mol^{-1} compared to M_n = 52 kg mol^{-1} for the PFDPP-TT polymer as determined by GPC. In addition the shorter alkyl side chains of PDBF-*co*-TT might also be beneficial for molecular packing of the polymer backbone, leading to a higher degree of crystallinity and hence to a better phase separation, charge generation and collection. In fact, it would be interesting to study the photophysics of the structurally similar but better performing polymers DT-PDPP-TT and PDBF-*co*-TT, in order to see whether the loss channels identified for PTDPP-TT and PFDPP-TT are also relevant in these systems.

8.2 INFLUENCE OF THE PROCESSING CONDITIONS ON MORPHOLOGY AND PERFORMANCE OF PDPP5T:PC$_{71}$BM PHOTOVOLTAIC DEVICES

We have shown that spin-coating the photoactive PDPP5T:PC$_{71}$BM layer from a solvent mixture of chloroform and o-DCB in a ratio of 9:1 by volume is drastically enhancing the device performance compared to spin-coating the photoactive layer from chloroform as the only solvent. The PCE could be improved from 0.9 to 4.9 %. This difference in device performance was reflected in the surface morphology determined by AFM. In the less efficient blend spin-coated only from chloroform, large PCBM domains with diameters around 400 nm have formed which are embedded in a polymer rich matrix. However, when the donor and acceptor materials were spin-coated from a chloroform/o-DCB solvent mixture, the surface images showed a rather fine grained structure with seemingly intimately mixed donor and acceptor domains, which are clearly more beneficial for charge generation and collection.

Kouijzer et al. investigated the morphology of PDPP5T:PC$_{71}$BM blends spin-coated from chloroform in more detail with AFM, TEM and cross-

sectional TEM on samples prepared with a focused ion beam.[184] In addition they modeled the film formation of this ternary solvent:polymer:fullerene blend in dependence of the individual component concentrations and the drying time (i.e. the surface thickness) on the basis of Flory-Huggins theory. They found that besides the large PCBM domains, there are smaller PCBM domains or even single PCBM molecules dispersed in the polymer rich matrix. With increasing film thickness, the PCBM concentration in the polymer rich matrix is increasing and at the same time the large PCBM domains are increasing in size. For the performance of OSCs this implies that charges created at the large PCBM domains are easily swept out of the device, due to the pure polymer and PCBM domains, respectively, while charges created at the small PCBM domain within the polymer rich matrix are more difficult to extract and might ultimately contribute to the photocurrent to a much lesser extend.

Here, we investigated PDPP5T:$PC_{71}BM$ blend films with a film thickness around 104 nm, representing a rather thin photoactive layer, where according to Kouijzer et al. a significant amount of small PCBM domains must be present in the polymer rich matrix. Figure 62 shows schematics of the morphologies of PDPP5T:$PC_{71}BM$ solar cells prepared without (a) and with o-DCB (b) together with the photophysical processes occurring in theses blends and their timescales.

The results of our photophysical experiments acquired by means of time-resolved photoluminescence spectroscopy and transient absorption spectroscopy are in line with the morphological studies presented above. With TR-PL we observed the decay of PCBM excitons created within the large domains in the blend spin-coated from chloroform. We could show that quenching of the initially created PCBM excitons at the D/A-interface is inefficient. Quenching of excitons created in the smaller PCBM domains is most probably efficient and these excitons will hence not contribute to the photoluminescence signal. On the other hand in the PDPP5T:$PC_{71}BM$ blend film prepared with o-DCB we found that losses due to incomplete PCBM exciton quenching are small, confirming the observation of smaller and more intermixed polymer and fullerene domains.

With TA spectroscopy we found that charge generation from PCBM excitons in the blend prepared without o-DCB occurred fast, within roughly 20 ps, while charge generation from PCBM excitons in the blend prepared with o-DCB was diffusion limited, occurring within around 200 ps. This result shows, that in the blend prepared without o-DCB charge generation from the small PCBM domains is efficient and fast, due to the limited size of the PCBM domains. However, in the OPV device the electrons created in these domains are difficult to extract, due to the absence of percolation pathways to the aluminum electrode, leading to a lower device performance. On the other hand, in the blend prepared with o-DCB charge generation from PCBM ex-

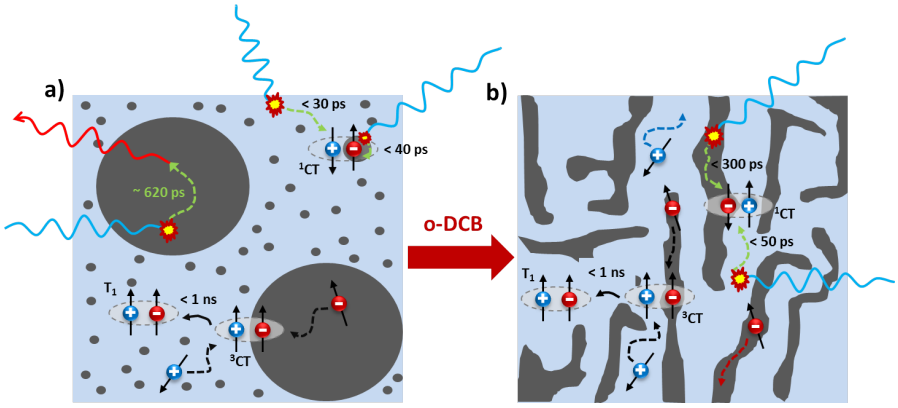

Figure 62: Schematics of the morphologies of PDPP5T:$PC_{71}BM$ active layers in solar cells prepared without o-DCB (a) and prepared with o-DCB (b). The morphology of the blend prepared without o-DCB (a) is characterized by large PCBM domains (dark gray) embedded in a polymer rich matrix (light blue), which itself contains smaller PCBM domains. In the blend prepared with o-DCB the polymer and PCBM domains are more intimately mixed and percolation pathways to the electrodes exist. Photophysical processes occurring in the blend systems are sketched in the schematics as well. Laser excitation is indicated by the light blue wavy lines. Excitons diffuse through the materials (green dashed arrows) and reach the D/A-interface within a certain diffusion time indicated in the schematics or decay non-radiatively or radiatively by emitting a photon (red wavy line), which we can detect in the TR-PL experiments. Free charges can either migrate to the interface (black dashed arrows) and recombine non-geminately into the polymers triplet state via a triplet charge transfer state (black solid arrows) or free electrons and holes migrate through the fullerene and donor domains (dashed red and blue arrows, respectively), in direction of the electrodes to be finally extracted from the device. The latter process of charge carrier extraction is facilitated in the blend prepared with o-DCB, due to the pronounced interpenetrating polymer/fullerene network.

citons is diffusion-limited, probably due to the larger extent of the PCBM domains. At the same time, these larger PCBM domains that are finely intermixed with polymer domains provide a better charge percolation network, facilitating the extraction of charge carriers from the device.

Furthermore, charge generation in both blend systems is efficient as the dynamics of charge recombination is clearly fluence dependent, indicative of nongeminate recombination of free charge carriers.

Interestingly, also in these blend systems we observed the formation of triplet excitons on the PDPP5T polymer via recombination of free charge carriers on the sub-ns timescale. The formation of triplet excitons in polymer/fullerene systems will be discussed in more detail in the following section.

8.3 TRIPLET STATE FORMATION IN LOW-BANDGAP/FULLERENE PHOTOVOLTAIC BLENDS

In all four photovoltaic blend systems investigated in this work, i.e. PTDPP-TT:$PC_{71}BM$, PFDPP-TT:$PC_{71}BM$, PDPP5T:$PC_{71}BM$ prepared with o-DCB, and PDPP5T:$PC_{71}BM$ prepared without o-DCB, we observed the formation of triplet states on the sub-ns timescale. Furthermore, in all blend systems the onset of triplet state generation corresponding to the rise of the triplet-induced absorption signal was laser intensity dependent, which led us to the conclusion that the underlying mechanism of triplet state generation is bimolecular recombination of free charges via triplet charge transfer states. These results are very similar to recent findings of our group on other low-bandgap polymer:fullerene systems, namely PCPDTBT:PCBM, PSBTBT:PCBM,[205] and PBDTTT-C:PCBM,[172] where we also observed intensity dependent formation of polymer triplet states on the sub-ns timescale. In addition, Rao et al. and Chow et al. made the observation of triplet state formation via nongeminate charge recombination in PIDT-PhanQ:fullerene blends and also in a PCPDTBT:PCBM blend by means of TA spectroscopy.[168, 169]

Figure 63 illustrates possible photophysical processes occurring in the investigated photovoltaic blends. When two oppositely charged free carriers encounter at the interface they may form loosely-bound charge transfer states prior to recombination.[206, 169, 207] Due to the uncorrelated spins of the free charges, charge transfer states with triplet (^{3}CT) or singlet (^{1}CT) spin character are created in a ratio of 3:1, according to spin statistics. These interfacial CT states can either re-dissociate into free charges, spin flip from ^{1}CT to ^{3}CT or vice versa, or recombine directly to the ground state. In addition, the ^{3}CT states can populate the polymer's triplet state which eventually decays to the ground state. The triplet state of the polymer can be populated, if the energy of the polymer's T_1 state is lower than that of the interfacial ^{3}CT state, allowing for a downhill energy transfer process, which is in kinetic competition with the re-dissociation of the ^{3}CT state. The population of the polymer triplet state via nongeminate recombination of free charges and the intermediate ^{3}CT state adds an additional loss channel to the efficiency limiting processes in organic solar cells.[205]

Another generation mechanism of polymer triplet states is intersystem crossing (ISC) of initially generated interfacial ^{1}CT states created by singlet exciton dissociation, followed by energy transfer to the polymer triplet state. Such a generation mechanism was proposed by Dimitrov et al. for a blend of a silaindacenodithiophene-based copolymer and $PC_{71}BM$ and by Di Nuzzo et al. for a PCPDTBT:$PC_{61}BM$ blend.[170, 166] However, this generation mechanism was ruled out by Etzold et al. for PCPDTBT:$PC_{61}BM$ and PSBTBT:$PC_{61}BM$ blends,

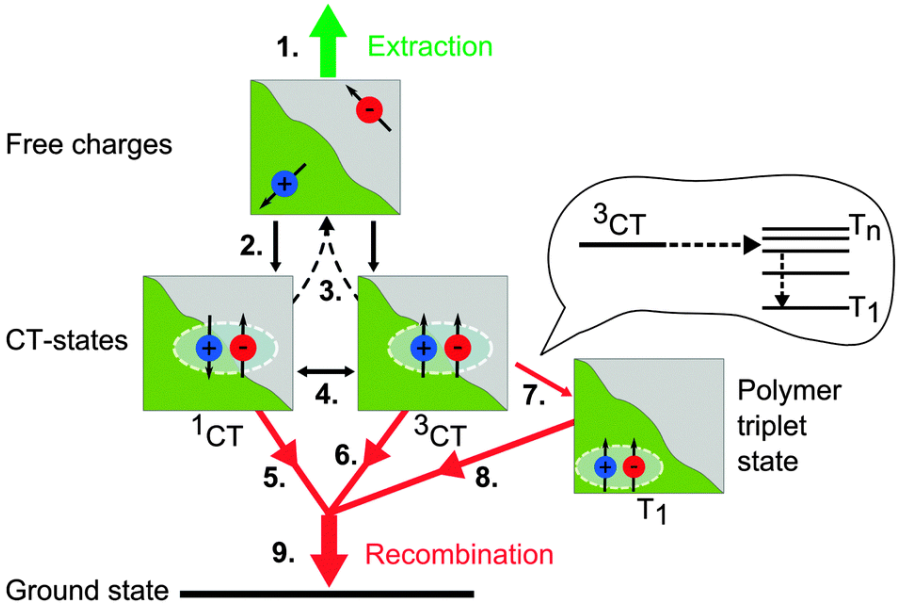

Figure 63: Scheme of possible photophysical processes occurring in low-bandgap polymer/fullerene BHJ solar cells. The extraction of free charge carriers (green) (1.) is in kinetic competition with the recombination of charges (red) (9.). Free charges of opposite polarity may encounter at the D/A-interface to form loosely bound charge transfer states with either tripet (^{3}CT) or singlet character (^{1}CT) in a ratio of 3:1 (2.). These interfacial CT states can either redissociate into free charges (3.), change their spin by ISC (4.), or recombine to the ground state (5. and 6.). In addition ^{3}CT states can populate the polymer triplet state via energy transfer (7.), if T_1 is lower in energy than ^{3}CT. The polymer triplet states undergo triplet-triplet or triplet-charge annihilation. Reproduced from Etzold et al.[205] - Published by The Royal Society of Chemistry.

due to the CT state lifetime of a few hundred picoseconds measured in these systems,[208, 209] which seems too short to allow for efficient ISC.[205]

In the systems studied here, we do not have any explicit information about the lifetimes of the interfacial CT states. Nonetheless, we also rule out triplet state formation via ISC of initially created interfacial CT states, since, firstly the intensity dependence of the triplet state formation is very pronounced and secondly triplets are created at early times already, even at times shorter than the time-resolution of our TA setup of ~ 150 fs. This ultrafast formation of the polymer triplet state is not entirely clarified. In the PDPP5T:$PC_{71}BM$ blends we observed ultrafast charge generation upon excitation of the polymer. Hence, it is likely, that charges are recombining already at the sub-ps timescale and form triplet states on an ultrafast timescale. On the other hand it is also possible that triplet states in the polymer:fullerene blends are formed via fast singlet fission, since such a

fast generation of triplet states was also observed in the TA pump-probe measurements of the pristine polymer films.

A strategy to block the loss channel of triplet state formation would be to design low-bandgap polymers, where the T_1 state is higher in energy than the ^{3}CT state. However, this is a challenging task, because at the same time a high V_{OC} and a small bandgap is desired. An alternative approach to reduce charge recombination via triplet states was proposed by Rao et al.[168] They showed that wavefunction delocalization, due to extended crystalline donor and acceptor domains, facilitates the re-dissociation of loosely-bound interfacial CT states in PIDT-PhanQ:fullerene blends and that thermal energy can enhance the re-dissociation rate. The finding of Rao et al. that crystalline domains might enhance the re-dissociation rate of ^{3}CT states into free charges was underlined by the results of Etzold et al.[205] They observed less triplet state formation and longer charge carrier lifetimes in the more crystalline and better performing PSBTBT:PCBM blend than in the less crystalline and less well performing PCPDTBT:PCBM blends. Another strategy to suppress the formation of triplet states was presented by Basel et al.[173] They could reduce the yield of triplet state generation in a PTB7:PC_{61}BM system by doping the blend with the spin 1/2 radical galvinoxyl. This method enhanced the PCE of their PTB7:PC_{61}BM solar cells by 30 %.

It has to be noted however, that the formation of triplet states in the various low-bandgap polymer/fullerene systems has been observed by TA spectroscopy under open circuit conditions, where all the generated free charges eventually have to recombine, and at illumination intensities higher than 1 sun. So the question to be addressed in further studies is, whether the formation of triplet states via nongeminate recombination is a fundamental loss channel in OSC devices under operating conditions, i.e. with an applied bias and at solar illumination conditions similar to AM 1.5G.

BIBLIOGRAPHY

[1] P. V. Kamat, "Meeting the Clean Energy Demand: Nanostructure Architectures for Solar Energy Conversion," *J. Phys. Chem. C*, vol. 111, no. 7, pp. 2834–2860, 2007.

[2] J.-L. Brédas and J. R. Durrant, "Organic photovoltaics.," *Accounts of chemical research*, vol. 42, no. 11, pp. 1689–1690, 2009.

[3] P. B. Weisz, "Basic Choices and Constraints on Long-Term Energy Supplies," *Physics Today*, vol. 57, no. 7, p. 47, 2004.

[4] IPCC, *Climate Change 2014: Synthesis Report. Contribution of Working Groups I, II and III to the Fifth Assessment Report of the Intergovernmental Panel on Climate Change*. Intergovernmental Panel on Climate Change, 2014.

[5] D. S. Battisti and R. L. Naylor, "Historical Warnings of Future Food Insecurity with Unprecedented Seasonal Heat," *Science*, vol. 323, pp. 240–244, Jan. 2009.

[6] E. Bundgaard and F. Krebs, "Low band gap polymers for organic photovoltaics," *Solar Energy Materials and Solar Cells*, vol. 91, pp. 954–985, July 2007.

[7] ISE, "Photovoltaics Report," tech. rep., Fraunhofer Institute for Solar Energy Systems, 2015.

[8] NREL, "Best Research-Cell Efficiencies," 2015.

[9] C. J. Brabec, S. Gowrisanker, J. J. M. Halls, D. Laird, S. Jia, and S. P. Williams, "Polymer-fullerene bulk-heterojunction solar cells," *Advanced Materials*, vol. 22, no. 34, pp. 3839–3856, 2010.

[10] K. J. Kaufmann, P. L. Dutton, T. L. Netzel, J. S. Leigh, and P. M. Rentzepis, "Picosecond Kinetics of Events Leading to Reaction Center Bacteriochlorophyll Oxidation," *Science*, vol. 188, pp. 1301–1304, June 1975.

[11] L. Sun, L. Hammarström, B. Åkermark, and S. Styring, "Towards artificial photosynthesis: ruthenium-manganese chemistry for energy production," *Chemical Society Reviews*, vol. 30, no. 1, pp. 36–49, 2001.

[12] S. Iwata and J. Barber, "Structure of photosystem II and molecular architecture of the oxygen-evolving centre," *Current Opinion in Structural Biology*, vol. 14, pp. 447–453, Aug. 2004.

[13] A. Harriman, "Unusually Slow Charge Recombination in Molecular Dyads," *Angewandte Chemie International Edition*, vol. 43, pp. 4985–4987, Sept. 2004.

[14] J. Melomedov, J. R. Ochsmann, M. Meister, F. Laquai, and K. Heinze, "Tuning Reductive and Oxidative Photoinduced Electron Transfer in Amide-Linked Anthraquinone-Porphyrin-Ferrocene Architectures," *European Journal of Inorganic Chemistry*, vol. 2014, pp. 1984–2001, Apr. 2014.

[15] C. K. Chiang, C. R. Fincher, Y. W. Park, A. J. Heeger, H. Shirakawa, E. J. Louis, S. C. Gau, and A. G. MacDiarmid, "Electrical conductivity in doped polyacetylene," *Physical Review Letters*, vol. 39, no. 17, pp. 1098–1101, 1977.

[16] A. J. Heeger, "Semiconducting and Metallic Polymers: The Fourth Generation of Polymeric Materials (Nobel Lecture)," *Angewandte Chemie International Edition*, vol. 40, pp. 2591–2611, July 2001.

[17] H. Haken and H. C. Wolf, *Molekülphysik und Quantenchemie*. Berlin, Heidelberg: Springer-Verlag, 2006.

[18] R. E. Dickerson and I. Geis, *Chemistry, Matter and the Universe: Integrated Approach to General Chemistry*. Benjamin-Cummings Publishing Co.,Subs. of Addison Wesley Longman, 1976.

[19] W. Demtröder, *Atoms, Molecules and Photons*. Berlin, Heidelberg: Springer-Verlag, 2010.

[20] A. Einstein, "Zur Quantentheorie der Strahlung," *Physikalische Gesellschaft Zürich, Mitteilungen*, vol. 18, pp. 47–62, 1916.

[21] B. Valeur, *Molecular Fluorescence: Principles and Applications*. Weinheim: Wiley-VCH Verlag GmbH & Co. KGaA, 2001.

[22] J. R. Ochsmann, "Untersuchung der Dynamik des Maltosebindungsproteins während des Transports von Maltose durch den ABC-Maltosetransporter mittels zeitaufgelöster Fluoreszenzspektroskopie," Diplomarbeit, Freie Universität Berlin, 2010.

[23] B. Gregg, "Excitonic Solar Cells," *American Chemical Society*, pp. 4688–4698, 2003.

[24] B. C. Thompson and J. M. J. Fréchet, "Polymer-fullerene composite solar cells," *Angewandte Chemie - International Edition*, vol. 47, no. 1, pp. 58–77, 2008.

[25] J. Frenkel, "On the Transformation of light into Heat in Solids. I," *Physical Review*, vol. 37, pp. 17–44, Jan. 1931.

[26] G. H. Wannier, "The Structure of Electronic Excitation Levels in Insulating Crystals," *Physical Review*, vol. 52, pp. 191–197, Aug. 1937.

[27] W. Y. Liang, "Excitons," *Physics Education*, vol. 5, p. 003, July 1970.

[28] M. Schwoerer and H. C. Wolf, *Organic Molecular Solids*. Weinheim: WILEY-VCH Verlag GmBH u. Co. KGaA, 2005.

[29] G. Lanzani, *The Photophysics Behind Photovoltaics and Photonics*. John Wiley and Sons, 2012.

[30] M. Pope and C. E. Swenberg, *Electronic Processes in Organic Crystals and Polymers*. New York: Oxford University Press, Inc., 2nd ed. ed., 1999.

[31] T. Förster, Z. Energiewanderung, and F. Von, "Zwischenmolekulare Energiewanderung und Fluoreszenz," *Annalen der Physik*, vol. 248, no. 1938, pp. 55–75, 1939.

[32] I. G. Scheblykin, A. Yartsev, T. Pullerits, V. Gulbinas, and V. Sundström, "Excited state and charge photogeneration dynamics in conjugated polymers," *Journal of Physical Chemistry B*, vol. 111, no. 23, pp. 6303–6321, 2007.

[33] E. Collini and G. D. Scholes, "Coherent Intrachain Energy Migration in a Conjugated Polymer at Room Temperature," *Science*, no. January, pp. 369–373, 2009.

[34] I. A. Howard, *Loss Mechanisms in High Open-Circuit Voltage Organic Solar Cells*. PhD thesis, University of Cambridge, 2009.

[35] D. L. Dexter, "A Theory of Sensitized Luminescence in Solids," *The Journal of Chemical Physics*, vol. 21, no. 5, p. 836, 1953.

[36] UCDavis, "Dexter Energy Transfer," 2015.

[37] M. C. Scharber and N. S. Sariciftci, "Efficiency of bulk-heterojunction organic solar cells," *Progress in Polymer Science*, vol. 38, no. 12, pp. 1929–1940, 2013.

[38] N. S. Sariciftci, L. Smilowitz, A. J. Heeger, and F. Wudl, "Photoinduced electron transfer from a conducting polymer to buckminsterfullerene.," *Science (New York, N.Y.)*, vol. 258, no. 5087, pp. 1474–1476, 1992.

[39] D. W. Gehrig, *Unraveling Efficiency-Limiting Processes in Organic Solar Cells by Ultrafast Spectroscopy - Impact of Chemical Structure and Morphology on Photophysics and Efficiency*. PhD thesis, Johannes Gutenberg-Universität Mainz, 2015.

[40] F. Etzold, *A Photophysical Study of Excited State Dynamics in Donor-Acceptor Copolymer Photovoltaic Blends*. PhD thesis, Johannes Gutenberg-Universität Mainz, 2014.

[41] O. V. Mikhnenko, H. Azimi, M. Scharber, M. Morana, P. W. M. Blom, and M. A. Loi, "Exciton diffusion length in narrow bandgap polymers," 2012.

[42] C. W. Tang, "Two-layer organic photovoltaic cell," *Applied Physics Letters*, vol. 48, no. 2, pp. 183–185, 1986.

[43] G. Yu, J. Gao, J. C. Hummelen, F. Wudl, and A. J. Heeger, "Polymer Photovoltaic Cells: Enhanced Efficiencies via a Network of Internal Donor-Acceptor Heterojunctions," 1995.

[44] H. Hoppe and N. S. Sariciftci, "Morphology of polymer/-fullerene bulk heterojunction solar cells," *Journal of Materials Chemistry*, vol. 16, no. 1, p. 45, 2006.

[45] H. Hoppe and N. Sariciftci, "Polymer solar cells," in *Photoresponsive Polymers II*, no. October 2007, pp. 1–86, Springer-Verlag, 2008.

[46] P. Stallinga, "Theory of electrical characterization of (organic) semiconductors," 2015.

[47] Wikipedia, "Schottky barrier," 2015.

[48] H. Hoppe and N. S. Sariciftci, "Organic solar cells: An overview," *Journal of Materials Research*, vol. 19, no. 07, pp. 1924–1945, 2004.

[49] C. Tanase, E. J. Meijer, P. W. M. Blom, and D. M. De Leeuw, "Unification of the hole transport in polymeric field-effect transistors and light-emitting diodes.," *Physical review letters*, vol. 91, no. 21, p. 216601, 2003.

[50] T. M. Clarke and J. R. Durrant, "Charge Photogeneration in Organic Solar Cells," *Chem. Rev.*, vol. 110, pp. 6736–6767, 2010.

[51] R. A. Marcus, "On the Theory of Oxidation-Reduction Reactions Involving Electron Transfer. I," *The Journal of Chemical Physics*, vol. 24, no. 5, p. 966, 1956.

[52] M. R. Wasielewski, "Photoinduced electron transfer in supramolecular systems for artificial photosynthesis," *Chemical Reviews*, vol. 92, no. 3, pp. 435–461, 1992.

[53] J. L. Brédas, D. Beljonne, J. Cornil, J. P. Calbert, Z. Shuai, and R. Silbey, "Electronic structure of p-conjugated oligomers and polymers: a quantum-chemical approach to transport properties," *Synthetic Metals*, vol. 125, no. 1, pp. 107–116, 2001.

[54] G. L. Closs, L. T. Calcaterra, N. J. Green, K. W. Penfield, and J. R. Miller, "Distance, stereoelectronic effects, and the Marcus inverted region in intramolecular electron transfer in organic radical anions," *The Journal of Physical Chemistry*, vol. 90, no. 16, pp. 3673–3683, 1986.

[55] L. Onsager, "Initial Recombination of Ions," *Physical Review*, vol. 54, pp. 554–557, 1938.

[56] C. L. Braun, "Electric field assisted dissociation of charge transfer states as a mechanism of photocarrier production," *The Journal of Chemical Physics*, vol. 80, no. 9, p. 4157, 1984.

[57] F. Bloch, "Über die Quantenmechanik der Elektronen in Kristallgittern," *Zeitschrift für Physik*, vol. 52, pp. 555–600, July 1929.

[58] K. Müllen and G. Wegner, "What does materials science learn from conjugated oligomers?," *Advanced Materials*, vol. 10, pp. 433–436, Apr. 1998.

[59] B. Baumeier, "Charge and Energy Transfer Dynamics in Molecular Systems," 2015.

[60] H. Bassler, "Charge Transport in Disordered Organic Photoconductors," *Physica. Status. Solidi. B, Basic Research*, vol. 175, 1993.

[61] P. W. M. Blom, M. J. M. de Jong, and M. G. van Munster, "Electric-field and temperature dependence of the hole mobility in poly(p-phenylene vinylene)," *Physical Review B*, vol. 55, pp. R656–R659, Jan. 1997.

[62] R. Richert, H. Bässler, B. Ries, B. Movaghar, and M. Grünewald, "Frustrated energy relaxation in an organic glass," *Philosophical Magazine Letters*, vol. 59, pp. 95–102, Feb. 1989.

[63] B. Movaghar, B. Ries, and M. Grünewald, "Diffusion and relaxation of energy in disordered systems: Departure from mean-field theories," *Physical Review B*, vol. 34, pp. 5574–5582, Oct. 1986.

[64] B. Ries, H. Bässler, M. Grünewald, and B. Movaghar, "Monte Carlo study of relaxation and diffusion in glassy systems," *Physical Review B*, vol. 37, pp. 5508–5517, Apr. 1988.

[65] H. Kim, *Organic Lasing: Correlation between Molecular Structure, Optical and Optoelectronic Properties*. PhD thesis, Johannes Gutenberg-Universität Mainz, 2012.

[66] A. Miller and E. Abrahams, "Impurity Conduction at Low Concentrations," *Physical Review*, vol. 120, pp. 745–755, Nov. 1960.

[67] V. Coropceanu, J. Cornil, D. A. da Silva Filho, Y. Olivier, R. Silbey, and J.-L. Brédas, "Charge Transport in Organic Semiconductors," *Chemical Reviews*, vol. 107, pp. 926–952, Apr. 2007.

[68] I. A. Howard and F. Laquai, "Optical Probes of Charge Generation and Recombination in Bulk Heterojunction Organic Solar Cells," *Macromolecular Chemistry and Physics*, vol. 211, no. 19, pp. 2063–2070, 2010.

[69] S. Westenhoff, I. A. Howard, J. M. Hodgkiss, K. R. Kirov, H. A. Bronstein, C. K. Williams, N. C. Greenham, and R. H. Friend, "Charge Recombination in Organic Photovoltaic Devices with High Open-Circuit Voltages," *Journal of the American Chemical Society*, vol. 130, pp. 13653–13658, Oct. 2008.

[70] R. Mauer, *Charge Generation, Transport and Recombination in Organic Solar Cells*. PhD thesis, Johannes Gutenberg-Universität Mainz, 2011.

[71] C. Deibel, A. Baumann, and V. Dyakonov, "Polaron recombination in pristine and annealed bulk heterojunction solar cells," *Applied Physics Letters*, vol. 93, no. 16, p. 163303, 2008.

[72] G. Juška, K. Arlauskas, J. Stuchlik, and R. Österbacka, "Non-Langevin bimolecular recombination in low-mobility materials," *Journal of Non-Crystalline Solids*, vol. 352, no. 9-20 SPEC. ISS., pp. 1167–1171, 2006.

[73] T. M. Clarke, F. C. Jamieson, and J. R. Durrant, "Transient Absorption Studies of Bimolecular Recombination Dynamics in Polythiophene/Fullerene Blend Films," *The Journal of Physical Chemistry C*, vol. 113, pp. 20934–20941, Dec. 2009.

[74] C. G. Shuttle, B. O'Regan, A. M. Ballantyne, J. Nelson, D. D. C. Bradley, J. de Mello, and J. R. Durrant, "Experimental determination of the rate law for charge carrier decay in a polythiophene: Fullerene solar cell," *Applied Physics Letters*, vol. 92, no. 9, p. 093311, 2008.

[75] G. JusÌŒka, K. GenevicÌŒius, N. NekrasÌŒas, G. SliauzÌŒys, and R. OÌ^sterbacka, "Two dimensional Langevin recombination in regioregular poly(3-hexylthiophene)," *Applied Physics Letters*, vol. 95, no. 1, p. 013303, 2009.

[76] N. S. Sariciftci, D. Braun, C. Zhang, V. I. Srdanov, A. J. Heeger, G. Stucky, and F. Wudl, "Semiconducting polymer-buckminsterfullerene heterojunctions: Diodes, photodiodes, and photovoltaic cells," *Applied Physics Letters*, vol. 62, no. 6, pp. 585–587, 1993.

[77] J. J. M. Halls, C. A. Walsh, N. Greenham, C., E. A. Marseglia, R. Friend, H., S. C. Moratti, A. Holmes, and B., "Efficient photodiodes from interpenetrating polymer networks," *Nature*, vol. 376, pp. 498–500, Aug. 1995.

[78] F. Wudl and G. Srdanov, "Conducting polymer formed of poly(2-methoxy,5-(2'-ethyl-hexyloxy)-p-phenylenevinylene)," 1993.

[79] J. C. Hummelen, B. W. Knight, F. LePeq, F. Wudl, J. Yao, and C. L. Wilkins, "Preparation and Characterization of Fulleroid and Methanofullerene Derivatives," *The Journal of Organic Chemistry*, vol. 60, pp. 532–538, Feb. 1995.

[80] C. J. Brabec, S. E. Shaheen, C. Winder, N. S. Sariciftci, and P. Denk, "Effect of LiF/metal electrodes on the performance of plastic solar cells," *Applied Physics Letters*, vol. 80, no. 7, pp. 1288–1290, 2002.

[81] M. M. Wienk, J. M. Kroon, W. J. H. Verhees, J. Knol, J. C. Hummelen, P. a. van Hal, and R. a. J. Janssen, "Efficient methano[70]fullerene/MDMO-PPV bulk heterojunction photovoltaic cells.," *Angewandte Chemie (International ed. in English)*, vol. 42, no. 29, pp. 3371–3375, 2003.

[82] M. D. Irwin, D. B. Buchholz, A. W. Hains, R. P. H. Chang, and T. J. Marks, "p-Type semiconducting nickel oxide as an efficiency-enhancing anode interfacial layer in polymer bulk-heterojunction solar cells," *Proceedings of the National Academy of Sciences*, vol. 105, no. 8, pp. 2783–2787, 2008.

[83] I. Etxebarria, J. Ajuria, and R. Pacios, "Solution-processable polymeric solar cells: A review on materials, strategies and cell architectures to overcome 10%," *Organic Electronics*, vol. 19, pp. 34–60, 2015.

[84] F. C. Krebs, M. Biancardo, B. Winther-Jensen, H. Spanggard, and J. Alstrup, "Strategies for incorporation of polymer photovoltaics into garments and textiles," *Solar Energy Materials and Solar Cells*, vol. 90, pp. 1058–1067, May 2006.

[85] F. C. Krebs, H. Spanggard, T. Kjær, M. Biancardo, and J. Alstrup, "Large area plastic solar cell modules," *Materials Science and Engineering: B*, vol. 138, pp. 106–111, Mar. 2007.

[86] M. T. Dang, L. Hirsch, and G. Wantz, "P3HT:PCBM, best seller in polymer photovoltaic research," *Advanced Materials*, vol. 23, no. 31, pp. 3597–3602, 2011.

[87] N. Blouin, A. Michaud, D. Gendron, S. Wakim, E. Blair, R. Neagu-Plesu, M. Belletête, G. Durocher, Y. Tao, and

M. Leclerc, "Toward a Rational Design of Poly(2,7-Carbazole) Derivatives for Solar Cells," *Journal of the American Chemical Society*, vol. 130, pp. 732–742, Jan. 2008.

[88] N. Blouin, A. Michaud, and M. Leclerc, "A low-bandgap poly(2,7-carbazole) derivative for use in high-performance solar cells," *Advanced Materials*, vol. 19, no. 17, pp. 2295–2300, 2007.

[89] S. H. Park, A. Roy, S. Beaupré, S. Cho, N. Coates, J. S. Moon, D. Moses, M. Leclerc, K. Lee, and A. J. Heeger, "Bulk heterojunction solar cells with internal quantum efficiency approaching 100%," *Nature Photonics*, vol. 3, pp. 297–302, May 2009.

[90] H. Lu, B. Akgun, and T. P. Russell, "Morphological Characterization of a Low-Bandgap Crystalline Polymer:PCBM Bulk Heterojunction Solar Cells," *Advanced Energy Materials*, vol. 1, pp. 870–878, Oct. 2011.

[91] S. Albrecht, S. Schäfer, I. Lange, S. Yilmaz, I. Dumsch, S. Allard, U. Scherf, A. Hertwig, and D. Neher, "Light management in PCPDTBT:PC70BM solar cells: A comparison of standard and inverted device structures," *Organic Electronics*, vol. 13, pp. 615–622, Apr. 2012.

[92] Y. Liang, D. Feng, Y. Wu, S.-T. Tsai, G. Li, C. Ray, and L. Yu, "Highly Efficient Solar Cell Polymers Developed via Fine-Tuning of Structural and Electronic Properties," *Journal of the American Chemical Society*, vol. 131, pp. 7792–7799, June 2009.

[93] Z. He, C. Zhong, S. Su, M. Xu, H. Wu, and Y. Cao, "Enhanced power-conversion efficiency in polymer solar cells using an inverted device structure," *Nature Photonics*, vol. 6, no. 9, pp. 593–597, 2012.

[94] Y. Liu, J. Zhao, Z. Li, C. Mu, W. Ma, H. Hu, K. Jiang, H. Lin, H. Ade, and H. Yan, "Multiple Cases of High-Efficiency Polymer Solar Cells," *Nature Communications*, vol. 5, no. 9, pp. 1–8, 2014.

[95] I. Etxebarria, J. Ajuria, and R. Pacios, "Polymer:fullerene solar cells: materials, processing issues, and cell layouts to reach power conversion efficiency over 10%, a review," *Journal of Photonics for Energy*, vol. 5, no. 1, p. 057214, 2015.

[96] Y.-C. Huang, C.-S. Tsao, C.-M. Chuang, C.-H. Lee, F.-H. Hsu, H.-C. Cha, C.-Y. Chen, T.-H. Lin, C.-J. Su, U.-S. Jeng, and W.-F. Su, "Small- and Wide-Angle X-ray Scattering Characterization of Bulk Heterojunction Polymer Solar Cells with Different Fullerene Derivatives," *The Journal of Physical Chemistry C*, vol. 116, pp. 10238–10244, May 2012.

[97] Y. He, H.-Y. Chen, J. Hou, and Y. Li, "Indeneâ^'C 60 Bisadduct: A New Acceptor for High-Performance Polymer Solar Cells," *Journal of the American Chemical Society*, vol. 132, pp. 1377–1382, Feb. 2010.

[98] G. Zhao, Y. He, and Y. Li, "6.5% Efficiency of Polymer Solar Cells Based on poly(3-hexylthiophene) and Indene-C60 Bisadduct by Device Optimization," *Advanced Materials*, vol. 22, pp. 4355–4358, Oct. 2010.

[99] S. Rajaram, R. Shivanna, S. K. Kandappa, and K. S. Narayan, "Nonplanar Perylene Diimides as Potential Alternatives to Fullerenes in Organic Solar Cells," *The Journal of Physical Chemistry Letters*, vol. 3, pp. 2405–2408, Sept. 2012.

[100] J. Zhao, Y. Li, H. Lin, Y. Liu, K. Jiang, C. Mu, T. Ma, J. Y. Lin Lai, H. Hu, D. Yu, and H. Yan, "High-efficiency non-fullerene organic solar cells enabled by a difluorobenzothiadiazole-based donor polymer combined with a properly matched small molecule acceptor," *Energy Environ. Sci.*, vol. 8, no. 2, pp. 520–525, 2015.

[101] F. G. Brunetti, X. Gong, M. Tong, A. J. Heeger, and F. Wudl, "Strain and Hückel Aromaticity: Driving Forces for a Promising New Generation of Electron Acceptors in Organic Electronics," *Angewandte Chemie International Edition*, vol. 49, pp. 532–536, Jan. 2010.

[102] P. Sonar, G.-M. Ng, T. T. Lin, A. Dodabalapur, and Z.-K. Chen, "Solution processable low bandgap diketopyrrolopyrrole (DPP) based derivatives: novel acceptors for organic solar cells," *Journal of Materials Chemistry*, vol. 20, no. 18, p. 3626, 2010.

[103] P. E. Schwenn, K. Gui, A. M. Nardes, K. B. Krueger, K. H. Lee, K. Mutkins, H. Rubinstein-Dunlop, P. E. Shaw, N. Kopidakis, P. L. Burn, and P. Meredith, "A Small Molecule Non-fullerene Electron Acceptor for Organic Solar Cells," *Advanced Energy Materials*, vol. 1, pp. 73–81, Jan. 2011.

[104] Y. Shu, Y.-F. Lim, Z. Li, B. Purushothaman, R. Hallani, J. E. Kim, S. R. Parkin, G. G. Malliaras, and J. E. Anthony, "A survey of electron-deficient pentacenes as acceptors in polymer bulk heterojunction solar cells," *Chem. Sci.*, vol. 2, no. 2, pp. 363–368, 2011.

[105] E. Ahmed, G. Ren, F. S. Kim, E. C. Hollenbeck, and S. A. Jenekhe, "Design of New Electron Acceptor Materials for Organic Photovoltaics: Synthesis, Electron Transport,

Photophysics, and Photovoltaic Properties of Oligothiophene-Functionalized Naphthalene Diimides," *Chemistry of Materials*, vol. 23, pp. 4563–4577, Oct. 2011.

[106] H. Kim, S. Nam, J. Jeong, S. Lee, J. Seo, H. Han, and Y. Kim, "Organic solar cells based on conjugated polymers : History and recent advances," *Korean Journal of Chemical Engineering*, vol. 31, no. 7, pp. 1095–1104, 2014.

[107] J. T. Bloking, X. Han, A. T. Higgs, J. P. Kastrop, L. Pandey, J. E. Norton, C. Risko, C. E. Chen, J.-L. Brédas, M. D. McGehee, and A. Sellinger, "Solution-Processed Organic Solar Cells with Power Conversion Efficiencies of 2.5% using Benzothiadiazole/Imide-Based Acceptors," *Chemistry of Materials*, vol. 23, pp. 5484–5490, Dec. 2011.

[108] R. H. Friend, M. Granström, K. Petritsch, A. C. Arias, A. Lux, and M. R. Andersson, "Laminated fabrication of polymeric photovoltaic diodes," *Nature*, vol. 395, pp. 257–260, Sept. 1998.

[109] T. W. Holcombe, C. H. Woo, D. F. Kavulak, B. C. Thompson, and J. M. J. Freèchet, "All-Polymer Photovoltaic Devices of Poly(3-(4- n -octyl)-phenylthiophene) from Grignard Metathesis (GRIM) Polymerization," *Journal of the American Chemical Society*, vol. 131, pp. 14160–14161, Oct. 2009.

[110] T. Earmme, Y.-J. Hwang, N. M. Murari, S. Subramaniyan, and S. A. Jenekhe, "All-Polymer Solar Cells with 3.3% Efficiency Based on Naphthalene Diimide-Selenophene Copolymer Acceptor," *Journal of the American Chemical Society*, vol. 135, pp. 14960–14963, Oct. 2013.

[111] Y.-J. Hwang, T. Earmme, B. A. E. Courtright, F. N. Eberle, and S. A. Jenekhe, "n-Type Semiconducting Naphthalene Diimide-Perylene Diimide Copolymers: Controlling Crystallinity, Blend Morphology, and Compatibility Toward High-Performance All-Polymer Solar Cells," *Journal of the American Chemical Society*, vol. 137, pp. 4424–4434, Apr. 2015.

[112] NREL, "ASTM G173-03 Reference Spectra," 2015.

[113] Nanolearning, "Solar Spectrum and Air Mass," 2013.

[114] G. Li, R. Zhu, and Y. Yang, "Polymer solar cells," *Nature Photonics*, vol. 6, no. 3, pp. 153–161, 2012.

[115] M. C. Scharber, D. Mühlbacher, M. Koppe, P. Denk, C. Waldauf, A. J. Heeger, and C. J. Brabec, "Design Rules for Donors in Bulk-Heterojunction Solar Cellsâ€"Towards 10 % Energy-Conversion Efficiency," *Advanced Materials*, vol. 18, pp. 789–794, Mar. 2006.

[116] D. Chen, F. Liu, C. Wang, A. Nakahara, and T. P. Russell, "Bulk Heterojunction Photovoltaic Active Layers via Bilayer Interdiffusion," *Nano Letters*, vol. 11, pp. 2071–2078, May 2011.

[117] Y. Liang, Y. Wu, D. Feng, S.-T. Tsai, H.-J. Son, G. Li, and L. Yu, "Development of new semiconducting polymers for high performance solar cells.," *Journal of the American Chemical Society*, vol. 131, no. 1, pp. 56–57, 2009.

[118] H. Mangold, *Charge separation and recombination in novel polymeric absorber materials for organic solar cells - a photophysical study*. PhD thesis, Johannes Gutenberg-Universität Mainz, 2013.

[119] Y. Liang and L. Yu, "A New Class of Semiconducting Polymers for Bulk Heterojunction Solar Cells with Exceptionally High Performance," *Accounts of Chemical Research*, vol. 43, pp. 1227–1236, Sept. 2010.

[120] J. A. Pople, "Molecular Orbital Perturbation Theory. I. A Perturbation Method Based on Self-Consistent Orbitals," *Proceedings of the Royal Society A: Mathematical, Physical and Engineering Sciences*, vol. 233, pp. 233–241, Dec. 1955.

[121] H. Zhou, L. Yang, A. C. Stuart, S. C. Price, S. Liu, and W. You, "Development of Fluorinated Benzothiadiazole as a Structural Unit for a Polymer Solar Cell of 7 % Efficiency," *Angewandte Chemie International Edition*, vol. 50, pp. 2995–2998, Mar. 2011.

[122] T.-Y. Chu, J. Lu, S. Beaupreè, Y. Zhang, J.-R. Pouliot, S. Wakim, J. Zhou, M. Leclerc, Z. Li, J. Ding, and Y. Tao, "Bulk Heterojunction Solar Cells Using Thieno[3,4-c]pyrrole-4,6-dione and Dithieno[3,2-b:2′,3′-d]silole Copolymer with a Power Conversion Efficiency of 7.3%," *Journal of the American Chemical Society*, vol. 133, pp. 4250–4253, Mar. 2011.

[123] C. M. Amb, S. Chen, K. R. Graham, J. Subbiah, C. E. Small, F. So, and J. R. Reynolds, "Dithienogermole As a Fused Electron Donor in Bulk Heterojunction Solar Cells," *Journal of the American Chemical Society*, vol. 133, pp. 10062–10065, July 2011.

[124] L. Dou, W. H. Chang, J. Gao, C. C. Chen, J. You, and Y. Yang, "A selenium-substituted low-bandgap polymer with versatile photovoltaic applications," *Advanced Materials*, vol. 25, no. 6, pp. 825–831, 2013.

[125] K. H. Hendriks, G. H. L. Heintges, V. S. Gevaerts, M. M. Wienk, and R. a. J. Janssen, "High-molecular-weight regular alternating diketopyrrolopyrrole-based terpolymers for efficient organic solar cells," *Angewandte Chemie - International Edition*, vol. 52, no. 32, pp. 8341–8344, 2013.

[126] J.-H. Kim, M. Lee, H. Yang, and D.-H. Hwang, "A high molecular weight triisopropylsilylethynyl (TIPS)-benzodithiophene and diketopyrrolopyrrole-based copolymer for high performance organic photovoltaic cells," *Journal of Materials Chemistry A*, vol. 2, no. 18, pp. 6348–6352, 2014.

[127] J. Li, Y. Zhao, H. S. Tan, Y. Guo, C.-A. Di, G. Yu, Y. Liu, M. Lin, S. H. Lim, Y. Zhou, H. Su, and B. S. Ong, "A stable solution-processed polymer semiconductor with record high-mobility for printed transistors," *Scientific Reports*, vol. 2, p. 754, Oct. 2012.

[128] C. Kanimozhi, N. Yaacobi-gross, K. W. Chou, A. Amassian, T. D. Anthopoulos, and S. Patil, "Diketopyrrolopyrrole - Diketopyrrolopyrrole-Based Conjugated Copolymer for High-Mobility Organic Field-Effect Transistors," *J Am Chem Soc*, vol. 134, pp. 16532–16535, 2012.

[129] Y. N. Li, P. Sonar, L. Murphy, and W. Hong, "High mobility diketopyrrolopyrrole (DPP)-based organic semiconductor materials for organic thin film transistors and photovoltaics," *Energy & Environmental Science*, vol. 6, no. 6, pp. 1684–1710, 2013.

[130] B. Tieke, A. R. Rabindranath, K. Zhang, and Y. Zhu, "Conjugated polymers containing diketopyrrolopyrrole units in the main chain," *Beilstein J Org Chem*, vol. 6, pp. 830–845, 2010.

[131] D. G. Farnum, G. Mehta, G. G. Moore, and F. P. Siegal, "Attempted reformatskii reaction of benzonitrile, 1,4-diketo-3,6-diphenylpyrrolo[3,4-C]pyrrole. A lactam analogue of pentalene.," *Tetrahedron Letters*, vol. 15, pp. 2549–2552, Jan. 1974.

[132] A. Iqbal, M. Jost, R. Kirchmayr, J. Pfenninger, A. Rochat, and O. Wallquist, "The synthesis and properties of 1,4-diketopyrrolo[3,4-C]pyrroles," *Bulletin des Sociétés Chimiques Belges*, vol. 97, pp. 615–644, Sept. 2010.

[133] O. Wallquist and R. Lenz, "No Title," *Macromolecular Symposia*, vol. 187, pp. 617–630, Sept. 2002.

[134] S. R. Waldvogel, "Personal Conversation," 2014.

[135] Wikipedia, "Diketopyrrolopyrrol-Pigmente," 2015.

[136] M. Fukuda, K. Kodama, H. Yamamoto, and K. Mito, "Evaluation of new organic pigments as laser-active media for a solid-state dye laser," *Dyes and Pigments*, vol. 63, pp. 115–125, Nov. 2004.

[137] Z. Qiao, Y. Xu, S. Lin, J. Peng, and D. Cao, "Synthesis and characterization of red-emitting diketopyrrolopyrrole-alt-phenylenevinylene polymers," *Synthetic Metals*, vol. 160, pp. 1544–1550, July 2010.

[138] Y. Jiang, Y. Wang, J. Hua, J. Tang, B. Li, S. Qian, and H. Tian, "Multibranched triarylamine end-capped triazines with aggregation-induced emission and large two-photon absorption cross-sections," *Chemical Communications*, vol. 46, no. 26, p. 4689, 2010.

[139] M. M. Wienk, M. Turbiez, J. Gilot, and R. A. J. Janssen, "Narrow-Bandgap Diketo-Pyrrolo- Pyrrole Polymer Solar Cells: The Effect of Processing on the Performance," *Adv Mater*, vol. 20, no. 13, pp. 2556–2560, 2008.

[140] L. Bürgi, M. Turbiez, R. Pfeiffer, F. Bienewald, H.-J. Kirner, and C. Winnewisser, "High-Mobility Ambipolar Near-Infrared Light-Emitting Polymer Field-Effect Transistors," *Advanced Materials*, vol. 20, pp. 2217–2224, June 2008.

[141] S. Qu and H. Tian, "Diketopyrrolopyrrole (DPP)-based materials for organic photovoltaics," *Chemical Communications*, vol. 48, no. 25, p. 3039, 2012.

[142] J. C. Bijleveld, "Poly (diketopyrrolopyrrole- terthiophene) for Ambipolar Logic and Photovoltaics," *Journal of the . . .*, pp. 6–7, 2009.

[143] F. Liu, Y. Gu, C. Wang, W. Zhao, D. Chen, A. L. Briseno, and T. P. Russell, "Efficient Polymer Solar Cells Based on a Low Bandgap Semi-crystalline DPP Polymer-PCBM Blends," *Advanced Materials*, vol. 24, pp. 3947–3951, Aug. 2012.

[144] A. T. Yiu, P. M. Beaujuge, O. P. Lee, C. H. Woo, M. F. Toney, and J. M. J. Fréchet, "Side-Chain Tunability of Furan-Containing Low-Band-Gap Polymers Provides Control of Structural Order in Efficient Solar Cells," *Journal of the American Chemical Society*, vol. 134, pp. 2180–2185, Feb. 2012.

[145] C. H. Woo, P. M. Beaujuge, T. W. Holcombe, O. P. Lee, and J. M. J. Fréchet, "Incorporation of furan into low band-gap polymers for efficient solar cells," *Journal of the American Chemical Society*, vol. 132, no. 44, pp. 15547–15549, 2010.

[146] L. Dou, J. You, J. Yang, C.-C. Chen, Y. He, S. Murase, T. Moriarty, K. Emery, G. Li, and Y. Yang, "Tandem polymer solar cells featuring a spectrally matched low-bandgap polymer," *Nature Photonics*, vol. 6, no. 3, pp. 180–185, 2012.

[147] M. Meister, *Charge generation and recombination in hybrid organic/inorganic solar cells*. Phd thesis, Johannes Gutenberg-Universität Mainz, 2013.

[148] A. de Juan and R. Tauler, "Chemometrics applied to unravel multicomponent processes and mixtures," *Analytica Chimica Acta*, vol. 500, no. 1-2, pp. 195–210, 2003.

[149] J. Jaumot, R. Gargallo, A. de Juan, and R. Tauler, "A graphical user-friendly interface for MCR-ALS: a new tool for multivariate curve resolution in MATLAB," *Chemometrics and Intelligent Laboratory Systems*, vol. 76, no. 1, pp. 101–110, 2005.

[150] I. A. Howard, H. Mangold, F. Etzold, D. Gehrig, and F. Laquai, "Transient absorption data analysis by soft-modeling," in *Ultrafast Dynamics in Molecules, Nanostructures and Interfaces*, vol. Series in, World scientific, 2013.

[151] F. Laquai, *Electronic energy transfer processes and charge carrier transport in pi-conjugated polymers*. Phd thesis, Johannes Gutenberg-Universität Mainz, 2006.

[152] J. R. Ochsmann, D. Chandran, D. W. Gehrig, H. Anwar, P. K. Madathil, K.-S. Lee, and F. Laquai, "Triplet State Formation in Photovoltaic Blends of DPP-Type Copolymers and PC71BM," *Macromolecular Rapid Communications*, vol. 36, no. 11, pp. 1122–1128, 2015.

[153] W. Li, W. S. C. Roelofs, M. M. Wienk, and R. a. J. Janssen, "Enhancing the photocurrent in diketopyrrolopyrrole-based polymer solar cells via energy level control," *Journal of the American Chemical Society*, vol. 134, no. 33, pp. 13787–13795, 2012.

[154] V. S. Gevaerts, A. Furlan, M. M. Wienk, M. Turbiez, and R. A. J. Janssen, "Solution Processed Polymer Tandem Solar Cell Using Efficient Small and Wide bandgap Polymer:Fullerene Blends," *Advanced Materials*, vol. 24, pp. 2130–2134, Apr. 2012.

[155] G. D. Spyropoulos, P. Kubis, N. Li, L. Lucera, M. Salvador, D. Baran, F. Machui, T. Ameri, M. M. Voigt, and C. J. Brabec, "Flexible organic tandem solar modules: a story of up-scaling," in *SPIE 9184, Organic Photovoltaics XV* (Z. H. Kafafi, P. A. Lane, and I. D. W. Samuel, eds.), Oct. 2014.

[156] J. G. Tait, C. Wong, D. Cheyns, M. Turbiez, B. P. Rand, and P. Heremans, "Ultrasonic Spray Coating of 6.5% Efficient Diketopyrrolopyrrole-Based Organic Photovoltaics," *IEEE Journal of Photovoltaics*, vol. 4, pp. 1538–1544, Nov. 2014.

[157] J. G. Tait, T. Merckx, W. Li, C. Wong, R. Gehlhaar, D. Cheyns, M. Turbiez, and P. Heremans, "Determination of Solvent Systems for Blade Coating Thin Film Photovoltaics," *Advanced Functional Materials*, vol. 25, pp. 3393–3398, June 2015.

[158] N. Li, D. Baran, G. D. Spyropoulos, H. Zhang, S. Berny, M. Turbiez, T. Ameri, F. C. Krebs, and C. J. Brabec, "Environmentally Printing Efficient Organic Tandem Solar Cells with High Fill Factors: A Guideline Towards 20% Power Conversion Efficiency," *Advanced Energy Materials*, vol. 4, pp. n/a–n/a, Aug. 2014.

[159] J. Adams, G. D. Spyropoulos, M. Salvador, N. Li, S. Strohm, L. Lucera, S. Langner, F. Machui, H. Zhang, T. Ameri, M. M. Voigt, F. C. Krebs, and C. J. Brabec, "Air-processed organic tandem solar cells on glass: toward competitive operating lifetimes," *Energy Environ. Sci.*, vol. 8, no. 1, pp. 169–176, 2015.

[160] D. Bartesaghi, M. Turbiez, and L. J. A. Koster, "Charge transport and recombination in PDPP5T:[70]PCBM organic solar cells: The influence of morphology," *Organic Electronics*, vol. 15, pp. 3191–3202, Nov. 2014.

[161] S. Kouijzer, J. J. Michels, M. Van Den Berg, V. S. Gevaerts, M. Turbiez, M. M. Wienk, and R. a. J. Janssen, "Predicting morphologies of solution processed polymer:Fullerene blends," *Journal of the American Chemical Society*, vol. 135, no. 32, pp. 12057–12067, 2013.

[162] M. Pfannmöller, H. Heidari, L. Nanson, O. R. Lozman, M. Chrapa, T. Offermans, G. Nisato, and S. Bals, "Quantitative Tomography of Organic Photovoltaic Blends at the Nanoscale," *Nano Letters*, p. 150924132159008, 2015.

[163] J. J. van Franeker, M. Turbiez, W. Li, M. M. Wienk, and R. A. Janssen, "A real-time study of the benefits of co-solvents in polymer solar cell processing," *Nature Communications*, vol. 6, p. 6229, Feb. 2015.

[164] W. Li, W. S. C. Roelofs, M. M. Wienk, and R. A. J. Janssen, "Enhancing the Photocurrent in Diketopyrrolopyrrole-Based Polymer Solar Cells via Energy Level Control," *Journal of the American Chemical Society*, vol. 134, pp. 13787–13795, Aug. 2012.

[165] J. C. Bijleveld, V. S. Gevaerts, D. Di Nuzzo, M. Turbiez, S. G. Mathijssen, D. M. de Leeuw, M. M. Wienk, and R. A. Janssen, "Efficient solar cells based on an easily accessible diketopyrrolopyrrole polymer," *Adv Mater*, vol. 22, no. 35, pp. E242–6, 2010.

[166] D. Di Nuzzo, A. Aguirre, M. Shahid, V. S. Gevaerts, S. C. J. Meskers, and R. A. J. Janssen, "Improved Film Morphology Reduces Charge Carrier Recombination into the Triplet Excited State in a Small Bandgap Polymer-Fullerene Photovoltaic Cell," *Advanced Materials*, vol. 22, pp. 4321–4324, Oct. 2010.

[167] Y. W. Soon, H. Cho, J. Low, H. Bronstein, I. McCulloch, and J. R. Durrant, "Correlating triplet yield, singlet oxygen generation and photochemical stability in polymer/fullerene blend films," *Chemical Communications*, vol. 49, no. 13, pp. 1291–1293, 2013.

[168] A. Rao, P. C. Y. Chow, S. Gélinas, C. W. Schlenker, C.-Z. Li, H.-L. Yip, A. K.-Y. Jen, D. S. Ginger, and R. H. Friend, "The role of spin in the kinetic control of recombination in organic photovoltaics.," *Nature*, vol. 500, no. 7463, pp. 435–9, 2013.

[169] P. C. Y. Chow, S. Gélinas, A. Rao, and R. H. Friend, "Quantitative Bimolecular Recombination in Organic Photovoltaics through Triplet Exciton Formation," *J Am Chem Soc*, vol. 136, no. 9, pp. 3424–3429, 2014.

[170] S. D. Dimitrov, S. Wheeler, D. Niedzialek, B. C. Schroeder, H. Utzat, J. M. Frost, J. Yao, A. Gillett, P. S. Tuladhar, I. McCulloch, J. Nelson, and J. R. Durrant, "Polaron pair mediated triplet generation in polymer/fullerene blends," *Nature Communications*, vol. 6, p. 6501, Mar. 2015.

[171] F. Etzold, I. A. Howard, N. Forler, A. Melnyk, D. Andrienko, M. R. Hansen, and F. Laquai, "Sub-ns triplet state formation by non-geminate recombination in PSBTBT:PC 70 BM and PCPDTBT:PC 60 BM organic solar cells," *Energy Environ. Sci.*, vol. 8, no. 5, pp. 1511–1522, 2015.

[172] D. W. Gehrig, I. a. Howard, and F. Laquai, "Charge Carrier Generation Followed by Triplet State Formation, Annihilation, and Carrier Recreation in PBDTTT-C:PC $_{60}$ BM Photovoltaic Blends," *The Journal of Physical Chemistry C*, p. 150522140657008, 2015.

[173] T. Basel, U. Huynh, T. Zheng, T. Xu, L. Yu, and Z. V. Vardeny, "Optical, Electrical, and Magnetic Studies of Organic Solar Cells Based on Low Bandgap Copolymer with Spin 1/2 Radical Additives," *Advanced Functional Materials*, pp. n/a–n/a, 2015.

[174] S. Van Bavel, S. Veenstra, and J. Loos, "On the importance of morphology control in polymer solar cells," *Macromolecular Rapid Communications*, vol. 31, no. 21, pp. 1835–1845, 2010.

[175] M. a. Ruderer and P. Müller-Buschbaum, "Morphology of polymer-based bulk heterojunction films for organic photovoltaics," *Soft Matter*, vol. 7, no. 12, p. 5482, 2011.

[176] F. Liu, Y. Gu, J. W. Jung, W. H. Jo, and T. P. Russell, "On the morphology of polymer-based photovoltaics," *Journal of Polymer Science, Part B: Polymer Physics*, vol. 50, no. 15, pp. 1018–1044, 2012.

[177] M. Dante, a. Garcia, and T. Q. Nguyen, "Three-Dimensional Nanoscale Organization of Highly Efficient Low Band-Gap Conjugated Polymer Bulk Heterojunction Solar Cells," *Journal of Physical Chemistry C*, vol. 113, pp. 1596–1600, 2009.

[178] B. a. Collins, Z. Li, J. R. Tumbleston, E. Gann, C. R. Mcneill, and H. Ade, "Absolute measurement of domain composition and nanoscale size distribution explains performance in PTB7:PC71bm solar cells," *Advanced Energy Materials*, vol. 3, no. 1, pp. 65–74, 2013.

[179] M. J. Im, S. Y. Son, B. J. Moon, G. Y. Lee, J. H. Kim, and T. Park, "Improved photovoltaic performance by enhanced crystallinity of poly(3-hexyl)thiophene," *Organic Electronics: physics, materials, applications*, vol. 14, no. 11, pp. 3046–3051, 2013.

[180] L. J. a. Koster, "Charge carrier mobility in disordered organic blends for photovoltaics," *Physical Review B - Condensed Matter and Materials Physics*, vol. 81, no. 20, pp. 1–7, 2010.

[181] T. Martens, J. D'Haen, T. Munters, Z. Beelen, L. Goris, J. Manca, M. D'Olieslaeger, D. Vanderzande, L. De Schepper, and R. Andriessen, "Disclosure of the nanostructure of MDMO-PPV:PCBM bulk hetero-junction organic solar cells by a combination of SPM and TEM," *Synthetic Metals*, vol. 138, no. 1-2, pp. 243–247, 2003.

[182] F. Zhang, K. G. Jespersen, C. Björström, M. Svensson, M. R. Andersson, V. Sundström, K. Magnusson, E. Moons, A. Yartsev, and O. Inganäs, "Influence of solvent mixing on the morphology and performance of solar cells based on polyfluorene copolymer/fullerene blends," *Advanced Functional Materials*, vol. 16, no. 5, pp. 667–674, 2006.

[183] H. Lv, X. Zhao, W. Xu, H. Li, J. Chen, and X. Yang, "Improving performance of polymer solar cells based on PSBTBT/PC71BM via controlled solvent vapor annealing," *Organic Electronics*, vol. 14, no. 7, pp. 1874–1881, 2013.

[184] S. Kouijzer, J. J. Michels, M. van den Berg, V. S. Gevaerts, M. Turbiez, M. M. Wienk, and R. A. J. Janssen, "Predicting Morphologies of Solution Processed Polymer:Fullerene Blends," *Journal of the American Chemical Society*, vol. 135, pp. 12057–12067, Aug. 2013.

[185] D. Chen, A. Nakahara, D. Wei, D. Nordlund, and T. P. Russell, "P3HT/PCBM bulk heterojunction organic photovoltaics: Correlating efficiency and morphology," *Nano Letters*, vol. 11, no. 2, pp. 561–567, 2011.

[186] Y. Kim, S. Cook, S. M. Tuladhar, S. a. Choulis, J. Nelson, J. R. Durrant, D. D. C. Bradley, M. Giles, I. McCulloch, C.-S. Ha, and M. Ree, "A strong regioregularity effect in self-organizing conjugated polymer films and high-efficiency polythiophene:fullerene solar cells," *Nature Materials*, vol. 5, no. 3, pp. 197–203, 2006.

[187] R. Mauer, M. Kastler, and F. Laquai, "The Impact of Polymer Regioregularity on Charge Transport and Efficiency of P3HT:PCBM Photovoltaic Devices," *Advanced Functional Materials*, vol. 20, no. 13, pp. 2085–2092, 2010.

[188] D. M. DeLongchamp, R. J. Kline, and A. Herzing, "Nanoscale structure measurements for polymer-fullerene photovoltaics," *Energy & Environmental Science*, vol. 5, no. 3, p. 5980, 2012.

[189] A. Fedorov, M. N. Berberan-Santos, J.-P. Lef, and B. Valeur, "Picosecond time-resolved and steady-state studies of the polarization of the fluorescence of C60 and C70," *Chemical Physics Letters*, vol. 4, no. March, pp. 4–8, 1997.

[190] V. Yakutkin, S. Aleshchenkov, S. Chernov, T. Miteva, G. Nelles, A. Cheprakov, and S. Baluschev, "Towards the IR limit of the triplet-triplet annihilation-supported up-comersion: Tetraanthraporphyrin," *Chemistry - A European Journal*, vol. 14, no. 32, pp. 9846–9850, 2008.

[191] I. A. Howard, R. Mauer, M. Meister, and F. Laquai, "Effect of Morphology on Ultrafast Free Carrier Generation in Polythiophene:Fullerene Organic Solar Cells," *J Am Chem Soc*, vol. 132, no. 42, pp. 14866–14876, 2010.

[192] F. Etzold, I. A. Howard, N. Forler, D. M. Cho, M. Meister, H. Mangold, J. Shu, M. R. Hansen, K. Müllen, and F. Laquai, "The Effect of Solvent Additives on Morphology and Excited-State Dynamics in PCPDTBT:PCBM Photovoltaic Blends," *Journal of the American Chemical Society*, vol. 134, pp. 10569–10583, June 2012.

[193] F. Etzold, I. A. Howard, R. Mauer, M. Meister, T.-D. Kim, K.-S. Lee, N. S. Baek, and F. Laquai, "Ultrafast Exciton Dissociation Followed by Nongeminate Charge Recombination in PCDTBT:PCBM Photovoltaic Blends," *Journal of the American Chemical Society*, vol. 133, pp. 9469–9479, June 2011.

[194] D. W. Gehrig, I. A. Howard, S. Sweetnam, T. M. Burke, M. D. Mcgehee, and F. Laquai, "The Impact of Donor - Acceptor Phase Separation on the Charge Carrier Dynamics in pBTTT : PCBM Photovoltaic Blends," *Macromol. Rapid Commun.*, vol. 36, no. D, pp. 1054–1060, 2015.

[195] A. Assadi, C. Svensson, M. Willander, and O. InganaÌ^s, "Field-effect mobility of poly(3-hexylthiophene)," *Applied Physics Letters*, vol. 53, no. 3, p. 195, 1988.

[196] M. Morana, M. Wegscheider, A. Bonanni, N. Kopidakis, S. Shaheen, M. Scharber, Z. Zhu, D. Waller, R. Gaudiana, and C. Brabec, "Bipolar charge transport in PCPDTBT-PCBM bulk-heterojunctions for photovoltaic applications," *Advanced Functional Materials*, vol. 18, no. 12, pp. 1757–1766, 2008.

[197] K. Takagi, T. Nagase, T. Kobayashi, and H. Naito, "Electrical characterization of thieno[3,4-b]thiophene and benzodithiophene copolymer using field-effect transistor configuration," *Jpn. J. Appl. Phys.*, vol. 050305, pp. 5–9, 2014.

[198] S. Subramaniyan, F. S. Kim, G. Ren, H. Li, and S. a. Jenekhe, "High Mobility Thiazole - Diketopyrrolopyrrole Copolymer Semiconductors for High Performance Field-Effect Transistors and Photovoltaic Devices," *Macromolecules*, vol. 45, pp. 9029–9037, 2012.

[199] Z. Yi, X. Sun, Y. Zhao, Y. Guo, X. Chen, J. Qin, G. Yu, and Y. Liu, "Diketopyrrolopyrrole-Based π-Conjugated Copolymer Containing β-Unsubstituted Quintetthiophene Unit: A Promising Material Exhibiting High Hole-Mobility for Organic Thin-Film Transistors," *Chemistry of Materials*, vol. 24, no. 22, pp. 4350–4356, 2012.

[200] J. Melomedov, J. R. Ochsmann, M. Meister, F. Laquai, and K. Heinze, "Aminoferrocene and Ferrocene Amino Acid as Electron Donors in Modular Porphyrin-Ferrocene and Porphyrin-Ferrocene-Porphyrin Conjugates," *European Journal of Inorganic Chemistry*, vol. 2014, pp. 2902–2915, June 2014.

[201] D. Chandran, T. Marszalek, W. Zajaczkowski, P. K. Madathil, R. K. Vijayaraghavan, Y.-H. Koh, S.-y. Park, J. R. Ochsmann, W. Pisula, and K.-S. Lee, "Thin film morphology and charge carrier mobility of diketopyrrolopyrrole based conjugated polymers," *Polymer*, vol. 73, pp. 205–213, Sept. 2015.

[202] W. Li, K. H. Hendriks, W. S. Roelofs, Y. Kim, M. M. Wienk, and R. A. Janssen, "Efficient small bandgap polymer solar cells with high fill factors for 300 nm thick films," *Adv Mater*, vol. 25, no. 23, pp. 3182–3186, 2013.

[203] A. A. Bakulin, A. Rao, V. G. Pavelyev, P. H. M. van Loosdrecht, M. S. Pshenichnikov, D. Niedzialek, J. Cornil, D. Beljonne, and R. H. Friend, "The Role of Driving Energy and Delocalized States for Charge Separation in Organic Semiconductors," *Science*, vol. 335, pp. 1340–1344, Mar. 2012.

[204] Y. Li, P. Sonar, S. P. Singh, Z. E. Ooi, E. S. H. Lek, and M. Q. Y. Loh, "Poly(2,5-bis(2-octyldodecyl)-3,6-di(furan-2-yl)-2,5-dihydro-pyrrolo[3,4-c]pyrrole-1,4-dione-co-thieno[3,2-b]thiophene): a high performance polymer semiconductor for both organic thin film transistors and organic photovoltaics," *Physical Chemistry Chemical Physics*, vol. 14, no. 19, p. 7162, 2012.

[205] F. Etzold, I. a. Howard, N. Forler, A. Melnyk, D. Andrienko, M. R. Hansen, and F. Laquai, "Sub-ns triplet state formation by non-geminate recombination in PSBTBT:PC 70 BM and PCPDTBT:PC 60 BM organic solar cells," *Energy Environ. Sci.*, vol. 8, no. 5, pp. 1511–1522, 2015.

[206] A. J. Ferguson, N. Kopidakis, S. E. Shaheen, and G. Rumbles, "Dark Carriers, Trapping, and Activation Control of Carrier Recombination in Neat P3HT and P3HT:PCBM Blends," *The Journal of Physical Chemistry C*, vol. 115, pp. 23134–23148, Nov. 2011.

[207] I. A. Howard, F. Etzold, F. Laquai, and M. Kemerink, "Nonequilibrium Charge Dynamics in Organic Solar Cells," *Advanced Energy Materials*, vol. 4, pp. n/a–n/a, June 2014.

[208] D. Jarzab, F. Cordella, J. Gao, M. Scharber, H.-J. Egelhaaf, and M. A. Loi, "Low-Temperature Behaviour of Charge Transfer Excitons in Narrow-Bandgap Polymer-Based Bulk Heterojunctions," *Advanced Energy Materials*, vol. 1, pp. 604–609, July 2011.

[209] Y. Tamai, K. Tsuda, H. Ohkita, H. Benten, and S. Ito, "Charge-carrier generation in organic solar cells using crystalline donor polymers," *Phys. Chem. Chem. Phys.*, vol. 16, pp. 20338–20346, June 2014.